

A new approach to predicting Departure from Nucleate Boiling (DNB) from direct representation of boiling heat transfer physics

by
Etienne Demarly

B.S., Engineering, École supérieure d'électricité (Supélec), 2011
M.S., Engineering, École supérieure d'électricité (Supélec), 2012
M.S., Nuclear Engineering, Institut national des sciences et techniques nucléaires (INSTN), 2013

SUBMITTED TO THE
DEPARTMENT OF NUCLEAR SCIENCE AND ENGINEERING

IN PARTIAL FULFILLMENT OF THE REQUIREMENTS FOR THE DEGREE OF
DOCTOR OF PHILOSOPHY IN NUCLEAR SCIENCE AND ENGINEERING

AT THE
MASSACHUSETTS INSTITUTE OF TECHNOLOGY
February 2020

©2020 Massachusetts Institute of Technology
All rights reserved.

Author: _____
Etienne Demarly
Department of Nuclear Science and Engineering
January 3, 2020

Certified by: _____
Emilio Baglietto, Ph.D.
Associate Professor of Nuclear Science and Engineering
Thesis Supervisor

Certified by: _____
Jacopo Buongiorno, Ph.D.
TEPCO Professor of Nuclear Science and Engineering
Thesis Reader

Certified by: _____
John H. Lienhard V, Ph.D.
Abdul Latif Jameel Professor of Mechanical Engineering
Thesis Reader

Accepted by: _____
Ju Li, Ph.D.
Battelle Energy Alliance Professor of Nuclear Science and Engineering
and Professor of Materials Science and Engineering
Department Committee on Graduate Students

A new approach to predicting Departure from Nucleate Boiling (DNB) from direct representation of boiling heat transfer physics

by Etienne Demarly

Submitted to the Department of Nuclear Science and Engineering
on January 3, 2020 in Partial Fulfillment of the Requirements for the Degree of

Doctor of Philosophy
in Nuclear Science and Engineering

Abstract

Accurate prediction of the Departure from Nucleate Boiling (DNB) type of boiling crisis is essential for the design of Pressurized Water Reactors (PWR) and their fuel. Recent advances in the instrumentation of boiling experiments via infrared thermometry have provided new insights on DNB physics that were ignored in past modeling efforts.

The growing consensus from experimental studies that DNB is caused by a microhydrodynamic phenomenon at the boiling surface, instead of the classical macrohydrodynamic scale effects, has yet to be formulated into a working model and applied for simulation of high pressure conditions representative of PWRs. While the idea of an energy imbalance between wetted (in contact with liquid) and dry (in contact with vapor) areas has been suggested by multiple experimental groups [1–6] as a triggering mechanism for DNB, incorporating this new understanding into a functional boiling model remains an open challenge.

Existing approaches to model DNB have not demonstrated the capability to generally “predict” the occurrence of the boiling crisis due to two main reasons: (1) the incomplete or inaccurate physical description of the phenomenon, and/or (2) the absence of consideration of parameters of influence, such as the contact angle or the cavity size distribution which affect DNB. Their modeling capabilities are typically limited to the thermal hydraulic conditions they were initially validated against and are not suitable when extrapolated to new untested conditions.

The present work tackles the development of a new DNB model via a systematic approach that leverages understanding of the boiling crisis at the microscopic scale. From the hypothesized mechanism, a formulation is proposed and is then validated against high resolution data. The concept of heat partitioning for nucleate boiling offers a general framework where the total heat removed at the boiling surface is split between contributions from individual heat transfer mechanisms. In this formulation, the boiling crisis is identified as the onset of instability in the energy balance at the boiling wall.

The model formulation is extended to high pressure, representative of PWR conditions, and benchmarked against relevant DNB data, in comparison to the industry-standard W-3 correlation and CHF Lookup Table. The model is further adopted to evaluate the potential benefits of surface property alterations (contact angle, cavity distribution) in advanced nuclear fuel concepts aiming at delaying the boiling crisis limit.

Thesis Supervisor: Emilio Baglietto
Title: Associate Professor of Nuclear Science and Engineering

Thesis Reader: Jacopo Buongiorno
Title: TEPCO Professor of Nuclear Science and Engineering

Thesis Reader: John H. Lienhard V
Title: Abdul Latif Jameel Professor of Mechanical Engineering

Acknowledgements

The work presented in this thesis is the result of more than four years of work and research on boiling but I would even place the beginning of this American endeavor eight years ago when I was offered the opportunity to complete my engineering education with an internship at MIT. Back in 2012 my experience with CFD, thermalhydraulics, heat transfer and multiphase flows were limited and I still had everything to learn. The idea of pursuing a doctorate in my field was already in the back of my head while studying in France, but it's really my first research experience alongside professor Emilio Baglietto that cemented my decision to apply to MIT and come back for more. Without this first experience, the past eight years would have looked much different.

I am extremely grateful for professor Baglietto taking me in his group in the first place and advising me all along these past six years of graduate school. The practical and theoretical knowledge I accumulated over the years on CFD, heat transfer, boiling and other subjects is by large coming from him and will follow me long after I leave MIT.

The Consortium for Advanced Simulation of Light Water Reactors (CASL) funded my Ph.D. research from end to end and I am extremely thankful for this opportunity. I hope the results presented in this thesis will eventually find their way in the improvement of nuclear reactor design.

I would also like to thank my committee members, John H. Lienhard V and Jacopo Buongiorno who accepted to follow my progress and share their opinion on the research I produced as I was conducting my Ph.D.

The results I obtained were the product of long hours spent experimenting, debugging and refining my approach but none of it would have mattered without the fruitful collaboration with professor Bucci's experimental group (Abdrew Richenderfer, Artyom Kossolapov, Jee Hyun Seong). Without their data and post-processing, my thesis would have gone in a much different direction as the insights gained from their experimental loop proved central to my work.

The help provided by Xingang Zhao and professor Koroush Shirvan on Lookup Table interpolation and its result analysis proved extremely useful and helped me finalize my high pressure result discussion.

The collaboration with Ravikishore Kommajosyula during most of my Ph.D. research on DNB deserves more than a quick mention. More than a colleague, Ravi became one of my best friends and I cannot thank him enough for the help, support and suggestions he provided since he joined our group. We spent countless hours talking, brainstorming and debugging ideas and models related to boiling that most of the smart ideas that ended up unlocking major results in my work stemmed out of our common efforts. Ravi is not far behind me on his own doctorate and will make a great engineer and scientist after he graduates. I am proud to have worked alongside a great person like him.

Studying at MIT can be grueling at times and I've always found the support I needed within the group we unofficially named the "CFD Team". I believe I have had the unique privilege to be the

only student in the group to have known each and every visiting student, graduate student, UROP student, post-doc and research scientist who joined the CFD Team since 2012. It makes for a lot of friends to thank. I will always remember my first days in the United States and at MIT assembling the group's cluster with Joe Fricano, the 2012 group meetings held in NW12-306's office when the group was still small, the great times with Clemens Planck, the first generation of students in the group such as Sasha Tan Torres, Lindsey Gilman and Giancarlo Lenci. The second generation of students was just as supportive and great to hang out with as I always enjoyed the company of Nazar Lubchenko, Rosie Sugrue, Ugi Otgonbaatar, Mike Acton, Giulia Agostinelli, Carolyn Coyle, Javier Martinez, Zach Skirpan, Jinyong Feng, Kayen yau, Brian Casel, Eli Sanchez, Liangyu Xu and all of the other CFD team members.

As I started graduate school at MIT in 2013, I was lucky to be joined in the CFD Team by Ben Magolan who became one of my very best friends. We suffered together through the classes and qualifying exams at MIT and our friendship is one of the greatest outcomes of this doctorate. We spent so many weekend hanging out and/or working on class homework and projects together that I have now a lifetime of memories to remember my time at MIT for.

When I arrived at MIT, my experience with American universities was limited to cultural references that had crossed over the Atlantic ocean to France. Said otherwise: I didn't know much about what to expect. I joined the Fenway House Independent Living Group at MIT almost out of necessity in order to find affordable accommodation. I discovered a group with a long history and was able to interact with undergraduate MIT students from all over the world which was very enriching. Fenway friends will always be dear to me and I am eager to reconnect with the alumni who moved to California where I am going next (Annalisa pawlosky, Jake Whitcomb, Hrant Gharibyan and many others).

Back in 2013/2014 the situation at Fenway House was actually getting dire because of a long-standing recruitment issue. I am proud to have worked alongside Isaque Dutra to save Fenway House from impending shutdown. We were one corporation meeting away from pulling the plug on this fantastic adventure. Thankfully our last resort measures enabled a renewed interest from young undergraduates who soon joined the house and reinvigorated the group. I became the house manager for more than a year and did my best to convince MIT the house was on the right track. After 2016 I had to turn my focus more on my research but I am glad the group is still thriving and pursues the longstanding MIT tradition of Independent Living Groups. This story is not very well known and probably deserves a longer retelling.

While at MIT I discovered the martial art of Kyudo (Japanese traditional archery) which I became passionate about. The weekly practice became my much-needed break from MIT while the Byakko Kyudo Dojo group in Sommerville became one of my biggest support system while I was finishing my doctorate. I am eternally grateful for Don Seckler, Joyce Wu, Alex Mirles, Davie Van Vactor, Zhe Lu, Felita Go, Sayumi Inui, Sam Kanner and all the Kyudo practitioners for all wisdom I received and friendships I developed.

It is impossible to thank all the people who supported me all these years without thanking my pangga Carmela Flores. In the past three years she's provided countless efforts in order to make it easier for me to pursue my research and eventually graduate. She's the one who knows the most about my experience with graduate school and all the struggles I faced. I am forever thankful for her love and understanding as I had to revise the expected end of my Ph.D. multiple times. Now

that this chapter is closing we will be able to open a new one and take our relationship to new levels. I cannot wait.

Je voudrais finir ces remerciements en Français pour ma famille et mes amis. J'ai une pensée pour , mon ami d'enfance Marc Fouet qui a réussi à finir sa thèse et rejoindre la Californie avant moi. Ses conseils avisés et son soutien moral tout du long de mes six ans de *grad school* m'ont permis de garder le moral pendant les moments les plus durs. Je pense aussi a mes amis de prépa restés en France et en Allemagne, Eliott Varon, Roman Wisznia et Farid Skander que j'ai toujours eu plaisir à retrouver lors de mes passages à Paris. Je dois aussi beaucoup au soutien de mes camarades d'HFR (🇷🇺) Mehdi Aid et Florian Rappaport avec qui j'ai pu echanger en ligne et en personne pendant toutes ces longues années

J'ai essayé tout au long de la thèse de garder un contact avec la France. Il n'a pas toujours été possible d'être présent aux moments importants des six dernières années. N'ayant pas pu rentrer en France depuis deux ans, j'ai une pensée particulière pour mes parents Christophe et Chantal Demarly qui m'ont soutenu dans ma démarche depuis le début et qui sont, je le suis certain, fier de ma réussite. Je pense aussi à mon frère Romain qui a dû lui aussi suivre mes aventures de loin. Tout du long j'ai aussi pu m'appuyer sur le soutien de toute ma famille, en particulier mes grands-parents Jean-Paul "Papaul". Marie-Thérèse "Marie-Thé" Lécuyer et Raymond Demarly ainsi que mes nombreux cousins, oncles et tantes à la fois du côté Demarly et Lécuyer. S'il y a une chose que je regrette plus que tout dans cette thèse, c'est de ne pas avoir pu les voir plus souvent et longtemps. J'espère pouvoir y remédier dans les mois et années qui viennent.

Etienne Demarly,
Cambridge MA,
January 14, 2020

Contents

Abstract	3
Acknowledgements	5
Contents	8
List of Figures	11
List of Tables	15
Nomenclature	16
Preamble	19
Motivations	19
Objectives	20
Structure	20
1 Introduction	22
1.1 DNB phenomenon description	22
1.1.1 Initial discovery and observations	22
1.1.2 Large scale experimental campaigns	23
1.2 New generation of experimental insights	24
1.2.1 Micro-hydrodynamic investigations of DNB	25
1.2.2 Infrared thermometry instrumented experiments	25
1.3 Key features of nucleating bubbles that affect our understanding of boiling	27
1.3.1 Existence and properties of the microlayer underneath bubbles during their growth	27
1.3.2 Presence of a “Dry Spot” at the base of a bubble during its growth	30
1.4 Conclusion and perspectives	33
2 Current approaches to DNB modeling	36
2.1 Macro-hydrodynamics mechanisms	36
2.1.1 Dimensional analysis (Kutateladze - 1948)	36
2.1.2 Vapor column instabilities (Zuber - 1959)	37
2.1.3 Liquid sublayer dryout (Katto - 1990, Celata - 1994)	37
2.1.4 Bubble crowding theory (Weisman & Pei - 1984)	43
2.2 CHF correlations	44
2.3 Look-Up Tables	45
2.4 Recent proposal and advances in CHF modeling	47
2.5 Inconsistencies and model limitations of current approaches	48

3	MIT flow boiling loop	49
3.1	Experimental apparatus	49
3.2	Available experimental data sets and post-processing methods	51
3.3	List of test case conditions available for validation	54
4	Governing equations for wall boiling	56
4.1	Nucleate boiling framework	56
4.1.1	Forced Convection	57
4.1.2	Sliding Conduction	58
4.1.3	Evaporation	60
4.1.4	Solid Quenching	62
4.1.5	Nucleation Site Density and bubble interaction	63
4.2	Closure selection	67
4.2.1	Nucleation Site Density	68
4.2.2	Bubble Departure and Liftoff Diameters	71
4.2.3	Bubble growth time	74
4.2.4	Bubble wait time and bubble departure frequency	74
4.3	Framework Summary	75
5	DNB Model Development	77
5.1	DNB detection as a stability limit of heat partitioning	77
5.2	Dry area modeling	80
5.2.1	Initial representation of dry spots underneath individual bubbles	80
5.2.2	Effect of surface properties on dry spot diameters (contact angle)	81
5.2.3	Effect of bubble crowding on the surface on the dry spots (dry patch formation)	84
5.2.4	Complete DNB model	85
6	Model Assessment	86
6.1	Demonstration of model Applicability	86
6.1.1	Experimental test suite	88
6.1.2	Heat partitioning assessment	89
6.1.3	DNB predictions for varying mass fluxes	90
6.1.4	DNB predictions for varying surface contact angles	92
6.1.5	Insights summary	94
6.2	Model benchmarking using the MIT flow boiling loop database	94
6.2.1	Boiling curves and DNB results using modeled growth time	94
6.2.2	Boiling curves and DNB results using experimental growth time	101
6.3	Sensitivity study	107
6.4	Chapter summary	110
7	Model extension to high pressure conditions	112
7.1	Available high pressure integral data sets	112
7.1.1	DeBortoli et al. 1958	113
7.1.2	Jens and Lottes 1951	113
7.1.3	Hunt et al. 1955	113
7.1.4	Weatherhead 1963	113
7.2	Model formulation	113
7.2.1	Heat flux partitioning formulation	114

7.2.2	High pressure closures	119
7.3	High pressure DNB prediction results	122
7.3.1	Bubble departure diameter closure high pressure optimization	122
7.3.2	Model performance at high pressure	123
7.4	Model parameter sensitivity analysis	130
7.5	Prediction of high pressure behavior of advanced fuel	134
7.6	Conclusion and insights summary	135
Conclusion		137
7.7	Summary	137
7.8	Future Work	138
Bibliography		140
Appendices		152
A Vocabulary Definitions		152
B Numerical Implementation		153
C MIT Flow Boiling Results		157
D High pressure databases inputs and model CHF prediction		172
D.1	Jens and Lottes 1951	172
D.2	Hunt et al. 1955	173
D.3	Weatherhead, 1963	174

List of Figures

1.1	Nukiyama Boiling Curve	23
1.2	BETA Experimental setup (from [1])	26
1.3	Schematic representation of the shape of a microlayer underneath a nucleating bubble	28
1.4	Photographic evidence of interference patterns revealing the presence of a microlayer underneath a nucleating bubble. From Sharp [57]	29
1.5	Example of a nucleating bubble and the dry spot at its base. The bottom images are experimental measurements of Temperature and Heat Flux from Richenderfer [5]	31
1.6	Visible Dry Spots on a pool boiling heater at 0.2 bar (fluid: n-heptane). From Van Ouwkerk [73]	32
1.7	Dry spot visualization from infrared thermometry (fluid: FC-72). From Jung [3]	33
1.8	Dry spot visualization (fluid: water) with DEPICT (DEtection of Phase by Infrared Thermography). From Kim [74]	34
1.9	Dry spot visualization (fluid: water) using total reflection (right) and side view (left). From Chu [75]	35
1.10	Infrared images of a water flow boiling experiment. Temperature (left) and heat flux (right). 1 bar, $500 \text{ kg m}^{-2} \text{ s}^{-1}$, 10 K subcooling. Adapted from Richenderfer [6]	35
2.1	Schematic of Zuber [21] postulated DNB mechanism	38
2.2	Schematic of Lee and Mudawar postulated DNB mechanism (adapted from [88])	38
2.3	CHF prediction error scatters from Lee and Mudawar [88]. Left : Doroshchuk [89] database. Right : DeBortoli [42], Weatherhead [43] and others	39
2.4	CHF prediction error scatters from Katto [23]	40
2.5	CHF prediction error scatters from Celata 1994 [24]	41
2.6	CHF prediction error scatters from Celata et al. 1999 [25]	43
2.7	Schematic of Weisman and Pei postulated DNB mechanism (adapted from [22])	44
2.8	Description of Dry Spot and Dry Patch models from No and Ha (Adapted from [114])	48
3.1	Diagram of a top-down view of the camera instrumentation of Richenderfer's PETHER loop (from [5])	51
3.2	Heat flux activity metric example map with an overlay of the nucleation site coordinates (red crosses) detected with the post-processing algorithm. Conditions: 1 bar, 10 K subcooling, $1000 \text{ kg m}^{-2} \text{ s}^{-1}$, 2200 kW m^{-2} heat flux applied to the ITO	53
3.3	Example result of the bubble departure event detection for a single nucleation site signal. Conditions: 1 bar, 10 K subcooling, $1000 \text{ kg m}^{-2} \text{ s}^{-1}$, 2100 kW m^{-2} heat flux applied to the ITO	53
4.1	Microscale mechanisms modeled in Gilman's nucleate boiling framework	56
4.2	Gilman's boiling framework "Mind-map" (from [118])	57
4.3	Assumed shape of the liquid microlayer underneath a bubble	61
4.4	Top heating configuration as found in the MIT flow boiling loop [5, 6]	62
4.5	Hibiki and Ishii [127] nucleation site density model prediction plotted against multiple experimental databases	64
4.6	Li [130] nucleation site density model prediction for Borishanskii et al. database	65

4.7	Li [130] nucleation site density model prediction for Basu et al. database	65
4.8	Qualitative effect of the nucleation site interaction model	67
4.9	Quantitative example of the interaction model using a nucleation site density exponential curve with fixed bubble departure diameter and frequency	67
4.10	Stainless Steel cavity radius distribution from Yang and Kim [126] along with numerical fitting functions proposed by Hibiki and Ishii [127]	68
4.11	Sapphire-ITO heater SEM image (left) and measured cavity size distribution (right). Adapted from [6]	69
4.12	Nucleation site density fitting functions for each of the 14 MIT test cases, grouped by bulk subcooling (5 K, 10 K, 20 K, 25 K)	70
4.13	Diagram of the forces acting on a growing bubble on an inclined surface. Adapted from Mazzocco et al. [138]	71
4.14	Bubble departure diameter error scatter of Mazzocco et al. model [138] benchmarked against Klausner [133], Sugrue [140] and Guan [141] databases	73
4.15	Bubble liftoff diameter error scatter of Mazzocco et al. model [138] benchmarked against Zeng [134], Prodanovic [142] and Situ [143] databases	73
4.16	Scatter plot of Mazzocco et al. [138] bubble departure diameter predictions against MIT flow boiling data	73
4.17	Scatter plot of Kommajosyula's [122] bubble departure frequency predictions against MIT flow boiling data	75
5.1	Illustration of the qualitative behavior of the model. Main plot include the main heat flux partitions adding up to the total heat flux. The boiling curve goes through a peak, identified as the CHF. Top drawings represent the progressive crowding of the surface with bubbles, eventually creating dry patches. Bottom subplots track the number of bubbles on the heater, the statistical interaction and the dry area fraction	79
5.2	Fixed radius assumption for dry spot scaling between contact angle θ (left) and 90° (right)	82
5.3	Fixed volume assumption for dry spot scaling between contact angle θ (left) and 90° (right)	82
5.4	Contact angle dry spot scaling comparison. Fixed apparent radius vs fixed volume	84
5.5	Clustering effect when multiple bubbles create a larger dry patch	85
6.1	Diagram describing the process employed to demonstrate the DNB model validity, starting from the experimental infrared data, image processing techniques are used to extract useful boiling quantities which are used for the DNB model as closures with fitting functions. The resulting boiling curve and CHF are then compared to the experiment	87
6.2	Example fitting functions for both the nucleation site density (left) and the bubble departure frequency (right)	89
6.3	Comparison of experimental and modeled boiling curves for water at 1 bar, 10K subcooling and $1000 \text{ kg m}^{-2} \text{ s}^{-1}$. Boxes in the image compare modeled and experimental contributions of evaporation and single-phase heat transfer at two heat flux conditions. Adapted from [153]	90
6.4	Comparison of experimental and modeled boiling curves for ITO Heater #1 ($500 \text{ kg m}^{-2} \text{ s}^{-1}$, red) and Heater #2 ($1000 \text{ kg m}^{-2} \text{ s}^{-1}$, black). The table compares measured and predicted CHF values.	91

6.5	Comparison of experimental and modeled boiling curves for Heater #3 (ITO, red) and Heater #4 (LbL, black). The boxes show SEM images of the heater surfaces. The table compares measured and predicted CHF values.	93
6.6	boiling curves results of the MIT flow boiling database at atmospheric pressure when using Kommajosyula's growth time. Subplots represent inlet subcooling(from top to bottom, left to right): 5 K, 10 K, 20 K, 25 K	95
6.7	Case #1, 1 bar, 10 K subcooling, $500 \text{ kg m}^{-2} \text{ s}^{-1}$. Using Kommajosyula's growth time.	96
6.8	Case #9, 1 bar, 5 K subcooling, $2000 \text{ kg m}^{-2} \text{ s}^{-1}$. Using Kommajosyula's growth time.	98
6.9	Case #4, 1 bar, 25 K subcooling, $500 \text{ kg m}^{-2} \text{ s}^{-1}$. Using Kommajosyula's growth time.	99
6.10	Result error scatter of the MIT flow boiling database at low pressure when using Kommajosyula's growth time	100
6.11	Case #9, 1 bar, 5 K subcooling, $2000 \text{ kg m}^{-2} \text{ s}^{-1}$. Using Richenderfer's experimental growth time.	102
6.12	Case #4, 1 bar, 25 K subcooling, $500 \text{ kg m}^{-2} \text{ s}^{-1}$. Using Richenderfer's experimental growth time.	103
6.13	Result error scatter of the MIT flow boiling database at atmospheric pressure when using the complete DNB model	104
6.14	boiling curves results of the MIT flow boiling database at atmospheric pressure when using the complete DNB model	105
6.15	Input parameter sensitivity at atmospheric pressure conditions. Effect of a $\pm 30\%$ change in nucleation sites, departure diameter, departure frequency, growth time, dry spot coefficient and contact angle on boiling curves and CHF	108
6.16	Effect of a $\pm 30\%$ change in growth time on the error scatter at atmospheric pressure conditions	110
7.1	Ratio of thermal boundary layer thickness to the bubble departure diameter at CHF plotted against the bulk flow subcooling in high pressure databases	116
7.2	Revised shape of the liquid microlayer underneath a bubble, including the presence of a dry spot at its base	117
7.3	Wetted fraction underneath the bubble at $t^* = 1000$ from Guion [7]	119
7.4	Numerical fit of data extracted from Figure 7.3	119
7.5	Wall temperature dependency of the contact angle. Data from Bernardin [158] and Hayashi [165] (adapted from Hirose [166])	121
7.6	High pressure CHF predictions for three databases. Left: our model. Center: W3 correlation [97]. Right: 2006 Groeneveld Lookup Table [46]	124
7.7	Cumulative error distribution comparison between our model (left), the W3 correlation (center) and the 2006 Groeneveld Lookup Table (right)	125
7.8	Cumulative error distribution comparison as an aggregate (top-left), and per database. Weatherhead (top-right), Hunt et al. (bottom-left) and Jens & Lottes (bottom-right)	126
7.9	Parameter space (Reynolds number vs Subcooling) of the Weatherhead (blue), Hunt et al. (green) and Jens & Lottes (purple) databases	127
7.10	CHF relatives error for the three databases (Weatherhead, Jens and Lottes and Hunt et al.) plotted against outlet subcooling	128
7.11	CHF relatives error for the three databases (Weatherhead, Jens and Lottes and Hunt et al.) plotted against mass flux	128

7.12	Case 26. Subplots, left to right, top to bottom : Boiling Curve and CHF. Heat flux partitions. Microlayer and Inception heat flux. Bubble departure and liftoff diameters. Nucleation Site Density. Bubble Departure Frequency. Bubble growth and wait time. Dry area fraction. Sliding length	129
7.13	Case 79. Subplots, left to right, top to bottom : Boiling Curve and CHF. Heat flux partitions. Microlayer and Inception heat flux. Bubble departure and liftoff diameters. Nucleation Site Density. Bubble Departure Frequency. Bubble growth and wait time. Dry area fraction. Sliding length	130
7.14	Model parameter sensitivity at high pressure conditions. Effect of a $\pm 30\%$ change in nucleation sites, departure diameter, departure frequency, growth time, dry spot coefficient and contact angle on boiling curves and CHF	132
7.15	Error scatter of a $\pm 30\%$ change in departure diameter on CHF at high pressure conditions	133
7.16	Cumulative error density functions of the bubble departure diameter sensitivity analysis. Original Diameter, +30%, -30%	133
7.17	Nucleation site density sensitivity : original CHF predictions (x-axis) plotted against the same model with modified nucleation site density (10x original) (y-axis)	134
7.18	Contact angle sensitivity : original CHF predictions (40°)(x-axis) plotted against the same model with modified contact angle (20°) (y-axis)	135
C.1	Case #1, 1 bar, 10 K subcooling, $500 \text{ kg m}^{-2} \text{ s}^{-1}$	157
C.2	Case #2, 1 bar, 10 K subcooling, $750 \text{ kg m}^{-2} \text{ s}^{-1}$	158
C.3	Case #3, 1 bar, 10 K subcooling, $1000 \text{ kg m}^{-2} \text{ s}^{-1}$	159
C.4	Case #4, 1 bar, 25 K subcooling, $500 \text{ kg m}^{-2} \text{ s}^{-1}$	160
C.5	Case #5, 1 bar, 25 K subcooling, $750 \text{ kg m}^{-2} \text{ s}^{-1}$	161
C.6	Case #6, 1 bar, 25 K subcooling, $1000 \text{ kg m}^{-2} \text{ s}^{-1}$	162
C.7	Case #7, 1 bar, 5 K subcooling, $1000 \text{ kg m}^{-2} \text{ s}^{-1}$	163
C.8	Case #9, 1 bar, 5 K subcooling, $1500 \text{ kg m}^{-2} \text{ s}^{-1}$	164
C.9	Case #9, 1 bar, 5 K subcooling, $2000 \text{ kg m}^{-2} \text{ s}^{-1}$	165
C.10	Case #10, 1 bar, 10 K subcooling, $1000 \text{ kg m}^{-2} \text{ s}^{-1}$	166
C.11	Case #11, 1 bar, 10 K subcooling, $1500 \text{ kg m}^{-2} \text{ s}^{-1}$	167
C.12	Case #12, 1 bar, 10 K subcooling, $2000 \text{ kg m}^{-2} \text{ s}^{-1}$	168
C.13	Case #13, 1 bar, 20 K subcooling, $1000 \text{ kg m}^{-2} \text{ s}^{-1}$	169
C.14	Case #14, 1 bar, 20 K subcooling, $1500 \text{ kg m}^{-2} \text{ s}^{-1}$	170
C.15	Case #15, 1 bar, 20 K subcooling, $2000 \text{ kg m}^{-2} \text{ s}^{-1}$	171

List of Tables

2.1	Range of validity of the W3 CHF correlation parameter space	45
3.1	Test cases inputs and corresponding measured CHF	54
6.1	Test matrix of subcooled flow boiling experiments and CHF simulation results	88
6.2	CHF results, absolute and relative errors for the four heaters tested	93
6.3	CHF results and errors when using Kormajosyula's growth time	100
6.4	CHF results and errors when using the complete model (with experimental growth time)	106
7.1	Heater differences between laboratory tests and nuclear reactor applications	112
7.2	Tube Length, Diameter and L/D ratio for the three high pressure databases chosen	114
7.3	Performance comparison per database between our model and the W-3 correlation using absolute values of relative errors	125
7.4	Input conditions and experimental CHF for Weatherhead database case 26 and 79	128
D.1	Jens and Lottes[41] database inputs. 347 Stainless Steel, $L = 0.625$ m $D = 5.74$ mm, $P = 137.9$ bar	172
D.2	Hunt et al. [162] database inputs. "A" Nickel, $L = 0.318$ m, $D = 5.74$ mm, $P = 137.9$ bar	173
D.3	Weatherhead[43] database inputs. 304 Stainless Steel, $L = 0.457$ m, $P = 137.9$ bar	174

Nomenclature

Latin Symbols		
Notation	Description	Unit
A	Area	[m ²]
C	Constant (Equation 2.4)	[-]
Ca	Capillary Number	[-]
D	Diameter	[m]
c_p	Specific Heat	[J kg ⁻¹ K ⁻¹]
f	Frequency	[Hz]
F	Force	[N]
g	Standard Gravity / Gravitational Acceleration on Earth	[9.81 m s ⁻²]
G	Mass Flux	[kg m ⁻² s ⁻¹]
h_{fg}	Latent Heat	[J kg ⁻¹]
h	Enthalpy	[J kg ⁻¹]
Ja	Jacob Number	[-]
k	Thermal Conductivity	[W m ⁻¹ K ⁻¹]
K	Equation Constants	[-]
l	(Sliding) Length	[m]
L	(Heated) Length	[m]
n	Constant (Equation 2.35)	[-]
Nu	Nusselt Number	[-]
N''	Nucleation Site Density	[m ⁻²]
P	Pressure	[Pa]
P	Probability (Equation 4.37)	[-]
Pr	Prandlt Number	[-]
\dot{Q}/q''	Heat Flux	[W m ⁻²]
R	Radius	[m]
Re	Reynolds Number	[-]
S_{dry}	Dry area fraction coefficient	[-]
t	Time	[s]
T	Time Period	[s]
T	Temperature	[K]
u	Velocity	[m s ⁻¹]
U_b	Bubble Growth Rate	[m s ⁻¹]
V	Volume	[m ³]
x	Heater Depth (Equation 4.27)	[m]
x	Thermodynamic Quality	[-]
Greek Symbols		
Notation	Description	Unit
α	Void fraction, volume fraction of gas phase; $\alpha \equiv \alpha_g$	[-]
α^*	Wetted fraction (from Guion [7])	[-]
δ	(Micro Layer) Thickness	[m]

Continued on next page

Nomenclature – Continued from previous page

δ_*	Linear Scale of Capillary Disturbances (Equation 2.2)	[m]
Δ	Difference	[-]
ϵ	Surface Roughness	[m]
η	Thermal Diffusivity	[J m ⁻³ K ⁻¹]
π	3.14159265359...	[-]
μ	Dynamic Viscosity	[Pa s]
ρ	Density	[kg m ⁻³]
σ	Surface Tension	[N m ⁻¹]
θ	Contact Angle	[<i>circ</i>]
χ	Temperature Ratio (Equation 4.48)	[-]
ζ	Dry Area scaling coefficient (Equation 5.12)	[-]

Subscripts

Subscript	Description
<i>b</i>	Bubble
<i>B</i>	Buyoyancy Force (Equation 4.42)
<i>c</i>	Critical
<i>CP</i>	Contact Pressure Force (Equation 4.42)
<i>d</i>	Departure
<i>D</i>	Drag Force (Equation 4.42)
<i>dry</i>	Dry Area/Spot
<i>e</i>	Equilibrium
<i>ev</i>	Evaporation
<i>f</i>	Fluid Phase
<i>FB</i>	Flow Boiling (Equation 4.43)
<i>fc</i>	Forced Convection
<i>g</i>	Gas Phase
<i>g</i>	Growth (time)
<i>g</i>	Gravity Force (Equation 4.42)
<i>H</i>	Hydrodynamic Force (Equation 4.42)
<i>HI</i>	Hibiki Ishii (Nucleation Site Density)
<i>hy</i>	Hydraulic
<i>he</i>	Heated
<i>h/heater</i>	Heater
<i>i</i>	Initial
<i>in</i>	Inlet
<i>inc</i>	Inception
<i>L</i>	Lift Force (Equation 4.42)
<i>Li</i>	Li (Nucleation Site Density)
<i>LC</i>	Lemmert Chawla (Nucleation Site Density)
<i>lo</i>	Lift-Off
<i>ml/ML</i>	Micro Layer
<i>nb</i>	Nucleate Boiling
<i>out</i>	Outlet
<i>q</i>	Quenching
<i>s</i>	Surface
<i>Sx/Sy</i>	Shear Force (Equation 4.42)
<i>sat</i>	Saturation
<i>sl</i>	Sliding

Continued on next page

Nomenclature – Continued from previous page

<i>sc</i>	Sliding Conduction
<i>sub</i>	Subcooling
<i>sup</i>	Superheat
<i>vap</i>	Vapor
<i>w</i>	Wait (time)
<i>w/wall</i>	Wall
<i>wet</i>	Wetted Area

Acronyms

Acronym	Description
BETA	BETA Experiment from Theofanous [1, 2]
CFD	Computational Fluid Dynamics
CHF	Critical Heat Flux
CSR	Complete Spatial Randomness theory
COBRA-TF	Thermal Hydraulic Subchannel Code
DEPIcT	DEtection of Phase by Infrared Thermography
DNB	Departure from Nucleate Boiling
FC-72	Refrigerant fluid from 3M TM Fluorinert TM
HPC	High Performance Computing
ITO	Indium Tin Oxide
LbL	Layer-by-Layer
LUT	Look Up Tables
MCFD	Multiphase Computational Fluid Dynamics
RPI	Rensselaer Polytechnic Institute
ONB	Onset of Nucleate Boiling
PWR	Pressurized Water Reactor
RELAP-5	Thermal Hydraulic System Code
USSR	Union of Soviet Socialist Republics

Preamble

Although boiling has been used by humans for hundreds of thousands of years [8] and the first steam engines can be traced back to 1st-century Roman Egypt [9], its widespread use as an effective heat transfer mechanism came along the industrial revolution. The high heat transfer coefficients attained with boiling are the main reason it is now commonly found in many industrial systems ranging from nuclear power plants to chemical reactors and electronic chips cooling (vapor chamber). The boiling crisis has long been identified as an upper limit for this efficient heat transfer mode. At high heat fluxes the bubble nucleating regime can suddenly transition when vapor begins to cover the entire heating surface. This change in the heat transfer mode is associated with a sharp increase of the surface temperature. This phenomenon has been identified as a limiting factor when designing industrial systems that maximize heat removal through boiling. The mechanism causing this change is referred to as “Departure from Nucleate Boiling” (DNB) and The heat flux at which the boiling crisis occurs is called the “Critical Heat Flux” (CHF).

The vocabulary referring to the physics in question is varied and several terms can be used almost interchangeably. Some expressions have also evolved in time and create a confusing context for someone looking in the literature. Refer to Appendix A for a list of definitions that hold true in this document. The work in this thesis is focused on modeling and predicting the DNB, mechanism in subcooled flow boiling conditions.

Motivation

Despite being identified decades ago as a main limiting factor for subcooled flow boiling applications, DNB remains one of the most challenging thermal hydraulic phenomena to this day [10]. The literature on the subject is vast and spans decades of experimental, theoretical and modeling work. The desire to maximize heat transfer capabilities of industrial systems has been a constant motivation for the improvement of DNB predictions. One of the main driver for these improvements since the 1950s has been the nuclear industry. The occurrence of the boiling crisis in the context of a nuclear reactor could lead to the melting of the fuel cladding and subsequent loss of containment of radioactive materials kept inside the fuel elements. Therefore, the fuel design of a nuclear reactor requires a conservative prediction of the DNB occurrence to be used for its power rating. Any improvement in the DNB prediction capabilities could lead to better fuel design, improved safety margin and eventually allow for power uprates of the reactors.

One of the most promising avenues for thermal design optimization is the use of Computational Fluid Dynamics (CFD) simulations. The exceptional growth in High Performance Computing (HPC) seen in the past two decades has opened up opportunities for industrial applications. However, in the case of multiphase flow and especially boiling heat transfer, the models maturity necessary for a widespread industrial use has yet to be achieved [10].

Existing CFD models that predict the DNB transition are limited [11–18] and do not reflect the current understanding of DNB. Furthermore their prediction capabilities have been shown to be limited without additional calibration. The need for improved models capable of capturing the

relevant physics causing DNB is evident. Past understandings [19–25] relying on hydrodynamic theories of the boiling crisis have recently been challenged by a new generation of instrumented experiments [1–6, 26–35]. Past approaches such as Zuber’s vapor columns instability model [21], Kato [23] and Celata’s [24, 25] liquid sublayer dryout models, and Weisman and Pei’s bubble crowding model [22] inferred mechanisms by which the inflow of water to the boiling surface would be limited by hydrodynamic forces, but with improved instrumentation at the boiling surface, it is increasingly accepted that DNB is caused by micro-scale phenomena at the boiling surface which provoke the boiling crisis.

Despite the rapid progresses seen in the instrumentation and understanding of boiling experiments, it has not yet led to significant improvements in modeling of DNB. Insights on the causes of DNB uncovered by experimentalists have yet to materialize into a mechanistic model able to capture observed physical trends without a priori calibration.

Objectives

Within this context, the work presented in this thesis tackles the DNB type of boiling crisis and aims at proposing a new approach for its modeling. The overarching objectives of this work are listed below:

- Review and understand the state-of-the-art in DNB modeling and its limitations.
- Leverage the latest experimental and physical understanding of the microhydrodynamics phenomena leading to the boiling crisis.
- Propose a new mechanism for DNB.
- Assemble a complete model formulation.
- Demonstrate the validity of the proposed DNB physics using high fidelity experimental inputs.
- Propose a working set of closures and use them to benchmark the model against a low pressure, high fidelity database.
- Assess the potential for applicability of the model on integral DNB databases representing prototypical reactor conditions.

These steps correspond to the application of a rigorous scientific method approach to the DNB challenge.

Structure of the Thesis

In order to understand the physics behind DNB, a thorough review of previous work is needed. Experimental progresses are discussed from the original heated wire boiling crisis to the most recent high speed infrared thermometry techniques in chapter 1. The various types of efforts aimed at predicting DNB (mechanistic models, CHF closures, Look-Up Tables and others) and their current limitations are discussed in chapter 2. From these observations, the role of the surface dry area is hypothesized to be the main driver for triggering DNB.

The demonstration of this new approach will rely on the complete representation of heat partitioning through the various heat transfer mechanisms at the wall. It is described in chapter 4. The main source of high fidelity data used for the demonstration is the MIT flow boiling loop which is presented in chapter 3 along with the test case inputs that form the low pressure benchmark for our model.

The physical justifications behind the heat partitioning approach are developed and assembled into a complete model able to detect DNB and capture its physical trends (chapter 5). The model DNB detection capabilities are demonstrated in the first sections of chapter 6 while the latter sections are dedicated to the model benchmarking and sensitivity analysis.

In chapter 7, the model is adapted to high pressure conditions and benchmarked against a wide range of input parameters from DNB integral databases. This final chapter also includes a sensitivity analysis for high pressure conditions and leverages the new formulation to make initial predictions on the potential avenues for advanced nuclear fuel to delay the boiling crisis.

Chapter 1

Introduction

This review aims at listing important milestones that are directly relevant for the subcooled flow DNB modeling work. Other aspects of DNB that are not as relevant will only be briefly mentioned and referenced via review articles for interested readers.

Before reviewing various approaches and understanding of the physics behind DNB it is necessary to remind the reader that to this date, no universal theory exists or has been agreed upon. The extremely chaotic behavior of water boiling on a stove is the most obvious way to witness the challenges faced by thermal hydraulic scientists. The paradox between how common our real life experience with boiling is and how little knowledge we are able to derive analytically is notable. It also explains why for decades, experiments and empirical approaches have been carried out to improve our understanding of the various mechanisms at play. The following sections will cover four aspects pertaining to DNB research; section 1.1 covers the historical experiments and data collection efforts. In section 1.2 we focus on the latest experimental breakthroughs and new understandings being incorporated in the most recent modeling efforts. Finally, section 1.3 retraces the discovery and current understanding of the two main phenomenon of boiling that are key to accurate DNB predictions.

1.1 DNB phenomenon description

1.1.1 Initial discovery and observations

The earliest commonly accepted discussion of the boiling crisis is attributed to Nukiyama in 1934 [36] (often referenced via its 1966 reprint [37]). In this pioneering work, he describes the existence of a maximum heat flux being removed from an electrically heated wire inside a pool of water. The occurrence of a peak in the boiling curve (see Figure 1.1) represented a major departure from previous understanding of the boiling phenomenon. Until then, only the nucleate boiling part of the curve was known. In this regime, the heat removed from the wire is proportional to the superheat at the wall (i.e., the difference between the heater surface temperature and the liquid saturation temperature). Nukiyama was the first to report strong evidence that the boiling regime cannot be enhanced indefinitely but is effectively limited. He explained how vapor accumulation near the heating surface ultimately prevents direct contact of liquid water with the heater leading to the sudden decrease in heat transfer. The heat transfer mode transitions from steam bubble generation (nucleate boiling) to convection and radiation through a steam layer (film boiling), reduces heat transfer effectiveness and is thus accompanied by a superheat increase (for a given heat generation). Nukiyama also noted that the superheat region following the boiling crisis (negative slope in the boiling curve) is very unstable and cannot be observed unless the heater surface temperature is effectively controlled. The lowest point in the curve was also observed by Nukiyama but was later identified as the Leidenfrost point ¹.

¹Originally, Leidenfrost reported his discovery in 1756 [38] but remained largely unknown until his original work was translated from latin in 1966 [39].

The points labeled in Figure 1.1 refer to each step in the boiling curve.

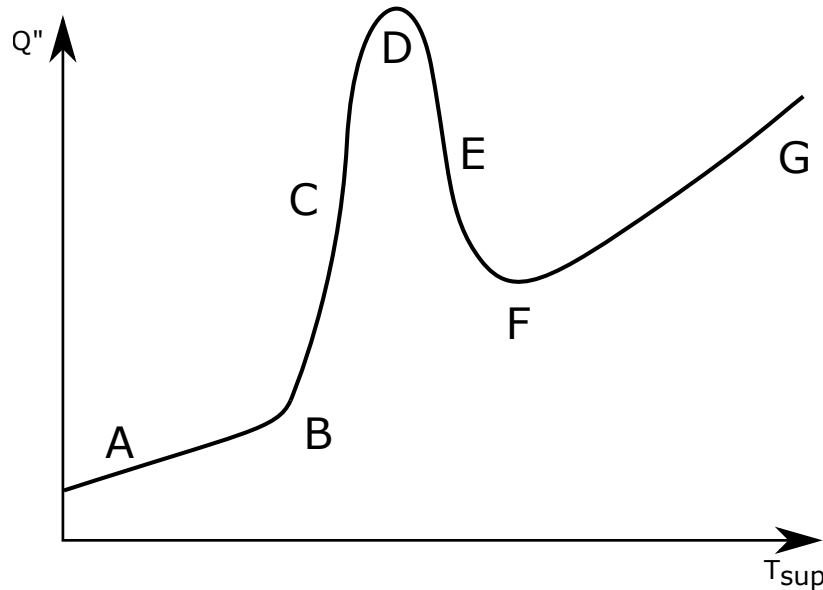


Figure 1.1: Nukiyama Boiling Curve

- **A** : Single phase region. No bubble nucleates yet, the heat is removed by convection.
- **B** : Onset of Nucleate Boiling (ONB). Temperature at which bubbles begin to nucleate and depart in the flow.
- **C** : Nucleate boiling region. More bubbles are generated as the wall temperature increases. The slope is very steep marking the efficiency of boiling as a heat removal method.
- **D** : Critical Heat Flux. Peak heat flux beyond which an increase of wall temperature is not associated with a rise in heat flux.
- **E** : Transition boiling. Region only attainable if the wall temperature is controlled instead of the heat generation.
- **F** : Leidenfrost Point.
- **G** : Film boiling. Post-CHF region where steam is in contact with the heating wall. Evaporation at the interface between the liquid and steam layer occurs via convection and radiation through the steam blanket.

1.1.2 Large scale experimental campaigns

The need for higher heat flux in industrial applications such as nuclear reactors drove experimentalists to study boiling heat transfer and its limits. Early on, McAdams [40] and later Jens and Lottes [41] correlations predicted flow boiling heat transfer coefficient. The latter study was the first in a long series of experimental campaigns aimed at the prediction of boiling heat transfer up to CHF in naval nuclear reactor. These initial studies conducted in the 1950s and early 1960s continue to be important sources for CHF data at high pressure. DeBortoli et al. [42] produced the

first compilation of CHF data by reporting results produced at the Bettis Atomic Power Laboratory and the Argonne National Laboratory up until 1958. Most of the data points in this report are for high pressure (above 100 bars), vertical round tubes that are most analogous to commercial reactor conditions but also include data for inclined or rectangular channels as well as downward flows. The report includes more than a thousand CHF data points. Weatherhead [43] later expanded the high pressure vertical round tube CHF data with 232 new conditions for a two tube diameters at a pressure of 137 bar.

This type of studies is referred to as "integral experiments" due to the lack of local observations and measurements during boiling. The nucleate boiling regime is usually not investigated and CHF data points are reported against the system parameters (geometry, heated length, tube diameter) and the flow conditions (pressure, mass flow rate or mass flux, inlet and outlet subcooling or enthalpy). In most cases the boiling surface temperature is tracked via thermocouples in order to detect the temperature excursion associated with DNB; in these studies, neither the boiling curve nor the void fraction distribution in the channel are available for validation purpose.

Groeneveld [44, 45] recently published an overview of CHF data compilations for water-cooled tubes he used to generate the latest [46] Look-up Tables² as well as new data sets that have been uncovered or published since 2007. The report contains an extensive list of CHF studies conducted over the past 60 years, their parameter space and the number of CHF points. This is a very good starting point when looking for CHF validation data sets. In his report, Groeneveld also discusses the important aspect of reproducibility of experimental results on the basis of studies conducted in Europe [47, 48] and the USSR [49] during the 1970s and 1980s. In each test campaign, independent laboratories were asked to conduct identical CHF tests and report their results for benchmarking. In the case of the soviet study, the metallic heater elements were provided from a single manufacturing source to each laboratory in order to remove a potential source of discrepancy. Both studies found discrepancies in the reported CHF data of $\pm 10\%$. The soviet study also reported larger uncertainties ($\pm 15 - 30\%$) for shorter heated lengths of 1m. These considerations are rarely mentioned when trying to validate CHF prediction models against experimental databases. Sometimes the reported experimental uncertainties are much lower than 10% but one could certainly argue it becomes questionable to expect prediction accuracy lower than 10% if the underlying experimental data carries such an inherent uncertainty.

1.2 New generation of experimental insights

For decades, researchers have been limited by the imaging techniques used to observe boiling. In the past twenty years, improvements in imaging capabilities have opened new ways to consider the physics behind DNB. A turning point was the renewed interest for effects related to the surface state of the heater. Early on, Rosenhow [50] had accounted for several surface effects in his pool boiling heat transfer correlation from 1951. The initial efforts by McAdams [40], Kutateladze [19, 20] and Zuber [21] to understand DNB focused on the thermal hydraulic effects on CHF (flow parameters, channel geometry) and largely ignored the potential effect of the boiling surface on the DNB. After the initial pushback and heated debate in the thermalhydraulic community [51], the agreed understanding regarding DNB has long been that of a hydrodynamic instability that concerned the vapor bubbles, columns and blankets, and their interaction with the liquid flow. This paradigm has recently changed and it is now common to see articles [1–6, 30–32] from

²standardized CHF values for 8 mm tubes tabulated against thermodynamic quality, pressure and mass flux

experimental groups noting how their observations of DNB are not compatible with hydrodynamic instability explanations. We will now explore the progresses and achievements that led to this new understanding of DNB.

1.2.1 Micro-hydrodynamic investigations of DNB

Theofanous and Dinh [1, 2] were among the first to purposely investigate the hydrodynamic hypothesis for CHF. They note several instances in the literature where experimental results seemed to contradict existing mechanistic understandings. The BETA experiment they conducted brings evidence that the hydrodynamic scales above the heater surface are distinct from the thermal scales at the boiling surface. They conclude that the order and regularity of thermal patterns contrast with the chaotic behavior of the two-phase flow above the surface.

The BETA experiment provides one of the most concrete and direct evidence disproving any hydrodynamics explanation for CHF. Theofanous built two identical pool boiling heater configurations seen in Figure 1.2. Configuration A is a traditional pool boiling experimental setup while Configuration B is identical to Configuration A in every ways except for the volume of water contained in the "pool". In Configuration A the volume of water is large enough to exceed the minimum height required by Kutateladze for hydrodynamics models to apply. Configuration B is only filled with a very thin layer of water which doesn't let any hydrodynamics develop above the heating surface since the water film thickness is much smaller than the characteristic size of vapor bubbles. Theofanous notes: "A subsequent implication is that since the presence of the liquid pool is only incidental, the burnout phenomenon can be studied in isolation by focusing on the heater-microlayer system alone". The most striking result comes from the fact that configuration A and B CHF values are identical, seemingly disproving the theories relating CHF with macroscopic hydrodynamic instabilities.

This study points toward further investigating the role of heater-surface as this parameter had been largely ignored in CHF modeling since the popularization of Zuber's vapor columns instability model. It also turns to the existence of irreversible dry spots as a new cause for triggering the boiling crisis. This last point will be revisited in chapter 2 and represents a starting point for our modeling effort.

1.2.2 Infrared thermometry instrumented experiments

When studying boiling and especially DNB, experimentalists are driven by the desire to access information at the finest time and geometric scale possible. Historically, optical systems were used to probe the boiling surface and detect boiling features such as the bubble size, its microlayer geometry [52] or local accumulation of vapor near the surface [22].

Visible light offers many advantages such as the availability of very high framerate of acquisition. Semeria [53], back in 1963 reported bubble sizes in a pool boiling experiment at high pressure, using a 8000 frames-per-second camera. Today, cameras can record high resolution images at even higher framerates (on the order of 100,000 frames per second). Visible light is nonetheless very limiting when observing boiling surfaces. The heater elements are usually opaque to visible light and therefore require conducting observations from a top-down or side perspective. The intense and chaotic boiling activity renders any observation of individual effects impossible. Even with a transparent heater allowing for back side recording, large quantities of vapor structures sitting on top of the heater prevent any quantitative measurement during vigorous boiling and DNB.

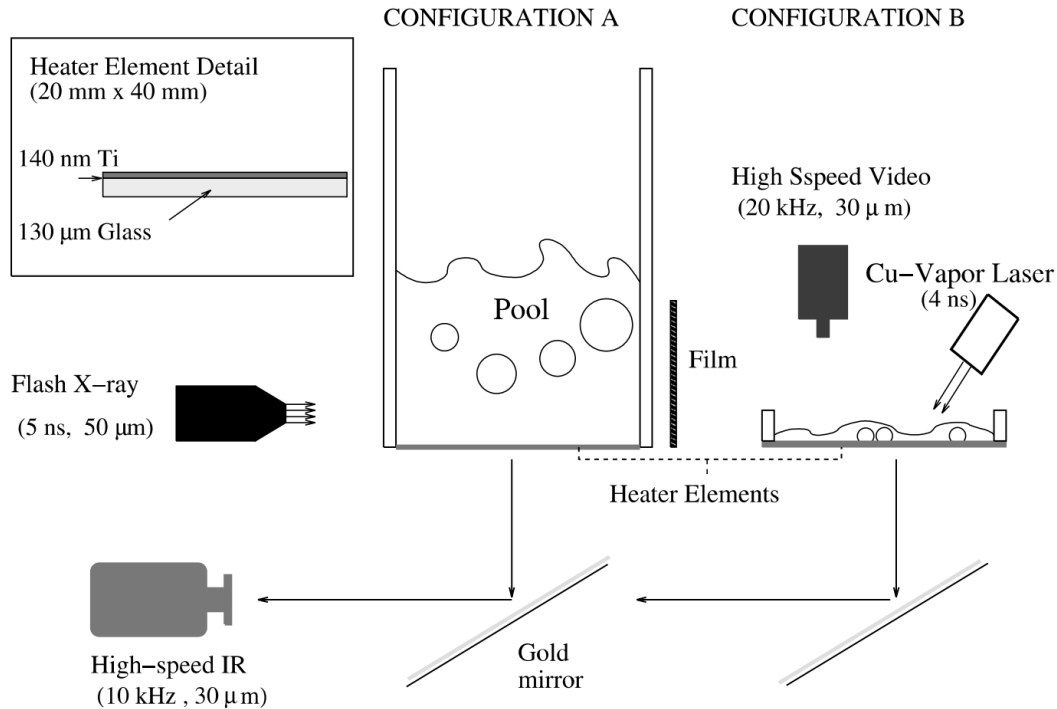


Figure 1.2: BETA Experimental setup (from [1])

Infrared radiation offers a much more interesting perspective in order to alleviate these limitations and access local surface information during boiling. Materials that would be opaque to visible light can become transparent or semi-transparent in the infrared spectrum, allowing for a backside imaging of the heating element in a boiling experiment. Even more interesting is the fact that infrared radiation emitted by an object is related to its temperature through Planck's law regarding the black body radiation spectrum³. This relationship is exploited to conduct infrared thermometry by calibrating the signal captured by an infrared camera and conducting numerical post-processing.

While the use of infrared cameras to image a boiling experiment is only 20 years old, it has become almost ubiquitous within the last 10 years. Chemat [54] used an infrared sensor to measure the bottom surface temperature of a microwave heating boiling experiment. But it is really Theofanous et al. [1] who provided the first infrared thermometry images of a boiling surface. The image resolution they obtained was limited but already showed clear circular patterns corresponding to bubble footprints affecting the local temperature field on the heater.

The experimental group at MIT under supervision of professor Buongiorno first, and later the group of professor Bucci have brought major advances to the field of high-speed infrared thermometry. Gerardi [26] first leveraged infrared thermometry and the use of an "Indium-Tin-Oxide" (ITO) heater surface deposited on sapphire substrates to study the effect of nano-engineered fluids on boiling and later investigated bubble growth during pool boiling, including its dry spot diameter

³ $B_{\lambda}(\lambda, T) = \frac{2hc^2}{\lambda^5} \frac{1}{e^{\frac{hc}{\lambda k_b T}} - 1}$, where $B_{\lambda}(\lambda, T)$ is the spectral radiance, $h = 6.62607015 \times 10^{-34}$ J s the Planck constant, c the speed of light in the medium, λ the wavelength and T the temperature.

[27]. Gerardi was also able to track most of the relevant nucleation parameters (bubble diameters, departure frequency, bubble growth and wait times) [28]. Kim [29] developed a technique to detect the triple contact line during bubble growth. He further refined this technique iteratively with Jung [3, 30–32] investigating the importance of triple contact line in triggering CHF as well as microlayer formation. Phillips [33] extended the infrared thermometry technique to flow boiling which is notable considering the lack of available flow boiling data.

Bucci [34] developed a framework to post-process the infrared images from the backside imaging of the heater surface. He was able to extract both the local temperature and heat flux field for each frame acquired by the camera. His approach considers the radiation and conduction phenomena to construct a finite difference inverse problem where the resulting infrared photons hitting the camera sensor are a known quantity, while the heater temperature generating these photons is an unknown boundary condition. The infrared radiation emitted by the heater surface can be absorbed by the substrate on which the heater is deposited. Materials like quartz and sapphire are semi-transparent in the infrared spectrum and will absorb a small fraction of the original photons. Heat conduction will also increase the substrate material temperature close to the heater level. This means that the radiation hitting the camera sensor also includes contributions coming from the substrate re-emitted radiation. In the end, the problem is formulated in a 3-D radiation conduction framework and solved using an iterative finite volume approximation.

Bucci's method has been used to generate high resolution images of the temperature and heat flux fields of the heater surface, and has become the starting point of further analysis and post-processing. Richenderfer [5, 6] leveraged this technique to process local boiling quantities such as: nucleation site density, bubble departure frequency as well as heat flux partitioning. The radiation-conduction inverse problem is recently being used by other groups [35] for similar purpose.

1.3 Key features of nucleating bubbles that affect our understanding of boiling

In subsection 1.2.1, we introduced the argument that the microscopic scale hydrodynamics of boiling are key to the understanding of the boiling crisis. The bubble microlayer and its dry spot are two of the most important features of a nucleating bubble on a heating surface and both relate to the triple contact point that defines the boundary between the solid heater, the liquid phase and the vapor bubble. We will describe each phenomenon separately in the following subsections.

1.3.1 Existence and properties of the microlayer underneath bubbles during their growth

The microlayer underneath a bubble is a thin liquid film created during the initial growth of the bubble. The bubble geometry and the typical shape of the microlayer are shown in Figure 1.3. At atmospheric pressure, a millimeter size bubble creates a microlayer thickness in the order of a few μm , thus creating a large scale difference and making direct observations of the microlayer difficult.

Moore and Mesler [55] first postulated its existence in 1956. They observed indirect evidence of the presence of a microlayer in the form of temperature fluctuations on a boiling surface. They hypothesized the creation and subsequent evaporation of a thin layer of liquid underneath the bubbles that would explain their observations. Hendricks and Sharp [56] further confirmed the

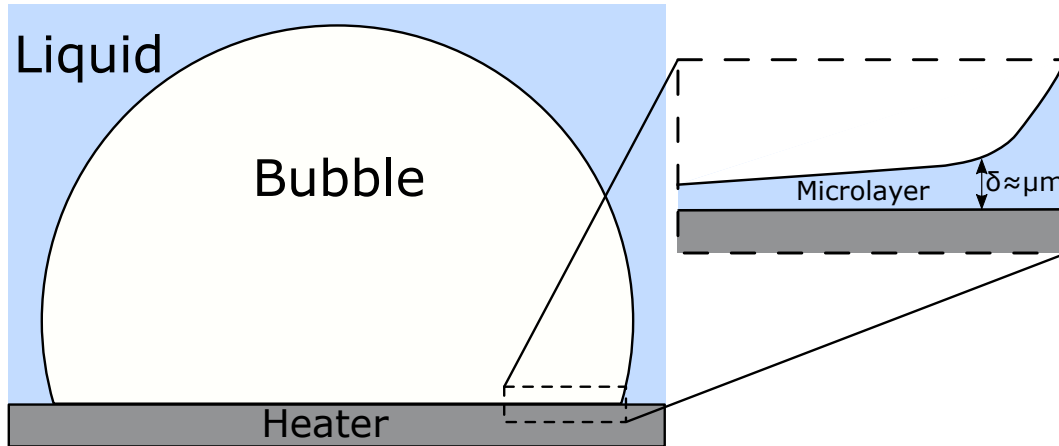


Figure 1.3: Schematic representation of the shape of a microlayer underneath a nucleating bubble

observations reported by Moore and Mesler. Their photographic and thermometric study showed a temperature drop below the bubble during its growth while the temperature would recover and increase after the bubble departure. These findings were consistent with the existence of a thin microlayer for which evaporation would be very effective and reduce the surface temperature locally.

These indirect observations were confirmed by experimental studies from Sharp [57] in 1964 and Hospeti and Mesler [58] in 1965. Sharp utilized interferometry in order to directly observe the existence of a microlayer underneath a bubble as shown in Figure 1.4, while Hospeti relied on an indirect technique where radioactive material in liquid solution would deposit in the immediate vicinity of nucleation sites. The radioactivity measured on the surface after the evaporation of several thousands of bubbles was indicative of the amount of liquid that evaporated and thus could be used to estimate the microlayer thickness.

Cooper and Lloyd [59] instrumented a single nucleation site generating bubbles in order to investigate the temperature evolution of the interface between the heater and microlayer. They evaluated the heat removed locally by the microlayer and deduced the initial microlayer thickness was in the order of $10\ \mu\text{m}$ for toluene and isopropyl alcohol boiling on a glass surface. Jawurek [60] used interference patterns in order to estimate the microlayer thickness and its evolution in time, reporting a thickness smaller than $1\ \mu\text{m}$ for methanol boiling on a glass surface.

Voutsinos and Judd [61] claimed the initial interferometric studies were flawed and underestimated the microlayer thickness. They proposed a revision to the technique employed, and reported thicknesses ranging from $0.8\ \mu\text{m}$ to $8\ \mu\text{m}$ that were consistent with earlier values reported by Moore and Mesler while much larger than the ones reported by Sharp [57] and Jawurek [60]. Judd and Hwang [52] expanded the original work from Voutsinos and Judd in order to estimate the importance of microlayer evaporation in the overall heat transfer at the wall and found it could account up to a third of the total heat removal. In the same series of studies, Fath and Judd [62] experimented with the influence of system pressure on microlayer evaporation. They compared atmospheric pressure results with sub-atmospheric conditions and concluded the microlayer evaporation contribution to the heat removal at the wall is even higher at lower pressure, reaching up to 40% of the total heat flux. They noted that the contribution of microlayer evaporation decreases with system pressure and hypothesized it could become insignificant at very high pressures, for

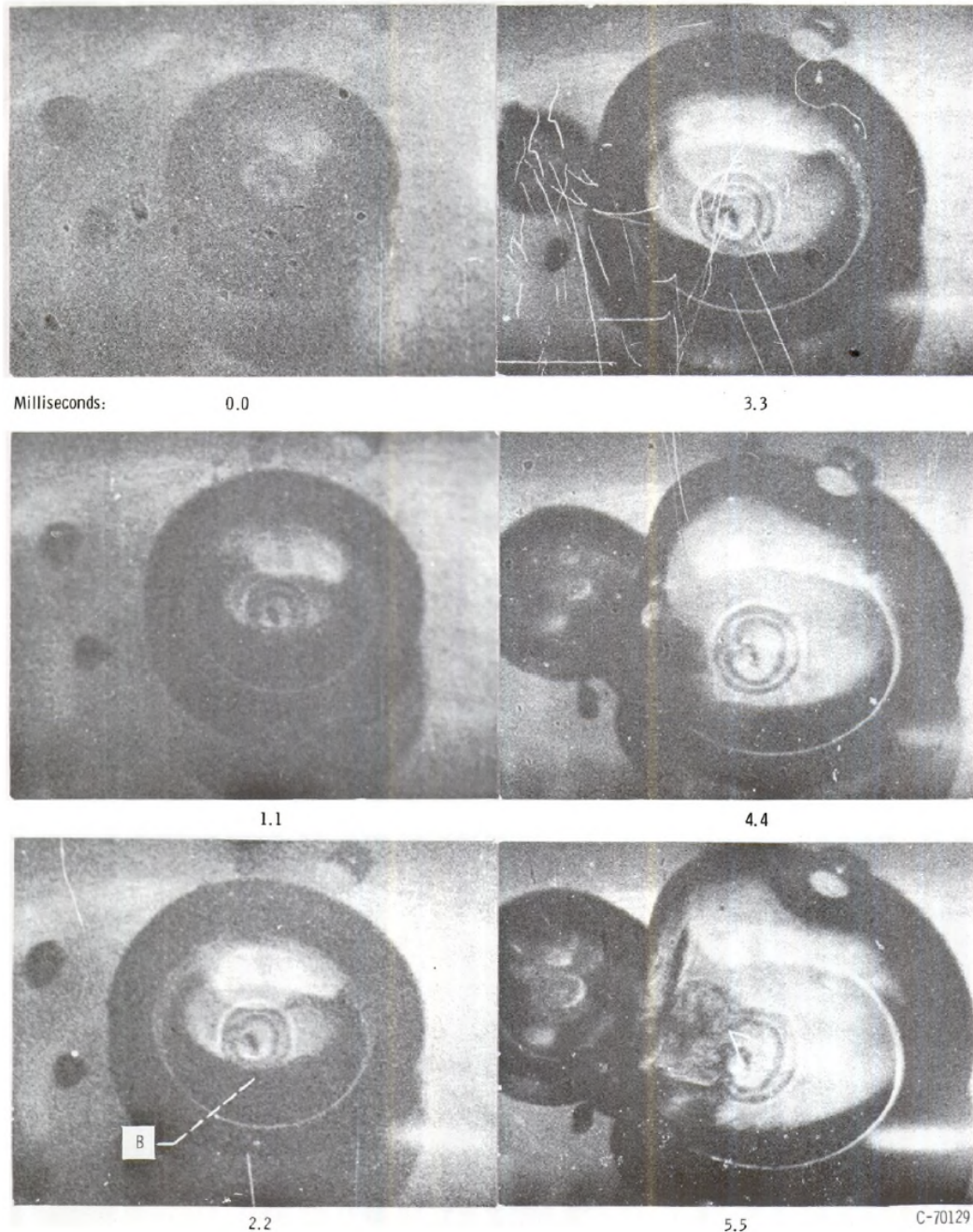


Figure 1.4: Photographic evidence of interference patterns revealing the presence of a microlayer underneath a nucleating bubble. From Sharp [57]

application such as PWRs.

Koffman and Plesset [63] were the first to obtain microlayer measurements for water using Jawurek's approach. They report an initial microlayer thickness of $1.85 \mu\text{m}$ for water while ethanol is 1.6 times larger. They also quantified the contribution of microlayer evaporation cannot exceed 50% of the total heat flux, especially at high subcooling. In these computations, it is always assumed that there is no significant radial water movement during the bubble growth, meaning the entirety

of the initial microlayer volume is evaporated.

Significant progress in the understanding of microlayer formation and evaporation is much more recent and leverages the advances in infrared instrumentation described in subsection 1.2.2. Kim and Buongiorno [29] proposed using infrared interferometry instead of visible light to measure the microlayer thickness. The technique, they baptized “DEPICT”, is also able to discriminate the phases in contact with the surface.

Gao et al. [64] relied on laser interferometry, similar to Koffman and Plesset’s [63] approach, to track the triple contact line as well as the microlayer thickness during bubble growth. They report microlayer thicknesses up to $4\ \mu\text{m}$ for ethanol on an Indium-Tin-Oxide (ITO) glass which are consistent with previous studies [59, 61, 63].

Jung and Kim [30, 31] applied a hybrid approach inspired by both Gao et al. and Kim and Buongiorno. They combined the laser interferometry technique of “Total Reflection” from Gao et al. to track the microlayer geometry and used infrared similar to Kim and Buongiorno’s [29] in order to track the temperature distribution underneath the bubble. They report microlayer thicknesses up to $3\ \mu\text{m}$. In their study, the microlayer contribution to the total heat flux is estimated to be 17%.

Recent direct numerical simulation based efforts by Guion [7, 65], Urbano [66] and Hänsch [67] have also shed further light on the dynamics of the microlayer, and are leveraged later in this thesis work.

1.3.2 Presence of a “Dry Spot” at the base of a bubble during its growth

The term “dry” is used in this context to refer to surfaces in contact with vapor instead of liquid during boiling. During the growth phase of a nucleating bubble, the triple contact line marking the boundary between the solid, liquid and gas phases stems out of the nucleation site. It quickly enlarges the heater surface in contact with the vapor and eventually retracts as the bubble necks down and departs from the nucleation site. Locally, the surface affected by the dry spot exhibits a transient temperature spike as the conduction through the vapor phase is a poor heat transfer mechanism. The qualitative shape of a dry spot during boiling as well as the experimental temperature and heat flux fields from Bucci and Richenderfer’s [5, 6, 34] experiment are shown in Figure 1.5. At the bottom of the images, a single large bubble footprint can be identified. The center of the bubble, where the dry spot is present, can be identified by locally high temperatures ($\approx 150^\circ\text{C}$) as well as low heat fluxes ($< 1\ \text{MW m}^{-2}$). Additionally, the bubble microlayer is observable in the form of a very high heat flux crescent ($\approx 8\ \text{MW m}^{-2}$) upstream of the bubble. The microlayer asymmetry underneath the bubble is explained by the upward flow which tilts the bubbles toward the downstream side. On the top part of the image, several large, irregular dry patches can also be seen and correspond to the coalescence of multiple smaller dry spots from different bubbles. This situation is dynamic; dry spots are regularly quenched as bubbles depart, until DNB is reached and an unquenchable spot develops and begins covering the entire heater.

The discovery of dry spots underneath a nucleating bubble followed a similar path to the studies of microlayer formation, as the two features of a growing bubble are physically close and related to each other via the triple contact line behavior. Partridge [68] first reported a triple contact line effect on the dry spot in 1929. In his study, he mentions that “With high rates of heat transfer the action beneath a bubble would be equivalent to a rapid drying-up of the thin edge of solution at the triple interface.”, which is an accurate assessment of the dry spot mechanism despite the

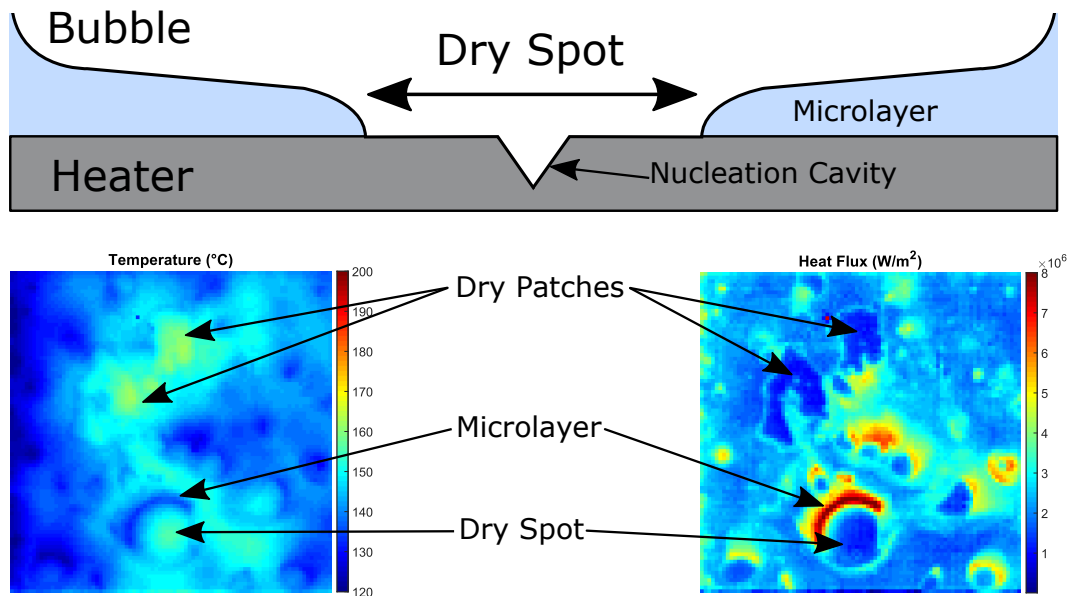


Figure 1.5: Example of a nucleating bubble and the dry spot at its base. The bottom images are experimental measurements of Temperature and Heat Flux from Richenderfer [5]

lack of direct photographic observation. Nukiyama [36, 37] briefly mentions Partridge in his original boiling crisis article but extensive studies investigating the phenomenon only began in the 1960s.

Sharp [57] provided the first photographic evidences of the existence of both a dry spot at the base of a bubble and a microlayer underneath the bubble (shown in Figure 1.4). Semeria [69] gave the most direct definition of dry spots as “Calefaction Spots”⁴ and provides a drawing that is not very different from current representations of dry spots. Semeria also notes these spots are accompanied by a local heater temperature rise, while direct measurements are extremely difficult. Kirby [70, 71] is also an early source of dry spots photographic evidence. Fiori and Bergles [72] first published a model for DNB that accounted for the presence of dry spots and their role in the boiling crisis. In particular, they realized the very local nature of CHF contrary to previous studies which instead considered the macroscopic film dryout was causing the temperature runoff. Their observation of heater surfaces after having experienced CHF, revealed the existence of pinholes that indicated the location where it occurred. Van Ouwerkerk [73] offers revealing photographs of a heater during boiling that display dry spot shapes and sizes. An example of the observed dry spots is shown in Figure 1.6. Voutsinos [61] was the first to develop the use of laser interferometry to track the dry spot behavior underneath a growing bubble.

Similar to the study of microlayers, the latest breakthrough occurred with the adoption of infrared thermometry allowing to probe the boiling surface at the most local scale. Theofanous [1, 2] finally demonstrated the local nature of CHF. The previously discussed BETA experiment subsection 1.2.1 lead Theofanous to conclude there is a great interest in investigating microlayer

⁴“Calefaction” is here used in its French meaning. English dictionaries (Collins, Merriam-Webster) only seem to refer to the term as “The act of heating / The state of being warm”. The French word “Caléfaction” is stronger and includes the effect of thermal isolation of a liquid from a heating surface. It is akin to the Leidenfrost effect in this sense. This is probably what Semeria meant here.



Figure 1.6: Visible Dry Spots on a pool boiling heater at 0.2 bar (fluid: n-heptane). From Van Ouwerkerk [73]

dynamics and growth of reversible and non-reversible dry patches. This avenue is explored separately by Kim [74] and Jung [3] who offer the clearest images to date of dry spots in a pool boiling experiment via high resolution infrared thermometry. Figure 1.7 shows the infrared thermometry results from Jung. The phase in contact with the heater is easily detected: the surfaces with low heat flux (right images, blue spots) and high temperature (left images, red spots) are dry while surfaces with higher temperature (left image, teal areas) and high heat flux (right images, orange areas) are wetted. Figure 1.8 shows example infrared images of a boiling surface for several subcooling (columns) and heat fluxes (rows). The DEPICT (DEtection of Phase by Infrared Thermography) method employed allows for a clear visualization of the phases in contact with the heater. The dry areas are in black while the white/grey areas correspond to the wetted surfaces.

Results from Kim [74] and Jung [3] are mostly consistent with each other and quantify for the first time the average dry area fraction along the boiling curve. Kim reports dry area fractions at CHF ranging from 20% in high subcooling cases up to 50% for saturated conditions. Jung observed dry area fraction of 18% at CHF. Chu [75, 76] also used total reflection methods with high speed cameras to observe the phases in contact with the surface. Chu reported dry area fractions at CHF between 50 to 55%. Figure 1.9 shows two visualizations of a single bubble from Chu. The left column is from a side view camera which offer limited perspective of the phase in contact with the heater. The right column is obtained via total reflection technique and produces a clear, almost binary image of the phases. In this figure, black pixels are wetted while white/grey pixels are dry.

The most advanced observations are usually the most recent. Kim [77] refined the DEPICT technique. Jung [4] recently improved the infrared thermometry technique in pool boiling to

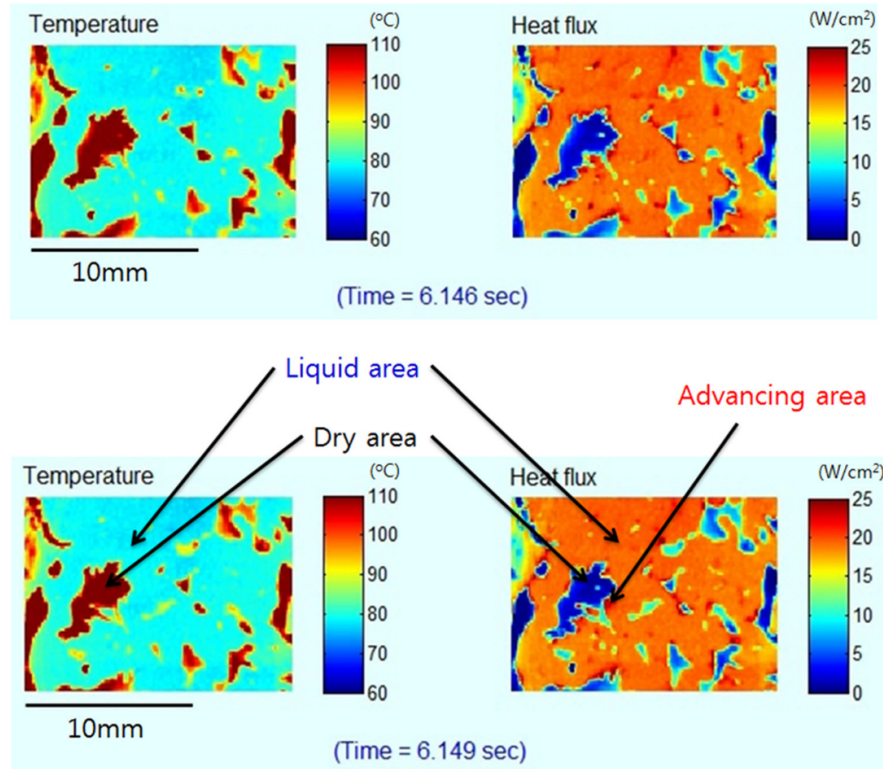


Figure 1.7: Dry spot visualization from infrared thermometry (fluid: FC-72). From Jung [3]

accurately track the triple contact line and dry area fraction on the heater. The reported dry area fraction at DNB for water at atmospheric pressure remains consistent with earlier studies (20-40%).

Almost all of the local dry area measurements described in this section are obtained in pool boiling conditions using water. Only few experiments were run with different fluids, such as Jung, who relied on FC-72 refrigerant, and some of the earliest studies from the 1960s which used organic fluids like methanol [57] or dichloromethane [61]. To this day, Bucci and Richenderfer [5, 6, 34] are the only ones who provide calibrated infrared thermometry as well as synchronized top-down high speed videos of a flow boiling experiment. Their contribution to understanding DNB mechanism is paramount to our effort. The high fidelity data they have produced is used in later chapters to validate the DNB model we propose. Richenderfer's dry spot images during flow boiling and up to CHF are consistent with earlier observations from Kim, Chu and Jung in pool boiling conditions. However, the dry area fractions at DNB observed by Richenderfer in flow boiling are much smaller than in pool boiling (on the order of 4 to 8%).

1.4 Conclusion and perspectives

Experimental progresses made over the last seventy years on boiling and CHF observation are tremendous and continue to be an active field of research. Imaging techniques such as infrared thermometry have opened up the possibility to probe the boiling surface with unprecedented precision. Such accuracy is necessary in order to complete our understanding of the physics at play during boiling. The complexity of the phenomenon limits our ability to distinguish individual effects as they are all happening simultaneously and influence each other.

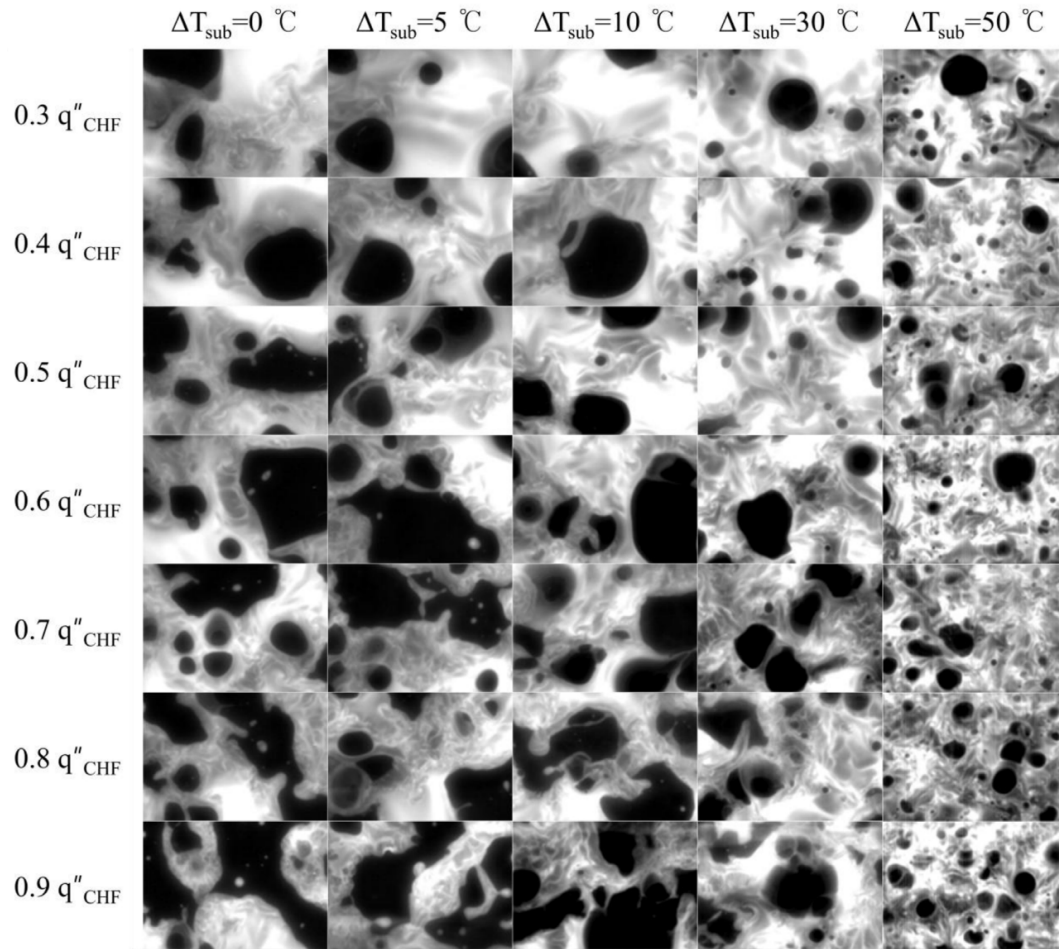


Figure 1.8: Dry spot visualization (fluid: water) with DEPIcT (DEtection of Phase by Infrared Thermography). From Kim [74]

Despite these challenges, scientists have proposed dozens of approaches and models to predict DNB based on the available data. The next chapter will cover the main approaches proposed over the past decades and their limitations when considering the most recent understanding we have described in this chapter.

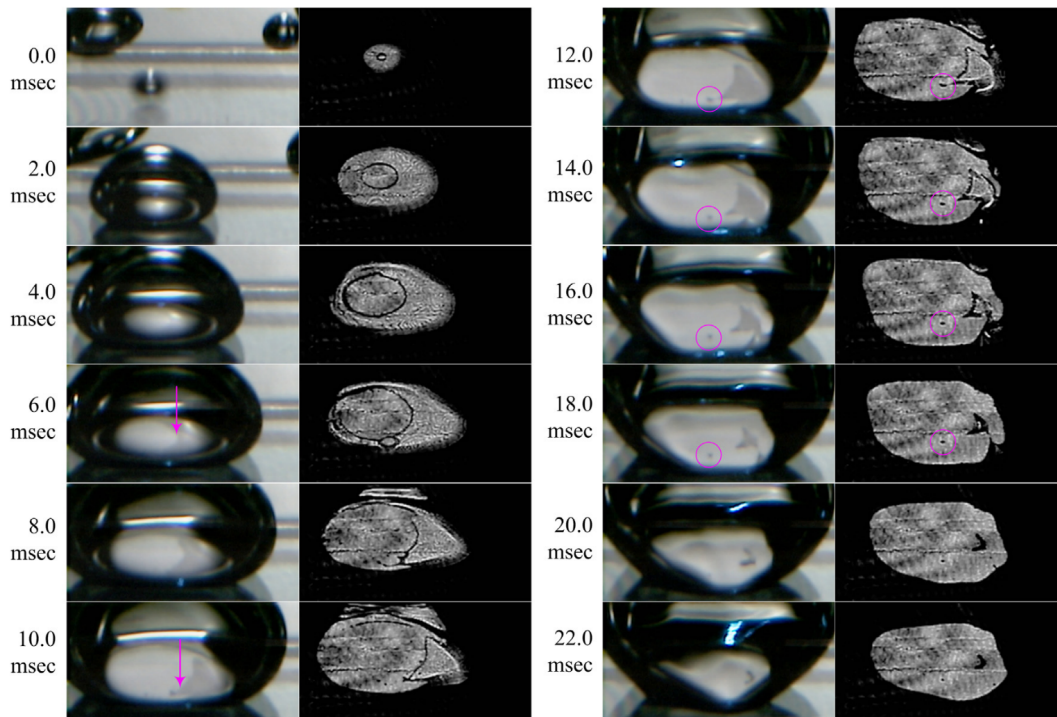


Figure 1.9: Dry spot visualization (fluid: water) using total reflection (right) and side view (left). From Chu [75]

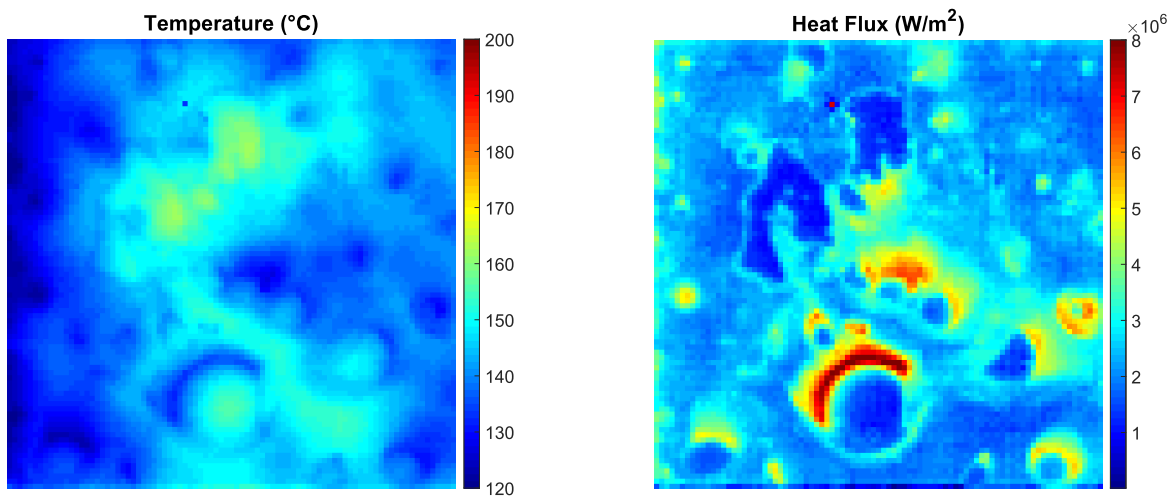


Figure 1.10: Infrared images of a water flow boiling experiment. Temperature (left) and heat flux (right). 1 bar, $500 \text{ kg m}^{-2} \text{ s}^{-1}$, 10 K subcooling. Adapted from Richenderfer [6]

Chapter 2

Current approaches to DNB modeling

Experimental observations and subsequent physical insights described in chapter 1 have been a source of inspiration for generations of scientists trying to model and predict CHF. Given the lack of a demonstrated, formal analytical description of bubble nucleation and DNB, many competing mechanisms have been proposed. In this chapter, we will describe the diverse attempts made over the past seventy years to capture the physics of DNB. We will distinguish three main types of approaches: the macro-hydrodynamics type of mechanisms, CHF correlations and Look-Up Tables (LUT). We will conclude the chapter with a review of recent attempts to model DNB that depart from the classic practice.

2.1 Macro-hydrodynamics mechanisms

One of the first idea to predict the occurrence of DNB is through experimental observations and mechanistic modeling. A scientist will postulate a mechanism triggering DNB and derive equations to describe it. A mathematical expression for CHF is then obtained from the balance between competing effects. The most referenced CHF model (Zuber's [21]) was one of the earliest attempt at capturing the mechanism causing DNB and multiple approaches have since branched out from his work. Mechanistic models rely almost exclusively on macroscopic scale hydrodynamics instability to explain the boiling crisis. In this section we will review the main approaches that have been proposed and are now well referenced but will not detail each and every single existing model. The reader can refer to several review articles that will provide detailed overviews of the field, including many aspects of CHF that are not considered in this work: Katto [78] gives an extensive overview of almost all aspects of CHF in the literature including microgravity boiling, transient boiling and other niche CHF conditions. Liang and Mudawar [79] propose a more recent (2018) update on pool boiling CHF, which covers a more narrow range of conditions but includes new models published since Katto's review. Finally, Celata [24, 80] conducted a thorough benchmarking of classic flow boiling DNB models and correlations.

2.1.1 Dimensional analysis (Kutateladze - 1948)

The first significant work on CHF mechanistic modeling is usually attributed to Kutateladze [19, 20] who proposed to quantify the physics at play during boiling crisis by relying on dimensional analysis to derive the resulting CHF expression. He postulated that CHF is driven by the competing effects of vapor inertia, surface tension and buoyancy when vapor is released from the heating surface as jets. In Kutateladze's work, the vapor jet velocity u_g is expressed as:

$$u_g = \frac{q''}{\rho_g h_{fg}} \quad (2.1)$$

where q'' is the wall heat flux, ρ_g the vapor density and h_{fg} the latent heat of vaporization. At CHF, Kutateladze balanced the kinetic energy of the departing vapor with the buoyancy force acting on the suspended liquid:

$$\rho_g u_g^2 \approx g (\rho_f - \rho_g) \delta_* \quad (2.2)$$

Where g is the gravitational acceleration, ρ_f is the liquid density and σ is the surface tension. δ_* is the linear scale of capillary disturbances, which is written as:

$$\delta_* = \left(\frac{\sigma}{g (\rho_f - \rho_g)} \right)^{1/2} \quad (2.3)$$

Equation 2.2 and 2.3 can be substituted in Equation 2.1 to obtain Kutateladze's CHF expression:

$$\dot{Q}_{CHF} = C h_{fg} \rho_g \left(\frac{\sigma g (\rho_f - \rho_g)}{\rho_g^2} \right)^{\frac{1}{4}} \quad (2.4)$$

The calibration constant C is equal to 0.16 in Kutateladze's original study but was later revised to 0.145 [81].

2.1.2 Vapor column instabilities (Zuber - 1959)

In his 1959's Ph.D. dissertation, Zuber [21] proposed that during boiling, bubbles generated from nucleation sites form vapor columns. When heat generation at the boiling surface increases beyond a critical point, the flow of steam jetting out of the nucleation sites becomes so intense that it blocks incoming liquid water from reaching the heater surface. When such a condition is reached the surface dries out and DNB occurs. Zuber's main postulate is that the boiling crisis is due to the interaction between Taylor's and Helmholtz's instabilities in the vapor columns as shown in Figure 2.1, where λ_H is Helmholtz length scale and λ_D is Taylor length scale. He extended Kutateladze's original equation to find Equation 2.5, where the calibration constant $C = \frac{\pi}{24} \approx 0.131$. Linehard and White [51] offer a revised and concise presentation of Zuber's model.

$$\dot{Q}_{CHF} = C h_{fg} \rho_g \left(\frac{\sigma g (\rho_f - \rho_g)}{\rho_g^2} \right)^{\frac{1}{4}} \left(\frac{\rho_f}{\rho_f + \rho_g} \right)^{\frac{1}{2}} \quad (2.5)$$

2.1.3 Liquid sublayer dryout (Katto - 1990, Celata - 1994)

Leveraging the experimental work from Gaertner and Westwater [82, 83], Hamamura and Katto [84] suggested a new type of mechanism causing CHF in pool boiling. They hypothesized that, at high heat flux, large bubbles form above the boiling surface and lead to the formation of a liquid layer trapped underneath. The vapor generated by the evaporation of the liquid sublayer reaches the large bubble through vapor columns stemming from the surface. In their model, CHF is reached when the liquid sublayer dries out before the vapor bubble departs from the surface.

Additional experimental evidence reinforcing the liquid sublayer theory in the context of subcooled flow boiling were brought forward by Tong [85], Fiori and Bergles [72], van der Molen [86] and Hino and Ueda [87]. Lee and Mudawar [88] were the first to adapt the liquid sublayer dryout approach to subcooled flow boiling DNB. The model they propose relies on three main assumptions:

- The vapor blanket velocity is equal to the superposition of the local liquid velocity and the relative vapor blanket velocity which is computed by a balance of buoyancy and drag forces exerted on the blanket.

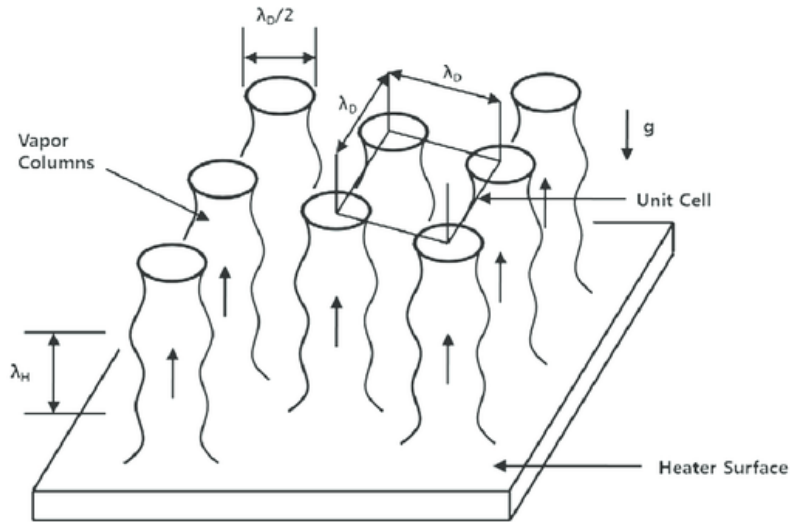


Figure 2.1: Schematic of Zuber [21] postulated DNB mechanism

- The length of the blanket is assumed to be equal to the critical Helmholtz wavelength.
- CHF occurs when the rate of liquid sublayer mass loss via evaporation exceeds the rate of liquid influx entering the sublayer

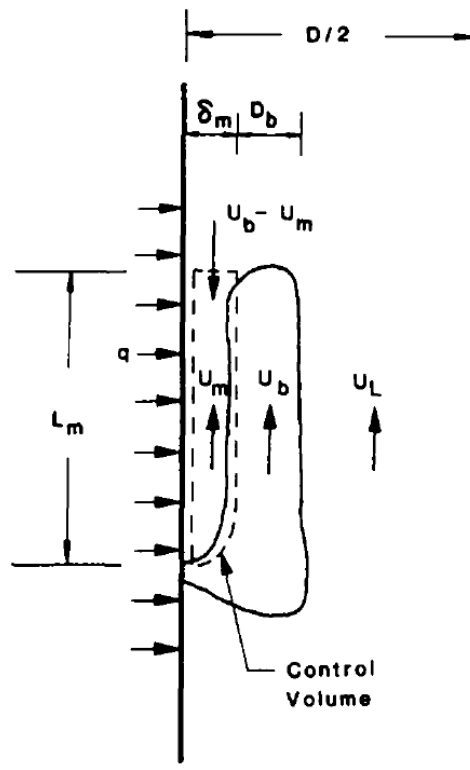


Figure 2.2: Schematic of Lee and Mudawar postulated DNB mechanism (adapted from [88])

The resulting DNB formulation is expressed as:

$$\dot{Q}_{CHF} = \frac{G_b \delta_b [h_{fg} a_b c_{p,f} (T_{sat} - T_f)]}{L_b} \quad (2.6)$$

Where G_b is the relative mass velocity of liquid, δ_b the sublayer thickness, h_{fg} the latent heat of evaporation, a_b an empirical constant, $c_{p,f}$ the fluid specific heat and L_b the vapor blanket length.

Lee and Mudawar proposed a set of closures to estimate each parameter as well as optimum empirical parameters depending on the closure choice. The validation study included water CHF data points from Doroshchuk [89] (560 points), DeBortoli [42], Weatherhead [43] and others (89 points). The dataset covered a large range of input parameters:

- Pressure : 4.9 MPa to 17.6 MPa
- Mass Flux : $1000 \text{ kg m}^{-2} \text{ s}^{-1}$ to $5200 \text{ kg m}^{-2} \text{ s}^{-1}$
- Tube Diameter : 4 mm to 16 mm
- Subcooling : 0 K to 59 K

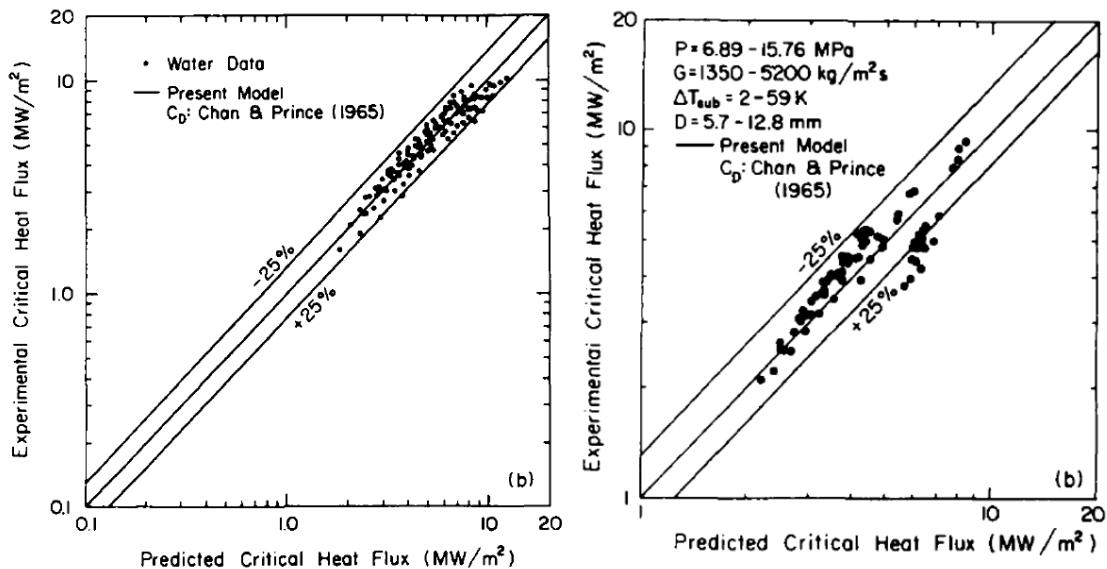


Figure 2.3: CHF prediction error scatters from Lee and Mudawar [88]. Left : Doroshchuk [89] database. Right : DeBortoli [42], Weatherhead [43] and others

The liquid sublayer dryout CHF hypothesis has been used by other groups to formulate alternative models. The main models in this family were proposed by Katto [23] and Celata [24, 25]. Katto's model extends the original pool boiling model to subcooled flow boiling and assumes the residence time of the vapor blanket τ is the limiting factor to DNB:

$$\dot{Q}_{CHF} = \frac{\delta_b \rho_f h_{fg}}{\tau} \quad (2.7)$$

$$\tau = \frac{L_b}{U_b} \quad (2.8)$$

$$L_b = \frac{2\pi\sigma(\rho_g + \rho_f)}{\rho_g \rho_f U_b^2} \delta = \frac{\pi(0.0584)^2}{2} \left(\frac{\rho_g}{\rho_f}\right)^{0.4} \left(1 + \frac{\rho_g}{\rho_f}\right) \frac{\sigma}{\rho_g} \left(\frac{\rho_g h_{fg}}{q_b''}\right)^2 \quad (2.9)$$

$$q_b'' = \dot{Q}_{CHF} - q_f'' c \quad (2.10)$$

Where L_b is the vapor blanket length and U_b the blanket velocity. The proposed CHF is then inversely proportional to the residence time τ .

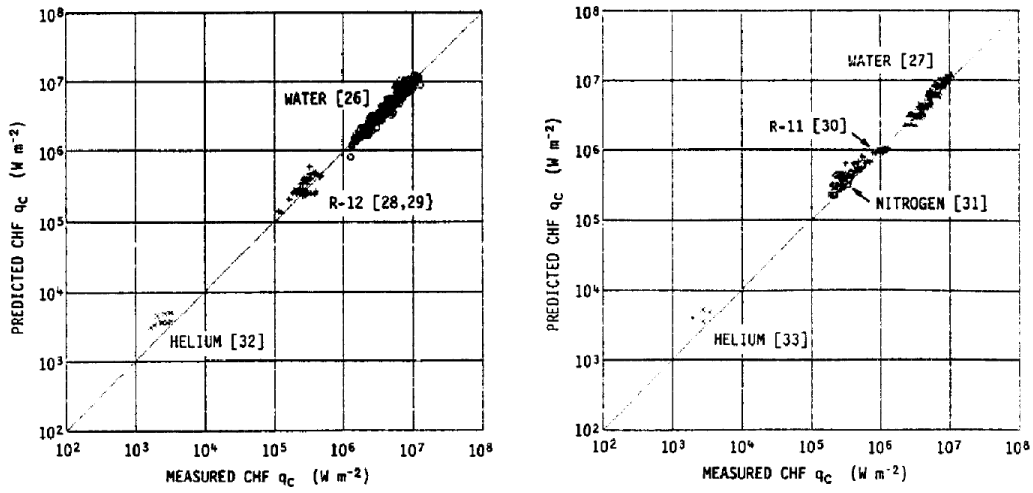


Figure 2.4: CHF prediction error scatters from Katto [23]

Celata's model [24] is very similar to Lee and Mudawar's liquid sublayer dryout model; the general mechanism triggering DNB is identical and many of the closures used are unchanged from Lee and Mudawar and Katto's models (vapor blanket length and velocity). The main difference in Celata's model stems from the liquid sublayer thickness modeling which is now formulated as the difference between the superheated layer thickness y^* and the vapor blanket equivalent diameter D_b .

$$\delta_b = y^* - D_b \quad (2.11)$$

The vapor blanket diameter is evaluated from an updated force balance model from Staub [90]:

$$D_b = \frac{32 \sigma f(\theta) \rho_f}{f G^2} \quad (2.12)$$

Where f is the friction factor and $f(\theta)$ is a function of the contact angle θ taken as 0.03 in Celata's model. The computation of y^* relies on the temperature distribution for turbulent flow in a tube by Martinelli [91]. Celata's model is benchmarked against a large data set (1888 points) covering a larger parameter space than Katto and Lee and Mudawar:

- Pressure : 0.1 MPa to 8.4 MPa
- Mass Flux : $1000 \text{ kg m}^{-2} \text{ s}^{-1}$ to $90\,000 \text{ kg m}^{-2} \text{ s}^{-1}$

- Tube Diameter : 0.3 mm to 25.4 mm
- Subcooling : 25 K to 255 K

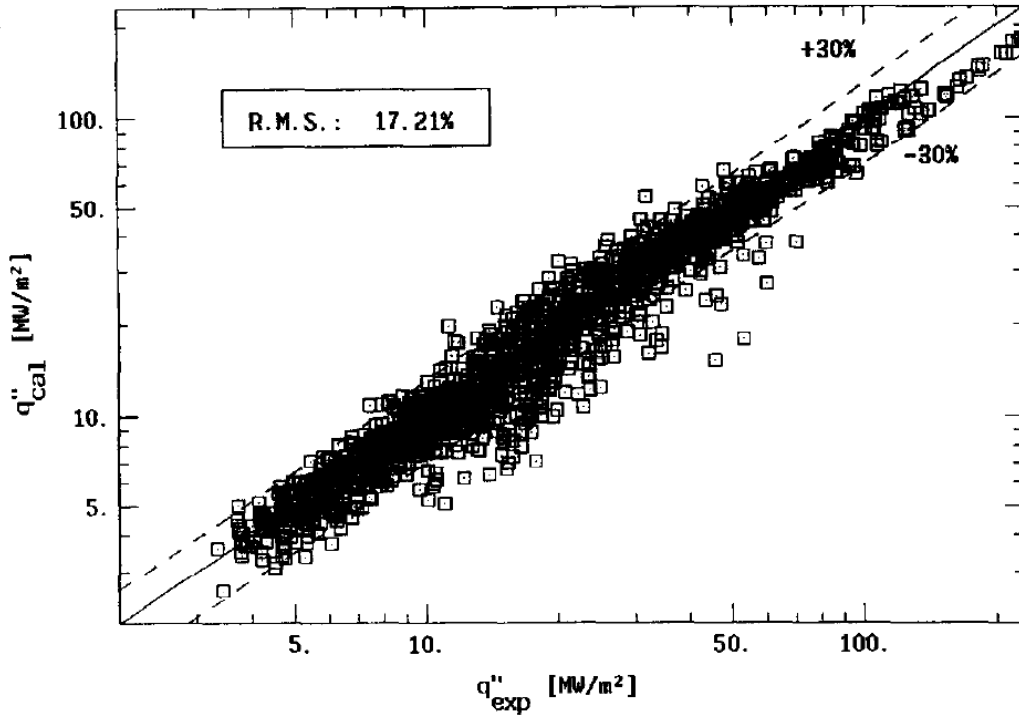


Figure 2.5: CHF prediction error scatters from Celata 1994 [24]

Celata, Cumo, Katto and Mariani together proposed the latest revision to the liquid sublayer dryout model in 1999 [25]. In this version, the CHF criterion is simplified as the authors argue that the growth of the vapor blanket is “strongly limited by adjacent blankets and by the steep velocity gradient”. They therefore assume that the vapor blanket thickness D_b is equivalent to the bubble departure diameter. After departing, the bubbles will coalesce into a distorted blanket of constant thickness. They postulate that the blanket can only exist at the near-wall region, inside the superheated liquid layer.

In this framework, CHF is detected when the superheated liquid layer thickness y^* is equal to the bubble departure diameter D_b .

$$y_{CHF}^* = D_b \quad (2.13)$$

D_b is computed from Equation 2.12 by Staub (previously proposed by Celata [24]). The friction factor is estimated with the Colebrook-White equation [92, 93] and the Levy rough surface model [94]:

$$\frac{1}{\sqrt{f}} = 1.14 - 2.0 \ln \left(\frac{0.72\sigma\rho_f}{fDG^2} + \frac{9.35}{Re\sqrt{f}} \right) \quad (2.14)$$

The authors rely on the temperature distribution by Martinelli [91] to solve for the wall temperature:

$$T(y^+) = T_w - QPr y^+ \quad 0 \leq y^+ \leq 5 \quad (2.15)$$

$$T(y^+) = T_w - 5QPr \left\{ Pr + \ln \left[1 + \left(\frac{y^+}{5} - 1 \right) \right] \right\} \quad 5 \leq y^+ \leq 30 \quad (2.16)$$

$$T(y^+) = T_w - 5Q \left[Pr + \ln(1 + 5Pr) + 0.5 \ln \left(\frac{y^+}{30} \right) \right] \quad y^+ \geq 30 \quad (2.17)$$

$$(2.18)$$

Where:

$$U_\tau = \left(\frac{\tau_w}{\rho_f} \right)^{0.5} \quad y^+ = \tau_w = \frac{fG^2}{8\rho_f} \quad y \frac{U_\tau}{\mu_f} \rho_f \quad Q = \frac{q''}{\rho_f c_{p,f} U_\tau} \quad (2.19)$$

$$Re = \frac{\rho u D}{\mu_f} \quad Pr = \frac{c_{p,f} \mu_f}{k_f} \quad (2.20)$$

The wall temperature is evaluated from the average exit temperature:

$$T_{out} = T_{in} + \frac{q'' 4L}{G D c_{p,f}} \quad (2.21)$$

The second equation to solve for the wall temperature is the integration of the temperature profile along the radius:

$$T_{out} = \frac{5}{y^+(R)} T_{out,1} + \frac{25}{y^+(R)} T_{out,2} + \frac{y^+(R) - 30}{y^+(R)} T_{out,3} \quad (2.22)$$

Where :

$$T_{out,1} = \frac{1}{5} \int_0^5 T(y^+) dy^+ \quad 0 \leq y^+ \leq 5 \quad (2.23)$$

$$T_{out,2} = \frac{1}{25} \int_5^{30} T(y^+) dy^+ \quad 5 \leq y^+ \leq 30 \quad (2.24)$$

$$T_{out,3} = \frac{1}{y^+(R) - 30} \int_{30}^{y^+(R)} T(y^+) dy^+ \quad y^+ \geq 30 \quad (2.25)$$

After T_w is known, the thickness of the superheat liquid layer y^* can be computed. This method, the authors claim, avoids the use of empirical correlations for the heat transfer coefficient (unlike previous liquid sublayer dryout models). The resulting model predictions against the same databases as Celata 1994 [24] are presented in Figure 2.6. The performance of the latest model is very similar compared to the earlier model: about 90% of the data points are predicted within $\pm 30\%$ with the 1999 model versus 84% for 1994's model. Standard deviations are also comparable (16.6% versus 16.4%). The authors note that the latest model[25], despite minimal improvements when compared to Celata's earlier model[24], is much simpler in its expression. They also concede that the model predictions suffer the most in conditions close to saturation where certain assumptions regarding the sublayer shape and size may no longer hold true.

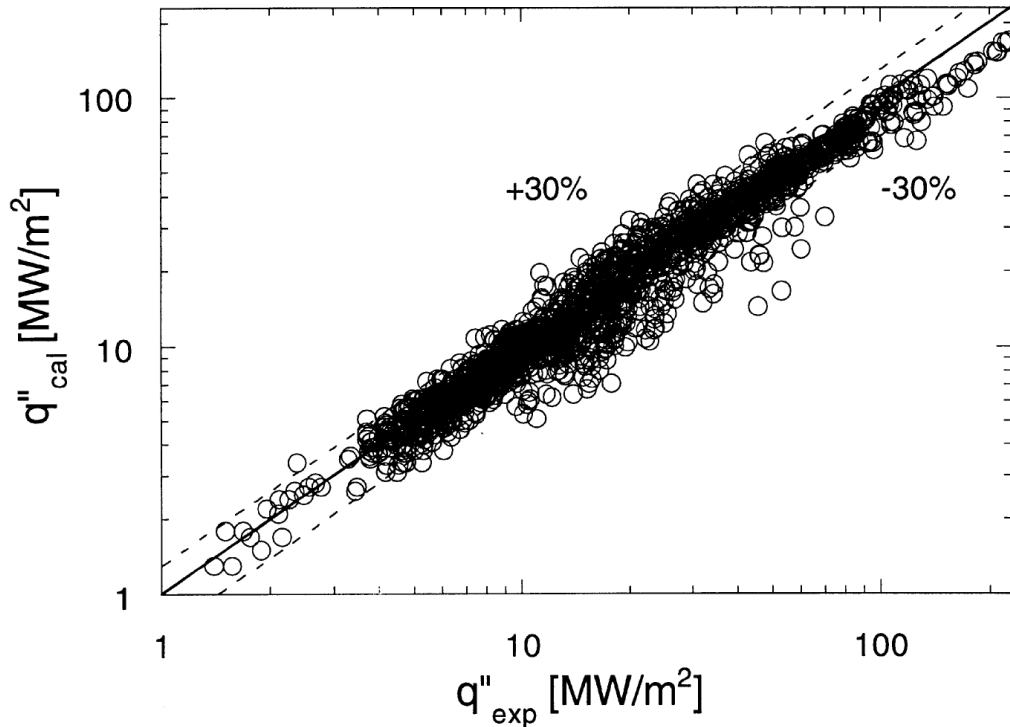


Figure 2.6: CHF prediction error scatters from Celata et al. 1999 [25]

2.1.4 Bubble crowding theory (Weisman & Pei - 1984)

Weisman and Pei proposed a CHF model [22] based on the existence of a bubbly layer accumulating into a vapor blanket near the heating wall as depicted in Figure 2.7. They claim CHF occurs when the vapor concentration in that near-wall bubbly layer reaches a critical value, which they estimate to be 82%. They report very good prediction for a wide range of subcooled flow boiling cases. They even claim their model performs much better than the reference W3 correlation (described in the next section).

However this new mechanistic approach has been criticized for being mainly empirical. Celata [80] questioned the validity of the near wall bubble crowding by citing a CHF experiment from Styrikovich [95] which reported near-wall void fraction at CHF as low as 30% and as high as 95%. More recently, Bruder [96] conducted a flow boiling experiment similar to the ones used by Weisman and Pei to justify their model. Bruder's experiment consisted of a vertical square channel instrumented with optical fiber probes that could measure void fraction near the heating wall. Bruder used Novec 649 (a refrigerant) as a fluid and reported void fraction profiles for various subcooling. At CHF, his results are consistent with Styrikovich's study and show a wide range of void fractions at critical conditions. Bruder's results at atmospheric pressure and fixed mass flux ($G \approx 1000 \text{ kg m}^{-2} \text{ s}^{-1}$) range from a low void fraction of 38% at 31K subcooling up to a highest value of 72% for 9K subcooling.

Despite the lack of strong experimental confirmations and the fact that this theory is quite different from Zuber's more popular model, Weisman and Pei's bubble crowding model has received renewed attention in the last 15 years for application in Multiphase Computational Fluid Dynamics (MCFD). The growth of MCFD has opened new avenues for engineers and researchers

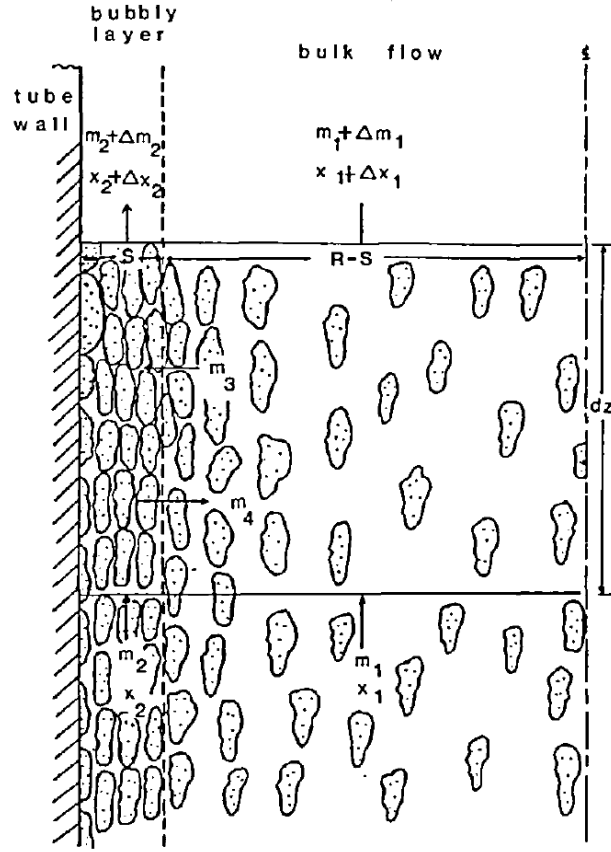


Figure 2.7: Schematic of Weisman and Pei postulated DNB mechanism (adapted from [22])

to simulate complex systems including boiling problems. CFD code developers had to implement a model able to drive the heat transfer transition from a nucleate boiling mode to a post-CHF mode based on a local parameter. Weisman and Pei's postulated bubbly layer critical value corresponded to an average void fraction of 82%. CFD codes can compute the average void fraction at an arbitrary near wall location and compare the resulting value to the critical number from Weisman and Pei's to drive the heat transfer mode transition. First implementations of this idea citing Weisman and Pei's initial article [22] are found in Alleborn [11] and Vyskocil and Macek [12]. This approach has become widely popular and adopted by multiple groups [13–18] since 2008.

2.2 CHF correlations

Faced with the complexity of the phenomenon and challenges associated with modeling the physics driving DNB, researchers have also pushed for more pragmatic approaches which ignore the physics at play and simply focus on predicting CHF from available inputs. These approaches are purely empirical and have to be considered from an engineering standpoint. While the question of which physics causes DNB has been up for debate for the past seventy years, engineers have had to dimension heat transfer systems leveraging practical CHF prediction tools.

The W3 correlation, also referred to as "Tong-67" [97] stemmed from efforts of the Westinghouse Electric Corporation to develop a predictive model for CHF that could be used in the design of

Pressurized Water Reactors (PWR) systems. The CHF, in the context of nuclear fuel is an upper limit for its power generation since the fuel cladding elements would not be able to withstand temperatures reached in a post-CHF regime. The W3 correlation is the result of a numerical optimization:

$$\dot{Q}_{CHF} = K_1 \cdot K_2 \cdot K_3 \cdot K_4 \cdot K_5 \quad (2.26)$$

$$K_1 = (2.022 - 0.06238P) + (0.1722 - 0.01427P) \exp((18177 - 0.5987P)x_e) \quad (2.27)$$

$$K_2 = (0.1484 - 1.596x_e + 0.1729x_e|x_e|) 2.36G + 3271 \quad (2.28)$$

$$K_3 = 1.157 - 0.869x_e \quad (2.29)$$

$$K_4 = 0.2664 + 0.8357 \exp(-124.1D_e) \quad (2.30)$$

$$K_5 = 0.8258 + 0.0003413 (h_f - h_{in}) \quad (2.31)$$

Variable	Description	Range	Unit
P	Pressure	5.5-16	MPa
G	Mass Flux	1356 - 6800	$\text{kg m}^{-2} \text{s}^{-1}$
D_{he}	Heated Diameter	15 - 18	mm
x_e	Equilibrium Thermodynamic Quality	-0.15 to 0.15	[-]
L	Heated Length	0.234 - 3.7	m

Table 2.1: Range of validity of the W3 CHF correlation parameter space

2.3 Look-Up Tables

Faced with the difficult challenge of understanding the mechanisms triggering DNB, several groups proposed a radically different approach to the problem. Instead of predicting CHF based on a physical mechanism, they would simply catalog and tabulate all available CHF data for a set of predefined conditions. The result of their work is published as a series of Look-Up Tables (LUT) spanning a very large range of thermal hydraulic conditions. The first LUT was published in russian by Doroshchuk [89] in 1975, which proposed a methodology relying on tabulating and normalizing CHF data for 8 mm vertical round tubes. This initial methodology was expanded by Groeneveld in Canada in 1986 [98], and updated in 1995 [99]. In parallel, the Soviet Union and then Russia continued their efforts on LUT which became public in 1991 [100]. The 2 groups merged their work and published a unified LUT in 2006 [46].

LUT are very practical and easy to use for engineering applications but also come with limitations. Tabulated data only concerns vertical round tubes with upward flow and the only fluid for which LUT are available is water. Also, data is tabulated against three parameters: pressure, equilibrium thermodynamic quality and mass flux. Therefore, in order to standardize the results, the data is given for a single 8 mm tube diameter. For diameters smaller or larger than the one tabulated for, the authors [99] proposed a scaling law.

For $0.002 \text{ m} \leq D_{hy} \leq 0.025 \text{ m}$,

$$\frac{\dot{Q}_{CHF}(D_{hy})}{\dot{Q}_{CHF}(0.008\text{ m})} = \left(\frac{0.008}{D_{hy}}\right)^{0.5} \quad (2.32)$$

and for $D_{hy} > 0.025\text{ m}$,

$$\frac{\dot{Q}_{CHF}(D_{hy})}{\dot{Q}_{CHF}(0.008\text{ m})} = 0.6 \quad (2.33)$$

The effect of tube diameter on CHF has been studied by other groups and different scaling laws have been proposed. Concurrently to Groeneveld's 1996 LUT update, Celata [101] reviewed the scaling laws proposed by Doroshchuk [89] and Smith [102] and compared them to Groeneveld's proposed scaling. He concluded that a single scaling law would provide the best fit for a wide range of pipe diameters, from 0.5 mm up to 32 mm. Celata's scaling is expressed as:

$$\frac{\dot{Q}_{CHF}(D_{hy})}{\dot{Q}_{CHF}(0.008\text{ m})} = \left(\frac{0.008}{D_{hy}}\right)^{1/3} \quad (2.34)$$

In a more recent review, Tanase et al. [103] reviewed the many scaling laws proposed over the years and their CHF prediction performance; his conclusion recommends three changes to Groeneveld's original scaling law:

$$\frac{\dot{Q}_{CHF}(D_{hy}\text{ mm})}{\dot{Q}_{CHF}(0.008\text{ m})} = \left(\frac{0.008}{D_{hy}}\right)^n \quad (2.35)$$

- (i) Generally, use $n = 0.4$ to 0.45 instead of 0.5 .
- (ii) In subcooled conditions, use $n = 0.25$ to 0.33 .
- (iii) At low mass flux ($G < 250\text{ kg m}^{-2}\text{ s}^{-1}$), use $n = -0.2$ to -0.3

The data produced in LUT is extensively post treated for outlier detection and smoothing purpose. Due to the varied raw data origins, there is an inherent uncertainty associated with LUT.

Gaps in the parameter space are also a source of uncertainty with LUT. The tables themselves cover the entire parameter space uniformly, but the underlying experimental data used for their generation may be lacking for certain range of conditions. Conditions where data is sparse include:

- (i) High mass flux and high thermodynamic qualities
- (ii) Low mass flux and low thermodynamic qualities (subcooled)
- (iii) Pressures ranging from 0.2 MPa to 0.5 MPa

Studies have also been conducted in order to assess the use of LUT for horizontal tubes [104], the use of heated diameter against hydraulic diameter for CHF scaling [105], and whether the thermodynamic quality should refer to the local or inlet value [106].

Finally, being normalized for a single tube of fixed diameter, LUT are blind to the geometry. Industrial applications such as nuclear fuel assemblies are often a far cry from the idealized geometry considered in LUT. The presence of spacers maintaining fuel rods in a tight bundle and significantly mixing the flow alters CHF. In this case, LUT results are modified to account for the actual geometry. The rod spacer effect cannot be derived analytically and require extensive experimental test campaigns in order to calibrate scaling coefficients.

2.4 Recent proposal and advances in CHF modeling

Trying to identify recent attempts to advance the modeling of CHF, we can cite Bricard et al. [107] who developed mechanistic models based on the idea of a nucleation site dryout. They already suspected CHF to be a very local phenomenon but were limited in their effort by the poor quality of observations available at the time. Their group postulated that the dry patch growth underneath a bubble causes a temperature rise. In their model CHF occurs when the temperature rise due to the dry spot becomes close to the Leidenfrost temperature. This idea has since been disproved by more recent experiments reporting that local wall temperatures remain much below the Leidenfrost point when CHF is triggered [6]. Nonetheless this idea of a non equilibrium situation at the dry spot level was expanded a few years later by Nikolayev [108, 109] while still remaining tied to macroscopic hydrodynamic theories.

J. Jung and S. J. Kim [3] suggested investigating the energy balance between wet and dry areas as a possible CHF triggering mechanism in their conclusion. However none of their subsequent publications explored that idea further. Recently, S. Jung and H. Kim argued [4], based on their observations in four experimental conditions, that the rewetting process fails when the triple contact line density from bubbles on the surface reaches a critical value of 1.5 mm^{-1} .

Ha and No [110, 111] proposed an early model for prediction of CHF based on dry spots by constraining their triggering mechanism to a critical number of dry spots (five) merging on the surface. Together with the assumption that nucleation sites are distributed randomly on the surface (see Gaertner [112]), they were able to compute the probability of a dry spot forming from the merging of at least five bubbles on the surface. The simple model proposed is expressed as:

$$q = q_b N'' (1 - P(n \geq n_c)) \quad (2.36)$$

Where q is the wall heat flux, q_b is the heat removed by a single bubble, N'' is the number of active nucleation sites, $P(n \geq n_c)$ is the probability more than n_c sites exist within the area of influence of a bubble. n_c is the critical number of sites causing DNB; Ha and No propose $n_c = 5$.

More recently, Choi, No and Kim [113] have proposed a new “Dry patch model”, which assumes there exists a critical size for dry patches (resulting from the coalescence of individual dry spots) which triggers the boiling crisis as the wall temperature reaches the Leidenfrost point. The computational method described relies on CFD simulations to predict the dry patch size corresponding to the region near the dry patch reaching the Leidenfrost temperature. The number of individual dry spots needed to coalesce into the critical patch size is then estimated, and finally, the merging probability is computed with an approach similar to Ha and No’s dry spot model [110, 111]. The equations proposed are:

$$K_{dry} = 1 - \frac{1}{2} \left[1 + \operatorname{erf} \left(\frac{\sqrt{\pi} R_{dry}}{\sqrt{2N''}} \left(\frac{1}{D_d^2} - N'' \right) \right) \right] \quad (2.37)$$

$$q''_{wall} = (1 - K_{dry}) q''_{nb} + K_{dry} q''_{vap} \quad (2.38)$$

Where K_{dry} is the dry area fraction corresponding to the probability of creation of a critical size dry patch. R_{dry} is the critical dry patch radius, N'' is the number of active nucleation sites, D_d is the bubble departure diameter, q''_{wall} is the total heat flux at the wall, q''_{nb} is the nucleate boiling heat flux and q''_{vap} is the heat flux removed directly by the vapor phase. Recently, No et al. [114] published a comparison of both the “Dry Spot” and “Dry patch” models, from which Figure 2.8 is adapted.

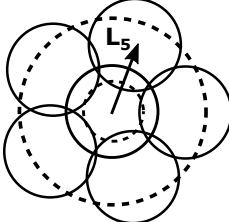
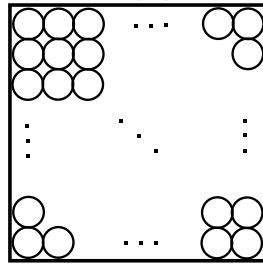
	Dry spot model	Dry patch model
Onset of unquenchable dry spot/patch formation	Unquenchable dry spot generation when a dry spot is surrounded by 5 neighbor bubbles in a cell.	Unquenchable dry patch generation when its number of dry spots reaches the critical one for coalescence of dry spots with its size exceeding Leidenfrost temperature at its peripheral.
		
Dry area fraction	$P(n) = \frac{e^{-\bar{N}A} (\bar{N}A)^n}{n!}$ $P(n \geq n_c) = 1 - \sum_{n=0}^{n_c-1} P(n)$	$n_{dry} = [(nR_{dry}^2)^{0.5}/D]^2$ $P(n \geq n_{dry}) = 1 - \sum_{n=0}^{n_{dry}-1} P(n)$

Figure 2.8: Description of Dry Spot and Dry Patch models from No and Ha (Adapted from[114])

2.5 Inconsistencies and model limitations of current approaches

CHF mechanistic models, correlations and Look-Up Tables are widely employed in the industry and can be found in subchannel and system codes like COBRA-TF and RELAP5. However, they are limited by their approach to predicting DNB: by ignoring the physics of boiling and DNB as described in chapter 1 (correlations and LUT) or postulating now disproved mechanisms (mechanistic models), they are unable to reproduce effects related to the heater surface properties. Moreover, they are all challenged by complex geometry effects on CHF. Corrective factors can be used to improve predictions for tube bundle geometry and spacer grid effect but have to be determined experimentally and constitute an *a posteriori* numerical fitting. Today, there is no model able to consistently predict CHF in complex geometries without extensive tuning. In order to alleviate these limitations, a new model should first aim at reproducing the current physical understanding of DNB and incorporate the micro-scale sensitivities that have been identified. Only then can this new model attempt to tackle complex flow conditions.

Chapter 3

MIT flow boiling loop

This chapter focuses on the main source of validation data that we will rely on in order to demonstrate the soundness of our approach. As described in chapter 1, the most advanced subcooled flow boiling imaging techniques have been produced by professor Bucci’s group at MIT [5, 6, 34].

The MIT Flow Boiling loop is the result of a multi-year effort to develop the experimental capability to measure boiling at its smallest scale with infrared and visible spectrum high speed video cameras, up to CHF. The experimental data used in this thesis in large part derive from Richenderfer’s thesis [5] as well as personal communication with professor Bucci and his team. The chapter first describes the experimental apparatus in section 3.1, then expands on the flow conditions that were acquired and the post-processing techniques that were deployed to extract fundamental boiling quantities in section 3.2. Finally, section 3.3 tabulates the datasets used for validation in the subsequent chapters.

3.1 Experimental apparatus

The experimental loop consists of a vertical rectangular channel of $1\text{ cm} \times 3\text{ cm}$ with an L/D of 60. The heater section drawn in Figure 3.1 shows the four viewing windows allowing for top-down and side view acquisitions with high-speed cameras while the back side window is for the infrared acquisition. The heater itself is made of a thin layer of Indium-Tin-Oxide (ITO) deposited on a sapphire substrate. The ITO film is 700 nm thick while the sapphire is 1 mm thick.

The infrared camera capturing the backside of the heater recorded series of images for 2 s at 2500 frames per second. High speed cameras could record the heater top and side view at 10,000 frames per second but offered limited use as soon as significant boiling occurred on the surface.

This data set offers the most detailed visualization of subcooled flow boiling to date, allowing the extraction of the fundamental boiling quantities needed to develop the model closures. The test campaign results detailed in Richenderfer’s thesis include both atmospheric and higher-than-atmospheric conditions (2, 5 and 10 bar).

Several features of this experimental test campaign are of note:

- **Spatial resolution:** The infrared image covers the $1 \times 1\text{ cm}$ heater with 87×87 pixels. It corresponds to a resolution of $1.32 \times 10^{-8}\text{ m}^2$ per pixel. This limits the size of the bubble footprints that can be resolved. At atmospheric pressure, bubbles reach diameters on the order of millimeters which can easily be distinguished on the surface. Cases with high subcooling ($\geq 50\text{ K}$) and/or higher than atmospheric pressure produce bubbles which are smaller than the area covered by a single pixel. Starting at 2 bar and especially at 5 bar and

10 bar, individual active nucleation sites become impossible to distinguish as soon as boiling begins.

- **Time Resolution:** The acquisition frequency of 2500 frames per second corresponds to a period of 0.4 ms and fundamentally limits the detection of fast periodic signals. Nyquist–Shannon sampling theorem [115] indicates that frequencies higher than 1250Hz cannot be resolved during the acquisition process and may create an apparent frequency saturation effect during post-processing.
- **Heater geometry:** The experimental flow channel was designed in order to generate a fully developed flow profile at the entrance of the heated section section. This is achieved by using an entrance region sufficiently long to let the flow develop ($L/D = 60$). The flow channel consists of a 3×1 cm square section. The flow is also preheated to desired temperatures in order to control the subcooling. With this approach, the temperature profile reaching the heating section is flat. Considering the small heater size (1×1 cm), the temperature profile is not fully developed along the heater. Consequently, the single phase heat transfer is very heterogeneous in the heater axial direction.
- **Heater material:** The sapphire substrate on which the ITO heating element is deposited is larger than the heating surface. The heat generated at the ITO-Water interface can be removed in two ways: either directly via nucleate boiling or by conduction through the solid sapphire. In the latter case, the heat diffuses in the surrounding sapphire and is then removed by forced convection in the sapphire-Water contact interface. This effect limits the fraction of the heat that will be directly removed by the ITO interface and is most visible at low heat fluxes before the onset of nucleate boiling. A high fidelity single phase CFD simulation using conjugate heat transfer to include the sapphire and ITO body revealed almost one third of the heat generated by the ITO was flowing through the sapphire and wasn't removed at its surface. This effect is accounted for in the numerical post-processing of the infrared camera acquisition in order to correctly estimate the heat removed directly by the fluid above the heater.

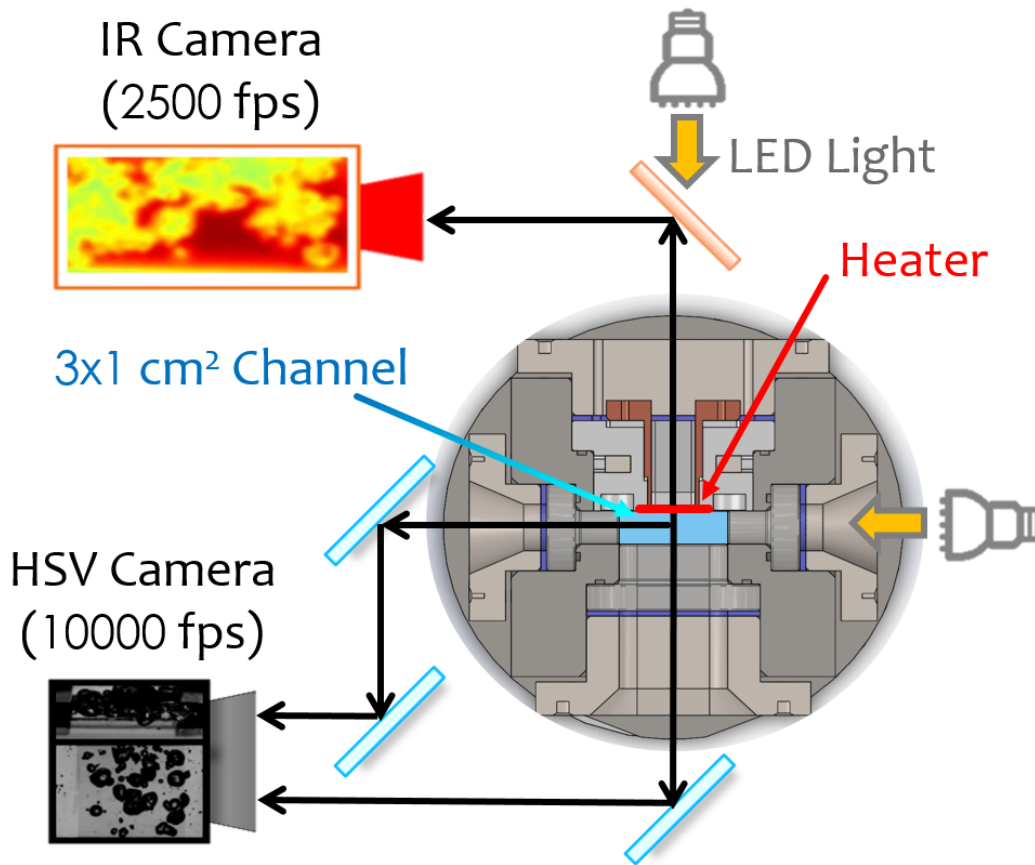


Figure 3.1: Diagram of a top-down view of the camera instrumentation of Richenderfer's PETHER loop (from [5])

3.2 Available experimental data sets and post-processing methods

The infrared camera used in the experimental campaign generated photon counts that were post-processed in order to obtain the heat flux emitted by the heating surface. Rather than using a static calibration curve, Bucci [34] developed a numerical scheme to converge to the exact temperature and heat flux distribution on the ITO surface that will emit the radiation measured by the camera sensor. This inverse radiation-conduction model was also used by Richenderfer [6] to generate the experimental database we leveraged in this work. Each flow condition included multiple heat generation rate that covered the entire boiling curve, starting from single phase convection up to CHF.

From these heat flux and temperature recordings, we developed processing scripts to extract basic information like the boiling curve as well as more advanced quantities such as the number of active bubble generating sites on the surface, the bubble departure frequency.

For a given test condition, the temperature and heat flux data post-processed from the raw infrared camera acquisition are represented as 3D matrices: $M(X, Y, T)$. The boiling curve is created by computing the time and space average for each condition of the boiling curve. The coordinate of

a point on the boiling curve is computed from the following equation:

$$\langle\langle T \rangle\rangle = \frac{1}{N_X N_Y N_T} \sum_{X=1}^{N_X} \sum_{Y=1}^{N_Y} \sum_{T=1}^{N_T} T(X, Y, T) \quad (3.1)$$

$$\langle\langle HF \rangle\rangle = \frac{1}{N_X N_Y N_T} \sum_{X=1}^{N_X} \sum_{Y=1}^{N_Y} \sum_{T=1}^{N_T} HF(X, Y, T) \quad (3.2)$$

Where N_X and N_Y are the infrared image resolution in x and y coordinates, and N_T the number of frames acquired.

Areas affected by bubble nucleation and departure cycles experience large fluctuations in time of their local heat flux while areas only subjected to single phase forced convection will experience smaller fluctuations. This allows for the detection of active nucleation sites via a metric quantifying the level of heat flux activity seen by each pixel. We created the following metric:

$$W_{sites}(X, Y) = \sum_{T=2}^{N_T} |HF(X, Y, T) - HF(X, Y, T - 1)|^m \quad (3.3)$$

The summation of the absolute difference between 2 subsequent heat flux samples produces a quantity similar to the time integration of the absolute value of the heat flux time derivative. The power factor m , can be used to enhance the high activity locations preferentially, similarly to a high pass filter, in order to facilitate the active nucleation site identification. We found that using a default value of $m = 1$ was sufficient in most cases. the resulting metric W_{sites} is a 2D image which contains high activity spots where bubbles have nucleated and low activity areas where no bubbles nucleated.

A Gaussian filter (low pass filter) may be used as a pre-processing step in order to smooth out numerical noise and avoid spurious detection of multiple sites in a single high activity spot. A pre-processing binary mask filter is also used to discard site coordinates which are not in a high activity region. The 75th percentile of the activity metric is used as a cutoff for the binary mask. Every pixel below this threshold is turned to zero, thus only leaving "islands" of high activity to be detected.

The pre-processed metric is then analyzed with a local high value detection algorithm in order to pinpoint the central location of each high activity spot, thus marking the coordinates of individual active nucleation sites. An example of the detection capabilities of the post-processing script is shown in Figure 3.2 for a single heat flux condition. The high activity regions in red and orange correspond to the bubble nucleation locations with the detected nucleation site location marked with a red cross. The low activity regions where no bubble nucleate are identifiable as blue and teal.

For each detected active nucleation site, a 1D time signal is extracted from windowing the heat flux matrix around the nucleation site coordinate (3×3 pixels) and running a simple space averaging step. The heat flux time signal of an active site experiences periodic peaks corresponding to bubble nucleation events. These peaks can easily be detected and tracked. Figure 3.3 shows the heat flux signal and the departure events that were detected when using this method for a single nucleation site. The number of frames between subsequent departures is a time period. The heat flux acquisition time (1 s) is sufficiently long to collect hundreds of departure events which are statistically post-treated.

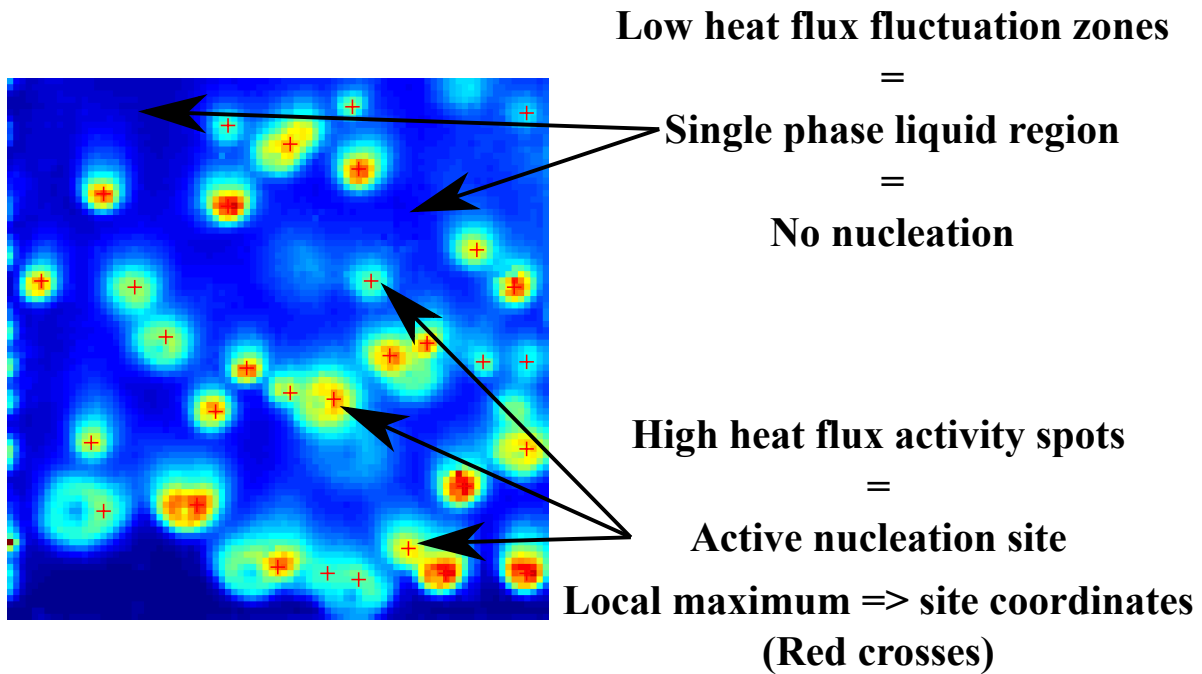


Figure 3.2: Heat flux activity metric example map with an overlay of the nucleation site coordinates (red crosses) detected with the post-processing algorithm. Conditions: 1 bar, 10 K subcooling, $1000 \text{ kg m}^{-2} \text{ s}^{-1}$, 2200 kW m^{-2} heat flux applied to the ITO

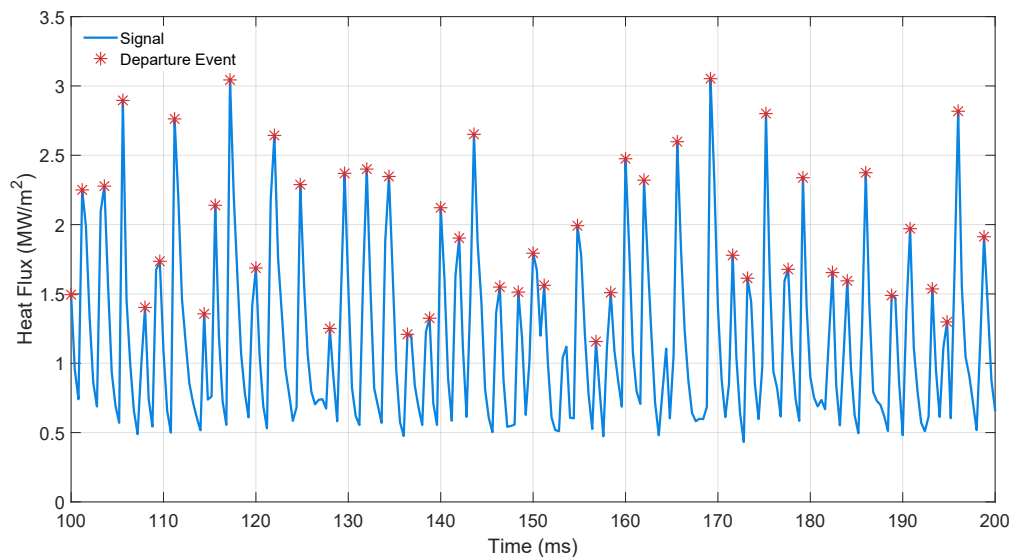


Figure 3.3: Example result of the bubble departure event detection for a single nucleation site signal. Conditions: 1 bar, 10 K subcooling, $1000 \text{ kg m}^{-2} \text{ s}^{-1}$, 2100 kW m^{-2} heat flux applied to the ITO

In theory, a simple mean average of the measured periods would be sufficient to characterize each site but in reality, spurious events such as a sliding bubble or experimental apparatus vibration can temporarily affect the time signal and alter the period measurement. These perturbations usually manifest as abnormally long departure periods in the signal. They can be filtered out of the period distribution by running a low pass filter which will exclude periods longer than the 95th percentile of the distribution.

After collecting the median period of every single nucleation site for a given heat flux condition, a new period distribution is created. This time representing the various characteristic time periods present on the heater surface. Similarly to the previous steps, abnormally high values are excluded from consideration via a low pass filter. Once the distribution is clean out of outliers, the median period is inverted to produce the average heater frequency for a particular condition. These processing steps are automated for all conditions and all cases.

3.3 List of test case conditions available for validation

In total, we compiled data sets for 18 cases (full boiling curves up to CHF) at 1 bar, of which we selected 14 for the validation study. Four cases were discarded as the time and/or space resolution of the infrared camera acquisition was not sufficient to accurately process the raw data and extract the number of active nucleation sites. The 14 cases are listed in Table 3.1 where a horizontal marker separates the first 6 cases that do not appear in Richenderfer’s thesis, from the following 8 which can be found in [5]. The second column of the table is used to mark the heaters that were reused from case to case as reported by Richenderfer.

Table 3.1: Test cases inputs and corresponding measured CHF

Case	Heater	Pressure (bar)	Subcooling (K)	Mass flux (kg/(m ² s))	Experimental CHF (MW/m ²)
1		1 ± 0.025	10 ± 0.5	500 ± 10	2.45 ± 0.05
2		1 ± 0.025	10 ± 0.5	750 ± 10	3.03 ± 0.05
3		1 ± 0.025	10 ± 0.5	1000 ± 10	3.33 ± 0.05
4		1 ± 0.025	25 ± 0.5	500 ± 10	4.28 ± 0.05
5		1 ± 0.025	25 ± 0.5	750 ± 10	4.88 ± 0.05
6		1 ± 0.025	25 ± 0.5	1000 ± 10	5.38 ± 0.05
7	A	1 ± 0.025	5 ± 0.5	1000 ± 10	3.48 ± 0.05
8	B	1 ± 0.025	5 ± 0.5	1500 ± 10	3.59 ± 0.05
9	B	1 ± 0.025	5 ± 0.5	2000 ± 10	4.22 ± 0.05
10	A	1 ± 0.025	10 ± 0.5	1000 ± 10	3.67 ± 0.05
11	A	1 ± 0.025	10 ± 0.5	1500 ± 10	4.60 ± 0.05
12	B	1 ± 0.025	10 ± 0.5	2000 ± 10	5.10 ± 0.05
13	C	1 ± 0.025	20 ± 0.5	1000 ± 10	4.57 ± 0.05
14	C	1 ± 0.025	20 ± 0.5	2000 ± 10	5.98 ± 0.05

Richenderfer also investigated the effect of the surface contact angle by varying the heater material. To this effect he tested a second type of heater based off the original Sapphire-ITO design. This alternative heater is called “Layer-by-Layer” (LbL) due to its fabrication process. A summary of the two heater types is as follow:

- **Sapphire-ITO heater.** A heater consisting of a 1mm thick, IR trans- parent Sapphire substrate,

coated with an IR opaque, electrically conductive Indium Tin Oxide (ITO) coating.

- **Super-hydrophilic heater.** A sapphire-ITO heater that has been coated with a 1 μm thick porous layer made of hydrophilic Silicon dioxide (SiO_2) nanoparticles, rendering the surface super-hydrophilic. Also referred to as a “Layer-by-Layer” (LbL) deposition.

The contact angle of a regular sapphire-ITO heater is approximately 85° while the LbL contact angle is effectively less than 5° . The LbL heater was only tested at one thermal hydraulic condition corresponding to the ITO case # 10: 1 bar, 10K subcooling and $1000 \text{ kg m}^{-2} \text{ s}^{-1}$.

Chapter 4

Governing equations for wall boiling

The approach to detect DNB that will be developed in the next chapter relies on the state-of-the-art understanding and modeling of the nucleate boiling regime which is the stable mode of heat removal prior to the boiling crisis occurrence. It is therefore essential to dedicate a significant effort to the mechanistic modeling of the wall boiling. This chapter reviews the governing equations that were developed for this aspect of the work. It first covers the heat partitioning framework and the mechanistic modeling of nucleate boiling in section 4.1. Then, the closure models which are necessary to form a complete formulation of the heat partitioning are described in section 4.2.

4.1 Nucleate boiling framework

The idea of partitioning the wall heat flux is not new; it was initially proposed by Judd [52] then adapted by Kurul and Podowski [116] in a model also known as the “RPI” heat partitioning. The nucleate boiling model from Gilman [117, 118] is one of the most recent frameworks proposed. It relies on a mechanistic approach and proposes four main modes of heat transfer observed during subcooled nucleate flow boiling. Each partition contributes to the total heat flux prediction. The resulting framework is more complex, better represents the boiling physics at the wall and creates interconnections between the partitioning terms enabling feedback mechanisms that improve the stability of the heat flux prediction.

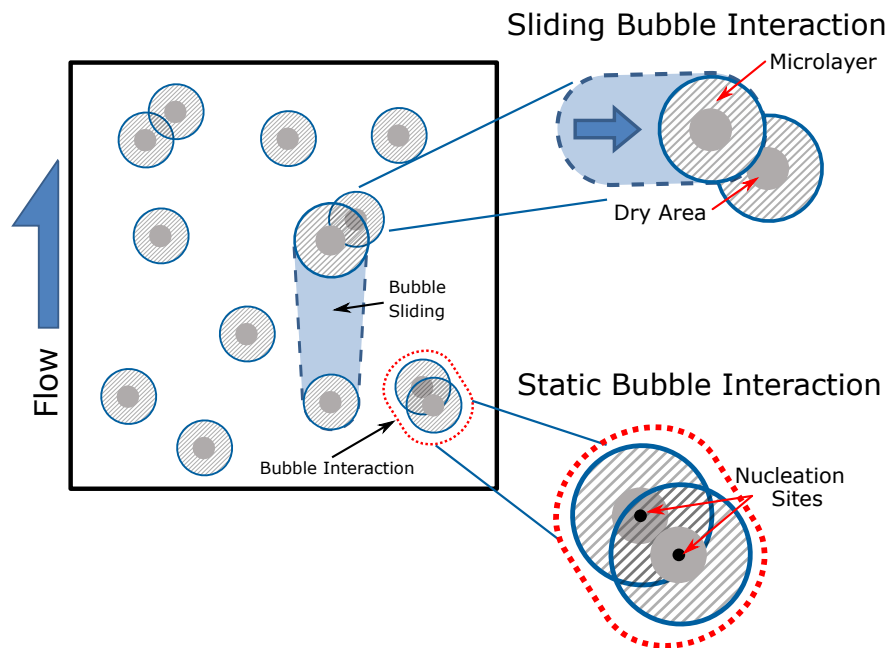


Figure 4.1: Microscale mechanisms modeled in Gilman’s nucleate boiling framework

Figure 4.1 illustrates the main mechanisms in Gilman’s flow boiling framework. Each circle represents the footprint of a bubble on the boiling surface which further subdivides into two regions: the microlayer region which contributes to the evaporation heat flux, and the dry spot which will drive the DNB transition. Bubbles will also slide along the surface after they depart their nucleation site, thus enhancing the local convective heat transfer until eventually they lift off to the flow or interact with another nucleating bubble on the surface. Gilman also accounts for a surface solid quenching effect related to the solid heater under the dry spot which can be superheated by a few degrees before being quenched as it is rewetted.

The partitioning equation is given in Equation 4.1, while Figure 4.2 summarizes the overall framework via its multiple inputs and outputs. The red clusters correspond to heat removal mechanisms modeled in the framework which combines into the total wall heat transfer (Black circle).

$$q''_{wall} = q''_{fc} + q''_{sc} + q''_q + q''_{ev} \quad (4.1)$$

Where q''_{wall} is the total heat flux at the wall, q''_{fc} is the forced convection heat flux component, q''_{sc} is the sliding conduction component, q''_q is the solid quenching partition, and q''_{ev} is the evaporation partition heat flux.

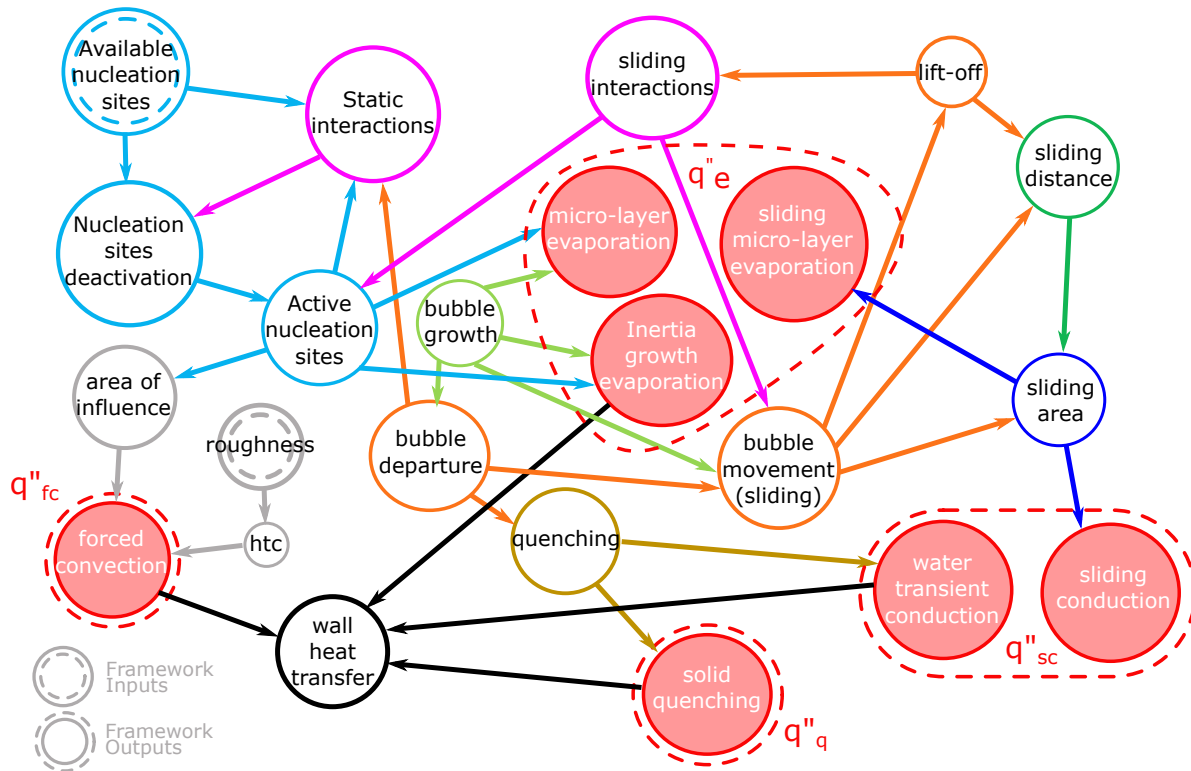


Figure 4.2: Gilman’s boiling framework "Mind-map" (from [118])

4.1.1 Forced Convection

In this model, forced convection is treated in a direct way. It relies on the prediction of a heat transfer coefficient h_{fc} that can be computed via a correlation or obtained in a CFD simulation.

$$\ddot{q}_{fc} = h_{fc} (T_w - T_f) = h_{fc} (\Delta T_{sup} + \Delta T_{sub}) \quad (4.2)$$

In our implementation we rely on a well established correlation from Dittus-Boelter [119, 120]¹. The equation relies on the Reynolds (Re) and Prandlt (Pr) adimensional numbers to calculate the Nusselt number (Nu):

$$Nu = 0.023 Re^{0.8} Pr^{0.4} \quad (4.3)$$

Where the Reynolds and Prandlt numbers are defined as:

$$Re = \frac{\rho_f u D_{hy}}{\mu_f} = \frac{GD_{hy}}{\mu} \quad (4.4)$$

$$Pr = \frac{c_{p,f} \mu_f}{k_f} \quad (4.5)$$

This correlation is valid for the following conditions:

$$0.6 \leq Pr \leq 160 \quad (4.6)$$

$$Re \gtrsim 10,000 \quad (4.7)$$

$$\frac{L}{D} \gtrsim 10 \quad (4.8)$$

In the case of the MIT flow boiling loop, we noted that the heater element is small and exposed to an incoming flat temperature profile creating a developing thermal boundary layer. In this context, the Dittus-Boelter correlation underestimates the heat transfer coefficient (it assumes a thicker, fully developed thermal boundary layer). We relied on the single phase portion of a single case (#1) boiling curve in order to set a corrective factor to the Dittus Boelter correlation. It was determined that a heat transfer coefficient multiplicative factor of 2.5 is able to correctly predict the single phase portion of all the boiling curves in our data set.

4.1.2 Sliding Conduction

On a vertical heater, bubbles that detach from the surface can either depart to the bulk and move away from the heater or they can remain close to the heater surface and slide parallel to the wall. In the latter case they will continue to grow and eventually depart to the bulk. This creates a distinction between bubbles that depart from their nucleation site and bubbles that lift-off to the bulk. During its departing and sliding period, a bubble will disrupt the thermal boundary layer in its path, leading cold liquid from the bulk to replace the space previously occupied by the bubble thus initiating a transient conduction in order to reform the boundary layer. Additionally, during sliding, the lubricating microlayer underneath the bubble will also contribute to the evaporation and growth of the bubble. This last effect is addressed in the evaporation partition in subsection 4.1.3. The transient conduction heat flux enhancement is accounted for in the sliding conduction term \ddot{q}_{sc} .

¹Dittus-Boelter correlation is so ubiquitous in heat transfer textbooks that it is sometimes difficult to find the original source of the equation. A curious reader may be interested in reading a short investigation from Winterton [121], "Where did the Dittus and Boelter equation come from?".

After the thermal boundary layer is disrupted we can assimilate the heat transfer mechanism to a 1D transient conduction in a semi-infinite plane. The transient conduction heat flux solution to this problem is given by:

$$q'' = \frac{k_f (T_w - T_f)}{\sqrt{\pi \eta_f t}} \quad (4.9)$$

The time needed for the boundary layer to reform is designated by t^* and can be expressed as the time interval when the forced convection heat flux becomes higher than the transient conduction heat flux. We can then express t^* as:

$$t^* = \left(\frac{k_f^2}{h_{fc}} \frac{1}{\pi \eta_f} \right) \quad (4.10)$$

The total heat flux contribution from transient conduction on a surface can then be obtained by integrating the transient heat flux over the t^* interval and averaging its contribution over the total bubble period. In the following equation, T is the bubble departure period also equal to $1/f$.

$$q''_{sc} = \frac{1}{T} \int_0^{t^*} \frac{k_f (T_w - T_f)}{\sqrt{\pi \eta_f t}} dt \quad (4.11)$$

$$q''_{sc} = \frac{2k_f (T_w - T_f)}{\sqrt{\pi \eta_f t^*}} t^* f \quad (4.12)$$

The contribution is then averaged on the heater area fraction affected by sliding. We can define the sliding area covered by a single sliding bubble as A_{sl} and obtain final equation from Gilman:

$$q''_{sc} = \frac{2k_f}{\sqrt{\pi \eta_f t^*}} t^* f A_{sl} N_b'' (T_w - T_f) \quad (4.13)$$

where k_f is the fluid conductivity, η_f is the liquid thermal diffusivity, t^* is the time needed to reform the thermal boundary layer, A_{sl} is the area disrupted by the sliding bubble, T_w is the wall temperature and T_f is the fluid temperature. The bubble velocity during sliding is assumed to be equal to the fluid velocity close to the wall. We can substitute t^* in Equation 4.13 with its expression from Equation 4.10 and obtain a simpler equation for q''_{sc} :

$$q''_{sc} = 2h_{fc} A_{sl} t^* f N_b'' (\Delta T_{sub} + \Delta T_{sup}) \quad (4.14)$$

The total area affected by sliding is expressed as the product of the sliding length times the average bubble diameter between its departure from the nucleation site and its liftoff to the bulk. When a bubble slides the total sliding length l is limited to the average distance between two active nucleation sites $1/\sqrt{N_b''}$.

$$A_{sl} = l \times \left(\frac{D_{lo} - D_d}{2} \right) \quad (4.15)$$

Since the forced convection partition applies to the entire surface that is not dry, if q''_{fc} and q''_{sc} are left as-is, the area affected by sliding would be double counted in the model and receive contribution of both the forced convection and sliding conduction. In order to remediate this issue we can simply remove the contribution from forced convection on the surface affected by sliding

during the time period needed to reform the boundary layer. The forced convection component which applies to the area affected by sliding is expressed as:

$$\dot{q}_{fc,extra}'' = h_{fc} A_{sl} t^* f N_b'' (\Delta T_{sub} + \Delta T_{sup}) \quad (4.16)$$

Where $t^* f$ is the fraction of time during the total period when sliding is enhancing the heat transfer and $A_{sl} N_b''$ is the overall surface area fraction affected by sliding. If we remove this extra term from \dot{q}_{sc}'' we obtain a new expression:

$$\dot{q}_{sc}'' = 2h_{fc} A_{sl} t^* f N_b'' (\Delta T_{sub} + \Delta T_{sup}) - \dot{q}_{fc,extra}'' \quad (4.17)$$

$$\dot{q}_{sc}'' = 2h_{fc} A_{sl} t^* f N_b'' (\Delta T_{sub} + \Delta T_{sup}) - h_{fc} A_{sl} t^* f N_b'' (\Delta T_{sub} + \Delta T_{sup}) \quad (4.18)$$

$$\dot{q}_{sc}'' = h_{fc} A_{sl} t^* f N_b'' (\Delta T_{sub} + \Delta T_{sup}) \quad (4.19)$$

In the end, the sliding conduction term simplifies to half of the term proposed by Gilman. This approach to handle both the forced convection and sliding conduction terms is much simpler than Gilman's original approach.

4.1.3 Evaporation

The evaporation partition component quantifies the average heat flux used to evaporate liquid to vapor at the surface. This term is further divided into two separate physical effects occurring during the formation and growth of a bubble. The inertia-controlled phase corresponds to the rapid growth at the beginning of a bubble nucleation called "inception". Then, the bubble growth is fueled by the evaporation of a liquid microlayer underneath the bubble during the diffusion-controlled phase. These two effects are added up to make the total evaporation heat flux:

$$\dot{q}_{ev}'' = \dot{q}_{ev,inc}'' + \dot{q}_{ev,ml}'' \quad (4.20)$$

4.1.3.1 Inception Evaporation

The inception component is given by:

$$\dot{q}_{ev,inc}'' = \frac{4}{3} \pi \left(\frac{D_{inc}}{2} \right)^3 \rho_g h_{fg} f N_b'' \quad (4.21)$$

Where D_{inc} is the bubble diameter at the end of the inception phase, ρ_g the density of the gas phase, h_{fg} the latent heat of the fluid, f the bubble departure frequency and N_b'' the active nucleating bubble density. Gerardi [26, 27] observed the bubble inception diameter to be roughly half of the bubble departure diameter. This result was found for water at atmospheric pressure in pool boiling. This is consistent with Jung [32] who reports a similar range. As a baseline we can use:

$$D_{inc} = \frac{D_d}{2} \quad (4.22)$$

4.1.3.2 Microlayer Evaporation

The micro layer component is given by:

$$\dot{q}_{ev,ml}'' = V_{ml} \rho_l h_{fg} f N_b'' \quad (4.23)$$

Where V_{ml} is the volume of liquid trapped in the microlayer after the inception phase, ρ_l the liquid phase density, h_{fg} the latent heat of the fluid, f the bubble departure frequency and N_b'' the active

nucleating bubble density. Gilman proposed that the microlayer have a maximum thickness δ which goes to zero at the center of the bubble.

Gerardi [26, 27] reports the cold spot radius under the bubble during its growth is roughly half of the outer bubble diameter. Since the microlayer is very thin, its evaporation creates a very high local heat flux and a cold spot can be observed. Assuming that the cold spot diameter Gerardi observes is equivalent to the microlayer extension diameter we can use the following relation:

$$V_{ml} = \frac{2}{3} \pi \left(\frac{D_d}{4} \right)^2 \delta \quad (4.24)$$

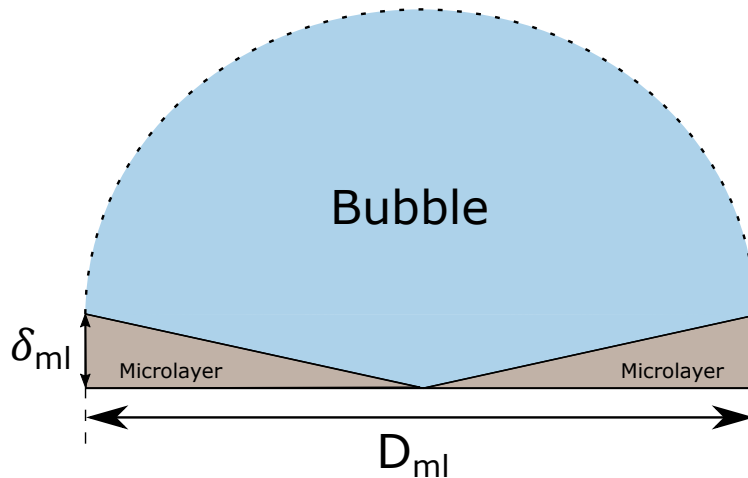


Figure 4.3: Assumed shape of the liquid microlayer underneath a bubble

Experiments from Kim and Buongiorno [29] then Jung and Kim [30–32] for water in pool boiling at atmospheric pressure reveal typical microlayer thickness of the order of $1 \mu\text{m}$ to $5 \mu\text{m}$. Their laser interferometry measurements are also consistent with older optical measurements by Koffman [63], providing a good starting point for water at low pressure.

In this work we use $\delta = 4 \mu\text{m}$ which corresponds to the initial microlayer thickness observed by Kim as well as Jung. Additionally it was found to provide accurate evaporation partition in the nucleate boiling regime for Richenderfer's cases (see Kommajosyula [122]).

It should be noted that all of the references used to estimate the microlayer volume use water at low pressure in pool boiling environments. The formulation adopted here is therefore limited by such conditions, and where flow boiling experimental observations of microlayers are extremely rare, we rely on pool boiling experiments. We will revisit the pressure scaling aspect of this contribution in the next chapter when extending the model applicability.

Gilman [118] also adds a second contribution in the microlayer corresponding to the evaporation of a microlayer existing underneath the bubble while sliding but refrain from proposing a model due to the lack of experimental data available in the literature. In this work, this contribution is also ignored as it is expected to be negligible in relation to the sliding conduction.

4.1.4 Solid Quenching

The solid quenching contribution tracks the average heat removal associated with the superheating of the heater material directly under a growing bubble. Due to the presence of a dry spot under each bubble, the local heat transfer is temporarily reduced and the temperature inside the solid heater material can increase. The hot spot is periodically quenched when the bubble departs its nucleation site, and fresh water brings the material back to the saturation temperature. The corresponding equation for this effect is expressed by Gilman as:

$$q_q'' = \rho_h c_{ph} V_q \Delta T_h f N_b'' \quad (4.25)$$

Where ρ_h is the density of the heater material, c_{ph} the heater specific heat, V_q the volume of heater affected by the hot spot, ΔT_h the average superheat, f the bubble departure frequency and N_b'' the active nucleating bubble density. The volume affected by the superheating is assumed to be a hemisphere of size equivalent to the dry spot diameter:

$$V_q = \frac{2}{3} \pi \left(\frac{D_{dry}}{2} \right)^3 \quad (4.26)$$

This model contribution is neglected in the application to the experiment from Bucci and Richenderfer. The experimental configuration is top heated, meaning the hottest surface is in contact with the liquid while the backside of the Sapphire-ITO heater is contact with air (see Figure 4.4). Let's assume the process for superheating the heater is analog to a semi infinite slab of thickness 1 mm at T_{sat} , suddenly being exposed to a superheat of 2 K on one side. We want to evaluate how much temperature change is seen on the other side of the slab after the end of the growth phase. We approximate the growth time to 1 ms as reported by Richenderfer.

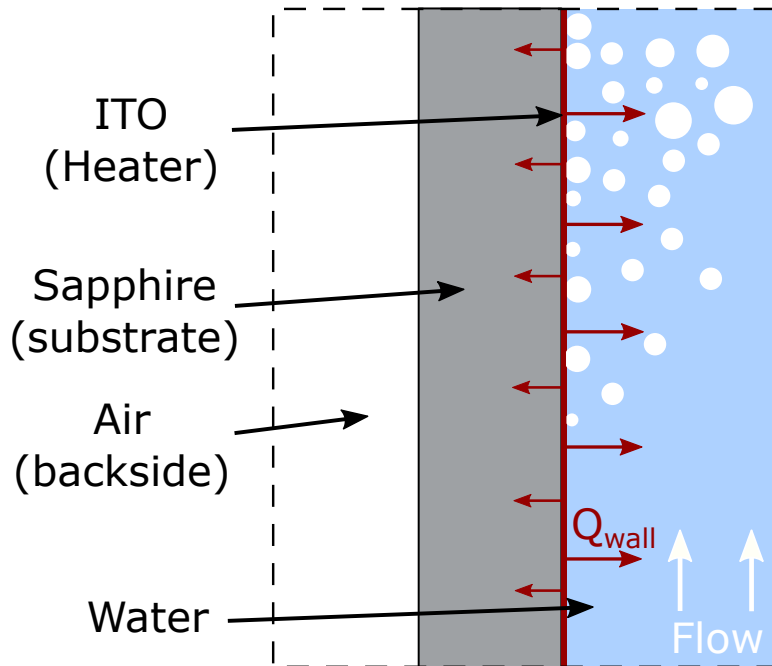


Figure 4.4: Top heating configuration as found in the MIT flow boiling loop [5, 6]

The semi-infinite slab conduction is a classic problem found in most heat transfer textbooks

[123], we can use the 1D solution :

$$\frac{T(x, t) - T_s}{T_i - T_s} = \operatorname{erf} \left(\frac{x}{2\sqrt{\eta t}} \right) \quad (4.27)$$

Where $T(x, t)$ is the temperature at a depth x and time t , T_s is the imposed surface temperature (here 2 K above T_{sat}), T_i is the initial slab temperature (here, T_{sat}) and η is the heater material thermal diffusivity. In our example, we consider typical sapphire properties:

$$\rho = 3980 \text{ kg m}^{-3} \quad (4.28)$$

$$c_p = 916 \text{ J kg}^{-1} \text{ K}^{-1} \quad (4.29)$$

$$k = 35 \text{ W m}^{-1} \text{ K}^{-1} \quad (4.30)$$

$$\eta = \frac{k}{\rho c_p} = 9.6 \times 10^{-6} \text{ m}^2 \text{ s}^{-1} \quad (4.31)$$

and from in Equation 4.27, we obtain:

$$\frac{T(\delta, t_g) - T_s}{T_i - T_s} = 1 - 5.31945 \times 10^{-13} = 0.99999 \dots \approx 1 \quad (4.32)$$

Therefore, we can approximate the temperature at a depth δ :

$$T(\delta, t_g) = T_i \quad (4.33)$$

Which demonstrates that the temperature on the opposite side of the slab is not affected by the change of temperature on the boiling surface. Even probing the mid point in the slab yields a negligible 0.03% temperature change. This simple evaluation allows us to confidently eliminate the quenching contribution for the Bucci and Richenderfer experiments.

4.1.5 Nucleation Site Density and bubble interaction

The mechanistic model we describe in this section relies on the accurate representation of individual mechanisms that affect heat transfer. The number of nucleation sites activating on the boiling surface is an input parameter for our model and represents information about the surface behavior that is necessary to model boiling. The nucleation site density represents the number of cavities that are actively generating bubbles for given thermal hydraulics conditions per unit area.

The prediction of nucleation site density has been studied in the past and several modeling approaches have been proposed. For instance, Lemmert and Chawla [124] proposed a functional form that is based on a power law:

$$N''_{LC} \approx (\Delta T_{sup})^A \quad (4.34)$$

Recent approaches have relied on the assumption there exist a distribution of cavity sizes on the surface and that they are randomly distributed on the surface. This theory is based on initial reporting from Gaertner [112] and later confirmation by Sultan and Judd [125] that the active cavities follow a Poisson distribution on the boiling surface. Yang and Kim [126] were the first to propose a model accounting for the cavity sizes as well as their conic angle as an input for their activation. Among the recent semi analytical approaches, Hibiki and Ishii's [127] is one of the most widely accepted models due to the extensive validation that was conducted. The model is expressed as follows:

$$N''_{HI} \approx \left[e^{A\Delta T_{sup}} - 1 \right] \quad (4.35)$$

The coefficients needed for the model are calibrated using Yang and Kim's [126] data. The sensitivity of the nucleation site density to the contact angle is derived empirically. Their model is benchmarked against Basu et al. experimental data [128] and the sensitivity to the fluid properties and system pressure is benchmarked using Borishanskii et al. results [129]. Overall the performance of Hibiki and Ishii's nucleation site density is well established and is shown in Figure 4.5.

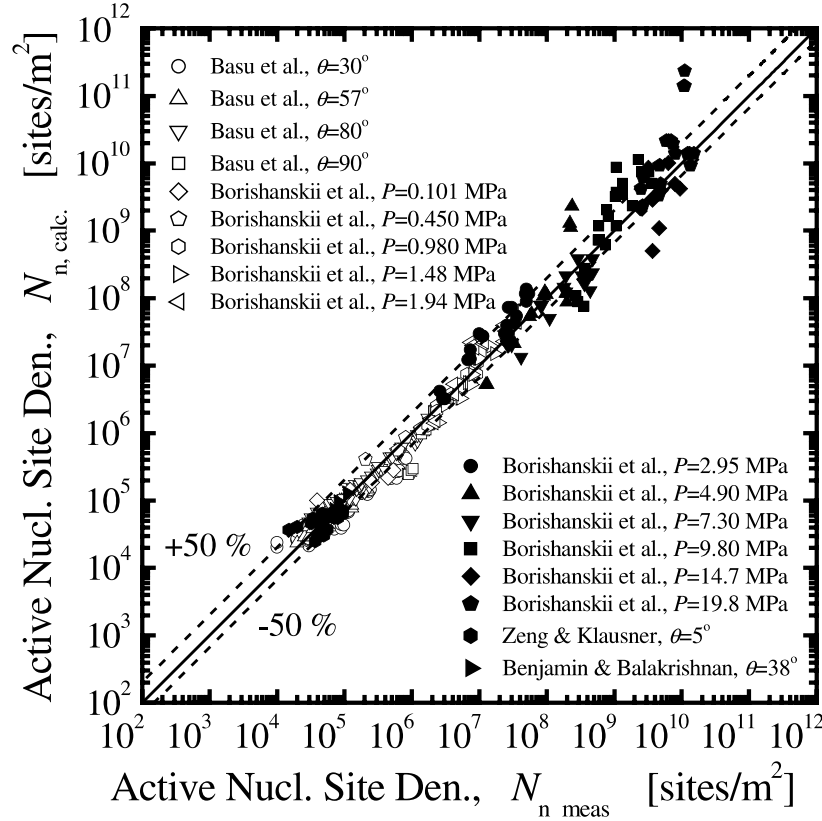


Figure 4.5: Hibiki and Ishii [127] nucleation site density model prediction plotted against multiple experimental databases

Recently, Li et al. [130] revisited the approach used by Hibiki and Ishii and proposed a new nucleation site model in the form of a nested power law which they argue performs better at high superheats compared to Hibiki and Ishii's model. The model they propose is in the form of a nested power function:

$$N''_{Li} \approx \Delta T_{sup}^{A\Delta T_{sup}+B} \quad (4.36)$$

Results from Li's nucleation site density model [130] are shown in Figure 4.6 and Figure 4.7. The main improvements in the prediction compared to Hibiki and Ishii's model are visible in Figure 4.6 for Borishanskii's data at high pressure (9.8 MPa and above) corresponding to experimental nucleation site densities between 1×10^9 site/m² to 1×10^{11} site/m².

Del Valle and Kenning [131] pointed out that the Poisson distribution was not always observable in their experiment and there exists a region nearby existing nucleation sites which exhibits lower

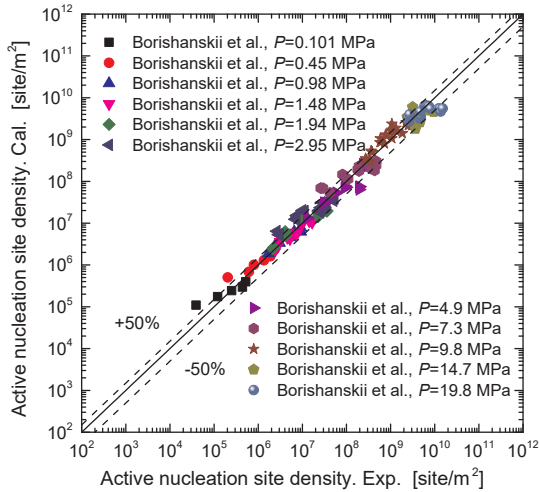


Figure 4.6: Li [130] nucleation site density model prediction for Borishanskii et al. database

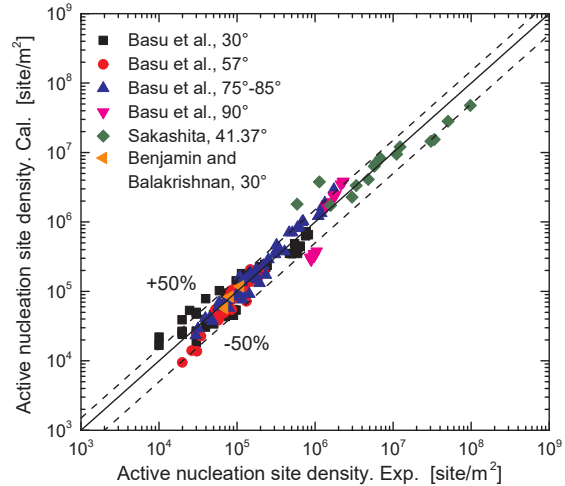


Figure 4.7: Li [130] nucleation site density model prediction for Basu et al. database

than expected active sites. They quantify this region to be twice the diameter of the departing bubbles. According to Del Valle and Kenning, this points toward an “inhibition” of nucleation within an area of influence near existing bubbles.

This point is generally ignored in the nucleation site density models presented previously. More generally, the validation approach usually taken is to validate the activation of the cavity distribution. However, when active sites begin to crowd the surface with nucleating bubbles, it becomes impossible for multiple sites to nucleate individual bubbles if they are too close to each other.

In a nucleate boiling framework, the term “nucleation site density” is always used as a proxy for the number of active sites generating bubbles per unit area (and thus contribution to the heat removal via evaporation). The distinction between sites that meet the activation criterion (based on their cavity radius) and sites that actually generate bubbles is rarely discussed and can cause confusion. Part of this issue motivated Li et al. to derive a new model. They pointed out convergence issues when using Hibiki and Ishii’s model to conduct boiling simulation in CFD due to the “extremely high values of the active nucleation site density in high heat flux conditions”. Indeed, as soon as it is used outside of its original validation envelope, the exponential nature of the model can predict extremely high numbers of nucleation sites that cannot physically represent the actual number of bubbles nucleating on the surface.

Gilman [117] proposed a statistical approach based on a Complete Spatial Randomness(CSR) theory [132] to distinguish the two quantities. It still relies on the main assumption that cavities on a heater are randomly distributed according to Poisson’s law which was experimentally confirmed by Gaertner [112]. While cavities may become activated based on their cavity radius and the surface superheat, the number of sites actually generating bubbles is physically limited by the size and frequency of such bubbles. At the limit, the heater can only be covered by bubbles and additional sites becoming “active” would not contribute to new bubbles nucleating. To account for this crowding effect, we propose a suppression mechanism based on the the probability that an

active nucleation site exists within one bubble radius of another one. Given a bubble generating site density N_b'' , bubble departure frequency f , bubble growth time t_g and a bubble departure diameter D , this probability P is expressed as:

$$P = 1 - e^{-ft_g N_b'' \pi (D_d/2)^2} \quad (4.37)$$

$$ft_g = \frac{t_g}{t_g + t_w} \quad (4.38)$$

Also, ft_g is a multiplicative coefficient in front of N_b'' to account for the fact that all bubbles are not present at the same time on the boiling surface. In conditions where the total bubble departure period is mainly composed of a large wait time, more bubbles can nucleate on a given surface compared to situations where most of the bubble period is coming from the growth phase. $ft_g N_b''$ then represent the number of bubbles present at the same time on average on a given surface. In the end, the bubble generating site density N_b'' is expressed as:

$$N_b'' = N'' (1 - P) = N'' e^{-\pi ft_g N_b'' \left(\frac{D_d}{2}\right)^2} \quad (4.39)$$

One issue stemming from Equation 4.39 is immediate: we aim to solve for N_b'' but it appears both on the right hand side and left hand side of the equation. Even worse, the right hand side term is inside an exponential function, making it non linear and very hard to solve analytically. Fortunately numerically solving this equation is relatively easy when using numerical schemes like Newton–Raphson or a bisection method. The qualitative behavior of this interaction modeling is described in Figure 4.8. The nucleation site density model in this figure comes from Hibiki and Ishii’s model [127] with fixed bubble frequency, growth time and departure diameter. The interaction model practical effect is a flattening of the number of bubbles generated compared to the cavities, which is by nature exponential. This is consistent with the physical limitation of the number of bubbles as the heater becomes crowded. This model also has the effect of creating a feedback mechanism between the different bubble nucleation closures, which tends to stabilize the evaporation partition and reduce sensitivities to the closures. This aspect of the model is developed later in the thesis.

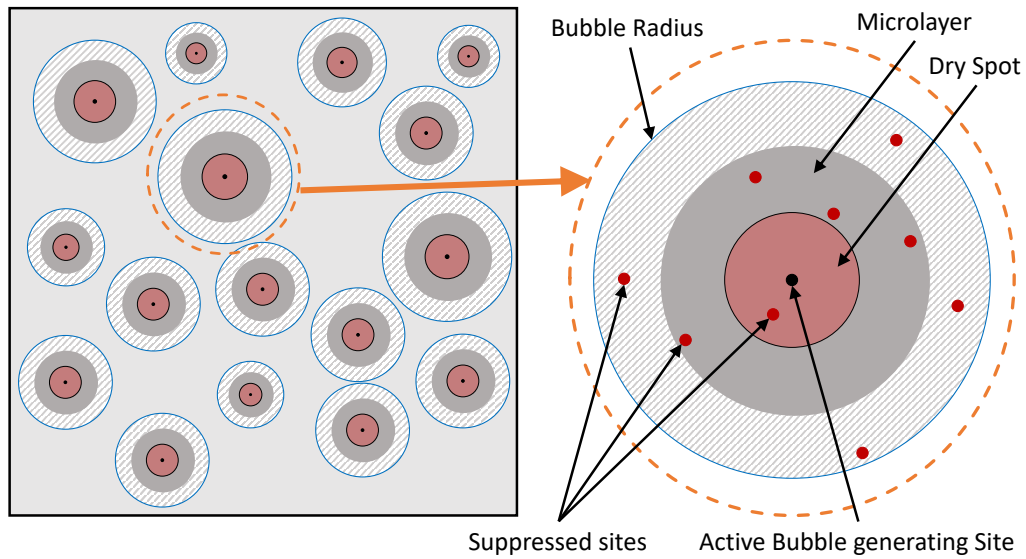


Figure 4.8: Qualitative effect of the nucleation site interaction model

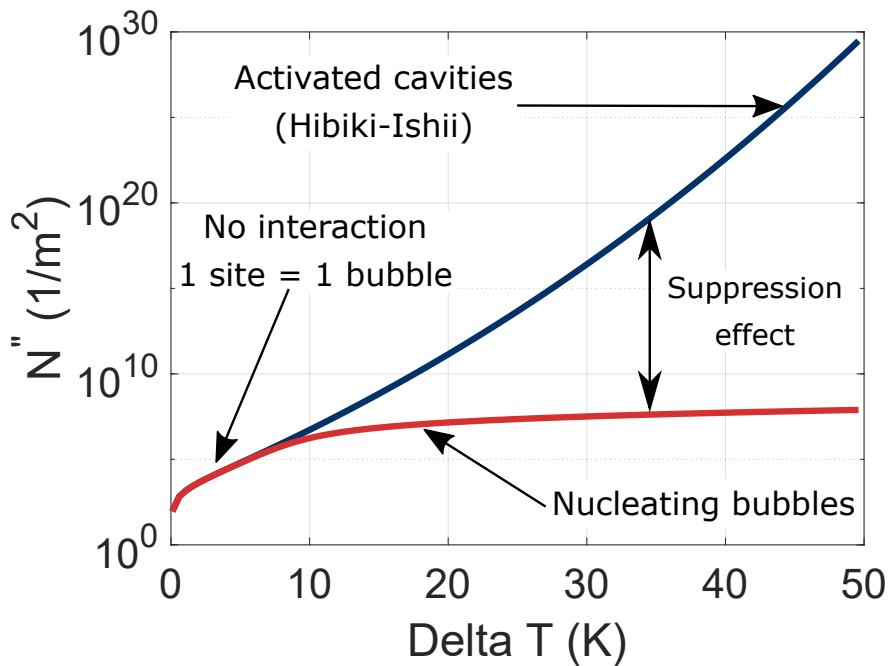


Figure 4.9: Quantitative example of the interaction model using a nucleation site density exponential curve with fixed bubble departure diameter and frequency

4.2 Closure selection

In this section we tackle the important selection of closures for fundamental boiling quantities in the partitioning model. The closures were selected to best fit the range of application with regards to the experimental conditions.

4.2.1 Nucleation Site Density

The activation of nucleation sites is strongly dependent on the surface characteristics of the boiling surface. In the case of the MIT flow boiling loop, the Sapphire-ITO heaters are nano-smooth, and the only sizable cavities present on the surface are coming from manufacturing defects. This type of surface is therefore very different compared to a metallic heater used in engineering applications.

For a typical stainless steel surface, Yang and Kim [126] measured the cavity radius distribution which was subsequently used by Hibiki and Ishii [127] to develop their nucleation site density correlation. The distribution is shown in Figure 4.10 along with the fitting functions proposed by Hibiki and Ishii. The experimental data points reported by Yang and Kim seem to indicate there is exponentially more available cavities as the cavity radius diminishes. Hibiki and Ishii's fitting functions tend to infinity as the radius tends to zero.

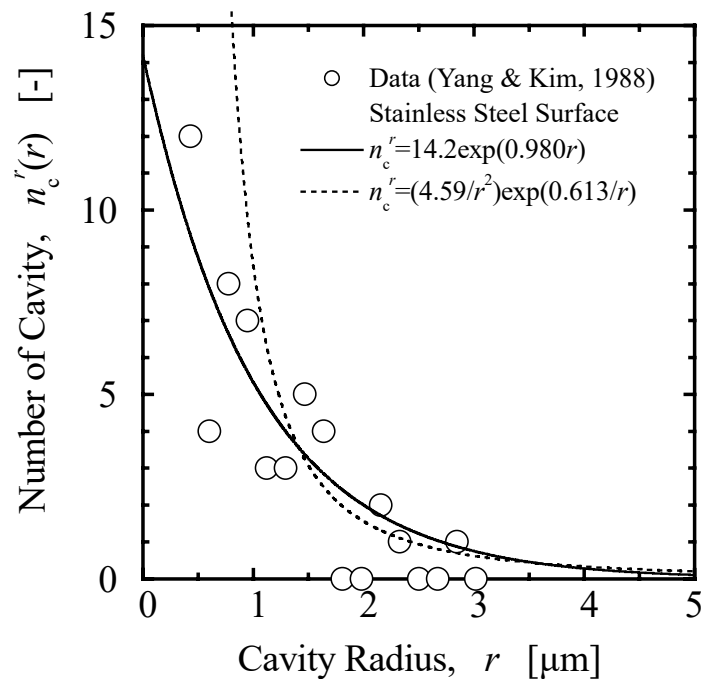


Figure 4.10: Stainless Steel cavity radius distribution from Yang and Kim [126] along with numerical fitting functions proposed by Hibiki and Ishii [127]

In the case of the sapphire-ITO surfaces engineered for the MIT flow boiling loop, the cavity radius distribution considerably differs from the results of Yang and Kim. Figure 4.11 shows the Scanning Electron Microscope (SEM) image (left) of a Sapphire-ITO heater element alongside the cavity size distribution (right) extracted from this image. The experimental distribution plot reveals a sharp drop in cavity sizes smaller than $6 \mu\text{m}$ and an absence of cavities smaller than $3 \mu\text{m}$.

Such a distribution cannot be modeled with fitting function such as the ones proposed by Hibiki and Ishii. Indeed, as the superheat increases, smaller cavities are activated, but in the case of Sapphire-ITO heaters, there are no more cavities to activate below $3 \mu\text{m}$. The experimental cavity size distribution varies from case to case due to the nature of the heater manufacturing defects and renders *a priori* modeling of the activation curve impossible.

Experimental fitting function of the nucleation site activation is therefore a necessary input for the model as it is impossible to predict boiling on a surface without knowing this fundamental boiling parameter. Nucleation site density is one of the very few quantities that has to be known in advance.

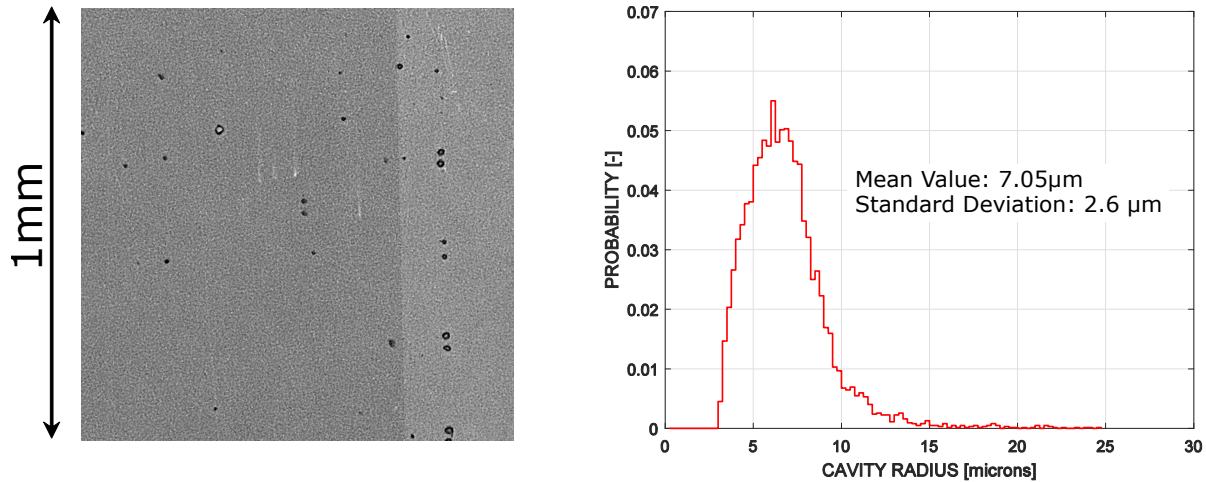


Figure 4.11: Sapphire-ITO heater SEM image (left) and measured cavity size distribution (right). Adapted from [6]

Because the distribution of cavities is unique to the number of fabrication defects, we will rely on a case-by-case fitting of the nucleation site density activation along the boiling curve. We elected to fit an exponential function to data extracted from infrared post-processing. Figure 4.12 displays a typical fit of experimental nucleation site density data.

The experimental curves shows an initial trend which is exponential in nature, meanwhile for all cases displayed, we observe a saturation effect at higher wall superheat. Physically, this is consistent with bubbles crowding the surface, which eventually limits the number of sites able to generate new bubbles. The distinct saturation level seen in the top left subplot in Figure 4.12 indicates the presence of smaller bubbles on the surface at higher mass fluxes ($1500 \text{ kg m}^{-2} \text{ s}^{-1}$ and $2000 \text{ kg m}^{-2} \text{ s}^{-1}$) which allows for a larger number of sites to generate bubbles before the surface becomes saturated.

Additionally, at higher superheat ($\gtrsim 30 \text{ K}$), the surface becomes crowded with bubbles, and post processed data is limited by the manner in which nucleation site locations are extracted from infrared images. The physical cavities are not detectable with infrared, only the presence of bubble footprints (high heat flux regions) indicates nucleation sites are active. As the surface becomes saturated with bubbles, it becomes much more difficult to identify individual sites on the surface and the resulting active nucleation sites are most likely underestimated.

The exponential fit conducted on data points corresponding to the early stages of nucleate boiling, before significant nucleation site interaction occurs, are not subject to this detection uncertainty. Instead of trying to match the experimental data during the saturation part of the boiling curve, the interaction physics is handled by the statistical model described in subsection 4.1.5.

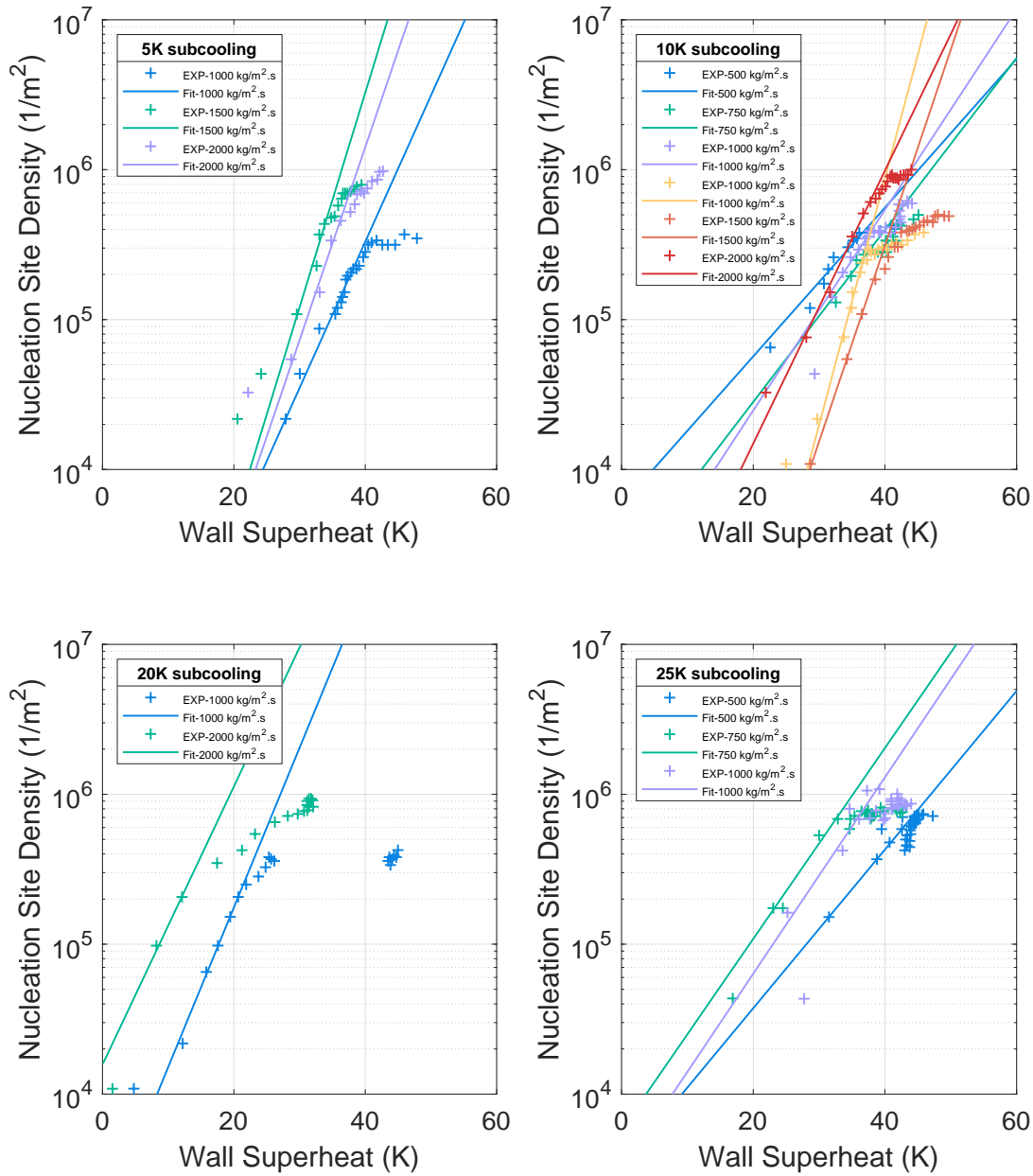


Figure 4.12: Nucleation site density fitting functions for each of the 14 MIT test cases, grouped by bulk subcooling (5 K, 10 K, 20 K, 25 K)

Note that in some rare cases, we also ignored the very first data point, usually because it corresponded to the activation of a single bubble, which can appear as an outlier compared to the rest of the data in Figure 4.12. A nucleation site density of $1 \times 10^4 \text{ m}^{-2}$ corresponds to one bubble detected on the $1 \times 1 \text{ cm}^2$ experiment heater surface, while $1 \times 10^6 \text{ m}^{-2}$ corresponds to 100 bubbles detected.

4.2.2 Bubble Departure and Liftoff Diameters

The size of departing bubbles is a challenging parameter to capture. In the heat partitioning described in the previous section, the bubble departure diameter is present in several equations. It is especially important in the evaporation heat flux component as it is included in the form of a cubic term in the inception component (Equation 4.21), and as a quadratic term in the microlayer evaporation component via its volume (Equation 4.24). The liftoff diameter is more limited as it only relates to the bubble sliding length and area affected by the transient conduction. Many models do not even include or mention the possibility of sliding bubbles. We needed to rely on a model that would predict both the departure and liftoff diameter in a consistent manner.

A mechanistic approach to predicting the departure and liftoff can be assembled by tracking the forces acting on a bubble of a given size and finding the size at which it will depart due to an imbalance of forces. Many force balance models have been proposed over the years. The first attempt for boiling applications is attributed to Klausner [133] and was followed by several notable contributions [134–137]. These models were all plagued with limited applicability due to oversimplification of the physical representation, and parameter fittings to specific databases. The force balance approach to the departure diameter is described in the following equations modeling the forces acting on a growing bubble at the surface. A diagram summary of the forces is shown in Figure 4.13. If we call x the direction of the flow and y the direction orthogonal to the heating surface, the departure to the bulk condition can be written as:

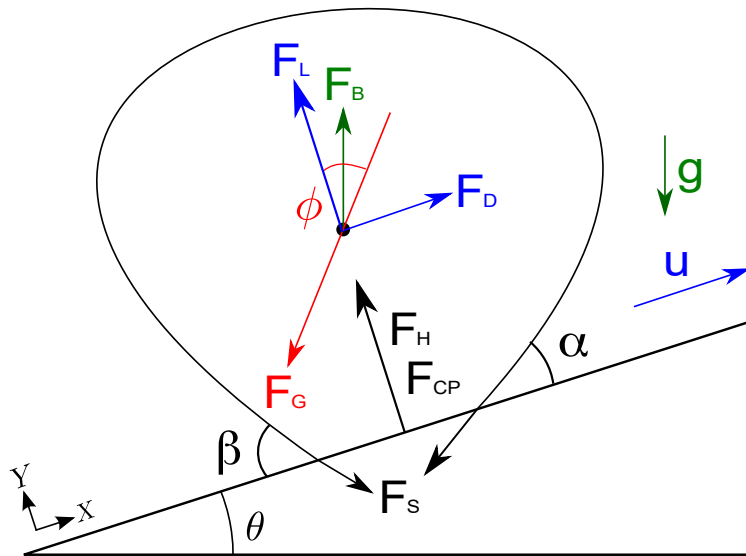


Figure 4.13: Diagram of the forces acting on a growing bubble on an inclined surface. Adapted from Mazzocco et al. [138]

$$\begin{cases} \sum F_x < 0 \\ \sum F_y > 0 \end{cases} \quad (4.40)$$

and the departure leading to sliding is:

$$\begin{cases} \sum F_x > 0 \\ \sum F_y < 0 \end{cases} \quad (4.41)$$

When a bubble departs and slides along the surface it will continue to grow and eventually liftoff to the bulk when $\sum F_y > 0$.

$$\begin{cases} \sum F_x = -F_{Sx} + F_B \sin \theta - F_G \sin \phi + F_D \\ \sum F_y = -F_{Sy} + F_B \cos \theta - F_G \cos \phi + F_L + F_{CP} + F_H \end{cases} \quad (4.42)$$

Where F_S is the shear force, F_B the buoyancy force, F_G the bubble growth force, F_D the drag force, F_L the lift force, F_{CP} the contact pressure force and F_H the hydrodynamic force.

Only recently, Mazzocco and Kommajosyula [138] attempted to alleviate certain limitations from existing force balance models and provided a more generally applicable, mechanistic model for the prediction of bubble departure and liftoff diameters. Their work revised each force acting on a bubble and proposed a more consistent formulation.

The main contribution from their work is a new approach to the bubble growth modeling which is inspired from the work of Plesset and Zwick [139]. Generally, the bubble grows with \sqrt{t} and depends on two factors : the evaporation of the microlayer and the evaporation or condensation (if the flow is saturated or subcooled) happening with the surrounding fluid. The general equation for the bubble radius at a given time is:

$$R(t) = (K_{ML} + K_{FB}) \sqrt{t} \quad (4.43)$$

Where K_{ML} is the growth constant associated with the microlayer evaporation and K_{FB} is the growth constant due to flow boiling. Mazzocco proposes:

$$Ja_* = \frac{\rho_f c_{pf} \Delta T}{\rho_f h_{fg}} \quad (4.44)$$

$$K_{ML} = 2 \left(\frac{\pi^2 + 1}{\pi^2 \sqrt{\pi}} \right) \left(\frac{1}{\sqrt{Pr_f}} \right) Ja_* \sqrt{\eta_f} \quad (4.45)$$

$$K_{FB} = \chi K_{PB} \quad (4.46)$$

$$K_{PB} = 2 \sqrt{\frac{3}{\pi}} Ja_* \sqrt{\eta_f} \quad (4.47)$$

$$\chi = \frac{T_{sat} - T_{bulk}}{T_{wall} - T_{sat}} \quad (4.48)$$

The time dependent bubble radius expression then drives the bubble growth force as:

$$F_G = \frac{1}{2} \pi \rho_f (K_{ML} + K_{FB})^4 \quad (4.49)$$

Their model was validated against multiple databases for both the departure [133, 140, 141] and liftoff [134, 142, 143] diameters. It compared extremely well with other force balance models as can be seen in Figure 4.14 and Figure 4.15. In the case of upward subcooled flow boiling that is of interest in our work, we show in Figure 4.16 the predictions of Mazzocco's model against experimental departure diameter data extracted from high speed videos and infrared acquisition. The results capture the data trend much better than Kocamustafaogullari's bubble departure diameter model [144] which is not sensitive to flow parameters (subcooling, mass flux).

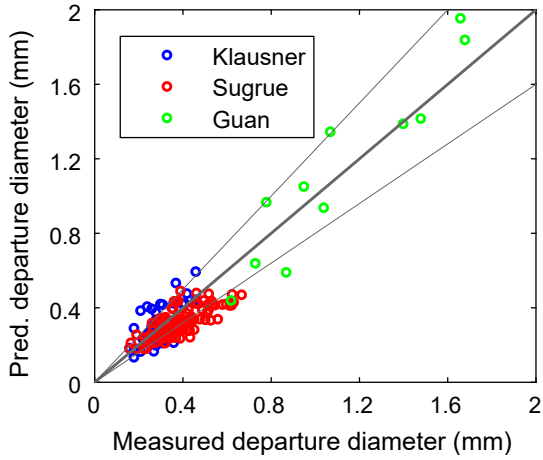


Figure 4.14: Bubble departure diameter error scatter of Mazzocco et al. model [138] benchmarked against Klausner [133], Sugrue [140] and Guan [141] databases

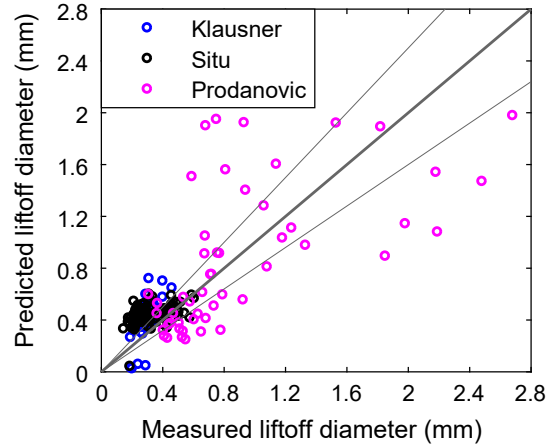


Figure 4.15: Bubble liftoff diameter error scatter of Mazzocco et al. model [138] benchmarked against Zeng [134], Prodanovic [142] and Situ [143] databases

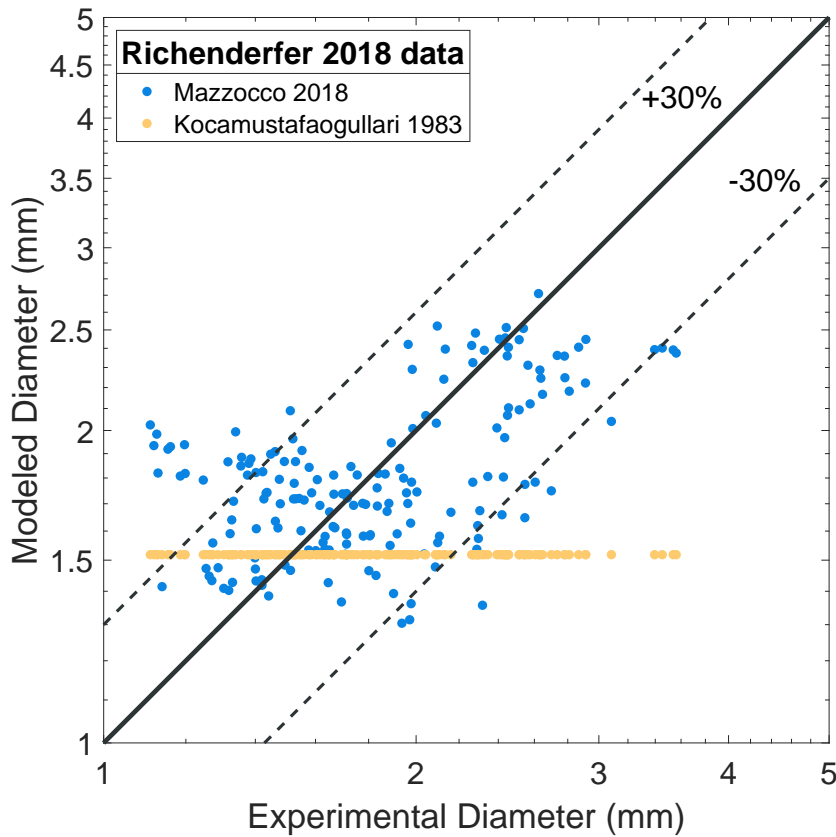


Figure 4.16: Scatter plot of Mazzocco et al. [138] bubble departure diameter predictions against MIT flow boiling data

4.2.3 Bubble growth time

The bubble growth time represent the time between the initial nucleation of a bubble and its departure from the cavity. This quantity is particularly relevant for CHF because dry spots only exist on the surface during the growth phase and therefore will strongly affect the dry area fraction. The growth time is also present in the nucleation site density interaction and is paired with the bubble departure frequency as ft_g . This non dimensional number represent the fraction of time a bubble is present on the surface compared to its overall nucleation period. Since the growth time is bounded by the departure event, it directly relates to the bubble departure diameter.

In that effect, Mazzocco's bubble departure diameter model [138] already models the time evolution of the bubble radius and its departure size. By substituting half of the departure diameter in the left hand side of Equation 4.43 we can solve for the corresponding growth time:

$$t_g = \left(\frac{D_d}{2(K_{ML} + K_{FB})} \right)^2 \quad (4.50)$$

4.2.4 Bubble wait time and bubble departure frequency

The bubble wait time represents the time necessary for the liquid to reform a superheated layer on top of a nucleation site after the departure of a bubble. The nucleation of a subsequent bubble requires the liquid layer above the nucleation site to reach a certain superheat. The exact superheat required to nucleate is actually quite difficult to predict; the most common assumption was proposed by Hsu [145] and depends on the cavity size. This nucleation condition is also known as the "Hsu criterion". According to Hsu's criterion, we can compute the activation condition of a specified cavity size, which can then be used to derive a characteristic wait time from the surface cavity size distribution. However, in most engineering application, the cavity size distribution is unknown, and modeling the bubble wait time has been practically out of reach for most applications.

One approach is to consider that the wait time for water is usually much larger than the growth time. With this assumption, one can assimilate the wait time to the bubble departure period and simply rely on bubble departure frequency models. Unfortunately, the literature regarding bubble departure frequency is also limited and old models such as the model from Cole [146] are still in use to this day. Attempts by Situ [147] are notable but his conclusion are that models developed for pool boiling do not perform well in flow boiling conditions and existing models from Basu [148] and Podowski [149] fail to reproduce databases other than the ones they were developed against. Situ's own model is only able to predict the departure frequency with a mean error of 113%. Based on these observations Kommajosyula [122] has proposed a cavity size independent wait time model that considers two contributions:

- Jakob number of subcooling: which measures the amount of energy required to bring the thermal boundary layer to saturation after the heater surface is quenched by subcooled liquid.
- Wall superheat: which can be assimilated as the potential driving new nucleation.

The resulting model was tested against data from the MIT flow boiling loop as well as databases from Basu [150] and Yoo [151]. The proposed equation is:

$$t_w = 0.0061 \left(\frac{Ja_{sub}^{0.6317}}{T_{sup}} \right) \quad (4.51)$$

The bubble frequency is then assembled from the wait and growth times:

$$f = \frac{1}{t_w + t_g} \quad (4.52)$$

Figure 4.17 compares the frequency predictions of Kormajosyula's models [122] with the correlation from Cole [146]

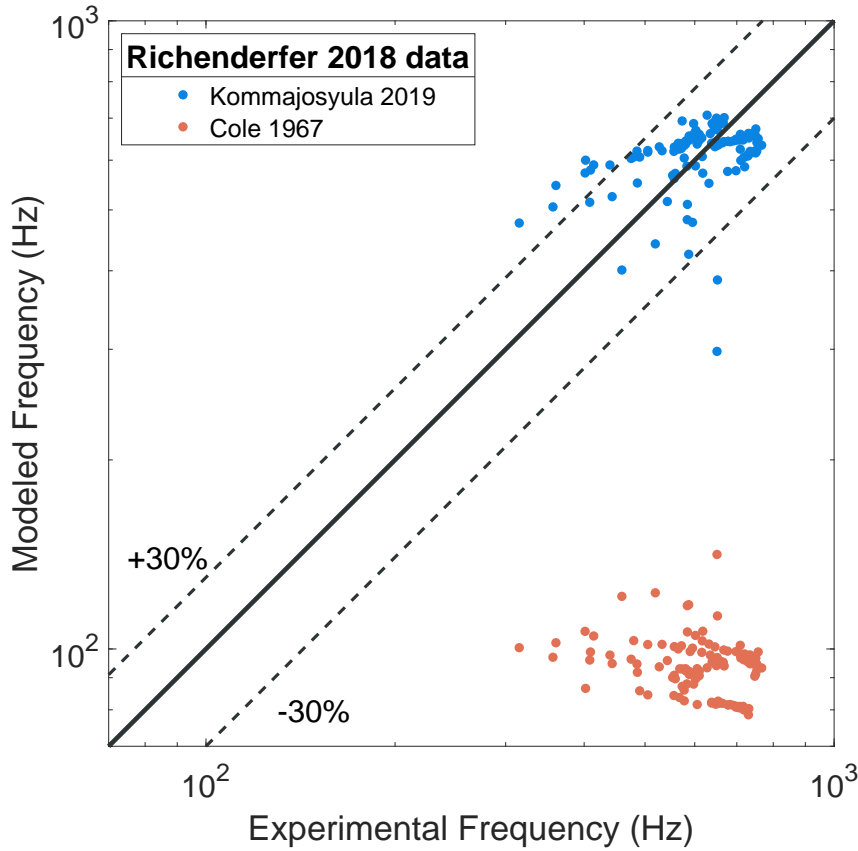


Figure 4.17: Scatter plot of Kormajosyula's [122] bubble departure frequency predictions against MIT flow boiling data

4.3 Framework Summary

In this chapter we have established a baseline framework to model nucleate boiling. This work expands on the formulation proposed by Gilman [117] by using the same four main heat removal mechanisms, and improves their formulation to better represent the conditions of the MIT flow boiling loop.

The nucleate boiling heat flux is partitioned in the following terms:

$$q''_{wall} = q''_{fc} + q''_{sc} + q''_{ev} + q''_q \quad (4.53)$$

The main contributions in the heat partitioning are summarized in the following list:

- **Force Convection (q''_{fc}):** this term representing the heat removed to the liquid phase, is computed via the Dittus-Boelter correlation which is enhanced in order to account for the developing thermal boundary layer thickness found on the MIT flow boiling loop heater.
- **Sliding Conduction (q''_{sc}):** this term representing the heat removed when sliding bubbles disrupt the thermal boundary layer which then reforms, is expressed as a function of the forced convection heat transfer coefficient and the boundary layer reformation time. The area affected by sliding is accounting for the forced convection mechanism in order to avoid double counting the heat removal.
- **Evaporation (q''_{ev}):** this term representing the heat removed by the evaporation mass transfer when bubble nucleate on the surface accounts for two mechanisms: the inception component due to the initial rapid growth of the bubble and the microlayer component due to the evaporation of a thin liquid film that forms underneath the bubble when it nucleates.
- **Quenching (q''_q):** this term representing the excess heat temporarily stored inside the solid heater underneath the bubble dry spot during its growth which gets quenched as the bubble departs its nucleation site, is equated to zero. A 1D analysis of the conditions found in the MIT flow boiling loop revealed that the upper estimate of the temperature rise during the bubble growth is negligible, thus rendering this term superfluous in the analysis.

Additionally, several other aspects of the nucleate boiling physics are modeled, such as:

- **Static Bubble Surface Interaction:** the statistical nucleation site suppression effect occurring when bubbles begin crowding the heated surface is modeled. The Complete Spatial Randomness (CSR) hypothesis is used as a base for a non linear interaction model which computes the nucleating bubble density as a distinct quantity from the number of active cavities provided by a closure.
- **Nucleation Site Density:** in the context of the MIT flow boiling loop, the sapphire-ITO heater surface specificity prevents the use of a generic nucleation site density closure. Case-by-case fitting functions are thus computed from post-processed experimental data and used as an input to the DNB prediction.
- **Bubble Departure and Liftoff Diameters:** a mechanistic model predicting both the departure and liftoff bubble diameters is used which provides improved prediction accuracy when applied to the MIT flow boiling loop conditions.
- **Bubble growth time:** the bubble growth time is derived as a submodel of the bubble departure diameter mechanistic representation.
- **Bubble wait time and frequency:** the bubble wait time is obtained from a closure validated both on external databases as well as the MIT flow boiling loop data set.

Taken together, the heat partitioning and the fundamental boiling quantity models form a closed framework mechanistically describing the nucleate flow boiling heat transfer. The effect of dry spots and the physics of DNB is not included yet at this stage and is the focus of the following chapter.

Chapter 5

DNB Model Development

Having reviewed the current understandings of DNB in chapter 1 and the fundamental limitations of existing models in chapter 2, we now propose a new approach to DNB detection. The detection of DNB via a physical representation of boiling phenomena is our main objective in this chapter. In order to do so we will advance a new wall heat partitioning formulation based on the nucleate boiling framework described in chapter 4 which is modified in order to incorporate the representation of dry and wetted surface contributions which is at the origin of DNB triggering.

The chapter is divided in two sections. The first one establishes the fundamental principles that allow for the detection of DNB via a mechanistic heat transfer representation. The second section is dedicated to the practical implementation of these principles into equations and to assembling a complete boiling model which extends up to DNB.

5.1 DNB detection as a stability limit of heat partitioning

The growing evidences pointing toward a micro-hydrodynamics cause for DNB were described in subsection 1.2.1. Observing that the local heat flux removed by surfaces in contact with vapor is orders of magnitude smaller than in the regions of local microlayer evaporation and convection to the liquid phase, we noted that a high fraction of “dry” areas on the boiling surface would necessarily impede the heat removal process. The wall superheat increases as evaporation becomes more vigorous (through the increase in active nucleation sites, bubble departure diameter and frequency); the nucleate boiling heat removal and the fraction of heating surface in contact with vapor are enhanced with increase in superheat.

These observations have led to establishing the main principle for the DNB detection model: its root cause is an instability between competing effects in nucleate boiling, where the enhancement of evaporation is associated with a larger dry area fraction on the boiling surface which suppresses the former. CHF corresponds to the tipping point between these opposite effects.

In other words, at DNB, the nucleate boiling enhancement, even if significant, is not able to compensate the increase in dry area on the heater. The reduction in available wetted surface constrains the maximum amount of heat removed through nucleate boiling. It is equivalent to a positive feedback loop which incrementally increases the surface temperature. It enhances boiling but also the dry area, which provokes an overall decrease in the heat removal capacity via nucleate boiling, ultimately leading to further increase in the surface temperature, cascading up to the next stable conditions where the surface is entirely in contact with the vapor phase (called a “Post-CHF” regime).

Starting from the proper representation of nucleate boiling and its heat partitioning, the boiling crisis represents the stability limit to the wall heat balance leading to the irreversible growth of surface dry-spots. With this philosophy in mind, our model qualitative behavior is illustrated in

Figure 5.1, where the total heat flux is computed as the sum of its partitioned components and CHF is the peak value of the overall heat partitioning.

The dry area fraction growth is caused by the accumulation of bubbles on the surface (top drawings) and the increase in their interaction and coalescence which leads to the formation of larger dry patches. As the dry area fraction increases, driven by bubble interaction (bottom-left and center subplot), the heat removal reaches its maximum. CHF occurs as the evaporation heat flux enhancement slows down and the dry area fraction continues to increase, which is described by the steep overall heat flux decrease.

We can also introduce the model in the form of representative equations. In Equation 5.1, q_{wall} is the wall heat input in Watts, q_{nb} is the total heat removed via nucleate boiling (heating up and evaporating the liquid phase) and q_{dry} is the heat removed directly by the gas phase. If we divide the equation by the total heater area A_{heater} , we obtain an heat flux expression in Equation 5.2.

$$q_{wall} = q_{nb} + q_{dry} \quad (5.1)$$

$$\frac{q_{wall}}{A_{heater}} = \frac{q_{nb}}{A_{heater}} + \frac{q_{dry}}{A_{heater}} \quad (5.2)$$

We can also consider the total heater area A_{heater} to be split between wet A_{wet} and dry A_{dry} areas in Equation 5.3.

$$A_{heater} = A_{dry} + A_{wet} \quad (5.3)$$

$$q''_{wall} = \frac{q_{nb}}{A_{wet}} \frac{A_{wet}}{A_{heater}} + \frac{q_{dry}}{A_{dry}} \frac{A_{dry}}{A_{heater}} \quad (5.4)$$

We then define the dry area fraction as S_{dry} in Equation 5.5, the nucleate boiling heat flux in Equation 5.6 and the dry heat flux in Equation 5.7

$$S_{dry} = \frac{A_{dry}}{A_{heater}} = \left(1 - \frac{A_{wet}}{A_{heater}} \right) \quad (5.5)$$

$$q''_{nb} = \frac{q_{nb}}{A_{wet}} \quad (5.6)$$

$$q''_{dry} = \frac{q_{dry}}{A_{dry}} \quad (5.7)$$

Thus we obtain the heat flux partition enabling DNB detection in Equation 5.8.

$$q''_{wall} = (1 - S_{dry}) q''_{nb} + S_{dry} q''_{dry} \quad (5.8)$$

In Equation 5.8, the total heat flux at the wall q''_{wall} is the sum of two terms, one representing the total amount of heat removed through nucleate boiling $(1 - S_{dry}) q''_{nb}$, the other representing heat removed directly through the gas phase $S_{dry} q''_{dry}$. During nucleate boiling, the overall heat removed by the gas phase is almost negligible. As discussed in section 1.3, the heat transfer coefficient to the gas phase remains small even close to DNB, leading to the extremely low heat fluxes observed inside dry spots with infrared thermometry.

In this framework, the wall heat flux maximum is the CHF and is defined as the zero of its temperature derivative:

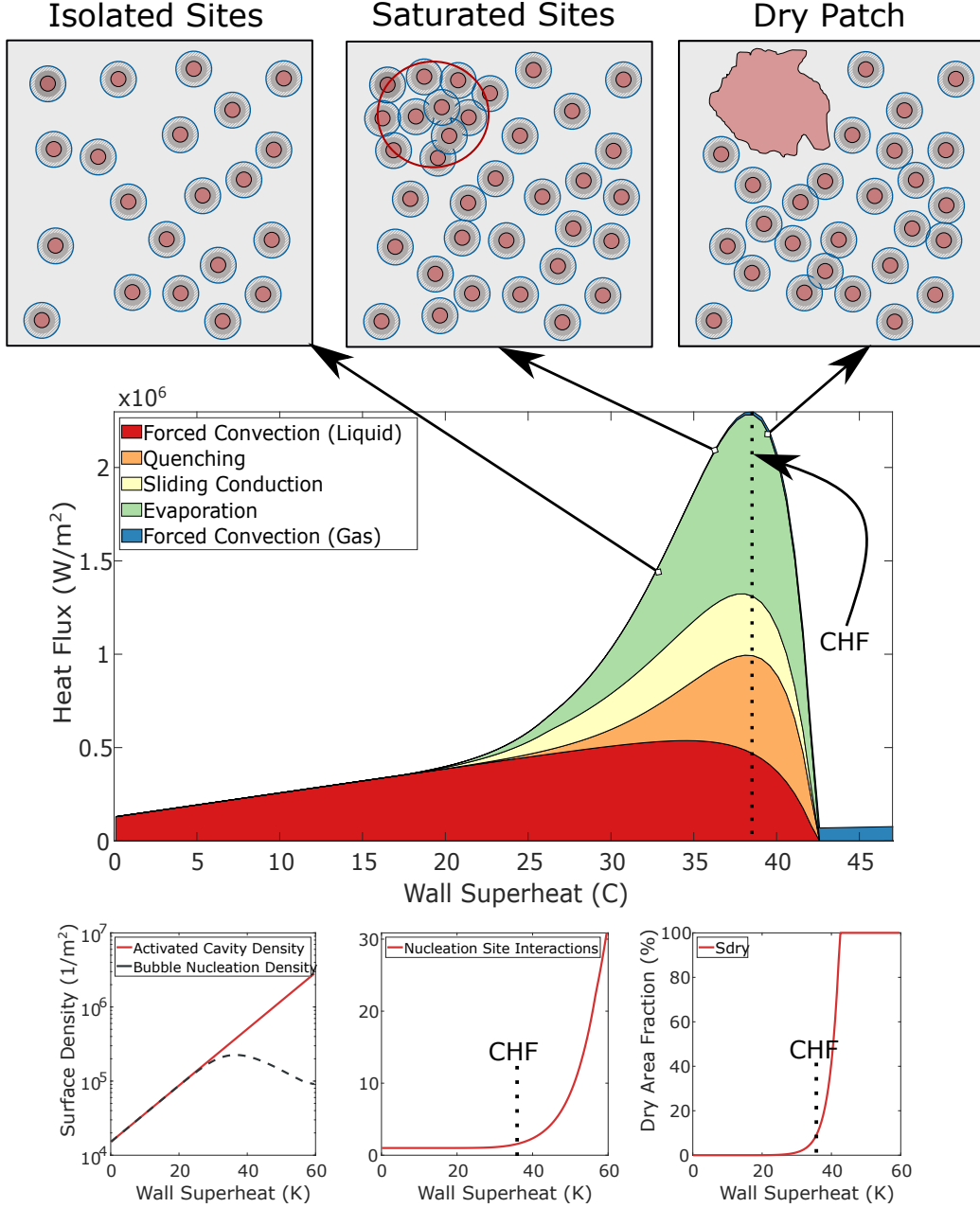


Figure 5.1: Illustration of the qualitative behavior of the model. Main plot include the main heat flux partitions adding up to the total heat flux. The boiling curve goes through a peak, identified as the CHF. Top drawings represent the progressive crowding of the surface with bubbles, eventually creating dry patches. Bottom subplots track the number of bubbles on the heater, the statistical interaction and the dry area fraction

$$\frac{\partial q''_{wall}}{\partial T_{wall}} = \frac{\partial (1 - S_{dry})}{\partial T_{wall}} q''_{nb} + (1 - S_{dry}) \frac{\partial q''_{nb}}{\partial T_{wall}} = 0 \quad (5.9)$$

$$\frac{\partial S_{dry}}{\partial T_{wall}} q''_{nb} = (1 - S_{dry}) \frac{\partial q''_{nb}}{\partial T_{wall}} \quad (5.10)$$

During nucleate boiling, $(1 - S_{dry})$, the wetted area fraction decreases monotonically with the wall superheat, while the nucleate boiling heat flux (q''_{nb}) is enhanced with higher wall superheat. DNB does not occur when the dry area reaches 100% but much earlier. Indeed the maximum wall heat flux corresponding to a zero of the wall heat flux derivative occurs before the entire nucleate boiling term is suppressed.

Given an appropriate set of modeling equation for both the nucleate boiling and the dry area fraction, this formulation can be solved in order to obtain the CHF condition. However, closures such as the active nucleation site density and the static bubble interaction described in chapter 4 are heavily non-linear, while being necessary to accurately model the nucleate boiling behavior. The dry area modeling described in the following section (section 5.2) also introduces non-linear equations to represent the expected dry spot behavior. The CHF prediction accuracy is closely tied to the proper representation of the nucleate boiling partition, the dry area fraction and their respective trends against the wall superheat. In the end, the resulting framework is complex and strongly non-linear and thus requires a numerical solution rather than an analytical one.

5.2 Dry area modeling

The principles for DNB detection have been laid in section 5.1 but have not been developed in the context of an actual boiling framework. This section will present the approach taken to represent the heat partitioning between wetted and dry area on the boiling surface. It will use the same boiling closures such as nucleation site density, bubble departure diameter etc. as the nucleate boiling framework presented in section 4.1. This ensures the consistency of the dry area modeling with the nucleate boiling framework we developed for this work, but also allows for updating/changing the nucleate boiling framework in the future when better options become available. Conversely, the dry area modeling can be modified independently from the nucleate boiling framework as better understandings of the dry area physics becomes available. The two pieces work together and use the same basic inputs (boiling closures) but will work independently.

5.2.1 Initial representation of dry spots underneath individual bubbles

Using the available boiling framework closures related to bubble nucleation we can derive a simple formula tracking the time and space average dry area fraction on a boiling surface. If we consider the dry spot area underneath each bubble as a disk of diameter D_{dry} and on average $ft_g N_b$ bubbles are present on a given heater surface A_h , the dry area fraction S_{dry} becomes:

$$S_{dry} = \frac{A_{dry}}{A_h} = \frac{ft_g N_b \pi \left(\frac{D_{dry}}{2}\right)^2}{A_h} = ft_g N_b'' \pi \left(\frac{D_{dry}}{2}\right)^2 \quad (5.11)$$

The only term left to model in this first approach is the size of the dry spot diameter. A reasonable assumption is to consider D_{dry} to be proportional to the bubble size D_d . This is consistent with experimental observations in pool boiling by Gerardi [26, 27] as well as Kim [29] and Jung [30, 31]. We can write:

$$D_{dry} = \zeta D_d \quad (5.12)$$

where ζ is a coefficient relating the average bubble departure diameter D_d to the average dry spot diameter D_{dry} . Equation 5.11 becomes:

$$S_{dry} = f t_g N_b'' \pi \left(\frac{\zeta D_d}{2} \right)^2 \quad (5.13)$$

This representation is both simple and powerful. As the wall superheat increases, the bubble departure diameter, frequency and nucleation site density increase and the growth time decreases leading to an overall increase of the dry area fraction on the surface. At low wall superheat the dry area fraction remains close to zero and does not impact the heat flux partitioning. As the superheat increases it will progressively become more important and suppress the nucleate boiling terms, eventually leading to a peak in overall heat flux corresponding to the detection of DNB.

5.2.2 Effect of surface properties on dry spot diameters (contact angle)

Experimental dependency of CHF on heater properties like wettability has been identified early on [83, 152] but is largely unaccounted for in most mechanistic and numerical CHF models. An hydrophilic surface will tend to produce a larger CHF than an hydrophobic one. A low contact angle will produce bubble footprints that are smaller and then to favor heater rewetting.

In our model, this means that the ratio between dry spot and bubble departure diameter is a function of the contact angle. We will use a reference contact angle of 90° and derive the contact angle effect from this point.

$$\frac{D_{dry}}{D_d} = \zeta_{90^\circ} K_\theta \quad (5.14)$$

Where ζ_{90° is the ratio of dry spot to bubble departure diameter on a 90° surface and K_θ is the contact angle effect. We can expect that:

$$\begin{aligned} \text{if } \theta < 90^\circ \text{ then } K_\theta < 1 \\ \text{if } \theta = 90^\circ \text{ then } K_\theta = 1 \\ \text{if } \theta > 90^\circ \text{ then } K_\theta > 1 \end{aligned}$$

We propose two approaches to this effect. The first one considers two bubbles of identical apparent radius sitting on two surfaces with different contact angles. The second one is very similar to the first one but instead of assuming an equal apparent radius, the two bubbles have an equal volume of vapor. In both cases we will ignore the advancing/receding contact angle distinction, the transient effect of a growing bubble and the triple contact line speed. Instead, we simply consider the change in dry footprint between two bubbles sitting on a flat surface. The only parameter varying being the contact angle.

5.2.2.1 Constant apparent bubble radius assumption

In this case we consider two bubbles of similar apparent radius. One is sitting on a surface with a 90° contact angle, thus forming a hemisphere, the other sitting on a surface with a contact angle θ . This situation is represented in Figure 5.2. We want to obtain the ratio between the dry spot radii in the two cases:

$$\frac{R_{dry,\theta}}{R_{dry,90^\circ}} \quad (5.15)$$

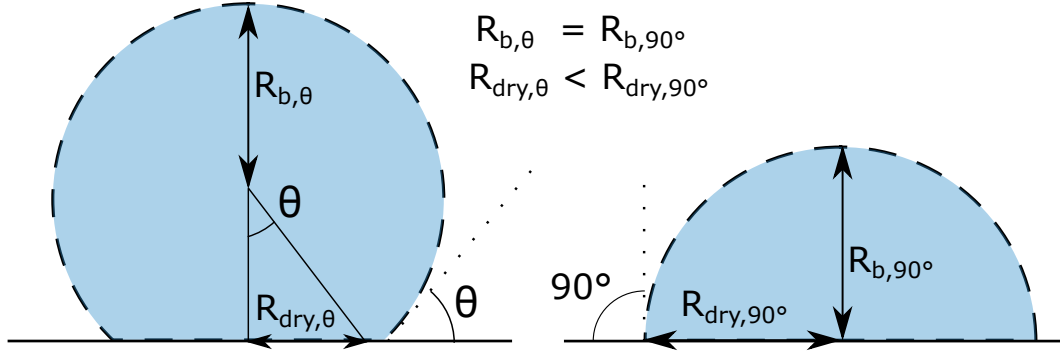


Figure 5.2: Fixed radius assumption for dry spot scaling between contact angle θ (left) and 90° (right)

For a surface with a contact angle θ , we can use trigonometry to relate the bubble radius, dry spot radius and the contact angle:

$$\sin(\theta) = \frac{R_{dry,\theta}}{R_b} \quad (5.16)$$

For a surface with a 90° contact angle, the dry spot radius is simply equal to the bubble radius.

$$R_{dry,90 \text{ deg}} = R_b \quad (5.17)$$

By substituting R_b with $R_{dry,90^\circ}$ in Equation 5.15 we obtain the desired relation between dry spot radii:

$$\frac{R_{dry,\theta}}{R_{dry,90^\circ}} = \sin(\theta) \quad (5.18)$$

5.2.2.2 Constant apparent bubble volume assumption

Another approach to the same question is to assume similar bubbles in terms of volume and how differently they would sit on surfaces of various contact angles. Figure 5.3 represents this alternative approach.

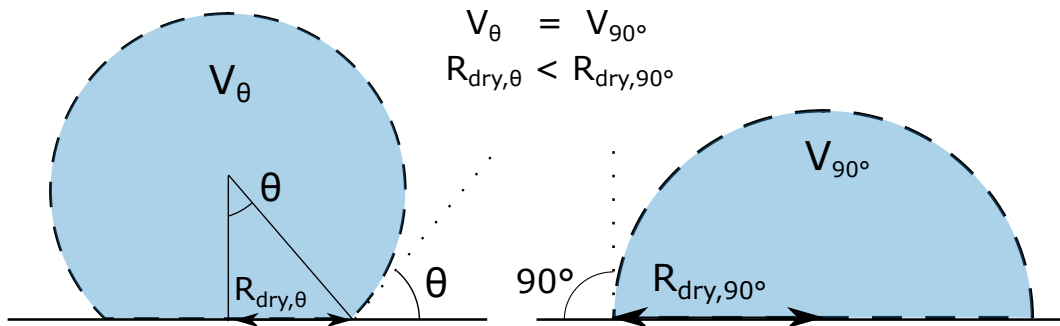


Figure 5.3: Fixed volume assumption for dry spot scaling between contact angle θ (left) and 90° (right)

The volume of a bubble sitting on a surface with a contact angle θ is expressed as the difference between the volume of a sphere of radius $R_{b,\theta}$ and the volume of a spherical cap of radius $R_{b,\theta}$ and

base radius $R_{dry,\theta}$.

$$V_\theta = \frac{4}{3}\pi R_{b,\theta}^3 - \frac{\pi}{3}R_{b,\theta}^3 (2 + \cos(\theta)) (1 - \cos(\theta))^2 \quad (5.19)$$

We can also express R_b as a function of θ and $R_{dry,\theta}$:

$$R_{b,\theta} = \frac{R_{dry,\theta}}{\sin \theta} \quad (5.20)$$

and simplify Equation 5.19 into:

$$V_\theta = \frac{\pi}{3} \left(\frac{R_{dry,\theta}}{\sin(\theta)} \right)^3 \left(4 - (2 + \cos(\theta)) (1 - \cos(\theta))^2 \right) \quad (5.21)$$

On the other hand, the volume of a bubble sitting on a surface of 90° contact angle is simply a half sphere:

$$V_{90^\circ} = \frac{2}{3}\pi R_{dry,90^\circ}^3 \quad (5.22)$$

by equating Equation 5.19 and Equation 5.22 we can derive the ratio of dry spot radii:

$$\frac{R_{dry,\theta}}{R_{dry,90^\circ}} = \frac{\sin(\theta)}{\left(2 \left(1 - \frac{1}{4} (2 + \cos(\theta)) (1 - \cos(\theta))^2 \right) \right)^{1/3}} \quad (5.23)$$

Now, we can compare the two approaches for contact angles ranging from 0° (super-hydrophilic) to 180° (super-hydrophobic). Figure 5.4 displays the comparison results. We can conclude that between 0° and 90° , both equations are relatively close and exhibit similar trends. For contact angles higher than 90° , the constant apparent radius assumption breaks down and results become abnormal because the apparent diameter is fictitious (below the surface). Equation 5.23 captures the dry spot increase for hydrophobic surfaces and correctly predicts an infinite dry spot radius when the contact angle tends toward 180° . In the 0 to 90° range, the difference between the two approaches is small and both can be used to represent the effect we are modeling.

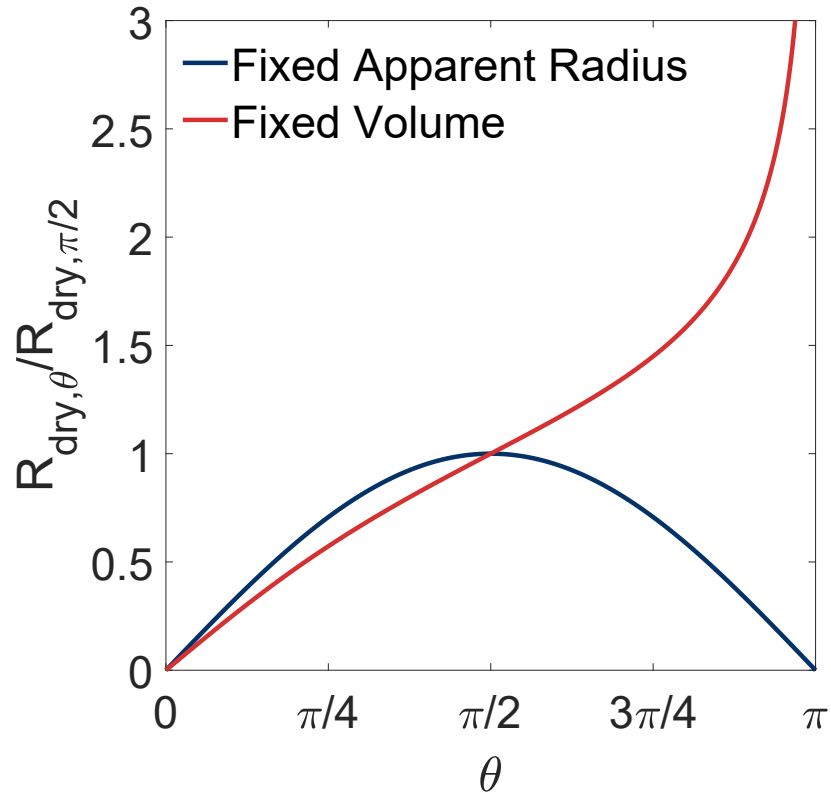


Figure 5.4: Contact angle dry spot scaling comparison. Fixed apparent radius vs fixed volume

5.2.3 Effect of bubble crowding on the surface on the dry spots (dry patch formation)

The initial dry spot representation is a good approximation when bubbles are isolated from each other and do not interact. However, we know that at high heat flux, the boiling surface will become crowded with bubbles and nucleation sites will be suppressed. This effect is modeled in subsection 4.1.5 to limit the number of nucleating bubbles on the surface. In this regime, at high heat fluxes, when the surface becomes saturated with bubbles, dry spots can also coalesce into larger and irregular “patches” and therefore enhance the dry area fraction on the surface as seen in Figure 1.5.

In order to account for this effect, we already introduced in Equation 4.37 a model tracking the probability of interaction that was developed for the nucleation site density characterization. When considering the effect on dry spots, the idea is to use the ratio between the number of active cavities N'' (given by a correlation like Hibiki and Ishii [127]) and the number of active bubble generating sites N_b'' to represent the number of interactions and drive the dry spot coalescence effect. Jung [4] notes the nucleation of “many tiny bubbles” in the regions that are rewetted after the departure of a large bubble, these tiny bubbles probably stem from small nucleation sites that are otherwise suppressed when a large bubble grows and they tend to disrupt water inflow and promote the dry spot. In our framework we will model this enhancement effect due to the crowding of the surface with a multiplicative factor, K_{CSR} , which enhances the individual bubble dry spot diameter in the dry area fraction Equation 5.11.

$$K_{CSR} = \frac{N''}{N_b''} = e^{\pi f t_g N_b'' \left(\frac{D_d}{2}\right)^2} \quad (5.24)$$

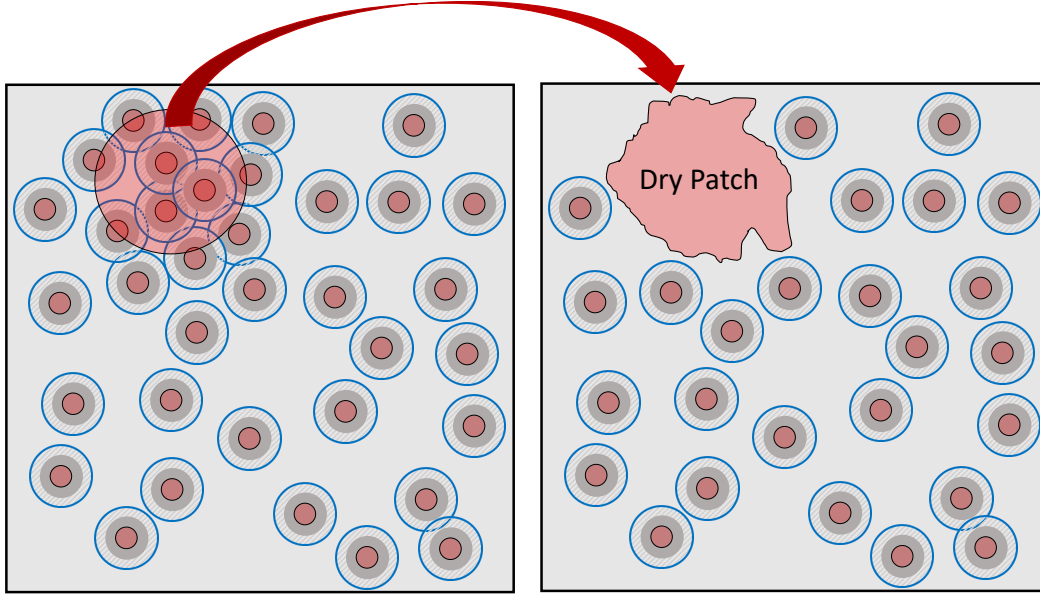


Figure 5.5: Clustering effect when multiple bubbles create a larger dry patch

5.2.4 Complete DNB model

When we assemble the initial dry area tracking with the bubble crowding mechanism and the contact angle scaling, we obtain the final expression for our modeled dry area fraction:

$$S_{dry} = f t_g N_b'' \pi \left(\zeta K_{CSR} K_\theta \frac{D_d}{2} \right) \quad (5.25)$$

Where :

$$K_{CSR} = e^{\pi f t_g N_b'' \left(\frac{D_d}{2}\right)^2} \quad (5.26)$$

$$K_\theta = \sin(\theta) \quad (5.27)$$

When combining the partition framework from chapter 4 with the DNB detection presented in this chapter, we can write the final equation for the wall heat flux as:

$$q''_{wall} = (1 - S_{dry}) q''_{nb} + S_{dry} q''_{gas} \quad (5.28)$$

$$q''_{nb} = q''_{fc} + q''_{ev} + q''_{sc} + q''_q \quad (5.29)$$

Leveraging experimental observations from Gerardi [27] and Jung [30] we bounded the value of ζ between 0 and 0.5. Then we relied on the dry area fraction estimates from Richenderfer [5] in case 1 described in Table 3.1 to derive the value of ζ that minimized the CHF error while matching the dry area fraction in that single case. We found $\zeta = 0.15$ would produce the most consistent prediction.

Chapter 6

Model Assessment

This chapter presents the model assessment against the low pressure data produced at the MIT flow boiling loop inputs discussed in chapter 3. The chapter is divided in three main sections which are as follow:

- **Demonstration of the Model Validity:** section 6.1 Presents evidences of the model ability to capture trends in the heat partition, boiling curve and DNB when adopting the measured closure quantities.
- **Model Benchmarking:** section 6.2 applies the complete model to 18 cases from the MIT flow boiling loop database, in combination with model as closures. Boiling curves and CHF results are presented and analyzed.
- **Sensitivity Analysis:** section 6.3 presents a sensitivity analysis conducted for six model parameters on a example case, and assesses the effect of the most sensitive parameter on the overall database CHF prediction.

The results presented in this chapter were produced using a 0D representation of the experimental conditions. At the DNB location, the thermal hydraulics parameters of a case (pressure, mass flux, subcooling, hydraulic diameter) and the wall temperature are the minimal set of inputs needed to evaluate the boiling closure, compute the heat flux partitions and the dry area fraction. The individual heat flux contributions and dry area are assembled to produce the predicted wall heat flux. By spanning a range of wall temperatures, the entire boiling curve can be reconstructed and the peak heat flux, corresponding to the DNB, detected. The model predictions can then be directly compared to the experimental measurements. The numerical implementation details that were developed in order to produce all the results presented in this chapter are described in Appendix B.

6.1 Demonstration of model Applicability

It is important to establish the potential for the new approach before assembling the complete formulation and run large validation studies. Here we will focus on demonstrating the behavior of the new model in multiple conditions, looking at the ability to reproduce experimental trends in heat flux partitioning and CHF. The results presented in this section have been published in [153].

The strategy employed in this section consists in leveraging the post-processed experimental data in order to generate accurate sets of closure inputs that are then fed to the model in order to generate boiling curves and estimate CHF. The strategy is also described in the form of a diagram in Figure 6.1. When applied to multiple conditions, we can observe and conclude whether the model captures experimental trends.

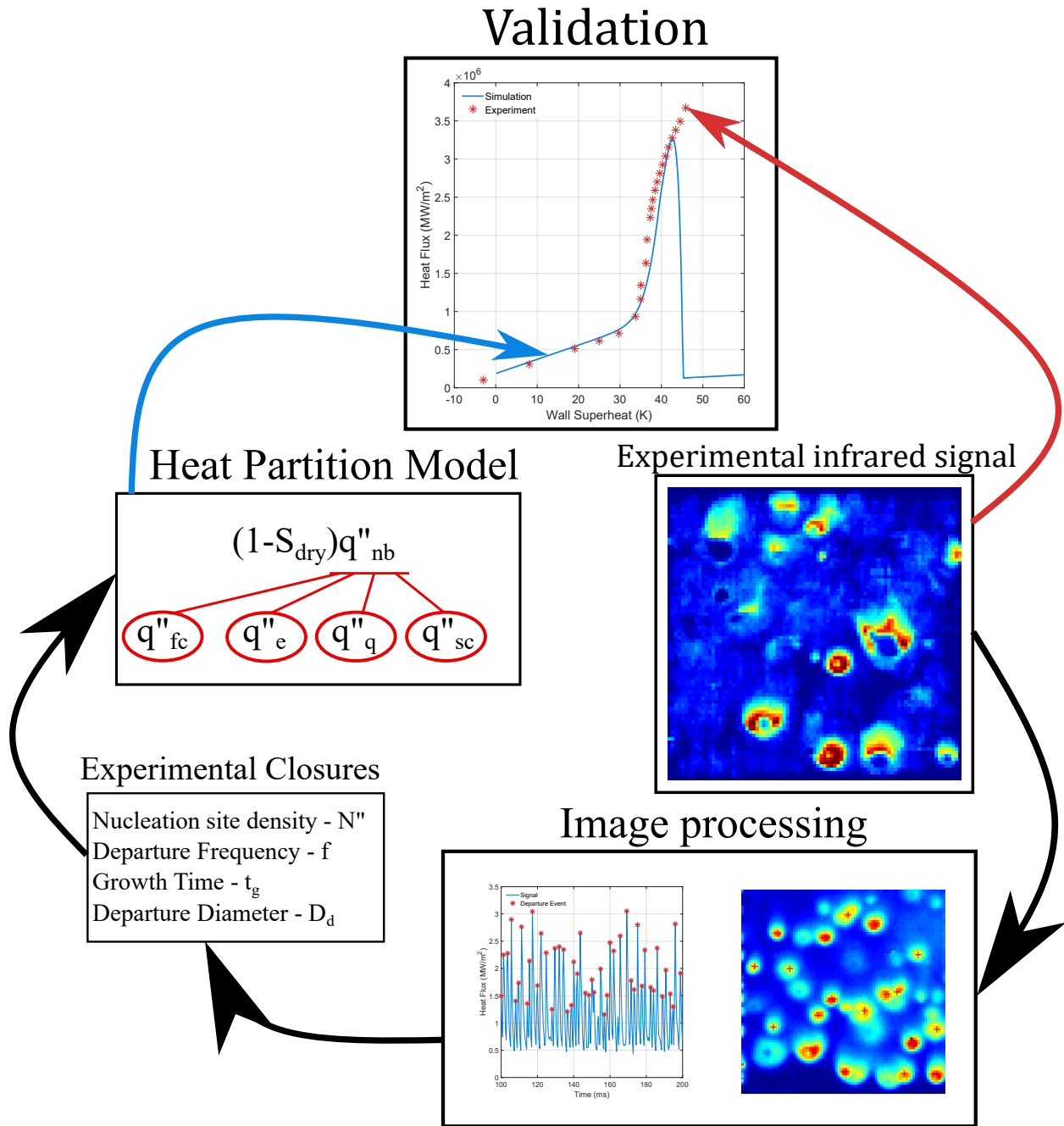


Figure 6.1: Diagram describing the process employed to demonstrate the DNB model validity, starting from the experimental infrared data, image processing techniques are used to extract useful boiling quantities which are used for the DNB model as closures with fitting functions. The resulting boiling curve and CHF are then compared to the experiment

Being able to predict accurate CHF, boiling curves and heat partition for multiple conditions, while inputting in the model the experimentally measured quantities, provides an uniquely strong evidence of the model applicability since we have eliminated the potential errors, uncertainties and biases coming from closure models. The strength of this approach is derived from the availability of accurate, high resolution, experimental measurements and is unique in that regard.

6.1.1 Experimental test suite

Richenderfer [5, 34] provided high speed infrared data for a flow boiling experiment with water. Due to limitations in the space and time resolutions of the infrared camera used by Richenderfer, cases with small bubbles and fast frequencies could not be used. For instance, every test conditions at pressures higher than atmospheric yielded very high uncertainties in the infrared post processing due to bubbles becoming close to the size of individual pixels and departure frequencies becoming of the order of or higher than the acquisition frame rate. Among the more than 40 test conditions presented in Richenderfer’s thesis, we selected four cases that provided the most precise results from advanced post-processing methods. We leveraged the following fundamental quantities from the experimental data: nucleation site density, bubble departure frequency and bubble growth time. Table 6.1 reports the test conditions that were selected.

The most notable cases are case #3 and the LbL test which investigate the effect of wettability on DNB. This sensitivity has been identified experimentally but is not captured by current DNB modeling approaches.

Table 6.1: Test matrix of subcooled flow boiling experiments and CHF simulation results

	Case #	Pressure (bar)	Subcooling (K)	Mass flux (kg/(m ² s))	Static contact angle (°)	Experimental CHF (MW/m ²)
ITO	1	1 ± 0.025	10 ± 0.5	500 ± 10	85	2.45 ± 0.05
	3	1 ± 0.025	10 ± 0.5	1000 ± 10	85	3.33 ± 0.05
	10	1 ± 0.025	10 ± 0.5	1000 ± 10	85	3.67 ± 0.05
LbL	[-]	1 ± 0.025	10 ± 0.5	1000 ± 10	< 5	4.42 ± 0.05

The post-processed data used as inputs for the model is fitted with appropriate functions in order to give a smooth behavior to the results. For each case, we used the following experimental inputs:

- **Nucleation Site Density:** The wall cavity density is related to the heater material and fabrication process. Each heater is unique and its site density activation is quantified experimentally. In the simulation, the experimental data input is provided with a fitted exponential function.
- **Bubble Departure and Liftoff Diameter:** Here we use the force balance model of Mazzocco [138] which has been successfully validated against data from Bucci and Richenderfer [6]. In this instance, the experimental trends are difficult to extract and produce large uncertainties especially at high heat fluxes. Indeed, the bubble departure diameter identification requires processing of a top-down high speed video (in visible light, not infrared) which becomes impossible when boiling is vigorous and individual bubbles cannot be distinguished. The force balance model allows us to extrapolate the departure diameter behavior at these conditions while being consistent with experimental low heat fluxes measurements.
- **Bubble Departure Frequency:** The heat flux signal from each active nucleation site is processed in order to extract its most likely period. The heater characteristic departure frequency for a given heat flux is obtained by averaging each nucleation site frequency. The resulting frequency data is then fitted with a linear function against wall superheat.

- **Bubble Growth Time:** Similarly to the frequency post processing, the growth time is extracted from the nucleation site heat flux signal. Richenderfer [5] reports experimental growth times that are almost always constant at 0.8 ms to 0.9 ms.

Figure 6.2 shows an example of the fitting functions employed for the nucleation site density and the bubble departure frequency for the following conditions: 1 bar, $1000 \text{ kg m}^{-2} \text{ s}^{-1}$

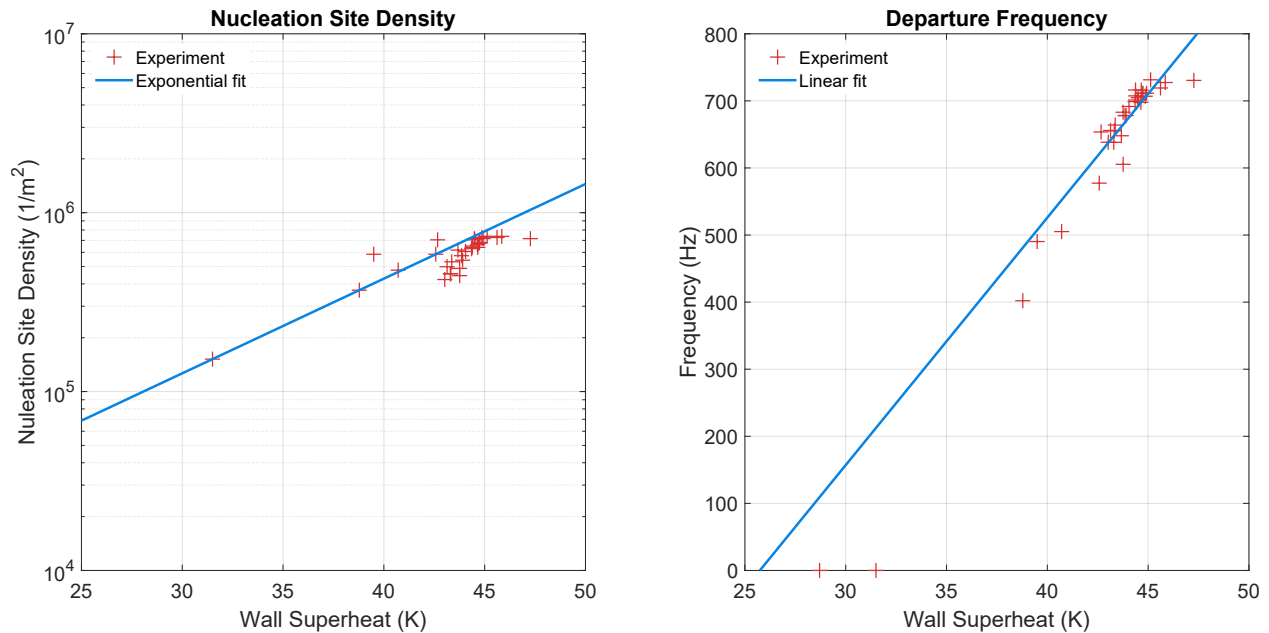


Figure 6.2: Example fitting functions for both the nucleation site density (left) and the bubble departure frequency (right)

6.1.2 Heat partitioning assessment

The accurate prediction of DNB in the model relies on the proper heat flux partitioning of the nucleate boiling regime. This component of the model is not imposed *a priori* and therefore we can assess the performance of the model in nucleate boiling before considering DNB predictions.

In Figure 6.3, experimental and simulation results for one condition (Heater #1 from Table 6.1) are plotted. We have access to two levels of information. First, the boiling curves are matching along the entire nucleate boiling regime, which is consistent with Gilman's initial findings at lower heat fluxes. Here we are able to extend the matching to the entire boiling curve up to DNB conditions. More importantly, the heat flux partitioning, which is plotted for two conditions along the nucleate curve exhibits excellent consistency with the experimental observations.

Ignoring the heat leaving to the vapor phase, which is negligible, we are able to reproduce the relative importance of evaporation compared to the other mechanisms exchanging heat with the liquid phase. At low heat flux, the evaporation contribution is near 20% while near DNB it is closer to 45%. Our model is able to capture the increase in the contribution of evaporation in the overall heat partitioning which reinforces the confidence in the ability of our framework to reproduce the physical trends that are necessary for DNB prediction.

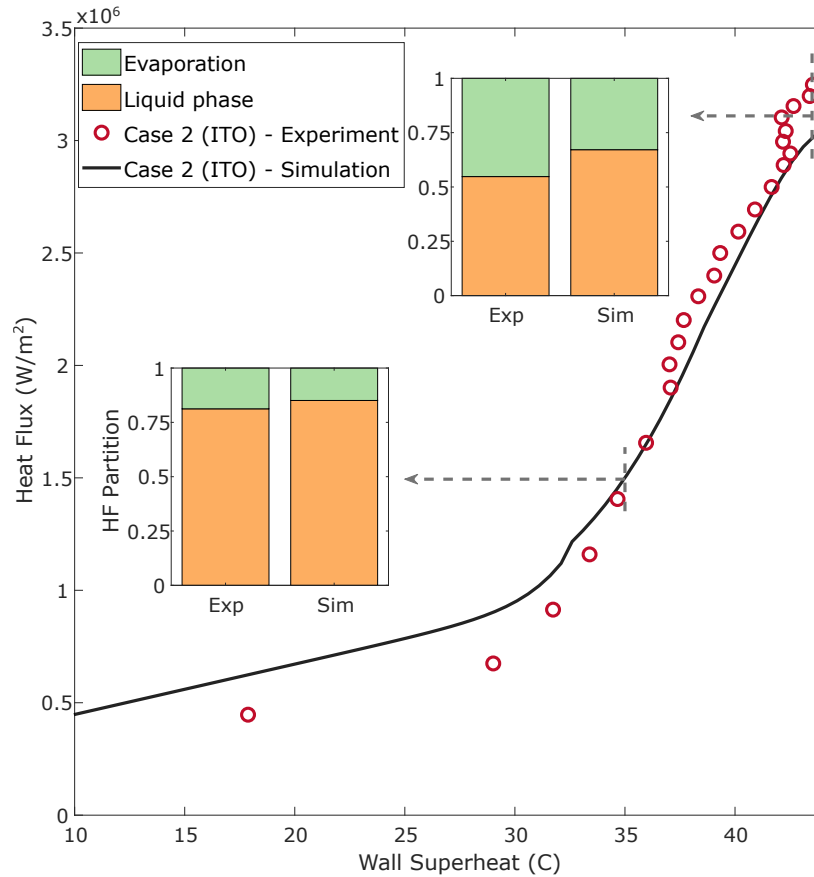


Figure 6.3: Comparison of experimental and modeled boiling curves for water at 1 bar, 10K subcooling and $1000 \text{ kg m}^{-2} \text{ s}^{-1}$. Boxes in the image compare modeled and experimental contributions of evaporation and single-phase heat transfer at two heat flux conditions. Adapted from [153]

6.1.3 DNB predictions for varying mass fluxes

Figure 6.4 compares the experimental and model results for Sapphire-ITO heaters with identical subcoolings but different mass fluxes of 500 and $1000 \text{ kg m}^{-2} \text{ s}^{-1}$. While it is well understood that in general higher mass flux leads to an increase in the overall heat transfer and higher CHF, it is interesting to see the effect on the separate physical mechanisms. Higher mass flux will increase the forced convection heat removal but also shorten the residence time of bubbles on the surface (growth time), leading to reduced interaction between bubbles, more nucleation site activation, which ultimately leads to a delayed CHF. The model captures this effect and accurately predicts CHF enhancement, when doubling the mass flux by finding a higher peak heat flux (CHF) as well as a higher wall temperature at which DNB occurs (38 K vs 45 K). In both conditions, the simulated CHF slightly underestimates the experimental CHF by 6.12% (at $500 \text{ kg m}^{-2} \text{ s}^{-1}$) and 10.30% (at $1000 \text{ kg m}^{-2} \text{ s}^{-1}$). The model predicts a relative CHF enhancement of 32.6% between the two conditions compared with the experimental enhancement of 38.8% .

Jens-Lottes flow boiling correlation [41] is also plotted in Figure 6.4 and underlines the necessity to account for the specificity of the Sapphire-ITO heater. Jens-Lottes nucleate boiling correlation cannot reproduce the ITO experiment due to the uniqueness of Sapphire-ITO heater surface

characteristics. These heaters consist of a resistive layer of ITO deposited on top of a sapphire substrate. The resulting heater surface in contact with water is nano smooth, and therefore mostly free of cavities. However, several μm scale manufacturing defects can be detected on the surface and correspond to the sites activating and nucleating bubbles during boiling. This type of surface behaves quite differently from usual metal heaters found in engineering conditions (e.g. rough steels) [154], for which Jens-Lottes correlation was developed. Its equation found in 6.1 shows the model is not sensitive to flow parameters like the mass flux and therefore doesn't predict any change in the boiling curve.

$$q''_{\text{Jens-Lottes}} = \left(\frac{1}{0.79} \exp\left(-\frac{P}{6.2}\right) \Delta T_{\text{wall}} \right)^4 \quad (6.1)$$

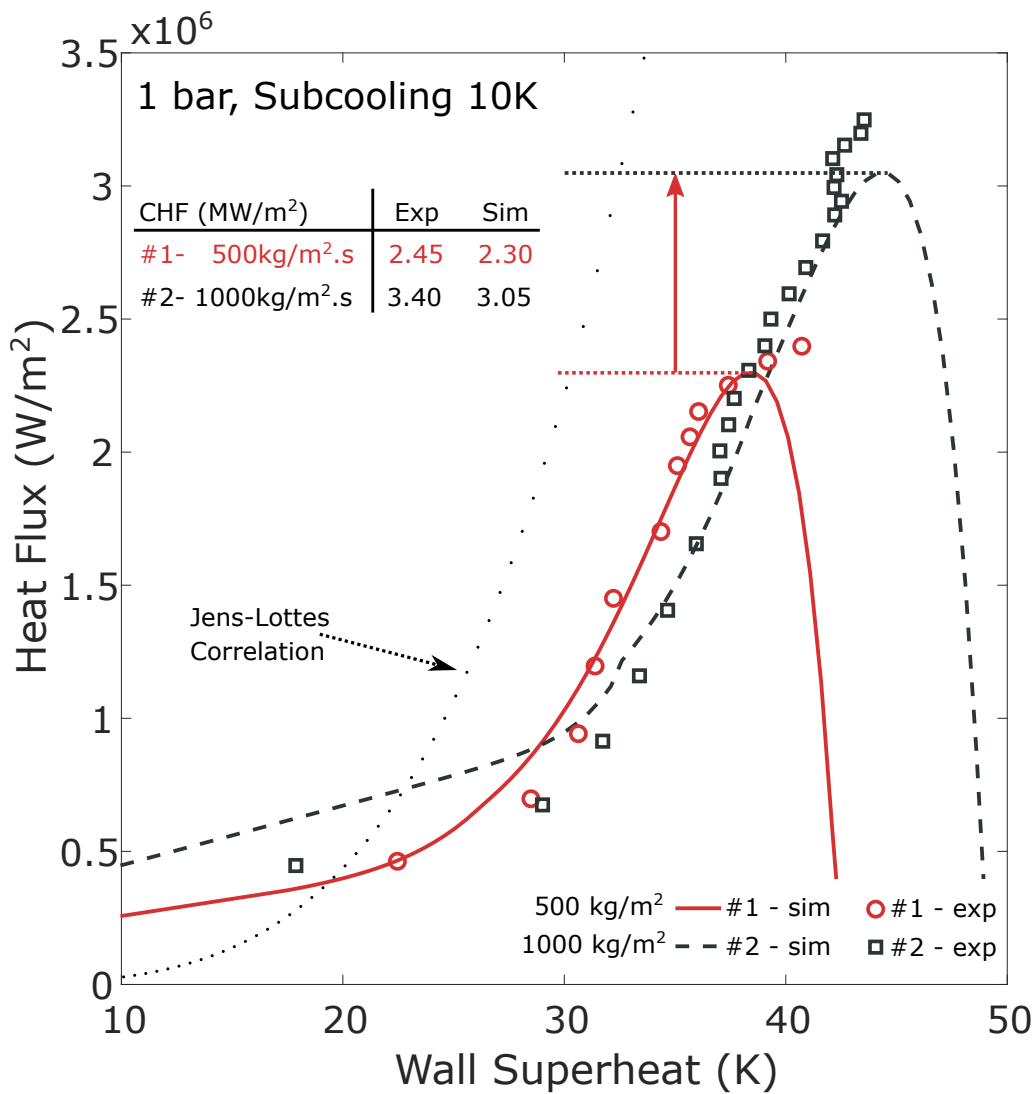


Figure 6.4: Comparison of experimental and modeled boiling curves for ITO Heater #1 ($500 \text{ kg m}^{-2} \text{ s}^{-1}$, red) and Heater #2 ($1000 \text{ kg m}^{-2} \text{ s}^{-1}$, black). The table compares measured and predicted CHF values.

6.1.4 DNB predictions for varying surface contact angles

The effect of wettability on CHF is relatively well established in pool boiling [155]: a lower contact angle (more hydrophilic surface) produces a higher CHF. The effect is well documented in pool boiling [156, 157]. Experimental studies investigating the role of the heater wettability on CHF in subcooled flow boiling are almost non-existent. Here we present one of the first experimental results of this kind. Experimental [5, 6] and model results for two heater types (Sapphire ITO and LbL) at similar conditions (1 bar pressure, 10 K subcooling, $1000 \text{ kg m}^{-2} \text{ s}^{-1}$ mass flux) are presented in Figure 6.5. Heater #3 is the baseline Sapphire-ITO type heater with a measured contact angle of 85° . Heater #4 started as a sapphire-ITO heater like #3 on which a thin porous layer of Silicon dioxide (SiO_2) nanoparticles was deposited. Nanoparticles modify the surface contact angle making it superhydrophilic while preserving the original cavity distribution.

The experimental results shown in Figure 6.5 exhibit a clear CHF enhancement with increased wettability. The boiling curves for the superhydrophilic Heater #4 (LbL) is shifted to higher superheats and CHF is enhanced by 16%. Our model's results are consistent with the experimental trend reported. In the nucleate boiling regime, we capture the onset of nucleate boiling as well as the nucleate boiling slopes for both heaters, thanks to the change of contact angle in the model. Indeed, a lower contact angle produces smaller bubble footprints which leads, for a given number of activated nucleation sites, to a lower evaporation heat flux. On the other hand, smaller bubble footprints have a direct impact on the dry area fraction on the surface. By reducing the effective dry area, the hydrophilic heater delays the dry spot growth and dry area enhancement. This allows for higher superheats to be reached, leading to more nucleation site activation and an overall heat flux increase. In the end, the LbL heater produces a higher CHF, albeit at a higher superheat than the regular ITO one (this effect was already noticed by Sadasivan in 1995 [156] for pool boiling).

The experimental results show a relative CHF enhancement of 17.2% while our model predicts a relative enhancement of 21.9%. One of the main discrepancies in our model is visible in the boiling curve of case #4. It appears the experimental curve consists of two distinct slopes. The first part, at superheats below 50°C , is well matched by our model while the second half of the nucleate boiling curve (superheats between 50°C and 65°C) is missed by our model. This may be explained by an unexpected nucleation site activation. Indeed, the experimental break of trend visible for heater #4 may have been caused by a case specific cavity size distribution which precludes activation of new cavities beyond 50°C . This could happen if the heater surface does not contain any cavities below a specific size. Since the experimental inputs like the nucleation site activation are extracted at lower superheats when bubble footprints in the infrared videos are easily identifiable, the model misses this effect on the boiling curve.

As shown with the previous results in Figure 6.4, Jens-Lottes correlation is not able to capture either boiling curves as it is not sensitive to any surface parameter. The predicted boiling curve is thus identical for both conditions. Furthermore, the correlation predicts much lower wall temperatures for a given heat flux than experimentally observed. This can be explained by the unusual cavity size distribution from the Sapphire-ITO heater, which requires higher superheats to begin nucleating.

CHF results and relative errors are listed in Table 6.2.

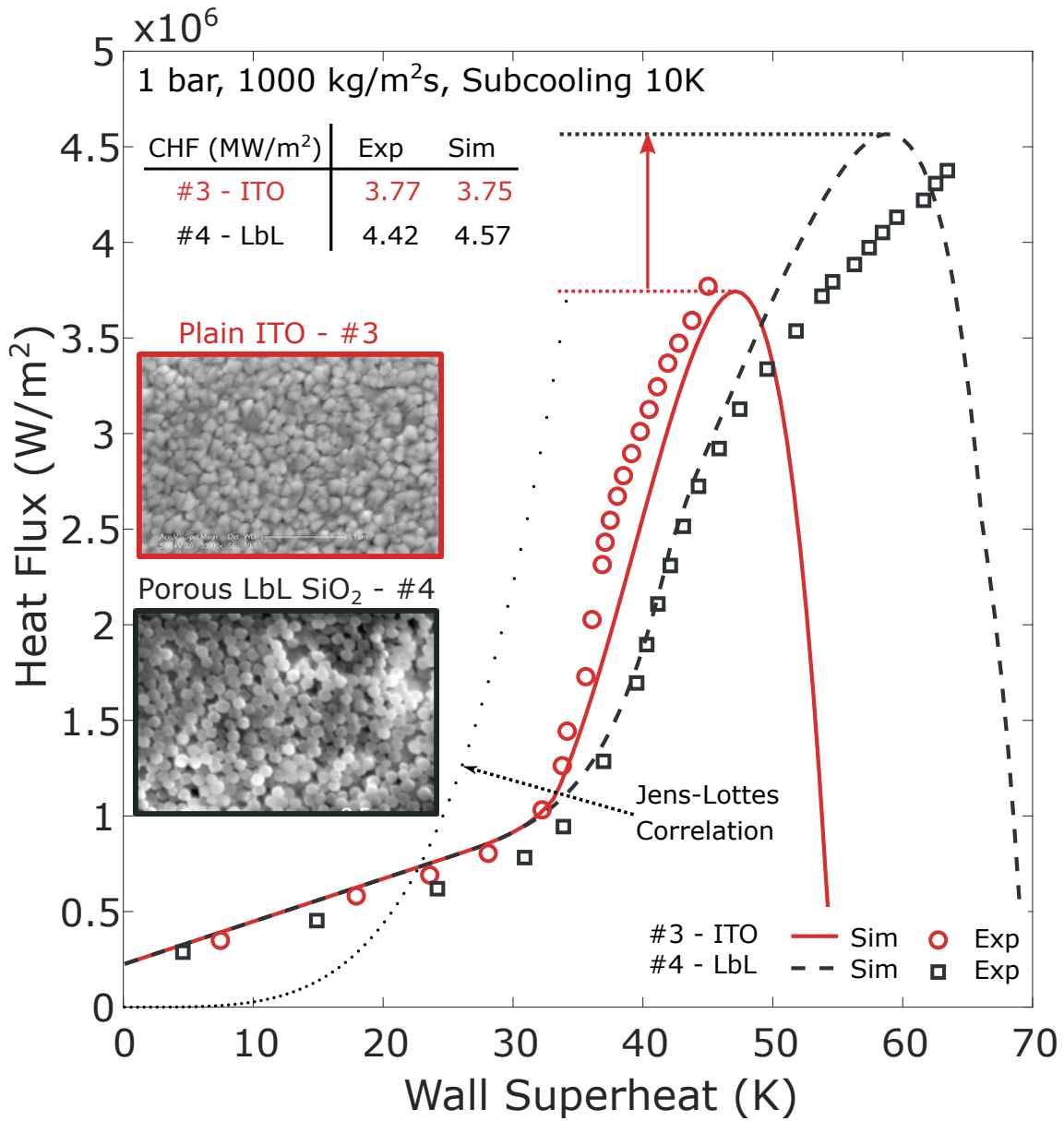


Figure 6.5: Comparison of experimental and modeled boiling curves for Heater #3 (ITO, red) and Heater #4 (LbL, black). The boxes show SEM images of the heater surfaces. The table compares measured and predicted CHF values.

Table 6.2: CHF results, absolute and relative errors for the four heaters tested

Heater #	Mass flux (kg/(m ² s))	Static contact angle (°)	Experimental CHF (MW/m ²)	Simulated CHF (MW/m ²)	Absolute error (MW/m ²)	Relative error (%)
1	500 ± 10	85	2.45 ± 0.05	2.30	-0.15	-6.12
2	1000 ± 10	85	3.40 ± 0.05	3.05	-0.35	-10.30
3	1000 ± 10	85	3.77 ± 0.05	3.75	-0.02	-0.53
4	1000 ± 10	< 5	4.42 ± 0.05	4.57	0.15	3.39

6.1.5 Insights summary

As we close this section we can draw several important conclusions on the behavior of the proposed model. We can list four major contributions from the results presented:

- **Mechanistic heat flux partitioning predictions:** The results presented in Figure 6.3 provides strong support to the applicability of the partitioning framework as long as the appropriate fundamental closure quantities are used. The nucleate boiling framework consistently predicts the split between heat transfer mechanisms. This ensures that the model is physically consistent, beyond simply matching the boiling curve in the nucleate boiling regime.
- **DNB detection mechanism:** The DNB detection idea, based on the heat partitioning between wet and dry area, is capable of predicting DNB across a range of conditions. The ability to detect DNB accurately for multiple flow rates, as well as heater surfaces is notable when compared to existing models. This approach is compatible with the latest experimental observations obtained with infrared imaging.
- **Mass flux sensitivity:** Results comparing increasing mass flux conditions in Figure 6.4 demonstrate the ability of the model to respond to a change in the flow parameters. The CHF enhancement due to a doubling of the mass flux is well reproduced by the model.
- **Surface effect sensitivity:** Sensitivity of flow boiling CHF to the heater wettability has been investigated as seen in Figure 6.5. The model successfully accounted for the effect of contact angle on both the boiling curve and CHF. At lower contact angle, the boiling curve is shifted to higher superheats and the CHF is enhanced. In the example we chose to display, the experimental CHF enhancement of 38.8% is well captured by the 32.6% our model predicts.

6.2 Model benchmarking using the MIT flow boiling loop database

After demonstrating the validity of the model framework, it is now necessary to provide closure models to quantify its predictive power across a wide range of flow conditions. The goal in this section is to evaluate the performance of our complete model across multiple cases spanning a wide range of flow conditions (mainly subcooling and mass flux) when relying on mechanistic closure for the modeling terms.

The complete model consists of the nucleate boiling heat flux partition (described in section 4.1), the dry area modeling (described in section 5.2) and finally the appropriate closure selection. Together, these models and closures are applied to the experimental conditions of the MIT flow boiling loop described in chapter 3 to predict boiling curves as well as DNB occurrences.

6.2.1 Boiling curves and DNB results using modeled growth time

The initial set of results are displayed in Figure 6.6. In this plot, the 14 simulated boiling curves are drawn alongside the corresponding experimental data points. The case numbers are listed in Table 3.1. The resulting CHF prediction is overestimated in all cases but one (25 K subcooling, $500 \text{ kg m}^{-2} \text{ s}^{-1}$) and the maximum relative error reaches 658%. Looking at the boiling curves, all cases are predicting the single phase and early nucleate boiling regime accurately but fail to capture the later part of the nucleate boiling regime by exhibiting steeper boiling curve slopes than measured experimentally.

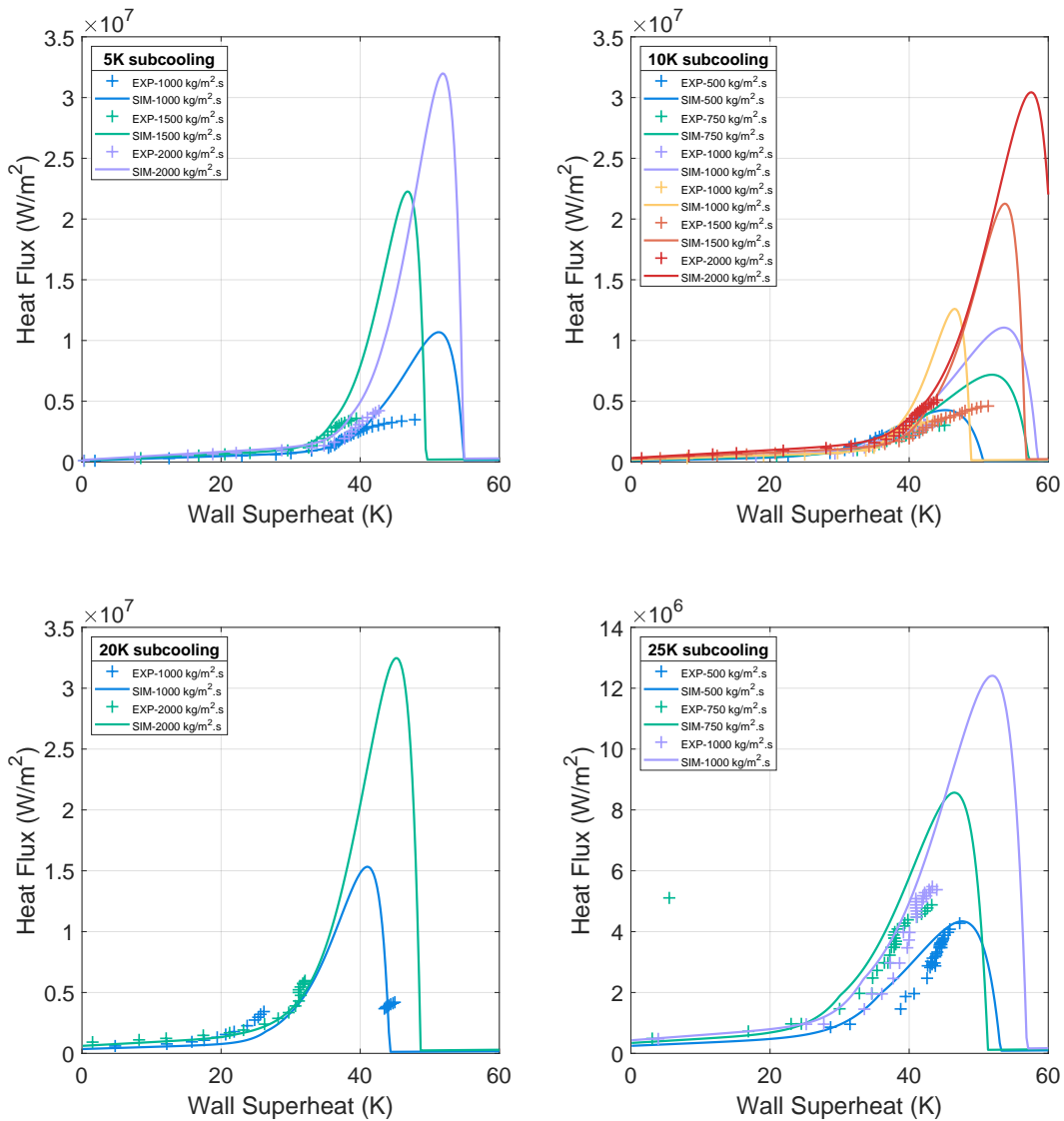


Figure 6.6: boiling curves results of the MIT flow boiling database at atmospheric pressure when using Kojima's growth time. Subplots represent inlet subcooling (from top to bottom, left to right): 5 K, 10 K, 20 K, 25 K

In order to understand the results of the model predictions, we can analyze a representative case shown in Figure 6.7.

In this case (5 K subcooling, $500 \text{ kg m}^{-2} \text{ s}^{-1}$), the boiling curve (top-left subplot) exhibits a characteristic behavior also observed in other cases; the single phase and early nucleate boiling regime are well predicted and match the experiment. The later part of the curve until CHF (above 35 K superheat) misses the change of slope in the experimental curve and its peak. The model predicts a 4.27 MW m^{-2} CHF, overestimating by 72.31% the experimental value of 2.45 MW m^{-2} .

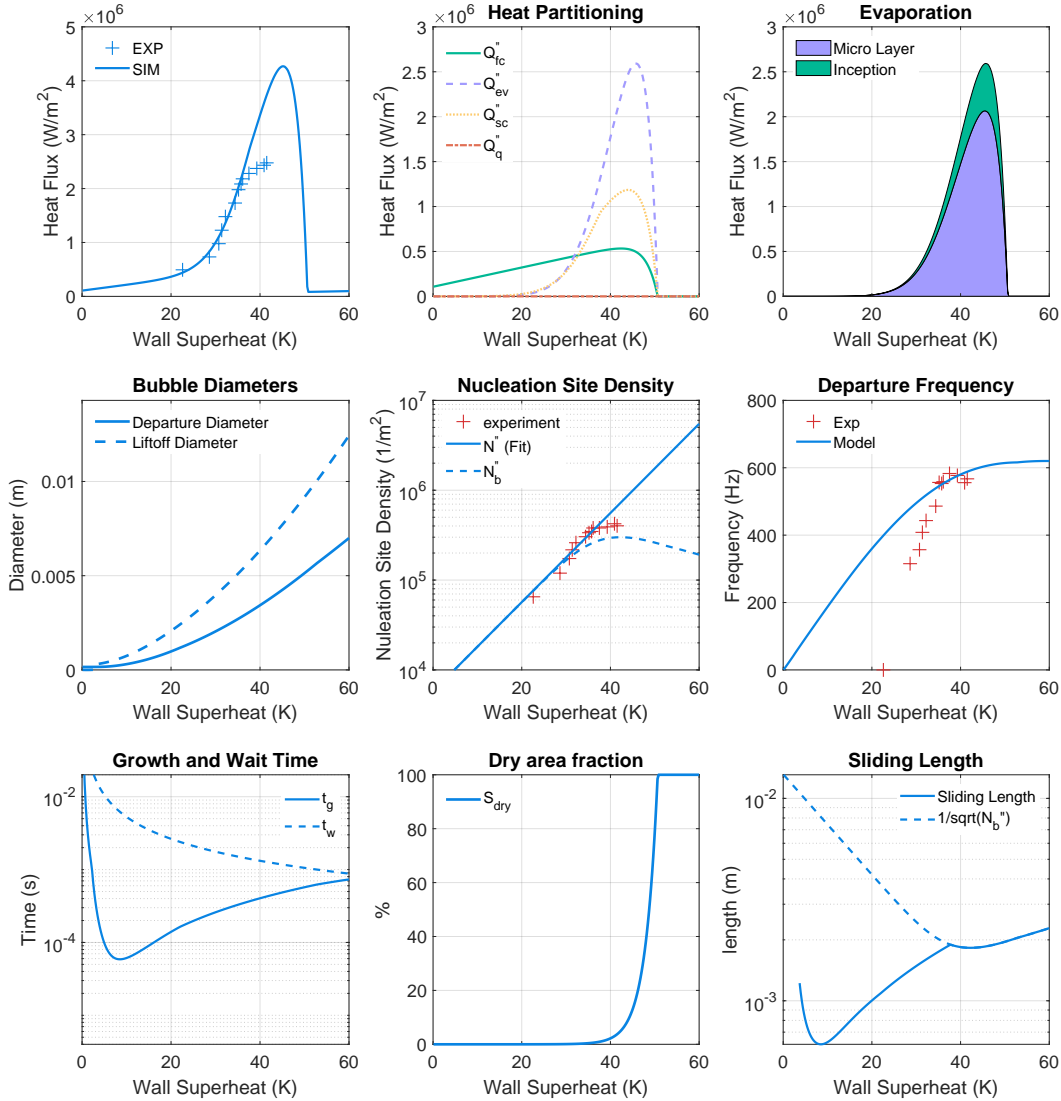


Figure 6.7: Case #1, 1 bar, 10 K subcooling, $500 \text{ kg m}^{-2} \text{ s}^{-1}$. Using Kommajosyula’s growth time.

The heat partitioning plot (top-center) reveals that in the nucleate boiling regime up to CHF, evaporation is the main contributor to the overall heat flux (60% at CHF), followed by the sliding conduction (28% at CHF). The evaporation contribution is dominated by the effect of the microlayer evaporation compared to the contribution of the inception evaporation (top-right subplot). The microlayer evaporation contributes to 80% of the evaporation mechanism.

The nucleation site density (middle-center subplot) is a boundary condition to our model and the exponential fit reproduces the experimental trend. The bubble departure diameter model (middle-left subplot) has been shown to capture the experimental trends in the MIT flow Boiling

loop (see Figure 4.16).

The bubble departure frequency prediction (middle-right subplot) does not capture the onset of nucleate boiling: experimental observations indicate there is no bubble being generated until 20 K to 25 K superheat while the model we selected predicts a non-zero frequency as soon as there is a superheat. However, in the main nucleate boiling region (30 K to 40 K superheat), the prediction error are the smallest at CHF conditions.

The wait and growth time (bottom-left subplot) indicate that the wait is the main contributor to the overall bubble period. In most of the nucleate boiling regime the predicted growth time is smaller by an order of magnitude when compared to the wait time. Additionally we can note here that the growth time at CHF is approximately $0.4 \mu\text{s}$ which is less than half of the experimental value reported by Richenderfer [5].

The dry area fraction (bottom-center subplot) remains negligible until 40 K superheat and then increases rapidly to 100% at 50 K. The peak heat flux is reached at a superheat of 43 K which corresponds to a dry area fraction of nearly 10%.

Case #9 results (5 K subcooling, $2000 \text{ kg m}^{-2} \text{ s}^{-1}$) are plotted in Figure 6.8. This is the case which shows the largest CHF error in the whole data set. One can note that the modeled growth time at CHF is 0.04 ms; 20 times smaller than values Richenderfer reported. Conversely, the case with the smallest error; Case #4 (1 bar, 25 K subcooling, $500 \text{ kg m}^{-2} \text{ s}^{-1}$), is displayed in Figure 6.9. In this case, the growth time at CHF is near 0.6 ms, only 25% lower than the experimental value.

In cases with the highest subcooling and mass flux (such as case #4 seen in Figure 6.9 and case #9 seen in Figure 6.8), sliding conduction becomes a major contributor in the overall partitioning. This trend is consistent but its magnitude is difficult to estimate given the absence of specific partitioning validation data.

It is reasonable to assume from these observations that the main discrepancy in the results originates from the growth time model which predicts values smaller than experimentally observed. The presumption that the growth time is the main reason behind the failure to predict CHF is supported by the fact that, when the modeled growth is in agreement with the experiment, results are consistent (Case #4), while the furthest it is from the experiment the worse the results become (Case #9).

The consequences of using a much smaller growth time are multiple: first, it directly reduces the dry area fraction as for given conditions as bubbles (and their dry spots) will have a shorter residence time on the boiling surface. Second, it also reduces the probability of interaction and allows for a larger number of bubble generating sites to coexist on the surface and therefore a higher evaporation heat flux for a given wall superheat.

We can visualize the CHF prediction performance of our model in a scatter plot as seen in Figure 6.10. The mean relative error for this data set is 275% and the median error is 238%. individual results are listed in Table 6.3.

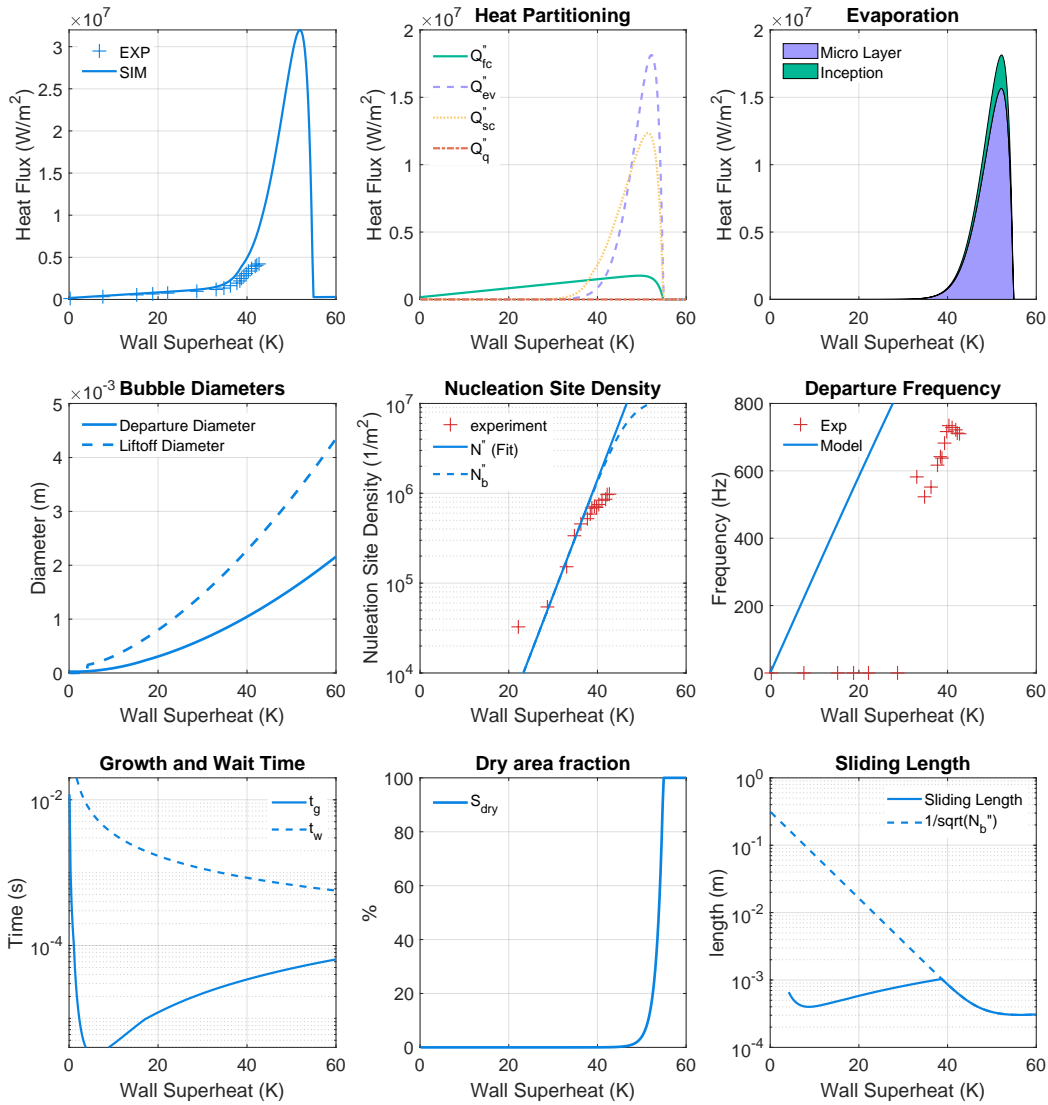


Figure 6.8: Case #9, 1 bar, 5 K subcooling, $2000 \text{ kg m}^{-2} \text{ s}^{-1}$. Using Kormajosyula's growth time.

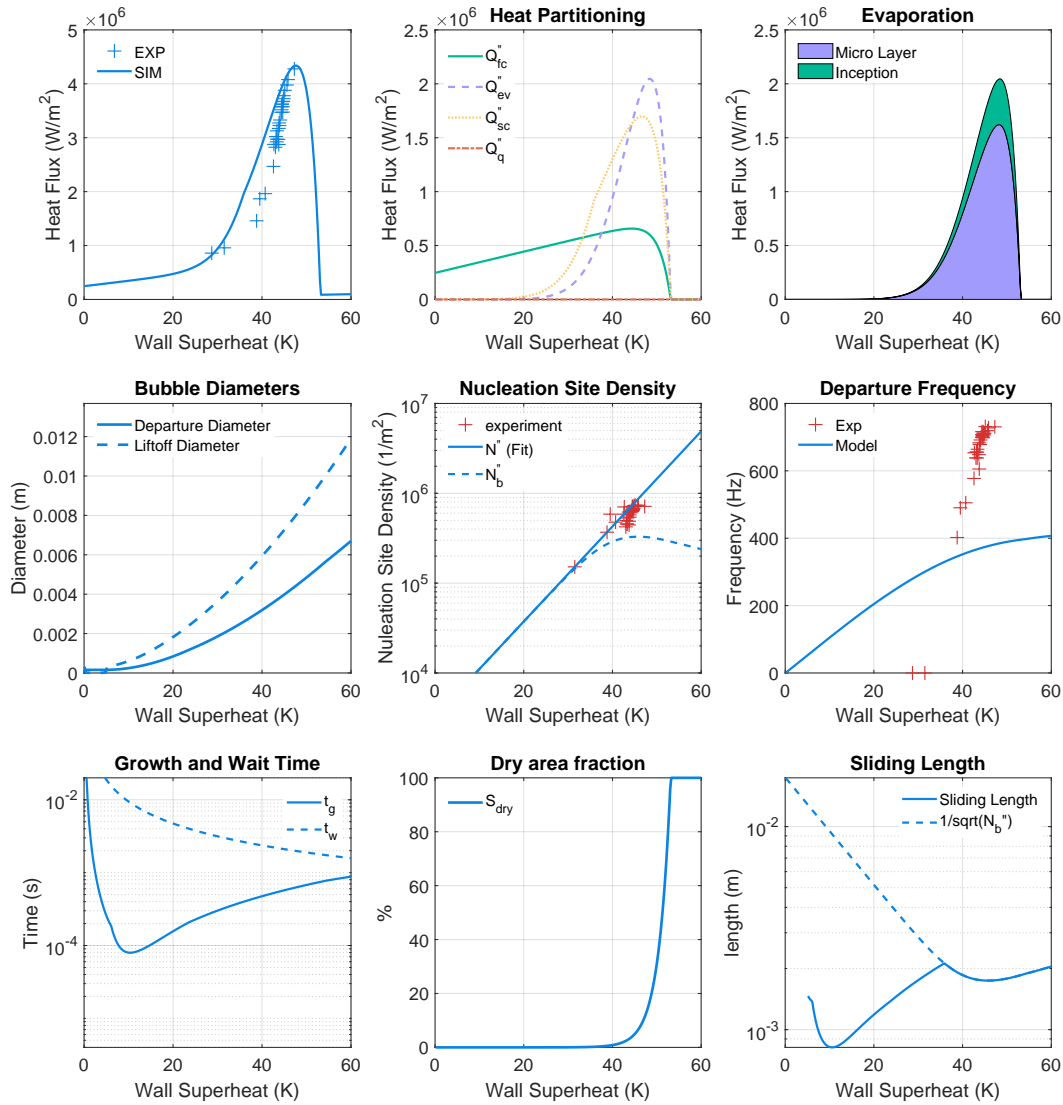


Figure 6.9: Case #4, 1 bar, 25 K subcooling, $500 \text{ kg m}^{-2} \text{ s}^{-1}$. Using Kommajosyula's growth time.

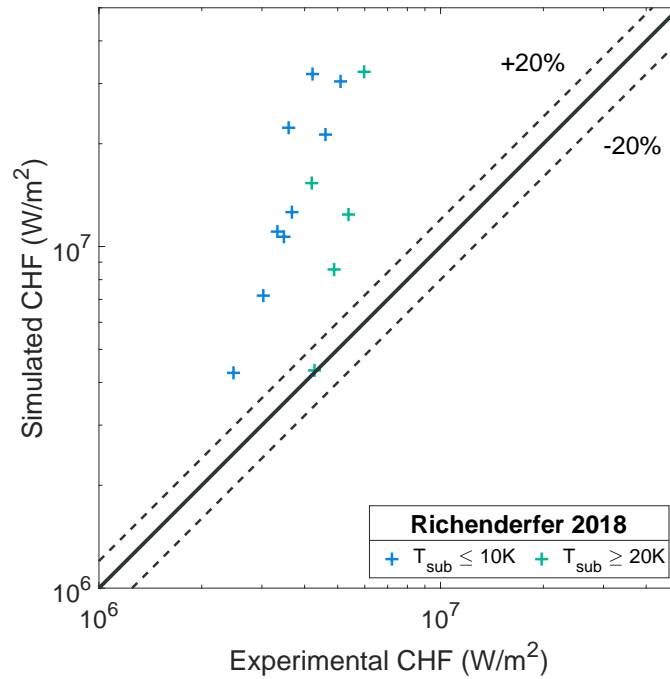


Figure 6.10: Result error scatter of the MIT flow boiling database at low pressure when using Kormajosyula’s growth time

Table 6.3: CHF results and errors when using Kormajosyula’s growth time

Heater #	Case	Subcooling (K)	Mass flux (kg/(m ² s))	Experimental CHF (MW/m ²)	Simulated CHF (MW/m ²)	relative error %
	1	10 ± 0.5	500 ± 10	2.45 ± 0.05	4.27	72.31
	2	10 ± 0.5	750 ± 10	3.03 ± 0.05	7.18	137.20
	3	10 ± 0.5	1000 ± 10	3.33 ± 0.05	11.06	232.12
	4	25 ± 0.5	500 ± 10	4.28 ± 0.05	4.34	1.45
	5	25 ± 0.5	750 ± 10	4.88 ± 0.05	8.57	75.57
	6	25 ± 0.5	1000 ± 10	5.38 ± 0.05	12.41	130.74
1	7	5 ± 0.5	1000 ± 10	3.48 ± 0.05	10.68	207.03
2	8	5 ± 0.5	1500 ± 10	3.59 ± 0.05	22.27	520.03
2	9	5 ± 0.5	2000 ± 10	4.22 ± 0.05	31.99	658.03
1	10	10 ± 0.5	1000 ± 10	3.67 ± 0.05	12.61	243.35
1	11	10 ± 0.5	1500 ± 10	4.60 ± 0.05	21.27	361.91
2	12	10 ± 0.5	2000 ± 10	5.10 ± 0.05	30.44	497.08
3	13	20 ± 0.5	1000 ± 10	4.57 ± 0.05	15.34	265.39
3	14	20 ± 0.5	2000 ± 10	5.98 ± 0.05	32.47	443.41

6.2.2 Boiling curves and DNB results using experimental growth time

While Kommajosyula's growth time model is physically sound and based on previously accepted principles, the results presented in the previous section indicate that the approach fails to predict growth for the experimental data set. The main weakness in Kommajosyula's model is the lack of dedicated growth time validation data. The validation study against Richenderfer data presented in subsection 4.2.3 and subsection 4.2.4, exhibited good performance but could only compare the total period (expressed as frequency) and did not distinguish between growth and wait times. Since for water at atmospheric pressure, the wait time is the main contributor to the overall period, the error in growth time did not appear clearly in the frequency validation. We can note the best and worse growth time predictions are on opposite sides of the parameter space. The best case is predicted for the higher subcooling (25 K) and lower mass flux ($500 \text{ kg m}^{-2} \text{ s}^{-1}$), while the worse prediction occurs in the lower subcooling (5 K) and higher mass flux ($2000 \text{ kg m}^{-2} \text{ s}^{-1}$) conditions.

Given the lack of maturity of the bubble growth time modeling, we must resort to leveraging directly the experimental measurements from Richenderfer. We tested the model's performance using Richenderfer's experimental growth time value of 0.8 ms while maintaining unchanged the rest of the closures.

Individual results for each of the 14 cases are displayed in Appendix C while a summary figure of all the boiling curves is found in Figure 6.13. The overall boiling curve behavior is considerably improved and the CHF predictions are in line with experimental trends. This is better seen in the final scatter plot for the whole data set in Figure 6.14. All the cases fall inside a $\pm 20\%$ error band.

Looking at two specific cases that were previously challenging, we can analyze the model behavior. In case #9, The boiling curve and CHF prediction presented in Figure 6.11 are significantly improved. The relative CHF error is brought down from 658% to 11.5%. Case #4, displayed in Figure 6.12 is now underpredicting CHF by 14.2%. This degradation of the performance of case #4 is due to the change in its frequency which used to match the experiment at CHF while it is now under-predicted thanks to the higher growth time.

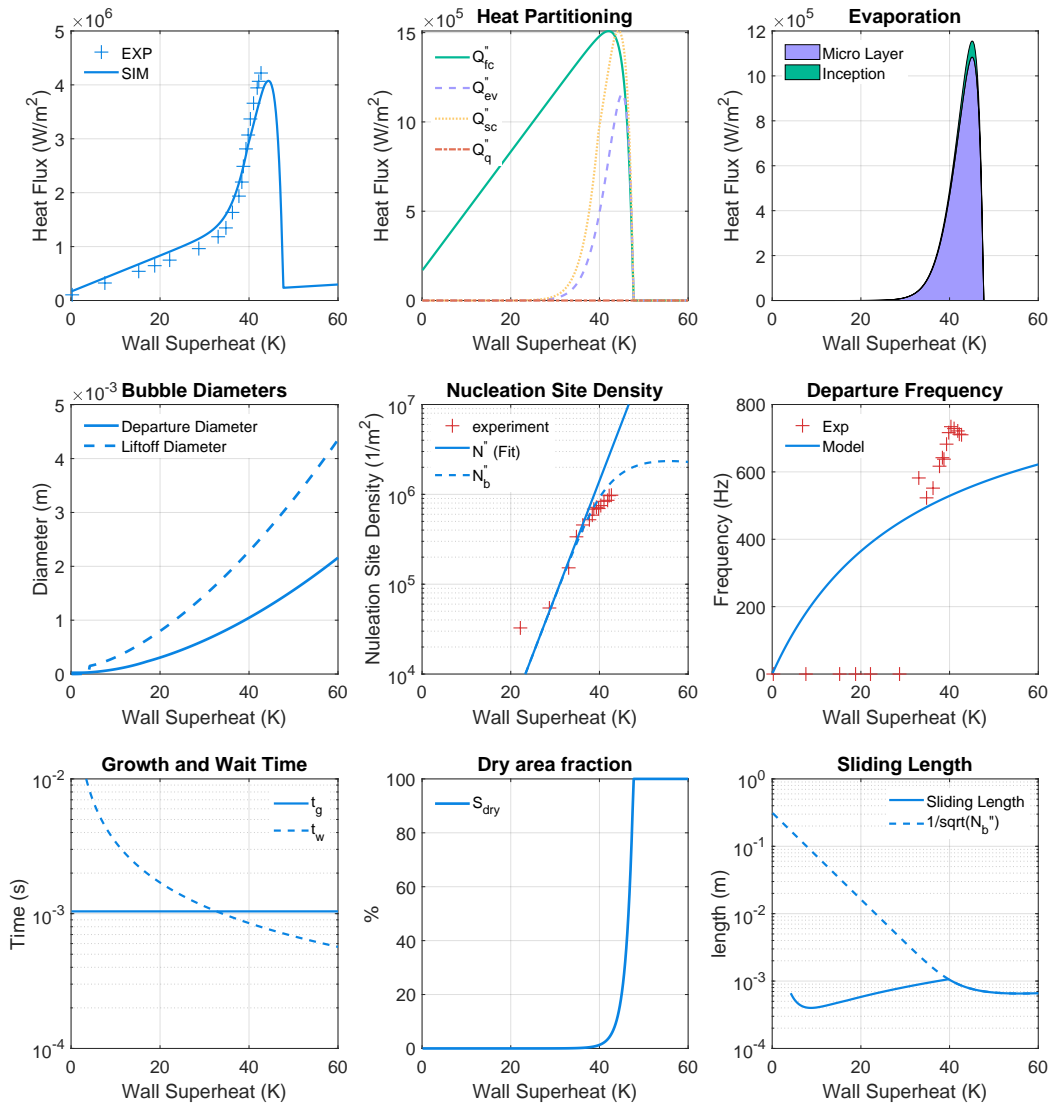


Figure 6.11: Case #9, 1 bar, 5 K subcooling, $2000 \text{ kg m}^{-2} \text{ s}^{-1}$. Using Richenderfer's experimental growth time.

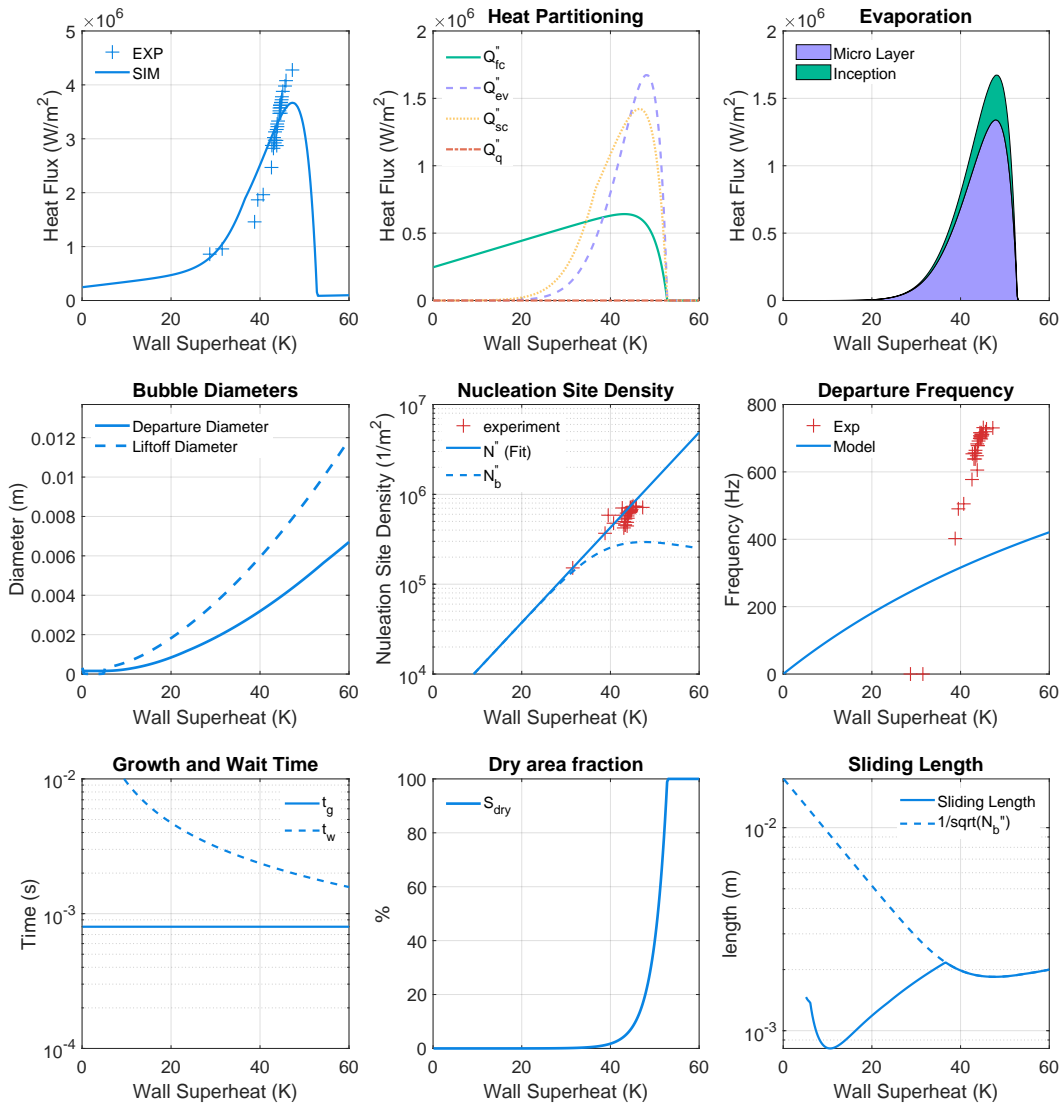


Figure 6.12: Case #4, 1 bar, 25 K subcooling, $500 \text{ kg m}^{-2} \text{ s}^{-1}$. Using Richenderfer's experimental growth time.

Table 6.4 lists the final CHF results and relative errors. The mean relative error for this data set is 2.43% while its median error is 4.97% and its standard deviation is 19.5%.

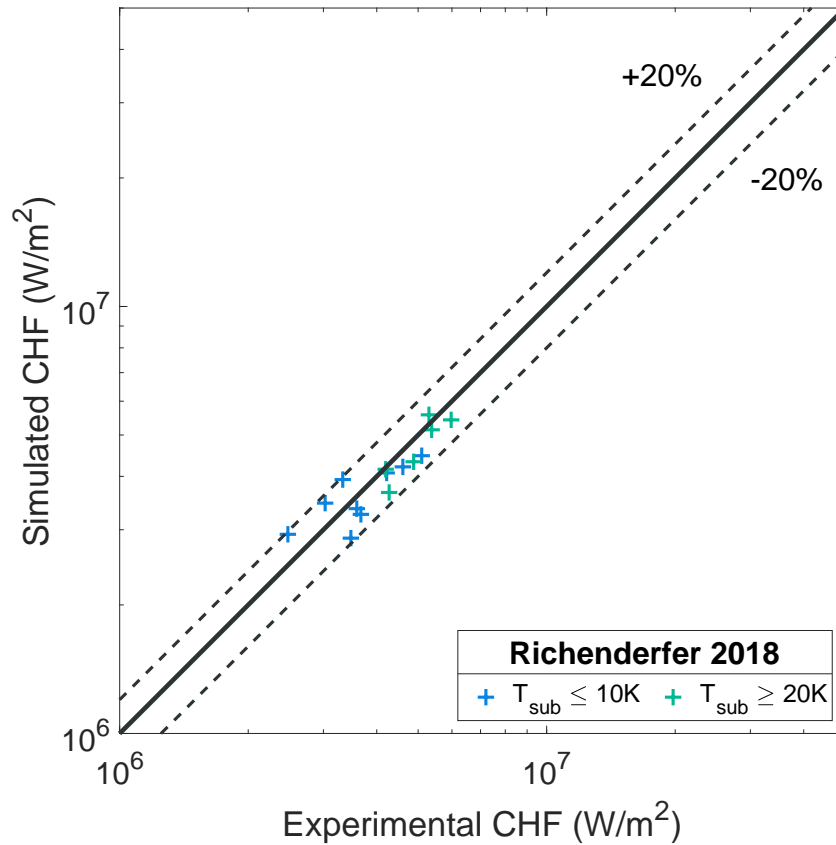


Figure 6.13: Result error scatter of the MIT flow boiling database at atmospheric pressure when using the complete DNB model

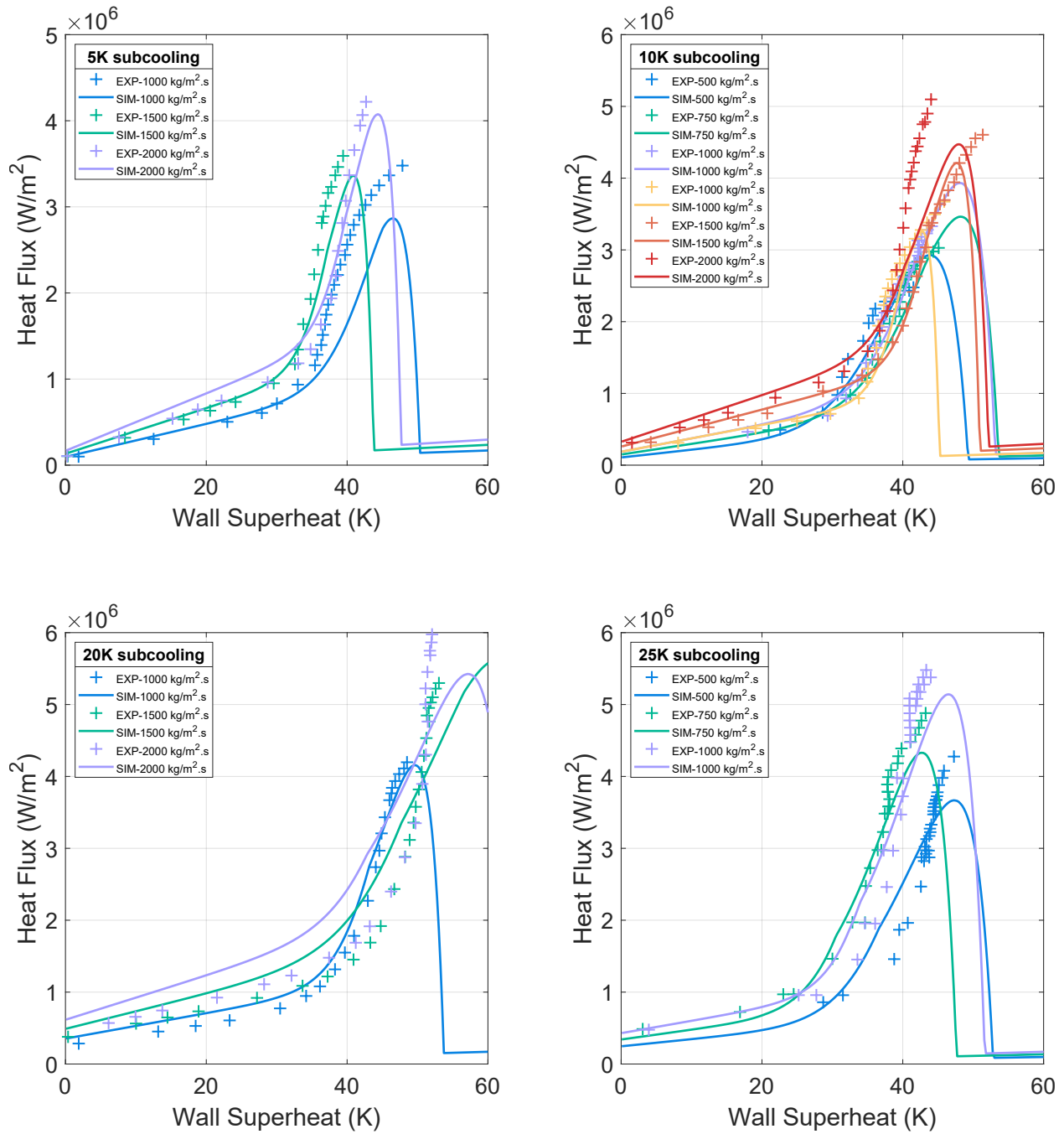


Figure 6.14: boiling curves results of the MIT flow boiling database at atmospheric pressure when using the complete DNB model

Table 6.4: CHF results and errors when using the complete model (with experimental growth time)

Heater #	Case	Subcooling (K)	Mass flux (kg/(m ² s))	Experimental CHF (MW/m ²)	Simulated CHF (MW/m ²)	relative error %
	1	10 ± 0.5	500 ± 10	2.45 ± 0.05	2.93	18.17
	2	10 ± 0.5	750 ± 10	3.03 ± 0.05	3.46	14.35
	3	10 ± 0.5	1000 ± 10	3.33 ± 0.05	3.93	18.08
	4	25 ± 0.5	500 ± 10	4.28 ± 0.05	3.67	-14.23
	5	25 ± 0.5	750 ± 10	4.88 ± 0.05	4.33	-11.31
	6	25 ± 0.5	1000 ± 10	5.38 ± 0.05	5.14	-4.39
1	7	5 ± 0.5	1000 ± 10	3.48 ± 0.05	3.36	-3.30
2	8	5 ± 0.5	1500 ± 10	3.59 ± 0.05	3.92	9.02
2	9	5 ± 0.5	2000 ± 10	4.22 ± 0.05	4.71	11.58
1	10	10 ± 0.5	1000 ± 10	3.67 ± 0.05	3.82	3.92
1	11	10 ± 0.5	1500 ± 10	4.60 ± 0.05	4.88	6.03
2	12	10 ± 0.5	2000 ± 10	5.10 ± 0.05	5.16	11.4
3	13	20 ± 0.5	1000 ± 10	4.57 ± 0.05	4.57	8.87
3	14	20 ± 0.5	2000 ± 10	5.98 ± 0.05	4.55	-23.87

The demonstration of consistent CHF prediction for experimentally measured growth time provides confidence on the capabilities of the model, as well as evidences of the importance of accurately predicting the bubble growth time. This aspect is particularly challenging for reactor applications as limits to the high speed infrared imaging detection capabilities are already visible in Richenderfer's work. The Nyquist–Shannon sampling theorem demonstrates that a signal should be sampled at least at twice the frequency of the information it is trying to capture. In our case, the infrared camera framerate of 2500 frames per second limits the ability to detect signals of frequencies higher than 1250 Hz. In terms of time periods, the experimental apparatus is not able to capture trends that are shorter than $1/1250 = 0.8$ ms. This physical limit to the signal processing prevented the use of Richenderfer's cases operating at pressures higher than atmospheric as the bubble departure frequencies become higher than the detection limit. Departure frequencies up to 2000 Hz were detected in single sites in a few high speed videos, acquired in those conditions from the top down at 10,000 frames per second. It allowed us to confirm this hypothesis when individual bubbles were still identifiable and their departure observable. Infrared camera should reach much higher framerates in order to capture the departure events along the entire boiling curve.

Given this challenge, it is important to dedicate attention to the sensitivity of the model to the growth time along with other parameters which depend on experimental observations. This is developed in the following section.

6.3 Sensitivity study

Given the complexity of the model formulation, it is important to also assess the relative weight of the various terms in the model, and the strong non-linearity which prevents intuitive predictions about the model sensitivity to input and closure parameters.

We will focus here on the sensitivity of the model to six parameters: the number of nucleation sites, the bubble departure diameter, the bubble departure frequency, the bubble growth time, the dry spot coefficient (ζ) and the contact angle. The methodology deployed consists of using a reference case and modify each parameter one by one by adding or subtracting an arbitrary fraction (here 30%) to the reference value. In this way we can compare the relative influence of each parameter and isolate the most sensitive ones. After identifying the parameter with the greatest sensitivity, it is then probed against the entire database.

The reference case results are presented in Figure 6.15 and the sensitivity to each parameter can be discussed separately:

- **Nucleation Sites:** this parameter is the least sensitive to changes thanks to the probabilistic interaction model. At CHF, the number of bubbles present on the surface is limited by their size as they crowd the surface. Therefore, nucleation site enhancements have little effect on the CHF since no more bubbles can be generated on the surface. Changes in the number of active nucleation site have almost no discernible effect on the CHF (less than 1% change).
- **Departure Diameter:** larger bubbles tend to increase CHF and decrease the superheat at which CHF occurs. This a valuable insight in that the complex boiling framework we have assembled provides robust predictions which minimizes the sensitivity to the bubble departure diameter input. Larger bubbles remove more heat from the surface but statistically interact more often, thus triggering DNB at a lower wall temperature due to the dry area

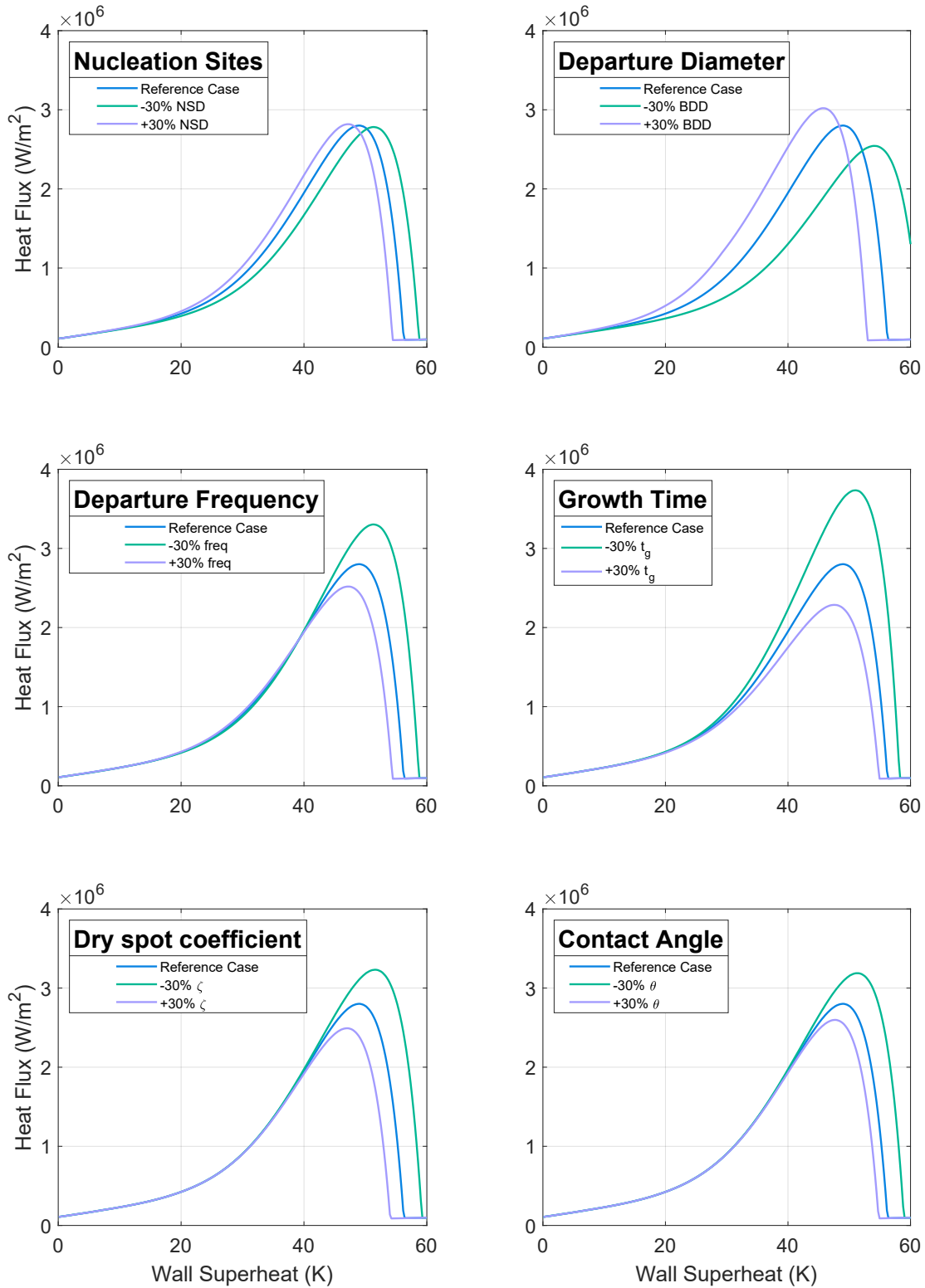


Figure 6.15: Input parameter sensitivity at atmospheric pressure conditions. Effect of a $\pm 30\%$ change in nucleation sites, departure diameter, departure frequency, growth time, dry spot coefficient and contact angle on boiling curves and CHF

fraction growing faster than with smaller bubbles. In a classic heat partitioning approach the feedback mechanism suppressing nucleation sites as the boiling surface becomes crowded with bubbles is absent, and a 30% change in departure diameter yields more than double the heat removed via evaporation. Instead, in the proposed model, with the inclusion of a physical feedback, the CHF enhancement due to a 30% bubble diameter change is limited to less than 10%.

- **Departure Frequency:** the model’s sensitivity to this closure is as follow: the results presented in Figure 6.15 show that a 30% frequency decrease yields an increase in CHF of 16% while a 30% frequency increase corresponds to a 10% lower CHF. This result can seem contradictory but since frequency is the only parameter modified while the growth time remains constant, the frequency test actually amounts to a bubble wait time test. In this context, a smaller frequency corresponds to a longer wait time for a given fixed growth time which decreases the fraction of time when bubbles are nucleating on the surface during the overall bubble nucleation cycle. In the end, a decrease in frequency leads to an increase in CHF and of the superheat at CHF.
- **Growth Time:** this input closure is the most sensitive parameter among the six we consider in this study as a 30% decrease in t_g leads to a CHF enhancement of nearly 34%. The growth time sensitivity is opposite to the frequency test described above. Increasing the growth time for a fixed frequency means that the dry spots are present on the surface for longer in proportion to the total bubble nucleation period. Higher growth times lead to an enhanced dry area fraction and an early DNB occurrence, thus reducing CHF.
- **Dry spot coefficient:** ζ is a parameter we estimated based on experimental observations at low pressure and early tests for low pressure simulations. There is an inherent uncertainty in this parameter which directly influences the resulting dry area fraction and ultimately the CHF detection. Contrary to the bubble diameter, frequency and nucleation site density, this parameter is not coupled to the rest of the framework and doesn’t beneficiate from feedback mechanisms. Therefore, its effect on CHF is direct: larger dry spot coefficient will trigger DNB earlier in the boiling curve leading to a lower CHF. In this case, a 30% decrease in ζ leads to a 14% enhancement of CHF.
- **Contact Angle:** The scaling of the dry spot based on the surface contact angle is relatively simple between 0° and 90° . Smaller contact angles lead to a reduction in bubble footprints on the surface and minimize the dry area fraction. This helps delaying DNB and pushing CHF to higher values. In this case the enhancement is limited as the original contact angle for Sapphire-ITO heaters is near 90° . However, for superhydrophilic surfaces with very low contact angles, the sensitivity to the actual value can become quite large. Similarly, superhydrophobic surfaces with contact angle approaching 180° will detect DNB as soon as bubble begin to nucleate as dry spots will tend to spread on the entire surface.

Among the six parameters, growth time is the one showing the largest effect on CHF predictions. Figure 6.16 displays three sets of results for the complete low pressure database presented in this chapter. The original results are plotted in blue while results from growth time enhancements of +30% and –30% are respectively in green and purple. This figure helps visualizing the global effect of growth time across the range of thermal hydraulic inputs. We can see that a reduction of 30% in growth time would move the mean CHF relative error above 30%. An increase of 30% would not be as consequential as the majority of the database would still lie within 20% of the experiment.

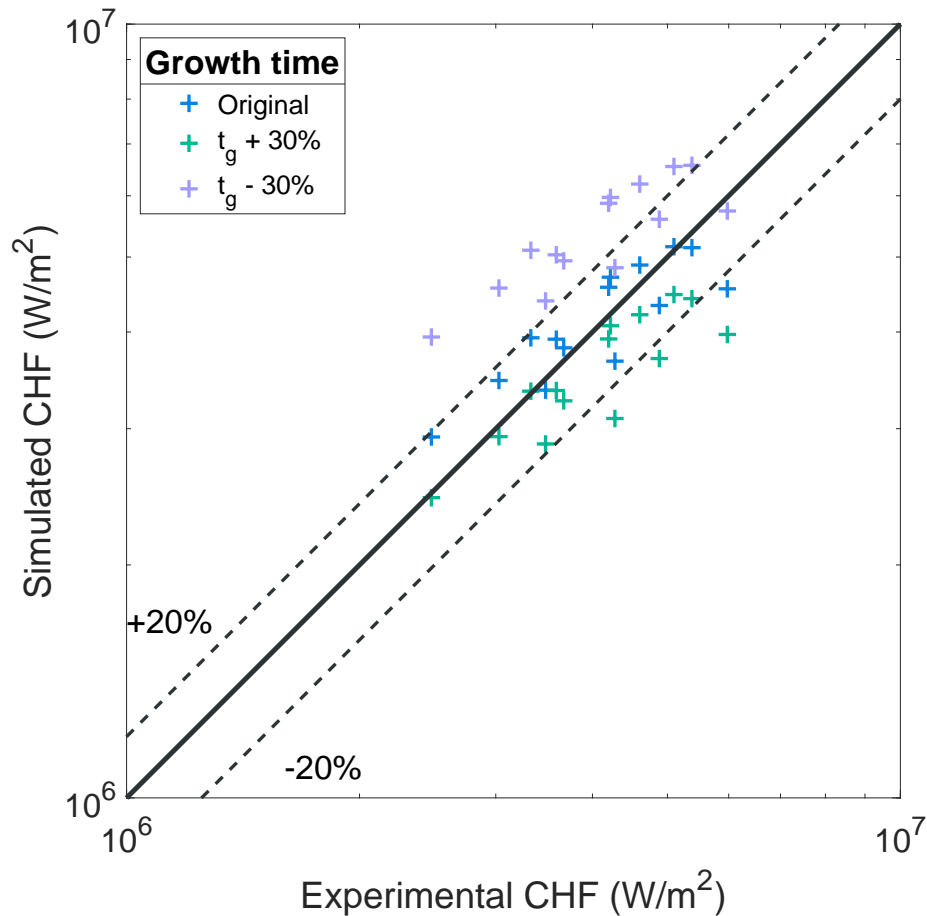


Figure 6.16: Effect of a $\pm 30\%$ change in growth time on the error scatter at atmospheric pressure conditions

6.4 Chapter summary

In this chapter we have demonstrated the feasibility of predicting subcooled flow boiling CHF by relying on a mechanistic representation of the heat partition at the wall, including the effect on the energy balance of the wetted and dry areas. The necessary inputs for our predictions are the thermal hydraulics external parameters (mass flux, subcooling, pressure) as well as the experimentally measured nucleation site density.

The model assessment evidenced the shortcomings of existing closures for growth time which leads to large overestimation of experimental CHFs. Estimating the growth time directly from the experimental measurements allows for demonstrating accurate CHF predictions across the parameter space. We obtained a final relative error scatter bounded by $\pm 20\%$ which confirmed that the initial poor predictions were due to the inability of the model to predict realistic growth times. The main insights gained from assembling a complete model and testing it against high quality flow boiling data can be summarized in the following points:

- **Complete set of consistent models:** We demonstrated the capability to assemble a complete

model along with its necessary closures in order to predict flow boiling and DNB. The nucleate boiling framework we advance is inspired from the physical representation proposed by Gilman and updated to take into account recent progresses, and extended in the context of CHF predictions, which was not explored at the time.

- **The importance of growth time modeling:** Initial tests showed the challenge of predicting growth time. The error in the growth time affects the CHF detection dramatically, the nucleate boiling curves are less sensitive because the growth time is mainly affecting the later part of the boiling curve when the surface becomes saturated with bubbles and the energy balance at the wall approaches CHF. The lack of high fidelity data is hindering the validation of growth time models and leads to situations where the predicted growth time can be off by orders of magnitude. Our CHF predictions rely on the accurate estimation of this fundamental boiling quantity. Better growth time models would be required in the future to support the general applicability of the method.
- **Quantitative CHF Predictions:** When given the right growth time, the DNB model we propose exhibits a very consistent behavior and is able to deliver accurate predictions of CHF across a wide gamut of flow conditions. We report an overall median CHF error of 4.97% and 19.5% standard deviation.

Chapter 7

Model extension to high pressure conditions

After demonstrating the applicability of our approach with available low pressure experiments, here we turn our attention to the model extension to prototypical reactor conditions. The heater design in the MIT flow boiling loop is quite different from the heat transfer material found in a PWR (fuel cladding). Commercial heat transfer surfaces such as the inside an industrial boiler or nuclear fuel cladding are made out of machined metals and alloys exhibiting very different behavior during boiling. We can compare the main discrepancies between them in the following table:

Table 7.1: Heater differences between laboratory tests and nuclear reactor applications

Surface	Laboratory Heater	Industrial Heater
Material	Sapphire-ITO	Metallic
Heat Source	Direct contact with fluid	Conducted through the heater
Contact Angle	$\approx 90^\circ$ [5]	$\approx 40^\circ$ [158]
Surface state	nano-smooth with few manufacturing defects	rough / machined

We have shown in chapter 5 that our model is able to capture material effects such as the surface wettability. However, the main challenge when predicting DNB for nuclear application stems from the very high operating pressure (155 bar) at which no experimental instrumentation has been able to observe fundamental closure quantities for the model. We want to confront our approach with realistic conditions encountered in industrial applications.

The available literature on high pressure subcooled flow boiling usually consists of “Integral” databases, meaning there is limited local instrumentation and CHF is reported against integral flow parameters (pressure, subcooling, mass flux). This limits our ability to analyze the behavior of the model and compare it to the experiment as we were able to do in low pressure experiments in chapter 6. In this chapter, we will describe the data sets we selected in section 7.1 and propose an extension of the model (heat partition and closures) in section 7.2 that is applicable to high pressure. We will benchmark its performance against one hundred and sixty seven test conditions from three databases in section 7.3. We also detail the model parameter sensitivity in section 7.4 with an approach similar to the one we presented in the low pressure chapter.

7.1 Available high pressure integral data sets

We selected databases at very high pressures (> 130 bar) for vertical subcooled flow boiling in round tubes. Due to the challenges and cost associated with high pressure testing, most of the available databases age back to the late 1950s and early 1960s during the early times of nuclear

power development. The databases we selected come from the extensive test campaigns run in the National Laboratories at a time when these expensive endeavors were necessary to design new nuclear reactors. More recent CHF sources do not cover the range of conditions [159, 160] we are looking for (low pressure, saturated flows) or are proprietary [161] and were not accessible.

7.1.1 DeBortoli et al. 1958

DeBortoli et al. [42] is a report relating efforts made at Bettis Atomic Power Laboratory regarding CHF in tubes at high pressure. The report also tabulates dozens of CHF databases from the early 1950s from other research laboratories. We decided to select databases that involved round tubes of diameters larger than 4 mm, operating at subcooled conditions and pressures higher than 130 bar. These parameters are representative of the challenges of predicting DNB in a Pressurized Water Reactor. Most of the databases tabulated by DeBortoli et al. were not selected due to the lack of applicability of our model (saturated flows) and/or conditions not directly relevant for PWR fuel conditions (inclined channels, downstream flows, micro-scale tube diameters, square channels). We selected two databases that matched our selection criteria. They are described in the following subsections.

7.1.2 Jens and Lottes 1951

The data set from Jens and Lottes at Argonne National Laboratory reported by DeBortoli is extracted from a larger report [41] from 1951. It is one of the earliest source of high pressure CHF data. Among all the tabulated results, we discriminated the saturated boiling cases from the subcooled ones at high pressure (137.9 bar). We selected 27 subcooled cases out of 60. The test used a 5.74 mm tube diameter. Inputs and experimental CHF used in our simulation are tabulated in Table D.1.

7.1.3 Hunt et al. 1955

This data set is from Bettis Atomic Power Laboratory[162] and consists of 93 cases for a vertical pipe of diameter 4.72 mm at 137.9 bar. Among these cases we selected 45 subcooled cases and did not include the 46 saturated cases. The experimental inputs are tabulated in Table D.2.

7.1.4 Weatherhead 1963

The third data set we selected is the most extensive one. It originated from Argonne National Laboratory in 1963 [43] and includes a large set of CHF results at high pressure (137.9 bar). The experiment was run with two pipe diameters, a 7.72 mm one and an 11.01 mm one. We selected 90 subcooled cases out of 232, thus excluding 139 saturated cases and 3 very high subcooling cases (> 70 K) that were outside of the applicability range of the closures we selected. Experimental inputs and CHF used in our simulation are tabulated in Table D.3.

7.2 Model formulation

The model presented in the previous chapter was developed with low pressure validation cases in mind and some of the assumptions made need to be revisited in order to extend it to high pressure conditions. We will cover changes made to each of the model's components, starting with the heat flux partition as well as the appropriate closure selection.

7.2.1 Heat flux partitioning formulation

7.2.1.1 Forced Convection

The forced convection model is unchanged as the Dittus Boelter correlation described in subsection 4.1.1 is appropriate for high pressure conditions.

$$\dot{q}_{fc}'' = h_{fc} (T_w - T_f) = h_{fc} (\Delta T_{sup} + \Delta T_{sub}) \quad (7.1)$$

$$Nu = 0.023 Re^{0.8} Pr^{0.4} \quad (7.2)$$

The Dittus Boelter correlation calls for a heated tube length/diameter ratio at least equal to 10.

$$L/D \geq 10 \quad (7.3)$$

As Table 7.2 shows below, the ratios for all three databases meet the correlations requirement and no further modification is needed.

Table 7.2: Tube Length, Diameter and L/D ratio for the three high pressure databases chosen

	Heated Length [in]	Diameter [in]	L/D [-]
Jens & Lottes	24.6	0.226	109
Hunt et al.	12	0.187	64.2
Weatherhead (7.72 mm)	18	0.304	59.2
Weatherhead (11.01 mm)	18	0.436	41.3

7.2.1.2 Sliding Conduction

Sliding conduction requires a modification to represent the high pressure conditions. The original low pressure equation (Equation 4.13) assumes the influx of water following the wake of a sliding bubble is at the bulk subcooled temperature. This was an appropriate assumption for the low pressure tests as the bubbles were large (several millimeters) and the thermal boundary layer wasn't fully developed along the heater length. However bubbles become much smaller at high pressure; down to the the order of a micrometer. At these scales it is not appropriate to assume bulk water, that can be very subcooled in certain cases, would rush in and disturb the boundary layer. Instead it is more likely to be saturated liquid from the immediate surrounding of the bubble. We can verify this hypothesis by considering that in a turbulent pipe flow, the developing length for the boundary layer is approximately:

$$L_{th} \approx 10 D \quad (7.4)$$

The Table 7.2 shows that in all three databases, this condition is met ($L/D \in [40; 110] \gg 10$). In a fully developed turbulent flow, for a liquid Prandlt number close to 1 (such as water), the turbulent thermal boundary layer thickness δ_{th} is equivalent to the viscous boundary layer δ . The turbulent velocity distribution is given by the "Law of the Wall" and the boundary layer thickness is defined as either $y^+ = 5$ or $y^+ = 30$ depending whether the buffer layer is included along with the viscous layer. y^+ is the dimensionless distance from the wall. We will consider the larger of the two definition to compare to the bubble size.

$$y^+ = \frac{yu_\tau}{\nu} \quad (7.5)$$

Where y is the distance from the wall, u_τ the shear velocity and ν the kinematic viscosity. u_τ is defined as:

$$u_\tau = \sqrt{\frac{\tau_w}{\rho_l}} \quad (7.6)$$

Where τ_w is the wall shear stress. It can be expressed using the fanning friction factor definition:

$$\tau_w = f \frac{G^2}{2\rho_l} \quad (7.7)$$

By substituting the previous two equations into the definition of y^+ , we can express the physical distance y as:

$$y = y^+ \frac{\mu}{G} \sqrt{2f} \quad (7.8)$$

When evaluated at $y^+ = 30$, we obtain the thermal boundary thickness:

$$\delta_{th} = 30 \frac{\mu}{G} \sqrt{2f} \quad (7.9)$$

The Fanning friction factor is numerically computed by solving the Colebrook-White equation [92, 93]:

$$\frac{1}{\sqrt{f}} = -3.6 \log_{10} \left[\frac{6.9}{Re} + \left(\frac{\epsilon}{3.7D} \right)^{10/9} \right] \quad (7.10)$$

Where ϵ is the surface roughness and D the inner pipe diameter. We can then compare the thermal thickness with the bubble departure diameter for each test case condition. The results are displayed in Figure 7.1.

We can see that in most cases the ratio is smaller than 1, meaning the sliding bubble will not disturb the subcooled flow in the bulk. Cases where this condition is not met ($\delta_{th}/D_d > 1$) correspond to cases with low subcooling where the difference between $T_w - T_{bulk}$ and $T_w - T_{sat}$ are small. Considering this observation, we propose to use the following expression for sliding conduction q''_{sc} in the very high pressure cases:

$$q''_{sc} = h_{fc} A_{sl} t^* f N_b'' (\Delta T_{sup}) \quad (7.11)$$

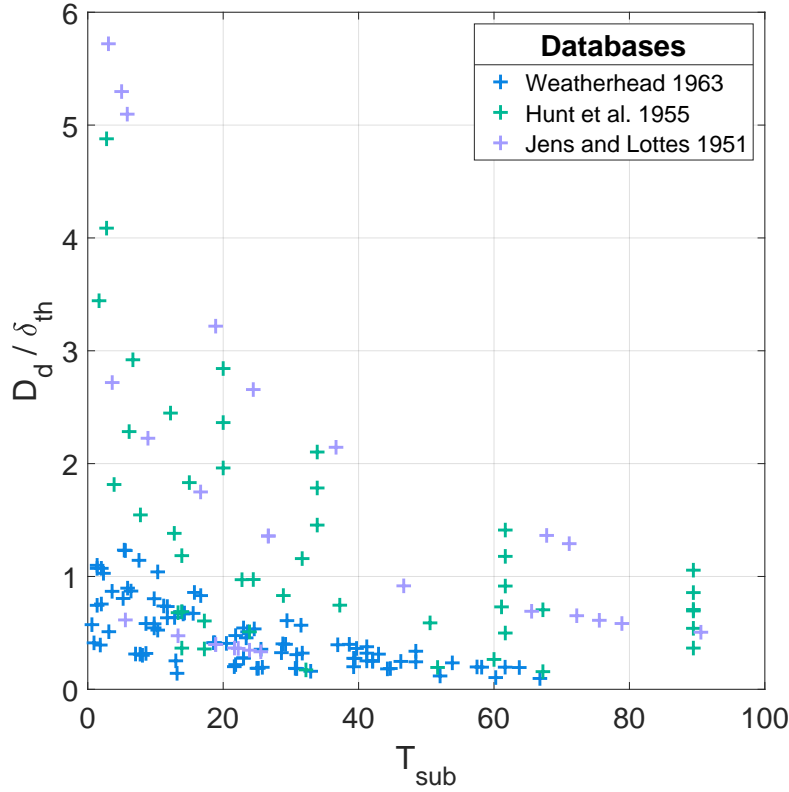


Figure 7.1: Ratio of thermal boundary layer thickness to the bubble departure diameter at CHF plotted against the bulk flow subcooling in high pressure databases

7.2.1.3 Solid Quenching

In the case of the MIT flow boiling loop, we determined in subsection 4.1.4 that the heat removed by Solid Quenching would be negligible in all conditions due to the non classic heater configuration. For the high pressure heated tubes that we are now considering, the heating element is not placed at the water interface unlike the MIT flow boiling but on the backside (direct current heating via copper bus bars). In these cases the heat must be conducted through the tube thickness in order to reach the fluid. The temperature distribution in the solid heater is thus inverted compared to the MIT flow boiling arrangement : the highest temperature is not at the flow interface like with a Sapphire-ITO heater but at the heated “backside” of the tube.

The accumulation of heat under the dry spot may not be insignificant compared with a direct contact heater like the Sapphire-ITO. We revert to using the original solid quenching equation described in subsection 4.1.4.

$$q_q'' = \rho_h c_{ph} V_q \Delta T_h f N_b'' \quad (7.12)$$

$$V_q = \frac{2}{3} \pi \left(\frac{D_{dry}}{2} \right)^3 \quad (7.13)$$

7.2.1.4 Evaporation via microlayer

At low pressures, the volume of microlayer was estimated from the experiment of Richenderfer and calibrated with a constant thickness and an extension radius equal to half of the departure diameter, creating a simple dependency on the bubble size. At high pressure conditions bubbles become very small, in the order of a micrometer at departure (Semeria [53]). Therefore the constant thickness approximation used at low pressure is fundamentally incompatible with the bubble scaling with pressure.

In order to estimate the volume of microlayer in a more rigorous way, we can leverage the DNS simulations and semi analytical work from Guion [7, 65] and Urbano [66] which provide additional microlayer insights. In particular, Guion notes the microlayer thickness scales with the square root of the Capillary number (Ca) defined as the ratio between the viscous force near the contact line and the surface tension force. He also describes the microlayer geometry and includes the tracking of the triple contact point in order to estimate the wetted area fraction underneath a bubble. These developments in the understanding of the physics controlling the microlayer formation help us revise our formulation. In order to account for the mobility of the triple contact line tracked by Guion, we will model the bubble shape near the wall surface as a truncated cone as shown in Figure 7.2. In this representation, we account for the existence of the dry spot diameter at the base of the bubble as soon as the microlayer is formed.

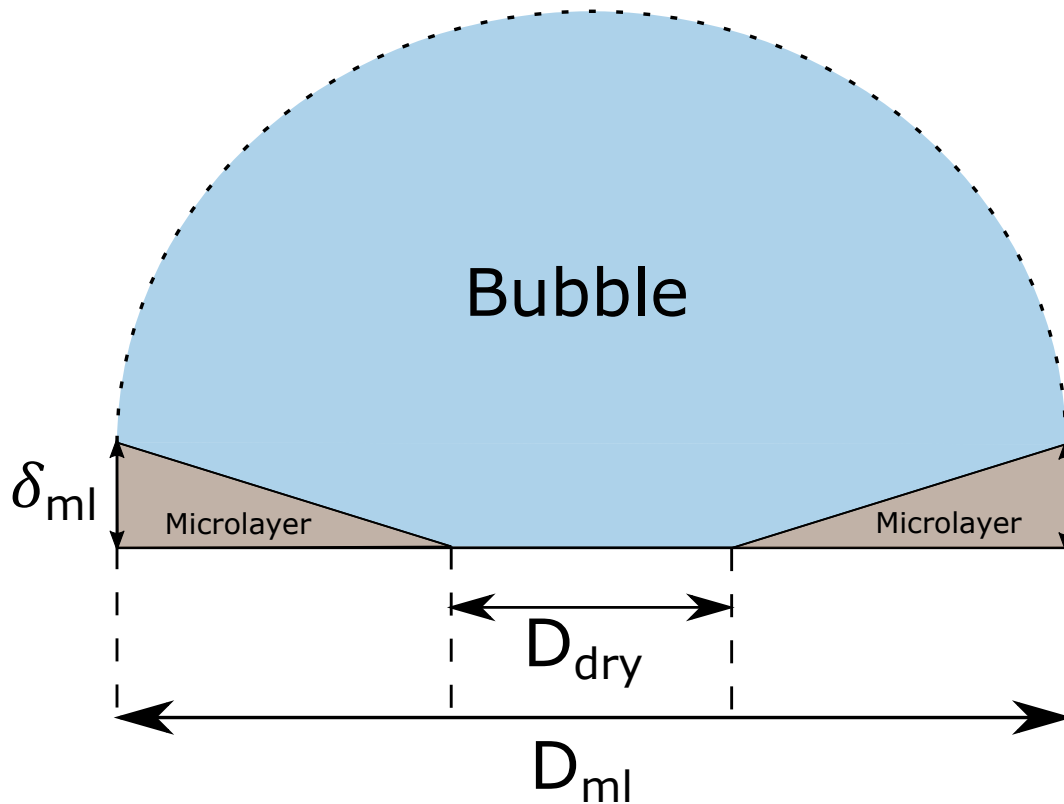


Figure 7.2: Revised shape of the liquid microlayer underneath a bubble, including the presence of a dry spot at its base

The analytical expression for the volume of microlayer is obtained by subtracting the truncated

cone volume (representing the base of the bubble) from the cylinder volume of height δ_{ml} and diameter D_{ml} :

$$V_{ml} = \pi\delta \left(\frac{D_{ml}}{2} \right)^2 - \frac{\pi}{3}\delta \left(\left(\frac{D_{dry}}{2} \right)^2 + \frac{D_{ml}D_{dry}}{4} + \left(\frac{D_{ml}}{2} \right)^2 \right) \quad (7.14)$$

Which simplifies in :

$$V_{ml} = \delta D_{ml}^2 \frac{\pi}{12} \left(2 - \left(\left(\frac{D_{dry}}{D_{ml}} \right)^2 + \frac{D_{dry}}{D_{ml}} \right) \right) \quad (7.15)$$

In order to compute the volume of microlayer through this equation, three inputs are required : δ the microlayer thickness, D_{ml} the microlayer extension diameter, D_{dry} the dry spot diameter.

$$Ca = \frac{\mu_l U_b}{\sigma} \quad (7.16)$$

$$\delta \propto \sqrt{Ca} \quad (7.17)$$

Where μ_l is the liquid viscosity, U_b the bubble growth rate (m/s) and σ the surface tension.

Following reports from Gerardi [26, 27] (albeit at low pressure), we can, in absence of better observations, express the microlayer extension radius D_{ml} as a function of the bubble departure diameter D_d :

$$D_{ml} \approx \frac{D_d}{2} \quad (7.18)$$

In a similar fashion, we can relate the dry spot diameter with the bubble diameter leveraging Guion's semi-analytical work[7, 65]. Guion maps wetted fraction contours from DNS simulations during bubble growth. The varying input parameters are the contact angle θ , the capillary number Ca and a non dimensional time t^* . Guion defines the wetted fraction as a simple expression :

$$\alpha^* = \left(1 - \frac{D_{dry}}{D_{ml}} \right) \quad (7.19)$$

The quantity $(1 - \alpha^*)$ then corresponds to the ratio of dry diameter to the microlayer diameter needed for the volume of microlayer equation. The original map used from Guion is shown in Figure 7.3. After digitizing the data and using a simple geometric scaling for the contact angle effect, the diameter ratio correlates well with the capillary number in a power law as seen in Figure 7.4.

$$\frac{D_{dry}}{D_{ml}} = 0.1237 \times (Ca)^{-0.373} \sin \theta \quad (7.20)$$

Early on, Fath and Judd[62] observed a decreasing trend for the importance of microlayer evaporation with pressure but lacked measurements at pressures higher than atmospheric. They hypothesized it would become insignificant at pressures found in PWRs (≈ 150 bar). Our modeling results are consistent with their hypothesis since they predict the disappearance of microlayer in all three databases we considered (all at pressures higher than 130 bar). Indeed, in every single case we simulated the volume of microlayer computed via Equation 7.15 is effectively zero. While direct experimental quantification is currently not possible in subcooled flow boiling at very high pressure, we will adopt this reasonable working hypothesis.

$$V_{ml} = 0 \quad (7.21)$$

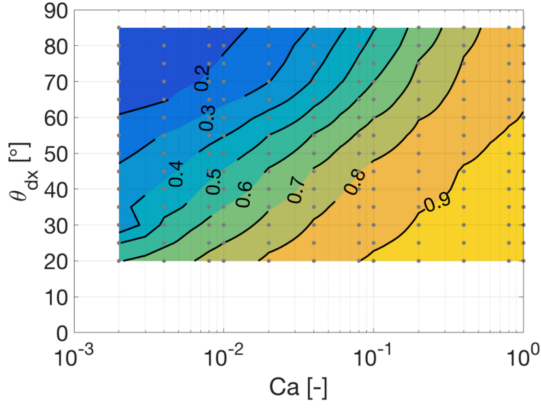


Figure 7.3: Wetted fraction underneath the bubble at $t^* = 1000$ from Guion [7]

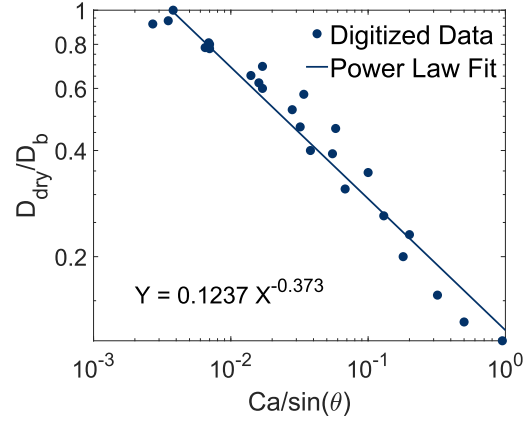


Figure 7.4: Numerical fit of data extracted from Figure 7.3

7.2.1.5 Evaporation via bubble inception

In the absence of a microlayer, the entire evaporative heat flux in the model formulation (Equation 4.20) originates from the bubble inception.

$$\dot{q}_{ev}'' = \dot{q}_{inc}'' \quad (7.22)$$

In this context, the inception diameter closure proposed in subsection 4.1.3 is not applicable. At low pressure, we related the inception diameter to a fraction of the departure diameter since the bubble growth is partially fueled by the microlayer evaporation. At very high pressure, without microlayer, bubbles will nucleate and depart as soon as their initial growth phase (inception) is over. In order to be consistent with this assumption, the inception diameter is therefore assumed to be equal to the departure diameter:

$$D_{inc} = D_d \quad (7.23)$$

7.2.1.6 Dry area Fraction

The dry area fraction relies on estimating the dry spot diameter under a single bubble. At low pressure we used estimates from pool boiling experiments and a calibration technique to set $\zeta = 0.15$. For high pressure conditions, data are not available from experiments to calibrate a constant. We can instead use the equation from the ratio of dry to microlayer diameter from Guion to introduce sensitivity to the capillary number. We can define a third scaling coefficient for the dry area fraction:

$$K_{Ca} = \frac{D_{dry}}{D_{ml}} = 0.1237 \times (Ca)^{-0.373} \quad (7.24)$$

Finally we obtain the modified dry area fraction:

$$S_{dry} = ft_g N_b'' \pi \left(\zeta K_{Ca} K_{CSR} K_\theta \frac{D_d}{2} \right) \quad (7.25)$$

7.2.2 High pressure closures

Several of the closures we relied on for the MIT flow boiling tests, cannot be applied directly to high pressure conditions. Such closures must be revisited and extended leveraging available

experimental and theoretical insights.

7.2.2.1 Bubble Departure Diameter

The bubble departure diameter is one of the biggest unknown at high pressure. No direct measurement exists for departure sizes in flow boiling. Even in pool boiling, only Kocamustafaogullari [144] claims to capture pressure scaling effects. He made use of the only pool boiling high pressure observations of departing bubbles, which were obtained by Sémeria [53], to drive a pressure scaling law.

Since Kocamustafaogullari's approach is focused on reproducing pool boiling departure sizes, his model is unable to account for flow boiling effects, which are known to be important at low pressure (see subsection 4.2.2). Additionally, Kocamustafaogullari notes that his model does not account for surface material effects such as the contact angle.

On the other hand, departure models developed for subcooled flow boiling like the one proposed by Tolubinsky and Kostanchuk [163] are calibrated for low pressure conditions:

$$D_d = D_0 \exp\left(-\frac{\Delta T_{sub}}{\Delta T_0}\right) \quad (7.26)$$

Where $D_0 = 0.6$ mm and $\Delta T_0 = 45$ K.

In order to alleviate the inherent limitations from Kocamustafaogullari's model, Kommajosyula [122] recently proposed a new correlation relying on physical trends observed in subcooled flow boiling at low pressure and incorporated the pressure scaling approach that Kocamustafaogullari proposed (using Sémeria [53] high pressure measurements). Kommajosyula proposed the following correlation:

$$D_d = 18.9 \times 10^{-6} \left(\frac{\rho_f - \rho_g}{\rho_f}\right)^{0.27} \times (Ja_{sup})^{0.78} \times (1 + Ja_{sub})^{-0.3} \times (u_{liquid})^{-0.26} \quad (7.27)$$

Where Ja_{sup} is the Jacob number for the wall superheat.

$$Ja_{sup} = \frac{\rho_f C_{p,l} \Delta T_{sup}}{\rho_g h_{fg}} \quad (7.28)$$

7.2.2.2 Nucleation Site Density

The heaters employed in the three selected test campaigns are metallic. Jens and Lottes [41] used 304 Stainless Steel while Weatherhead [43] used 347 Stainless Steel and Hunt et al. [162] used "type A" Nickel¹. In absence of additional information regarding the heaters surface state (contact angle, roughness, cavity sizes), we revert to the default closure of choice to estimate the number of nucleation sites. In this context, Hibiki and Ishii [127] is well validated and appropriate for metallic machined heaters.

¹DeBortoli doesn't specify which Nickel alloy "Type A" refers to and the original report is not accessible online. A contemporaneous ANL report [164] refers to both the 347 SS and "Type A" Nickel developed in the laboratory and provides chemical composition for the alloys. "Type A" refers to a Nickel alloy with 0.29% Manganese, 0.18% Iron, 0.05% Silicon and 0.03% Copper

7.2.2.3 Contact Angle

At atmospheric pressure, these metallic heaters usually exhibit a contact angle with water close to 90° , but it has been reported [158, 165] that the contact angle for metallic surfaces reduces with temperatures. Since the saturation temperature increases with pressure, we can assume the contact angle at very high pressure is lower than 90° . Hirose et al. [166] confirmed the surface temperature is the main factor influencing the contact angle and controlled for the influence of pressure and gas phase composition. Additionally, they showed the contact angle differences between metallic surfaces that may exist at low temperature become much more limited for surface temperatures higher than 150°C . At temperatures close to the high pressure saturation temperature ($\approx 300^\circ\text{C}$), We elected to use a contact angle of 40° for all metallic surfaces based on Hirose's findings.

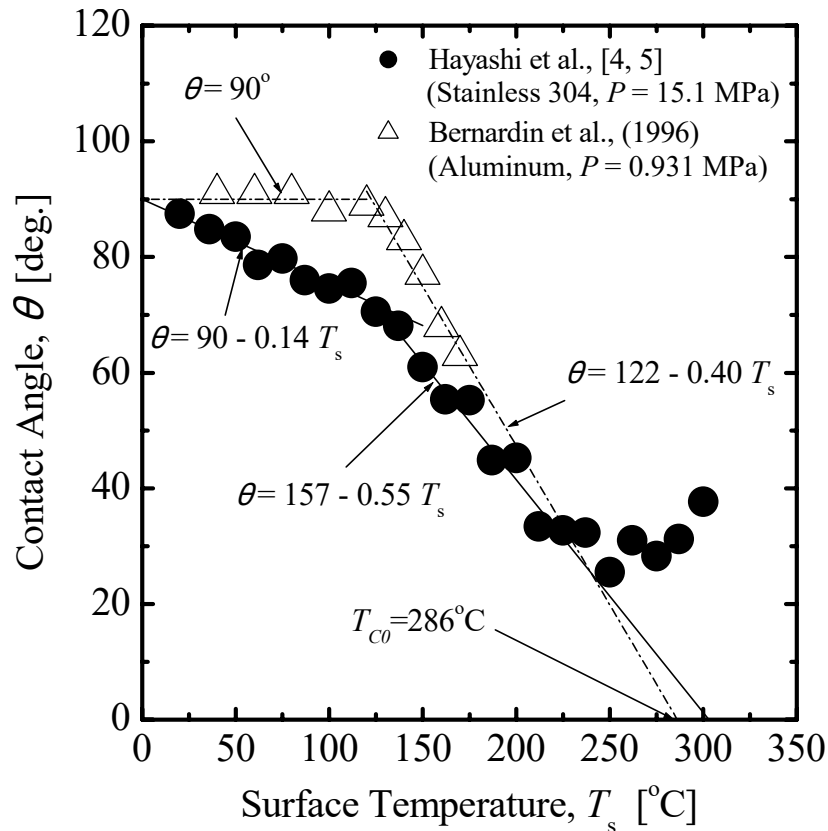


Figure 7.5: Wall temperature dependency of the contact angle. Data from Bernardin [158] and Hayashi [165] (adapted from Hirose [166])

7.2.2.4 Bubble Growth Time

Following the modifications of the microlayer and inception evaporation heat fluxes, we must also modify the growth time model for consistency. Indeed, at low pressure, the growth time model assumes the bubble growth is fueled by the microlayer evaporation. Since we modified the volume of microlayer for high pressure conditions, we effectively removed this contribution. Considering the entire growth phase of a bubble is now part of the “inception” of the bubble, the effective growth time should be much smaller than previously computed. At low pressure, the inception phase is usually neglected in the growth time computation as it represent less than $1/10^{th}$ of the overall growth phase. At high pressure, given the lack of any literature on the subject, we

hypothesized that the growth time is a fraction of the original low pressure estimation by dividing its value by a factor 10 to represent the rapid inception phase:

$$t_g = \frac{1}{10} \left(\frac{D_d}{2(K_{ML} + K_{FB})} \right)^2 \quad (7.29)$$

7.2.2.5 Bubble Wait Time

The bubble wait time is unchanged in the absence of any evidence requiring to modify the existing closure presented in subsection 4.2.4 :

$$t_w = 0.0061 \left(\frac{Ja_{sub}^{0.6317}}{T_{sup}} \right) \quad (7.30)$$

7.3 High pressure DNB prediction results

In this section we present the results obtained with the complete boiling model extension to high pressure. In doing so we assess the model's potential to be applied to nuclear fuel DNB predictions.

7.3.1 Bubble departure diameter closure high pressure optimization

During model testing, we found that the bubble nucleation site closure from Kommajosyula predicted departure sizes that were consistent with Sémeria's high pressure pool boiling observations (on the order of a few μm). However, in the flow boiling conditions we simulated and in the boiling framework we developed, these bubble sizes were found to be large enough to cause the dry area fraction to grow much faster compared to the nucleate boiling. In practice, bubbles diameters from $2\ \mu\text{m}$ to $10\ \mu\text{m}$ would cause DNB to occur so fast in the boiling curve that no significant evaporation could develop.

However, the experimental CHF data clearly shows a large enhancement compared to the forced convection heat transfer. This discrepancy between the simulation prediction and the experimental results led us to reconsider the bubble departure diameter closure. In subsection 7.2.2.1, we already discussed the lack of experimental bubble departure diameter data at high pressure, especially in flow boiling conditions. Given this observation and the fact that the bubble departure diameter closure is tied to many other closures and submodels in the framework (growth time, inception evaporation, nucleation site interaction, etc.), we propose an alternative approach.

Kommajosyula's model proposes functional expressions for the dependency of the departure diameter to multiple flow parameters. The coefficient fitting is limited by the validation data which is mainly obtained at low pressure. We propose to optimize the DNB prediction of our model on these fitting parameters in order to assess the existence of a bubble departure diameter closure which predicts the correct DNB. In this way we propose a best estimate for a bubble departure diameter closure at high pressure.

Compared to the original formulation from Kommajosyula, we altered one parameter in the original functional equation so that the velocity dependency is expressed via the non dimensional

Reynolds number instead of a dimensional velocity. The optimization process minimized a L2 error metric on the DNB prediction of the Weatherhead database (93 cases). The error metric is expressed as:

$$\|\phi\|_2 = \sum_{i=1}^N \left| \frac{(CHF_{exp,i} - \max(Q_{fc,sim,i})) - (CHF_{sim,i} - \max(Q_{fc,sim,i}))}{CHF_{exp,i} - \max(Q_{fc,sim,i})} \right|^2 \quad (7.31)$$

$$\|\phi\|_2 = \sum_{i=1}^N \left| \frac{CHF_{exp,i} - CHF_{sim,i}}{DNB_{exp,i} - \max(Q_{fc,sim,i})} \right|^2 \quad (7.32)$$

Where N is the total number of cases (here 93), $DNB_{exp,i}$ is the experimental CHF for case i , $CHF_{sim,i}$ is the model CHF prediction for case i and $\max(Q_{fc,sim,i})$ is the simulated forced convection contribution at CHF.

This error metric measures the relative error on the heat flux prediction at CHF. Instead of directly comparing DNB results, the metric we propose compares the heat flux error minus the forced convection contribution to the overall heat transfer. This enhances the relative error in cases where no significant evaporation is predicted. Indeed, if no evaporation occurs, the simulated CHF is entirely coming from forced convection, which, in some cases in the databases we consider, can reach up to 50% of the experimental CHF. Since the optimization is conducted on the bubble departure diameter, the evaporation and sliding conduction predictions are the main target.

The forced convection contribution is not sensitive to the bubble departure and should not influence the error metric. With this approach, cases where no significant evaporation is predicted (due to a poor prediction of the bubble departure diameter), yield a 100% error to the metric, no matter how significant the forced convection contribution to the CHF is.

After optimization on only one of the databases (Weatherhead [43]), we propose the following correlation:

$$D_d = 3.097 \times 10^{-5} \left(\frac{\rho_f - \rho_g}{\rho_f} \right)^{0.27} \times (Ja_{sup})^{0.78} \times (1 + Ja_{sub})^{-0.9702} \times (Re)^{-2.22 \times 10^{-4}} \quad (7.33)$$

Note : the Ja_{sup} exponent (0.78) is the only coefficient that wasn't part of the optimization search because the optimization metric relies on CHF predictions which are not tied to the accurate prediction of the wall superheat (this quantity was not measured in the experimental test campaigns). The superheat is not a factor that will influence the error metric in this process so we kept it as is. The Reynold power coefficient is very small, seemingly indicating a lack of sensitivity of the bubble departure diameter on the flow velocity at high pressure. The other two coefficients are within an order of magnitude of the original ones from Kommajosyula which lends credibility to his findings considering the large uncertainties at high pressure due to the lack of supporting validation data.

7.3.2 Model performance at high pressure

The results when using the optimized bubble departure expression are shown in the left subplot in Figure 7.6. The overall data trend is respected and the error for most cases is within $\pm 30\%$.

The Jens and Lottes and Hunt et al. databases show the largest errors. The second plot (center) in this figure represents predictions from the numerical correlation of choice for high pressure

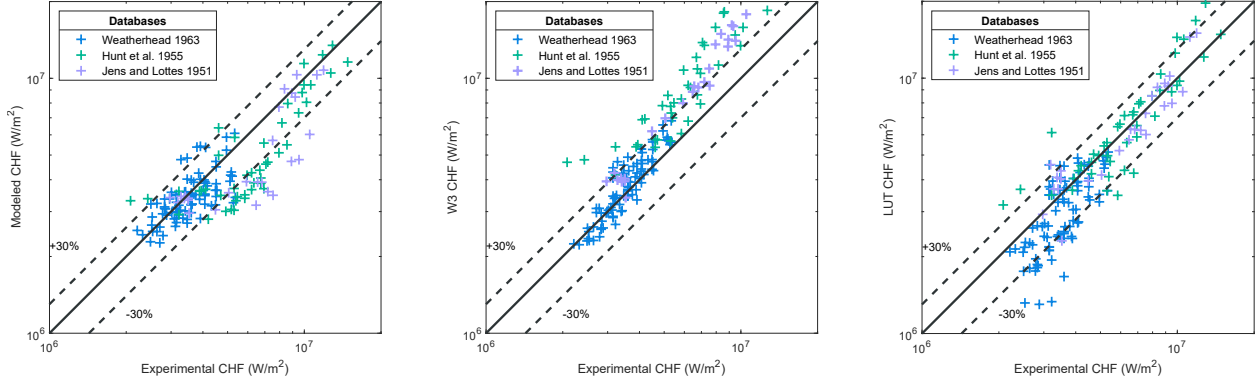


Figure 7.6: High pressure CHF predictions for three databases. Left: our model. Center: W3 correlation [97]. Right: 2006 Groeneveld Lookup Table [46]

CHF: Tong-67 [97], also referred to as the “W-3” correlation. The third plot in the figure (right) corresponds to the predictions from the 2006 Groeneveld Lookup Table [46] that were obtained using the experimental outlet quality as an input to the table (referred to as a “constant local conditions” approach by Groeneveld [46]).

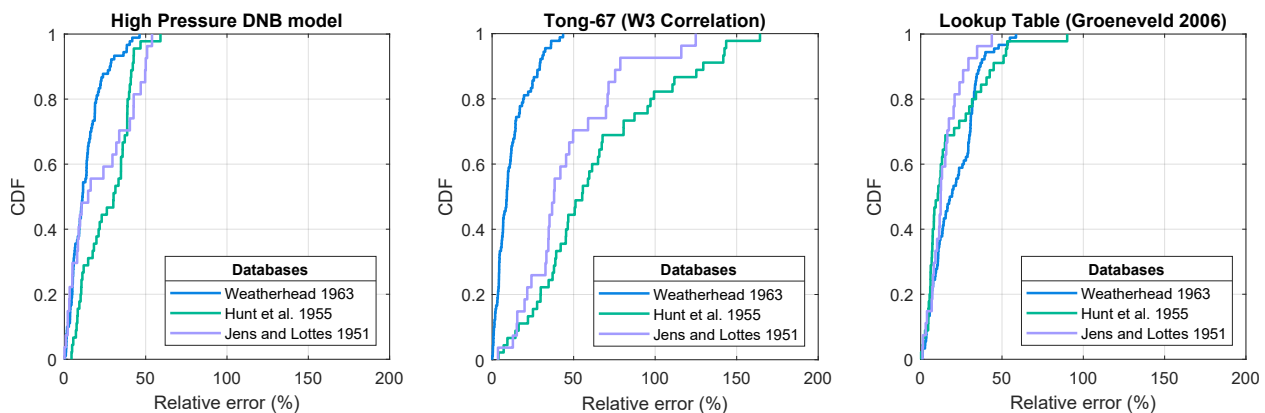
The side-by-side comparison shows interesting trends: The Weatherhead database prediction is more uniformly dispersed in our model than with the W-3 correlation but the later still includes a handful of points falling outside of the $\pm 30\%$ error range. In the end, the relative error means, medians and standard deviations are very similar as seen in Table 7.3. On the other hand, the other two databases are predicted with a larger scatter but our model predictions suffer most for CHF values between 5 to 8 MW m^{-2} while the W-3 predictions deteriorate very quickly and systematically overestimate CHF by more than 30%. The Lookup Table provides consistent predictions across all three databases although some of the most challenging Weatherhead cases are underpredicted. The Hunt et al. and the Jens and Lottes predictions from the Lookup Table are the best out of the three models.

One should note the W-3 correlation was numerically optimized over a set of 16 CHF databases including the Weatherhead database we are benchmarking against in this work. It is therefore not surprising to see the good performance of the W3 correlation when applied to this database. However, the database from Jens and Lottes uses a pipe diameter of 0.226 inch which is very close to the lower applicability limit of the W-3 correlation of 0.2 inch. The database from Hunt at al. uses 0.187 inch tubes and fall outside the applicability range of the correlation which may explain the poor predictions. In that regard, our model exhibit a more consistent behavior as our relative error standard deviation is less than half that of the W-3 correlation. When limiting our analysis to only the Weatherhead database, the difference in performance is much smaller and both median error and standard deviation are comparable.

Table 7.3: Performance comparison per database between our model and the W-3 correlation using absolute values of relative errors

	Total			Jens & Lottes			Hunt et al.			Weatherhead		
	Model	W3	LUT	Model	W3	LUT	Model	W3	LUT	Model	W3	LUT
Mean error	18.43%	31.96%	18.93%	13.28%	11.83%	20.61%	26.61%	63.70%	18.17%	21.97%	46.16%	14.62%
Median	13.85%	19.30%	13.63%	11.15%	9.03%	18.59%	30.26%	55.27%	10.53%	14.62%	38.01%	12.32%
Standard Deviation	14.50%	34.58%	14.91%	10.34%	10.47%	13.80%	14.40%	40.71%	18.70%	19.07%	29.45%	10.13%

The difference in performance between our model, the W3 correlation and the 2006 Lookup Table can also be visualized in Figure 7.7 in the form of a cumulative error distribution. We can see in this figure that our model is comparable to the Lookup Table while the W3 correlation suffers when applied to the Hunt et al. and the Jens and Lottes databases that were not included in the closure optimization. With our model, 95% of the predictions fall in within a $\pm 50\%$ error range while the W3 correlation can only achieve this level of performance when predicting the Weatherhead database. When predicting CHF's in the Hunt et al. and the Jens & Lottes databases with the W3 correlation, 95% of the points fall in a $\pm 140\%$ error range. The difference in behav-


Figure 7.7: Cumulative error distribution comparison between our model (left), the W3 correlation (center) and the 2006 Groeneveld Lookup Table (right)

ior between our model, the W3 correlation and the Lookup Table can be further investigated in Figure 7.8 by comparing the cumulative error distribution for each database as well as the overall aggregate performance when considering all data points together. The aggregate plot (top-left) shows our model outperforming the W3 correlation across the board and performing similarly to the Lookup Table. The database subplots reveal that our predictions are very similar to the W3 correlation in the Weatherhead database and better than the Lookup Table. Our model is slightly outperformed by the W3 correlation until the $\pm 25\%$ relative error band and tied if we consider larger error bands. The Lookup Table performance is poorer for all relative error bands. In this database, our model and the W3 can predict 80% of the data points within $\pm 20\%$ relative error while the Lookup Table is only able to predict 53% of the data points within the same margin of error.

The difference between our model and the W3 correlation is much more apparent in the other two subplots for the Hunt et al. (bottom-left) and Jens and Lottes (bottom-right) databases. The W3 correlation is very degraded in these two databases while our model is consistent. In the aggregate, 95% of the data points predicted by our model fall within $\pm 50\%$ of the experimental data.

In the case of the W3 correlation, 95% of the data points fall within $\pm 140\%$ of the experimental CHF.

In these two databases, the Lookup Table is able to outperform our model especially in the Hunt et al. database. When these results are combined with the Weatherhead database prediction, it allows the Lookup Table to exhibit a cumulative distribution function that is very similar to our model.

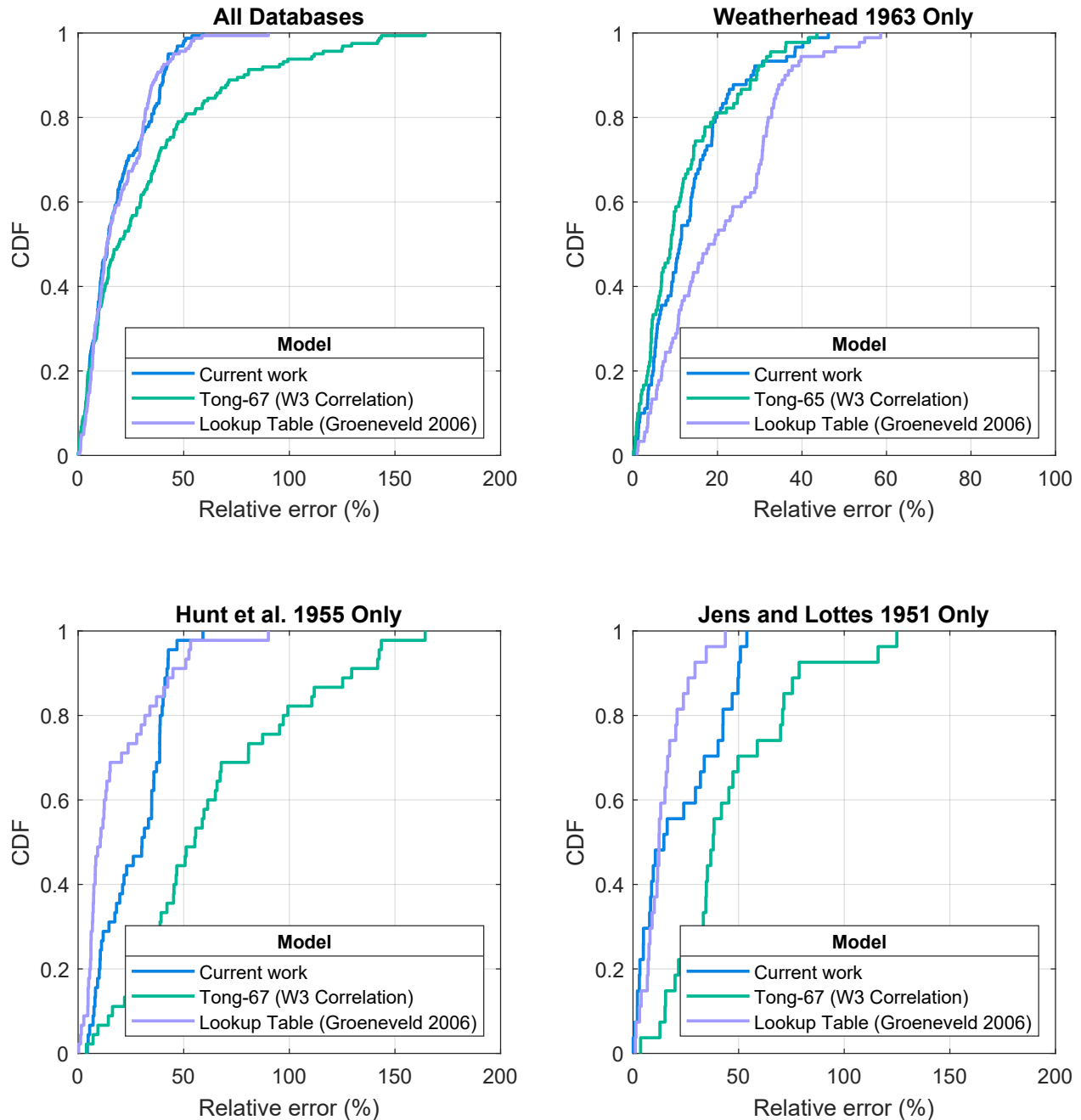


Figure 7.8: Cumulative error distribution comparison as an aggregate (top-left), and per database. Weatherhead (top-right), Hunt et al. (bottom-left) and Jens & Lottes (bottom-right)

The strength of the model's predictions when compared to the W3 correlation prediction is

especially noteworthy considering that the initial bubble departure diameter closure optimization only included the Weatherhead database. The other two databases (Hunt et al. and Jens and Lottes) cover a larger parameter space in terms of both subcooling and Reynolds number as can be seen in Figure 7.9. The model’s extrapolation outside of the parameter space it was originally optimized for is better behaved than the W3 correlation.

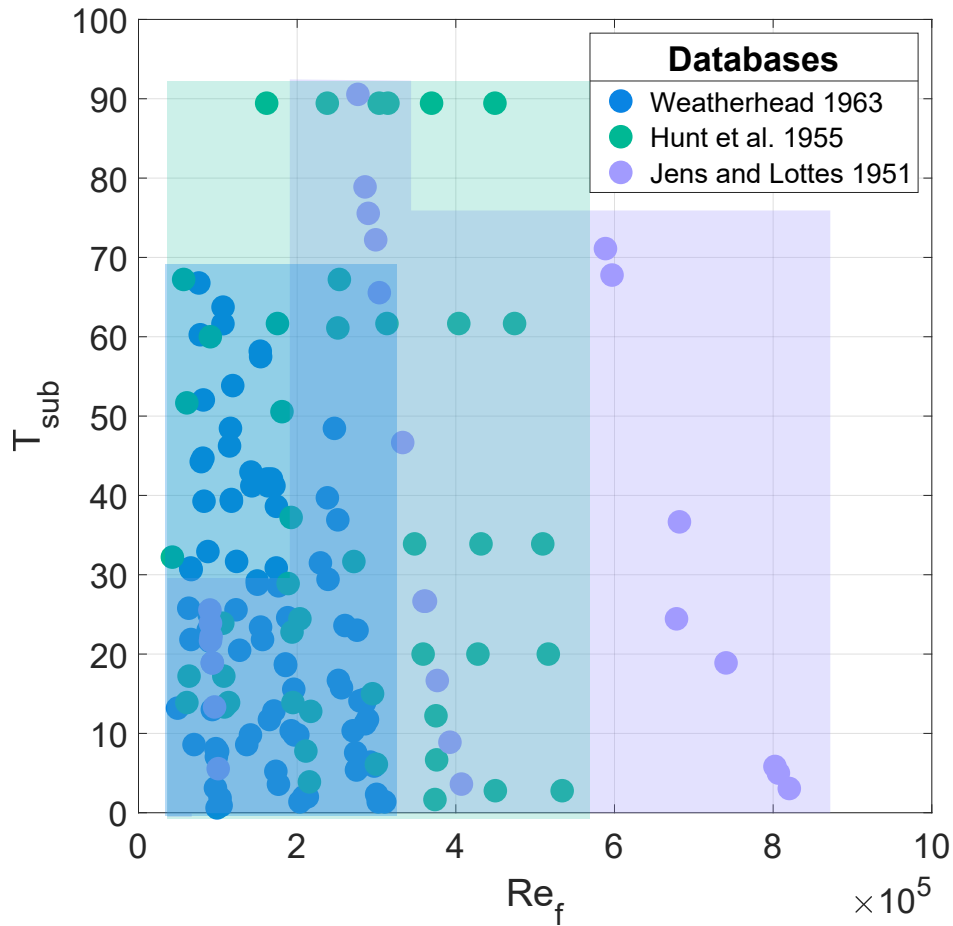


Figure 7.9: Parameter space (Reynolds number vs Subcooling) of the Weatherhead (blue), Hunt et al. (green) and Jens & Lottes (purple) databases

The cases that were the most challenging for our model (produced the largest errors) can be identified when looking conjointly at Figure 7.10 and Figure 7.11. Cases with the largest overestimation of CHF are found in the Jens and Lottes database, and correspond to the most extreme conditions encountered : lowest outlet subcooling and highest mass flux. These cases are the most challenging to predict and they stretch the validity of the fundamental boiling closures we selected.

On the other hand, cases with the largest underprediction are found in the Hunt et al. database and correspond to conditions with low subcooling (< 20 K) and the lowest mass flux ($1000 \text{ kg m}^{-2} \text{ s}^{-1}$) that are also the most challenging for the validity of the closures.

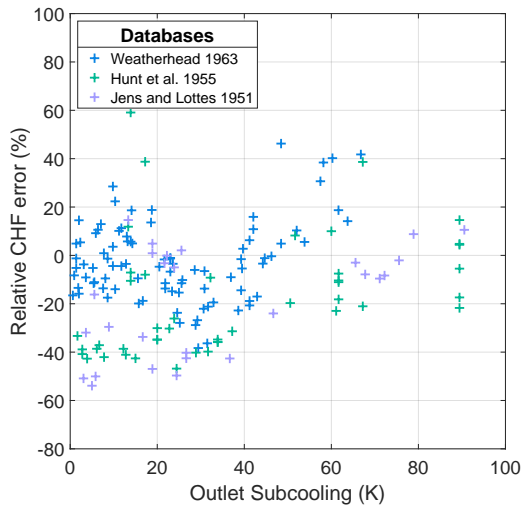


Figure 7.10: CHF relatives error for the three databases (Weatherhead, Jens and Lottes and Hunt et al.) plotted against outlet subcooling

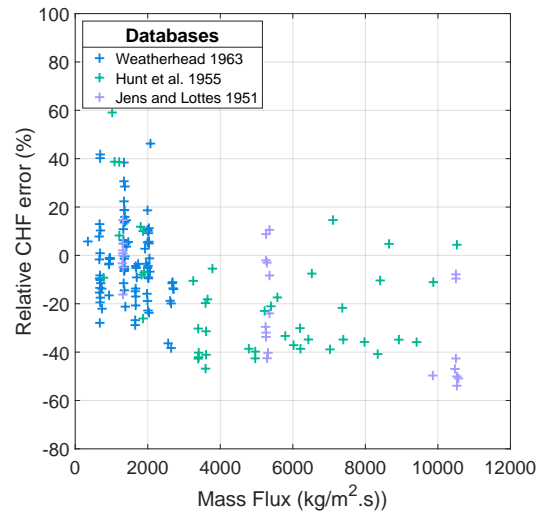


Figure 7.11: CHF relatives error for the three databases (Weatherhead, Jens and Lottes and Hunt et al.) plotted against mass flux

It would be impractical to analyze each individual case with dedicated figures. Instead we will present two cases selected on opposite edges of the parameter space in order to compare the similarities and the differences in the model's predictions. Case 26 shown in Figure 7.12 and Case 79 shown in Figure 7.13 are taken from the Weatherhead database. Their thermal hydraulic conditions as described in the following table:

Table 7.4: Input conditions and experimental CHF for Weatherhead database case 26 and 79

	Tube Diameter (mm)	Mass Flux ($\text{kg m}^{-2} \text{s}^{-1}$)	Subcooling (K)	Exp CHF (MW m^{-2})	Sim EXP (MW m^{-2})
Case 26	7.72	1397	48.5	4.50	4.52
Case 79	11.07	673	8	3.22	3.13

Our model predicts cases 26 and 79 CHF values extremely well ($< 3\%$ relative error) and show that two very different thermal hydraulic conditions can be captured. Indeed, in case 26, the high mass flux and subcooling create conditions where forced convection is a very effective heat removal mechanism; it corresponds to around 0.9 MW m^{-2} at CHF out of 4.5 MW m^{-2} total heat flux at the wall. We have also seen in chapter 3 that the transient conduction occurring during bubble sliding is actually proportional to the forced convection heat transfer coefficient: at CHF, sliding conduction is far from negligible and contributes to nearly 0.75 MW m^{-2} of the overall heat flux. Finally, evaporation is the main contributor to the heat removal with 2.9 MW m^{-2} .

We can also note that, in all of the high pressure cases, the absence of microlayer implies the entirety of the evaporation occurs via the initial "inception" phase. Compared to low pressure cases, bubble departure diameters are much smaller (less than $5 \mu\text{m}$), thus allowing the maximum number of active nucleation sites generating bubbles to grow by orders of magnitude (up to 10^{12} m^{-2}).

In case 79, the thermal hydraulic conditions are very different from case 26 as the subcooling

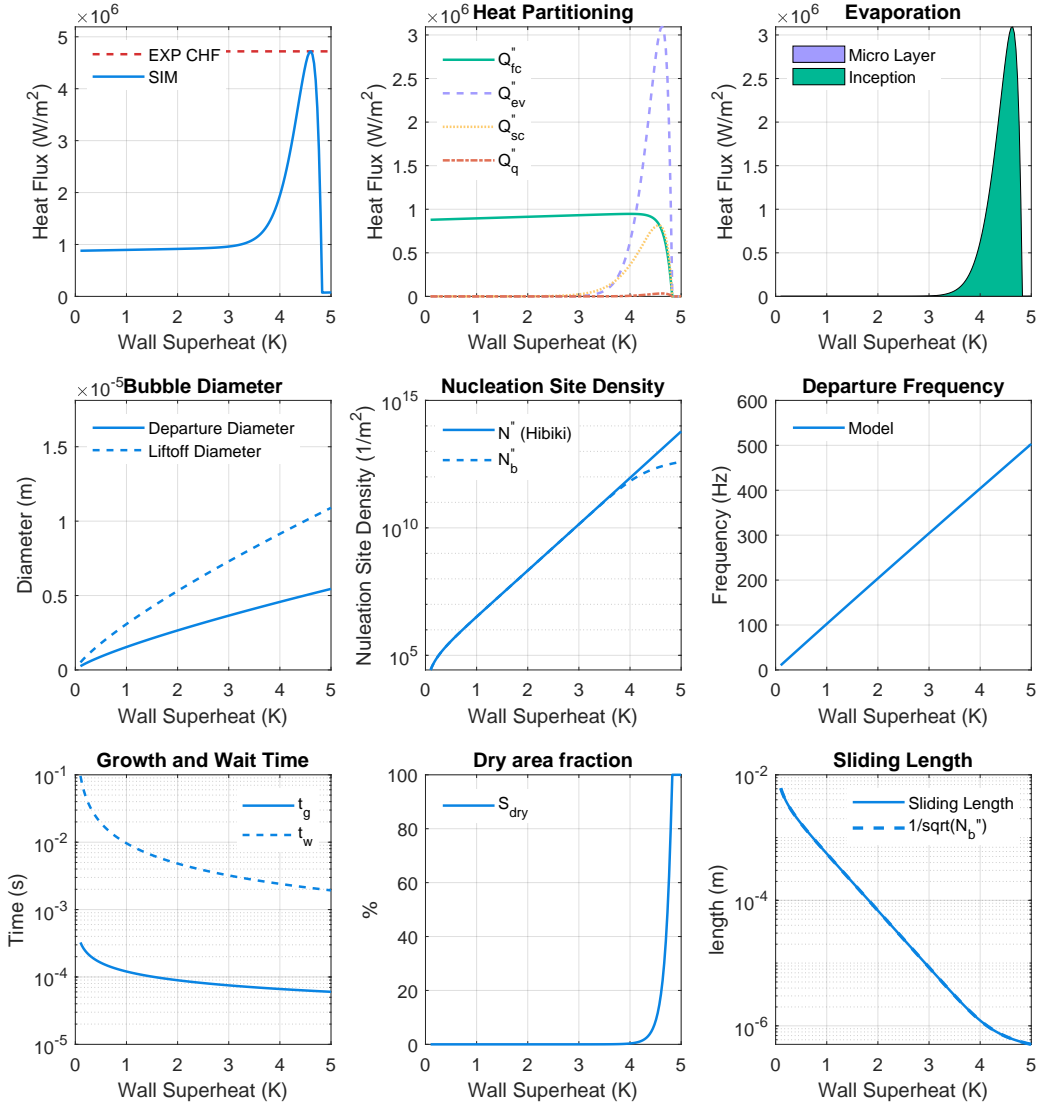


Figure 7.12: Case 26. Subplots, left to right, top to bottom : Boiling Curve and CHF. Heat flux partitions. Microlayer and Inception heat flux. Bubble departure and liftoff diameters. Nucleation Site Density. Bubble Departure Frequency. Bubble growth and wait time. Dry area fraction. Sliding length

is minimal (8 K) and the mass flux is less than half of the former case. The pipe diameter is also different (7.7 mm vs 11.1 mm) which leads to different Reynolds Number: 1.16×10^5 for case 26, 7.96×10^4 for case 79.

Contrary to case 26, forced convection in case 79 is not an efficient heat removal mechanism due to the low subcooling and low fluid velocity. Even when significant boiling occurs and many bubbles are generated, sliding conduction does not increase significantly either for the same reasons. At CHF, they each contribute to less than 0.15 MW m^{-2} . In these conditions, the bubble departure

diameter is roughly twice as large ($\approx 10 \mu\text{m}$ at CHF) thanks to the lower subcooling. Over 85% of the total heat is removed by evaporation at CHF (2.8 MW m^{-2}).

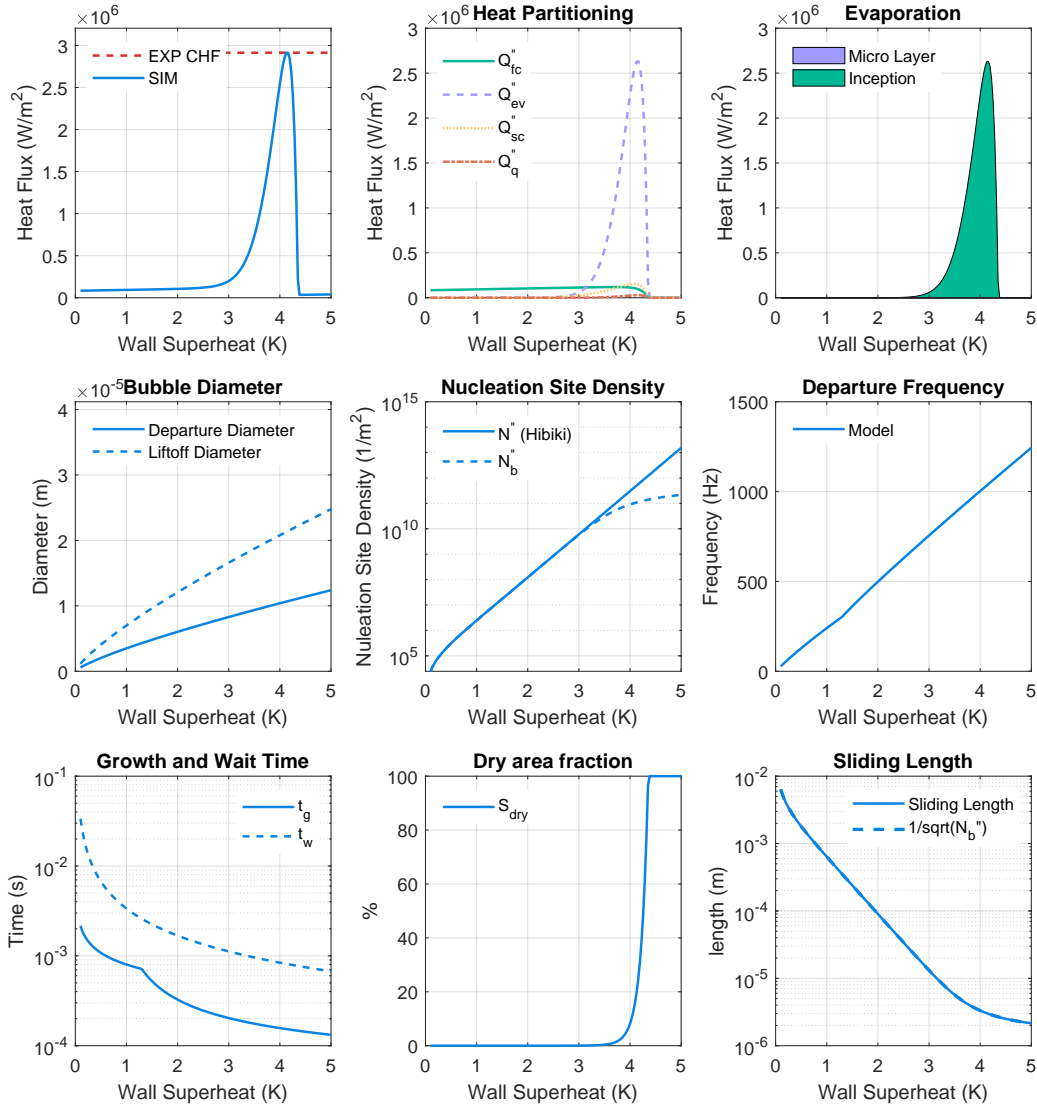


Figure 7.13: Case 79. Subplots, left to right, top to bottom : Boiling Curve and CHF. Heat flux partitions. Microlayer and Inception heat flux. Bubble departure and liftoff diameters. Nucleation Site Density. Bubble Departure Frequency. Bubble growth and wait time. Dry area fraction. Sliding length

7.4 Model parameter sensitivity analysis

In this section we will reproduce the sensitivity analysis that we developed in section 6.3, and analyze which model parameter is the most sensitive when using the model extension to high pressure. We show in Figure 7.14 the sensitivity on the same six parameters as in the low pressure

analysis : the number of nucleation sites, the bubble departure diameter, the bubble departure frequency, the bubble growth time, the dry spot coefficient (ζ) and the contact angle.

Immediately, the nucleation sites and departure frequency stand out as having almost no impact on CHF while the bubble departure diameter is the most sensitive parameter by far. This result is consistent with our modeling approach at high pressure, which relates many fundamental boiling quantities (growth and wait time, dry spot radius) to the departure diameter.

At CHF in high pressure conditions the supply of active nucleation sites far exceeds the number of bubbles that the surface can sustain. Therefore, a change in the number of active nucleation site will not impact the number of bubbles generated on the surface while a change in the departure diameter size will directly enhance or suppress the number of bubbles nucleating on the surface. This behavior was not observed in the low pressure sensitivity study due to the lower number of nucleation sites on Sapphire-ITO heaters. Finally, the growth time and contact angle are also sensitive parameters similarly to what was observed in the low pressure sensitivity analysis.

We can see in Figure 7.15 and Figure 7.16 that the sensitivity to the bubble departure diameter is high and changes of 30% can suppress or enhance CHF predictions. The effect is not symmetric as the reduction of the bubble departure diameter tends to affect the CHF much more than an enhancement of the departure diameter. This is especially visible in the cumulative error distribution functions (Figure 7.16) as the original bubble departure diameter predictions and the ones using $D_d + 30\%$ are very close while the cumulative error distribution for the $D_d - 30\%$ is much more degraded : 95% of the cases fall within a $\pm 125\%$ error band while the original diameter results send to predict 95% of the test cases within a $\pm 50\%$ error band.

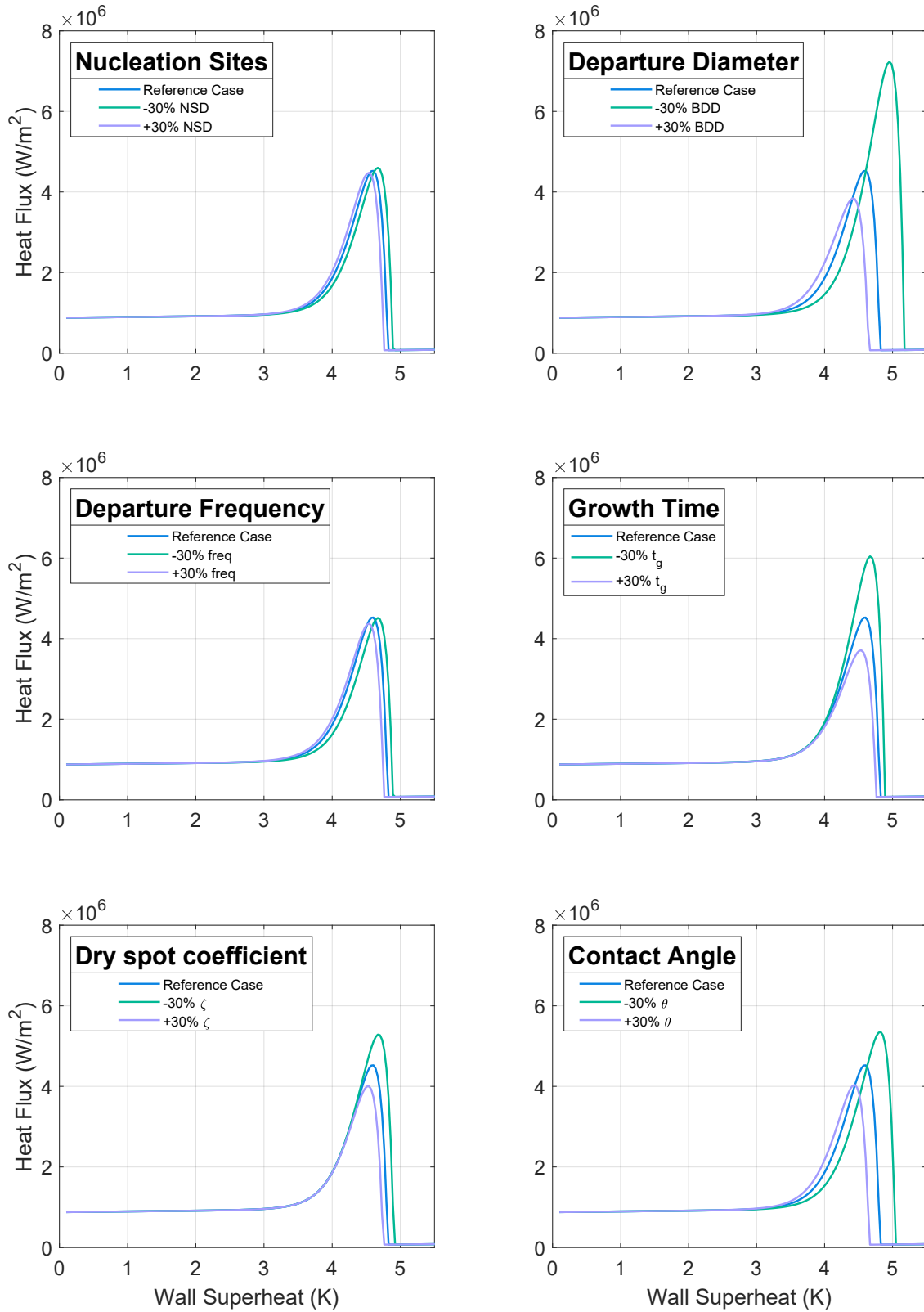


Figure 7.14: Model parameter sensitivity at high pressure conditions. Effect of a $\pm 30\%$ change in nucleation sites, departure diameter, departure frequency, growth time, dry spot coefficient and contact angle on boiling curves and CHF

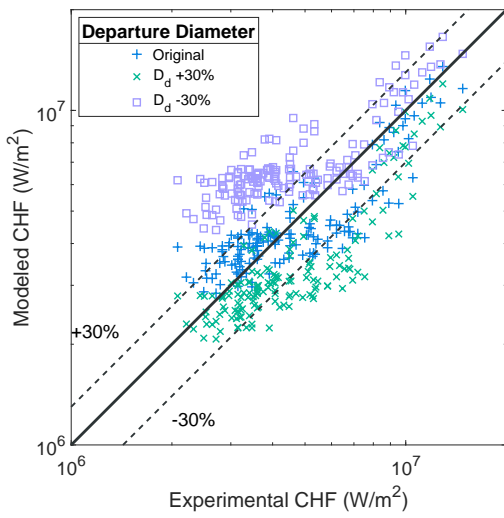


Figure 7.15: Error scatter of a $\pm 30\%$ change in departure diameter on CHF at high pressure conditions

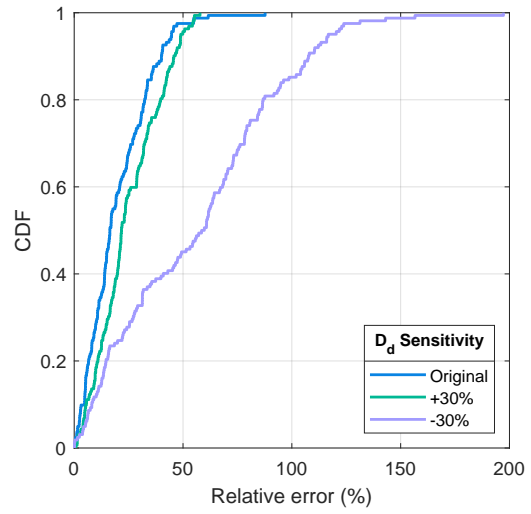


Figure 7.16: Cumulative error density functions of the bubble departure diameter sensitivity analysis. Original Diameter, +30%, -30%

7.5 Prediction of high pressure behavior of advanced fuel

In order to enhance the DNB limit of a heater, proposals exist to engineer surfaces to promote the number of nucleation sites or to modify the wettability by creating “super-hydrophilic” surfaces. As of now, the enhancements have been observed at low pressures and in most cases for pool boiling conditions. It is still unclear whether such modifications to the surfaces will effect CHF for high pressure flow boiling conditions. Having assembled an approach that includes the impact of surface characteristics on the boiling curves and CHF, we can leverage it to provide insights on the expected high pressure performance.

Figure 7.17 reports the effect on the model’s CHF predictions when the nucleation site density is enhanced by 10 compared to the baseline correlation. The x-axis is the original model value while the y-axis coordinate is the resulting CHF if nucleation sites are enhanced. The model predicts a reduction in CHF of less than 30% across the board. Although counter intuitive, the mechanism by which this result is explained is simple. As the number of active cavities on the surface is enhanced, more bubbles interact and suppress sites, thus enhancing the dry area fraction. In the end, the dry area enhancement is dominant and provokes a reduction in CHF.

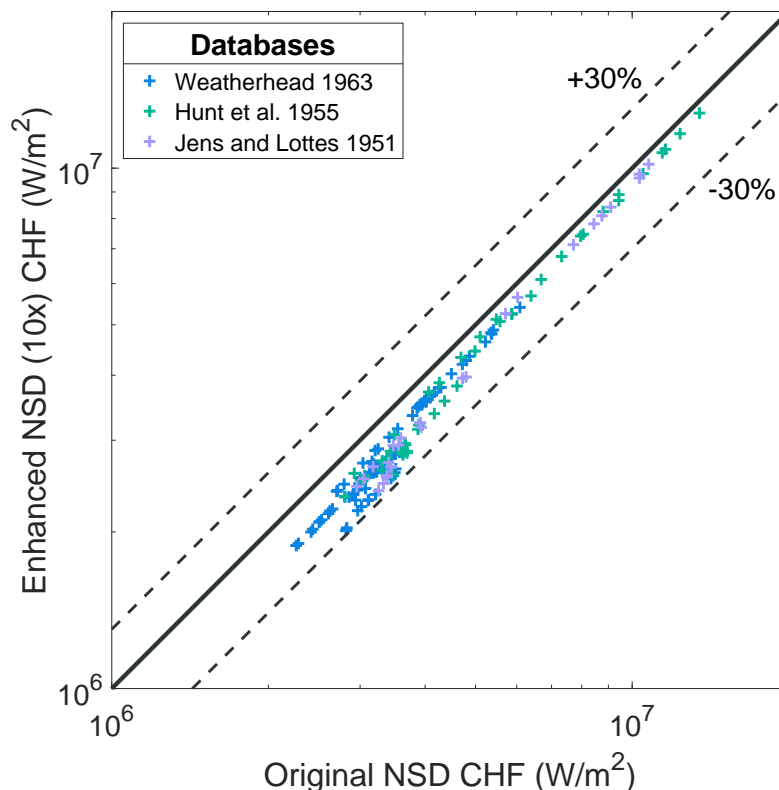


Figure 7.17: Nucleation site density sensitivity : original CHF predictions (x-axis) plotted against the same model with modified nucleation site density (10x original) (y-axis)

Another possibility is to modify the surface contact angle to a small value to render the surface hydrophilic and promote the wettability. This effectively reduces the dry area on the surface and can

delay the boiling crisis allowing a higher CHF. In this case, we use a contact angle of 20° consistently with the lower range in Guion's study [7, 65] to estimate the potential enhancements associated with this surface modification. The model predicts substantial CHF enhancements, up to about 50% compared to the baseline cases using a 40° contact angle as shown in Figure 7.18. While the scale of the enhancement is probably magnified by the lack of experimental investigations on the role of wettability at these high pressure conditions. Nonetheless, when considering engineered surfaces, the use of a more hydrophilic surface (lower contact angle) appears to be a more promising avenue for DNB enhancement than the altering the cavity distribution in order to control the nucleation site density.

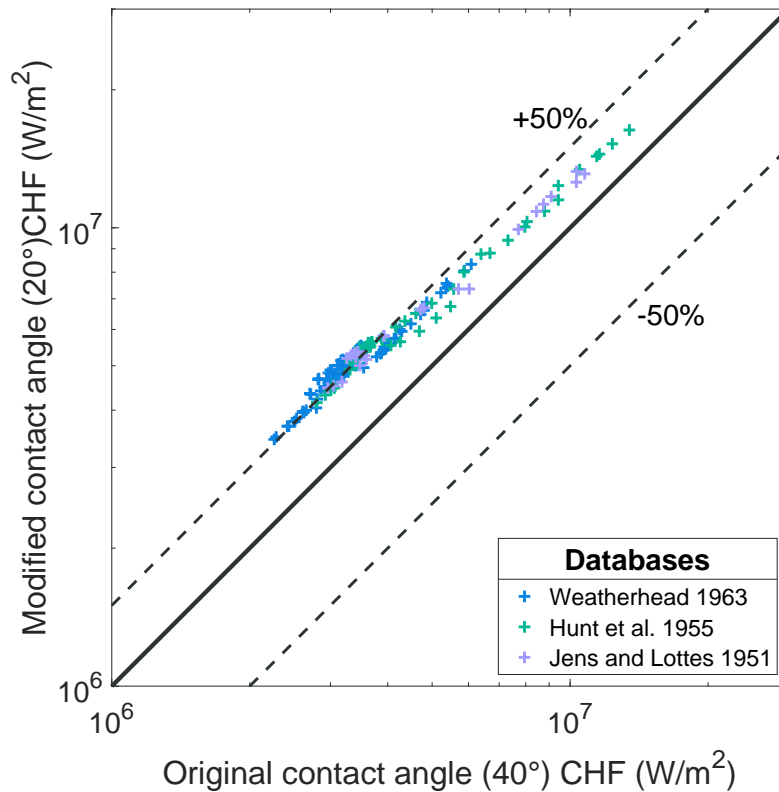


Figure 7.18: Contact angle sensitivity : original CHF predictions (40°)(x-axis) plotted against the same model with modified contact angle (20°) (y-axis)

7.6 Conclusion and insights summary

In this chapter we extended the model to high pressure conditions representative of PWR operation. At high pressure, we have to rely on several assumptions and extend closures and correlations to conditions outside of their original applicability range.

Despite these limitations, we propose an approach to predict CHF at high pressure. To do so, we modified the partitioning equations to account for dry area and microlayer volume scaling with the capillary number. We also modified the growth time due to the absence of microlayer.

The Dittus-Boelter forced convection closure proposed in this chapter offers an application range limited to the simple water pipe flows found in the benchmarking databases. The model extension to other working fluids and geometries would require the selection of a more generally applicable correlation. Alternatively, the CFD implementation of the model could eliminate the limitations stemming from the single phase forced convection heat transfer estimations.

In the nucleate boiling regime, since the fundamental boiling quantities are all connected to the bubble departure sizes, we optimized the closure given by Kommajosyula minimizing the overall error in the Weatherhead database.

The results we presented reproduce the physical trends correctly and with reasonable accuracy across all three databases. Cases with widely different thermal hydraulic conditions can be predicted with a single model. The global performance of our model is comparable to the *W-3* correlation when applied to the Weatherhead database and considerably better when compared to all three databases.

The sensitivity analysis we conducted revealed the bubble departure diameter is the most sensitive parameter in the model. A departure diameter reduced by 30% yields a significant degradation in the overall CHF prediction : The 95% cumulative distribution function jumped from 50% relative error to 140%. On the other hand, the overestimation of the departure diameter by 30% leads to a more limited effect : despite worse results, the 95% cumulative distribution function remained similar to the optimum result (50% relative error).

The new approach is fundamentally different from existing correlations as it can reproduce boiling CHF from a first principle based representation, but its generalization is limited by the closures that are necessary. Therefore, the ongoing challenges at high pressure only reinforce the need for a new generation of experimental test campaigns able to generate local high quality boiling data. They will be necessary in order to improve the prediction capabilities of the model. Fundamental boiling quantities like bubble departure diameters, frequency and growth time are still uncertain at reactor conditions and improved models and closures will have a direct impact on our ability to predict DNB.

Conclusion and future work

7.7 Summary

DNB modeling is instrumental for improving boiling heat transfer in engineering applications. The phenomenon has been studied for decades but no single model is widely accepted. Recent improvements in imaging techniques have opened new horizons for thermal hydraulics researchers to consider DNB as a local phenomenon occurring at the boiling surface at a microscale rather than in the flow above it. This change of paradigm is still recent and experimental techniques are constantly improving.

We have developed a complete DNB model based on an experimental consensus that the boiling crisis in subcooled flow boiling is related to the irreversible growth of dry area on the surface. We hypothesize that the heat flux partitioning between wetted and dry areas is key to triggering DNB as areas in direct contact with vapor limit the amount of heat that can be efficiently removed by nucleate boiling. This approach to tracking the dry and wetted area fraction on the surface to distribute heat fluxes is akin to a first principle energy balance.

With this simple but powerful idea we set out to demonstrate the potential of this new approach to DNB inception. We were successful in demonstrating the capability of the model to reproduce physical trends and capture surface effects such as wettability which no CHF model had included until now.

Inspired by promising initial results we have developed a consistent boiling framework that includes a nucleate boiling model inspired by Gilman [117] and a method to track the dry area fraction during boiling. We then validated the complete model against high quality experimental data from Richenderfer [5] and Bucci [34]. The resulting CHF predictions were able to capture both subcooling and mass flux trends.

Acknowledging that DNB predictions are especially needed for industrial high pressure applications we focused our effort to extending the model to these conditions. Several components of the model had to be altered leveraging the state of the art understanding of nucleate boiling at high pressure. Overall, the lack of a generally applicable bubble departure diameter model compelled us to optimize this closure component in order to demonstrate the applicability of our approach. The resulting model performance is comparable to the 2006 Lookup Table from Groeneveld and better than the W3 correlation in a large, high pressure benchmark consisting of 165 conditions from three databases. Finally we explored how surface engineering could affect CHF at high pressure. We considered two avenues for modified heater surfaces: nucleation site density enhancement and superhydrophilic surface.

Parameter sensitivity analysis was conducted at both low and very high pressure in order to evaluate the most critical inputs and parameters in the model. We evaluated six main variables and concluded that at low pressure the growth time is the most sensitive parameter. At high pressure, bubble departure diameter is the most sensitive input. In all cases the nucleation site density was

the least sensitive parameter.

7.8 Future Work

Suggestions for future work can be divided in three paths which should (and probably will) be explored simultaneously: experiments, model development and model validation.

First, new high fidelity experimental flow boiling and CHF databases should be assembled in order to continue improving our boiling understanding. Higher acquisition frequency and resolution, advanced image post-processing techniques and larger test conditions are all needed in order to help further our understanding of boiling. As we've seen in chapter 7, little is known about fundamental boiling quantities at high pressure. Improvements in experimental techniques can be categorized in four groups:

- Instrumentation upgrades such as higher framerate infrared cameras (5/10 kHz) associated with a resolution increase will enable the tracking of smaller and faster bubbles which are found in higher pressure and subcooling conditions.
- Larger test matrices will help further the assessment of the DNB model trends with the flow parameters (subcooling, mass flux) as well as the pressure scaling.
- Longer heating section would be suitable in order to minimize the effects due to the developing thermal boundary layer such as the strong temperature gradient along the axis of the flow.
- Better post-processing in order to accurately track the dry spots, heat partitions (in particular due to sliding and evaporation) and the fundamental boiling quantities (growth time, departure period, bubble sizes, nucleation sites) in more cases up to CHF.

The second aspect to envision in the future is the continuous improvements and modifications to the boiling framework. Almost each individual piece of the model we proposed could be revisited and improved, simplified or modified. Just as we proposed simplifications to Gilman's original heat flux partitioning model and Kommajosyula's closure improvements, several more iterations will be required to generalize and extend the model. Parts of the framework that were modeled with simple approaches due to the lack of experimental data should be revised as knowledge progresses. In particular we can note:

- The extension to saturated flow boiling as the current model is not sensitive to effects related to the flow quality and regime above the surface. In its current state the model is only validated for subcooled flow boiling.
- The extension to non vertical heater. In particular, horizontal heaters and inverted heating surfaces create challenges when considering the modeling approach for bubble nucleation, growth and departure. Specific submodels should be proposed for these conditions in order to extend the model applicability.
- The improvement of the heat partitioning models. For example, the actual quenching and sliding heat flux from the experiments could allow finer validation of the heat partitioning model.

- The revision of dry spot model, especially at very low contact angle ($\leq 5^\circ$) where the current modeling will predict very large CHF due to the quasi absence of dry area. The experimental confirmation of some of the dry area modeling modifications we proposed, such as the absence of microlayer at prototypical PWR conditions, would be a major breakthrough reinforcing the strength of our model.
- The inclusion and testing of alternative approaches to modeling the dry area fraction. For example, Zhang, Seong and Bucci [167] recently proposed a percolation approach to tracking the dry area fraction and its growth which offers a more microscopic approach to the modeling.
- The extension of the model to post-CHF conditions. The model structure is already designed to be able to capture the transition to post-CHF film boiling conditions. Dedicated studies could investigate the boiling crisis transition itself which is rarely captured by existing models.

Finally, the third aspect of future efforts concerns validation studies. As more high quality data becomes available, extended validation studies should be carried out in order to assess the performances and limitations of the model. As it stands, the model could be implemented as-is in a lump parameter code with ease but its real potential is in CFD. Indeed, just as Gilman's original work on nucleate boiling, our model is built in such a way it can easily be implemented as a subgrid boiling model for a CFD code. Initial testing of CFD implementation with an early DNB model was conducted in collaboration with Kommajosyula and showed results consistent with our 0-D numerical implementation in simple cases. This effort should be revisited in the near future with the now complete DNB model. The following development steps could be envisioned:

- Implement the current model equations in a multiphase CFD code.
- Develop efficient numerical solutions to treat implicit equations requiring iterative solving (statistical nucleation site interaction, bubble departure diameter force balance model) in order to speed up simulation time and minimize CPU overhead.
- Benchmark the CFD implementation against the databases presented in this thesis.
- Extend the model to complex geometries that are the most challenging to non-CFD DNB models (e.g. 5×5 fuel bundles with flow mixing vanes).

Bibliography

- [1] T. G. Theofanous, J. P. Tu, A. T. Dinh, and T. N. Dinh, "The Boiling Crisis Phenomenon Part I: nucleation and nucleate boiling heat transfer," *Experimental Thermal and Fluid Science*, vol. 26, pp. 775–792, 2002.
- [2] T. G. Theofanous, T. N. Dinh, J. P. Tu, and A. T. Dinh, "The boiling crisis phenomenon part II: Dryout dynamics and burnout," *Experimental Thermal and Fluid Science*, vol. 26, no. 6-7, pp. 793–810, 2002.
- [3] J. Jung, S. J. Kim, and J. Kim, "Observations of the Critical Heat Flux Process During Pool Boiling of FC-72," *Journal of Heat Transfer*, vol. 136, no. 4, p. 041501, 2013.
- [4] S. Jung and H. Kim, "Observation of the mechanism triggering critical heat flux in pool boiling of saturated water under atmospheric pressure," *International Journal of Heat and Mass Transfer*, vol. 128, pp. 229–238, 2019.
- [5] A. J. Richenderfer, *Experimental Study of Heat Flux Partitioning in Pressurized Subcooled Flow Boiling*. Phd, Massachusetts Institute of Technology, 2018.
- [6] A. Richenderfer, A. Kossolapov, J. H. Seong, G. Saccone, E. Demarly, R. Kommajosyula, E. Baglietto, J. Buongiorno, and M. Bucci, "Investigation of subcooled flow boiling and CHF using high-resolution diagnostics," *Experimental Thermal and Fluid Science*, vol. 99, no. June, pp. 35–58, 2018.
- [7] A. N. Guion, *Modeling and Simulation of Liquid Microlayer Formation and Evaporation in Nucleate Boiling using Computational Fluid Dynamics*. Ph.d., Massachusetts Institute of Technology, 2017.
- [8] J. Speth, "When Did Humans Learn to Boil?," *PaleoAnthropology*, pp. 54–67, 2015.
- [9] B. Woodcroft, *The Pneumatics of Hero of Alexandria: From the Original Greek*. London, UK: Charles Whittingham, 1851.
- [10] G. Yadigaroglu, "CMFD and the critical-heat-flux grand challenge in nuclear thermal-hydraulics - A letter to the Editor of this special issue," *International Journal of Multiphase Flow*, vol. 67, pp. 3–12, dec 2014.
- [11] N. Alleborn, R. Reinders, S. Lo, and A. Splawski, "Analysis of two-phase flows in pipes and subchannels under high pressure," in *Proc. of ExHFT-7, Krakow, Poland, June*, (Krakow, Poland), 2009.
- [12] L. Vyskocil and J. Macek, "CFD simulation of critical heat flux in a tube," in *Proc. CFD for Nuclear Reactor (CFD4NRS-3)*, (Bethesda, MD USA), pp. 1–13, 2010.
- [13] J. Yan, P. Yuan, P. F. Joffre, Z. E. Karoutas, and L. D. S. III, "CHF Model Development in Westinghouse," in *International seminar on Subchannel Analysis CFD modeling and verification, CHF experiment and benchmarking (ISACC-2013)*, (Xian, China), pp. 3–11, 2013.

- [14] J. Yan, L. D. S. III, and Z. Karoutas, "Departure From Nucleate Boiling Modeling Development for PWR Fuel," in *Proceedings of the 2013 21st International Conference on Nuclear Engineering (ICONE21)*, (Chengdu, China), pp. 1–6, 2013.
- [15] R. Zhang, T. Cong, W. Tian, S. Qiu, and G. Su, "Prediction of CHF in vertical heated tubes based on CFD methodology," *Progress in Nuclear Energy*, 2014.
- [16] Z. E. Karoutas, Y. Xu, L. D. Smith, P. F. Joffre, and Y. Sung, "Use of Cfd To Predict Critical Heat Flux in Rod Bundles," *Proceedings of 16th International Topical Meeting on Nuclear Reactor Thermohydraulics (NURETH-16)*, pp. 7609–7621, 2015.
- [17] S. Mimouni, C. Baudry, M. Guingo, J. Lavieville, N. Merigoux, and N. Mechitoua, "Computational multi-fluid dynamics predictions of critical heat flux in boiling flow," *Nuclear Engineering and Design*, vol. 299, pp. 28–36, 2016.
- [18] S. Mimouni, W. Benguigui, J. Lavieville, N. Merigoux, M. Guingo, C. Baudry, and O. Marfaing, "New nucleation boiling model devoted to high pressure flows," in *proc. 9th International Conference on Multiphase Flow (ICMF-2016)*, (Firenze, Italy), pp. 4–9, 2016.
- [19] S. S. Kutateladze, "On the transition to film boiling under natural convection," *Kotloturbostroenie*, vol. 3, pp. 10–12, 1948.
- [20] S. S. Kutateladze, "A hydrodynamic theory of changes in a boiling process under free convection," *Izvestia Akademia Nauk Otdelenie Tekhnicheski Nauk*, vol. 4, pp. 529–536, 1951.
- [21] N. Zuber, *Hydrodynamics Aspects of Boiling Heat Transfer*. Phd, University of California, Los Angeles, 1959.
- [22] J. Weisman and B. Pei, "Prediction of Critical Heat Flux in flow boiling at low qualities," *International Journal of Heat and Mass Transfer*, vol. 26, pp. 1463–1477, oct 1983.
- [23] Y. Katto, "A physical approach to critical heat flux of subcooled," *International Journal of Heat and Mass Transfer*, vol. 33, no. 4, pp. 611–620, 1990.
- [24] G. P. Celata, M. Cumo, and A. Mariani, "Assessment of correlations and models for the prediction of CHF in water subcooled flow boiling," *International Journal of Heat and Mass Transfer*, vol. 37, no. 2, pp. 237–255, 1994.
- [25] G. Celata, M. Cumo, Y. Katto, and A. Mariani, "Prediction of the critical heat flux in water subcooled flow boiling using a new mechanistic approach," *International Journal of Heat and Mass Transfer*, vol. 42, pp. 1457–1466, apr 1999.
- [26] C. D. Gerardi, *Investigation of the Pool Boiling Heat Transfer Enhancement of Nano- Engineered Fluids by means of High-Speed Infrared Thermography*. PhD thesis, Massachusetts Institute of Technology, 2009.
- [27] C. Gerardi, J. Buongiorno, L. wen Hu, and T. McKrell, "Study of bubble growth in water pool boiling through synchronized, infrared thermometry and high-speed video," *International Journal of Heat and Mass Transfer*, vol. 53, no. 19-20, pp. 4185–4192, 2010.
- [28] C. Gerardi, J. Buongiorno, L. wen Hu, and T. Mckrell, "Infrared thermometry study of nanofluid pool boiling phenomena," *Nanoscale Research Letters*, vol. 6, no. 1, pp. 1–17, 2011.

- [29] H. Kim and J. Buongiorno, "Detection of liquid-vapor-solid triple contact line in two-phase heat transfer phenomena using high-speed infrared thermometry," *International Journal of Multiphase Flow*, vol. 37, no. 2, pp. 166–172, 2011.
- [30] S. Jung and H. Kim, "An experimental method to simultaneously measure the dynamics and heat transfer associated with a single bubble during nucleate boiling on a horizontal surface," *International Journal of Heat and Mass Transfer*, vol. 73, pp. 365–375, 2014.
- [31] S. Jung and H. Kim, "An experimental study on heat transfer mechanisms in the microlayer using integrated total reflection, laser interferometry and infrared thermometry technique," *Heat Transfer Engineering*, vol. 36, no. 12, pp. 1002–1012, 2015.
- [32] S. Jung and H. Kim, "Hydrodynamic formation of a microlayer underneath a boiling bubble," *International Journal of Heat and Mass Transfer*, vol. 120, pp. 1229–1240, 2018.
- [33] B. A. Phillips, *Experimental Investigation of Subcooled Flow Boiling Using Synchronized High Speed Video, Infrared Thermography, and Particle Image Velocimetry*. PhD thesis, Massachusetts Institute of Technology, 2014.
- [34] M. Bucci, A. Richenderfer, G. Y. Su, T. McKrell, and J. Buongiorno, "A mechanistic IR calibration technique for boiling heat transfer investigations," *International Journal of Multiphase Flow*, vol. 83, pp. 115–127, 2016.
- [35] M. A. Amidu, S. Jung, and H. Kim, "Direct experimental measurement for partitioning of wall heat flux during subcooled flow boiling: Effect of bubble areas of influence factor," *International Journal of Heat and Mass Transfer*, vol. 127, pp. 515–533, 2018.
- [36] S. Nukiyama, "The maximum and minimum values of the heat Q transmitted from metal to boiling water under atmospheric pressure," *Japan Society of Mechanical Engineers*, vol. 37, pp. 367–374, 1934.
- [37] S. Nukiyama, "The maximum and minimum values of the heat Q transmitted from metal to boiling water under atmospheric pressure," *International Journal of Heat and Mass Transfer*, vol. 9, no. 12, pp. 1419–1433, 1966.
- [38] J. G. Leidenfrost, *De aquae communis nonnullis qualitatibus tractatus*. Ovenius, 1765.
- [39] J. G. Leidenfrost, "On the fixation of water in diverse fire," *International Journal of Heat and Mass Transfer*, vol. 9, pp. 1153–1166, 1966.
- [40] W. H. McAdams, W. E. Kennel, C. S. Minden, R. Carl, P. M. Picornell, and J. E. Dew, "Heat Transfer at High Rates to Water with Surface Boiling," *Industrial & Engineering Chemistry*, vol. 41, no. 9, pp. 1945–1953, 1949.
- [41] W. H. Jens and P. A. Lottes, "Analysis of heat transfer, burnout, pressure drop and density data for high-pressure water," tech. rep., Naval Reactor Division, Argonne National Laboratory, Chicago, IL, 1951.
- [42] R. A. DeBortoli, S. J. Green, S. W. LeTourneau, M. Troy, and A. Weiss, "Forced-Convection Heat Transfer Burnout Studies for Water in Rectangular Channels and Round Tubes at Pressures Above 500 psia," tech. rep., U.S. Atomic Energy Commission by Westinghouse Electric Corporation, Pittsburgh, PA, 1958.

- [43] R. Weatherhead, "Nucleate Boiling Characteristics and the Critical Heat Flux Occurrence in Subcooled Axial-flow Water Systems," tech. rep., Argonne national Laboratory, Argonne, IL, 1963.
- [44] D. C. Groeneveld, A. Ireland, J. Kaizer, and A. Vasic, "An overview of measurements, data compilations and prediction methods for the critical heat flux in water-cooled tubes," *Nuclear Engineering and Design*, vol. 331, no. November 2017, pp. 211–221, 2018.
- [45] D. C. Groeneveld, "Critical Heat Flux Data Used to Generate the 2006 Groeneveld Lookup Tables," tech. rep., United States Nuclear Regulatory Commission, 2019.
- [46] D. C. Groeneveld, J. Q. Shan, A. Z. Vasić, L. K. Leung, A. Durmayaz, J. Yang, S. C. Cheng, and A. Tanase, "The 2006 CHF look-up table," *Nuclear Engineering and Design*, vol. 237, no. 15-17 SPEC. ISS., pp. 1909–1922, 2007.
- [47] CISE, "Exercise on Reproducibility of Critical Heat Flux Date—Presentation of Experimental Results," in *Meeting of the European Two-Phase Group*, (Milan, Italy), 1970.
- [48] L. Nilsson, "Repeatability Tests of Critical Heat Flux Data for [the] 1970 Meeting of the European Two-phase Flow Group, Comparison of Results by Becker's Burnout Correlation," tech. rep., Aktiebolaget Atomenergi, Stockholm, Sweden, 1970.
- [49] P. L. Kirillov, O. L. Peskov, and N. P. Serdun, "Control Experiment on Critical Heat Transfer during Water Flow in Pipes," *Soviet Atomic Energy*, vol. 57, pp. 858–860, 1985.
- [50] W. M. Rohsenow, "A method of correlating heat transfer data for surface boiling of liquids," tech. rep., MIT Division of Industrial Cooperation, Cambridge, MA, 1951.
- [51] J. H. Lienhard and L. C. Witte, "An historical review of the hydrodynamic theory of boiling," *Reviews in Chemical Engineering*, vol. 3, no. 3-4, pp. 187–280, 1985.
- [52] R. L. Judd and K. S. Hwang, "A Comprehensive Model for Nucleate Pool Boiling Heat Transfer Including Microlayer Evaporation," *Journal of Heat Transfer*, vol. 98, no. 4, p. 623, 1976.
- [53] R. Séméria, "la cinématographie ultra-rapide et l'ébullition à haute pression," *La houille Blanche*, no. 6, pp. 679–686, 1963.
- [54] F. Chemat and E. Esveld, "Microwave super-heated boiling of organic liquids: Oigin, effect and application," *Chemical Engineering and Technology*, vol. 24, no. 7, pp. 735–744, 2001.
- [55] F. D. Moore and R. B. Mesler, "The measurement of rapid surface temperature fluctuations during nucleate boiling of water," *AIChE Journal*, vol. 7, no. 4, pp. 620–624, 1961.
- [56] R. C. Hendricks and R. R. Sharp, "Initiation of cooling due to bubble growth on a heating surface," tech. rep., National Aeronautics and Space Administration, 1964.
- [57] R. R. Sharp, "The nature of liquid film evaporation during nucleate boiling," tech. rep., NASA, Washington D.C., 1964.
- [58] N. B. Hospeti and R. B. Mesler, "Deposits Formed Beneath Bubbles During Nucleate Boiling of Radioactive Calcium Sulfate Solutions," *AIChE Journal*, pp. 662–665, 1965.

- [59] M. G. Cooper and A. J. Lloyd, "The microlayer in nucleate pool boiling," *International Journal of Heat and Mass Transfer*, vol. 12, no. 8, pp. 895–913, 1969.
- [60] H. H. Jawurek, "Simultaneous determination of microlayer geometry and bubble growth in nucleate boiling," *International Journal of Heat and Mass Transfer*, vol. 12, no. 8, pp. 843–848, 1969.
- [61] C. M. Voutsinos and R. L. Judd, "Laser Interferometric Investigation of the Microlayer Evaporation Phenomenon," *Journal of Heat Transfer*, vol. 97, no. 1, p. 88, 1975.
- [62] H. S. Fath and R. L. Judd, "Influence of System Pressure on Microlayer Evaporation Heat Transfer," *Journal of Heat Transfer*, vol. 100, no. 1, p. 49, 1978.
- [63] L. D. Koffman and M. S. Plesset, "Experimental Observations of the Microlayer in Vapor Bubble Growth on a Heated Solid," *Journal of Heat Transfer*, vol. 105, no. 3, p. 625, 1983.
- [64] M. Gao, L. Zhang, P. Cheng, and X. Quan, "An investigation of microlayer beneath nucleation bubble by laser interferometric method," *International Journal of Heat and Mass Transfer*, vol. 57, no. 1, pp. 183–189, 2013.
- [65] A. Guion, S. Afkhami, S. S. Zaleski, and J. Buongiorno, "Simulations of microlayer formation in nucleate boiling," *International Journal of Heat and Mass Transfer*, vol. 127, no. 4, pp. 1271–1284, 2018.
- [66] A. Urbano, S. Tanguy, G. Huber, and C. Colin, "Direct numerical simulation of nucleate boiling in micro-layer regime," *International Journal of Heat and Mass Transfer*, vol. 123, pp. 1128–1137, aug 2018.
- [67] S. Hänsch and S. Walker, "Microlayer formation and depletion beneath growing steam bubbles," *International Journal of Multiphase Flow*, vol. 111, pp. 241–263, feb 2019.
- [68] E. P. Partridge and A. H. White, "Mechanism of Formation of Calcium Sulfate Boiler Scale," *Industrial and Engineering Chemistry*, vol. 21, no. 9, pp. 834–838, 1929.
- [69] R. Semeria and B. Martinet, "Calefaction Spots on a Heating Wall: Temperature Distribution and Resorption," in *Proceedings of the Institution of Mechanical Engineers, Conference Proceedings*, vol. 180, (London, UK), pp. 192–205, SAGE Publications Sage, 1965.
- [70] G. Kirby, R. Staniforth, and L. Kinneir, "An investigation into a possible mechanism of subcooled burnout," tech. rep., United Kingdom Atomic Energy Authority, London, UK, 1966.
- [71] G. Kirby, R. Staniforth, and J. Kinneir, "A visual study of forced convection boiling. Part 2: Flow patterns and burnout for a round test section," tech. rep., United Kingdom Atomic Energy Authority, 1967.
- [72] M. P. Fiori and A. E. Bergles, "Model of Critical Heat Flux in Subcooled Flow Boiling," tech. rep., Massachusetts Institute of Technology, Cambridge, MA, 1968.
- [73] H. J. Van Ouwerkerk, "Burnout in pool boiling the stability of boiling mechanisms," *International Journal of Heat and Mass Transfer*, vol. 15, no. 1, pp. 25–34, 1972.

- [74] H. Kim, Y. Park, and J. Buongiorno, "Measurement of wetted area fraction in subcooled pool boiling of water using infrared thermography," *Nuclear Engineering and Design*, vol. 264, pp. 103–110, 2013.
- [75] I. C. Chu, H. C. No, and C. H. Song, "Visualization of boiling structure and critical heat flux phenomenon for a narrow heating surface in a horizontal pool of saturated water," *International Journal of Heat and Mass Transfer*, vol. 62, no. 1, pp. 142–152, 2013.
- [76] I. C. Chu, H. C. No, C. H. Song, and D. J. Euh, "Observation of critical heat flux mechanism in horizontal pool boiling of saturated water," *Nuclear Engineering and Design*, vol. 279, pp. 189–199, 2014.
- [77] D. E. Kim, J. Song, and H. Kim, "Simultaneous observation of dynamics and thermal evolution of irreversible dry spot at critical heat flux in pool boiling," *International Journal of Heat and Mass Transfer*, vol. 99, pp. 409–423, 2016.
- [78] Y. Katto, "Critical heat flux," *International Journal of Multiphase Flow*, vol. 20, no. SUPPL. 1, pp. 53–90, 1994.
- [79] G. Liang and I. Mudawar, "Pool boiling critical heat flux (CHF) – Part 1: Review of mechanisms, models, and correlations," *International Journal of Heat and Mass Transfer*, vol. 117, pp. 1352–1367, 2018.
- [80] G. P. Celata, M. Cumo, A. Mariani, M. Simoncini, and G. Zummo, "Rationalization of existing mechanistic models for the prediction of water subcooled flow boiling critical heat flux," *International Journal of Heat and Mass Transfer*, vol. 37, no. SUPPL. 1, pp. 347–360, 1994.
- [81] I. I. Gogonin and S. S. Kutateladze, "Critical heat flux as a function of heater size for a liquid boiling in a large enclosure," *Journal of Engineering Physics*, vol. 33, no. 5, pp. 1286–1289, 1977.
- [82] R. Gaertner and J. Westwater, "Population of active sites in nucleate boiling heat transfer," *Chem. Eng. Progr.*, jan 1960.
- [83] R. F. Gaertner, "Photographic Study of Nucleate Pool Boiling on a Horizontal Surface," *Journal of Heat Transfer*, vol. 87, no. 1, p. 17, 1965.
- [84] Y. Haramura and Y. Katto, "A new hydrodynamic model of critical heat flux, applicable widely to both pool and forced convection boiling on submerged bodies in saturated liquids," *International Journal of Heat and Mass Transfer*, vol. 26, pp. 389–399, mar 1983.
- [85] L. Tong, A. Bishop, and L. Efferdin, "A photographic study of subcooled boiling flow and DNB of Freon-113 in a vertical channel," in *ASME Paper 66-WA/HT-39, Winter Annual Meeting, ASME*, (New York, NY), 1966.
- [86] S. B. van der Molen and F. W. B. M. Galjee, "The boiling mechanism during burnout phenomena in subcooled two-phase water flows," in *Proceeding of International Heat Transfer Conference 6*, (Connecticut), pp. 381–385, Begellhouse, 1978.
- [87] R. Hino and T. Ueda, "Studies on heat transfer and flow characteristics in subcooled flow boiling—Part 2. Flow characteristics," *International Journal of Multiphase Flow*, vol. 11, pp. 283–297, may 1985.

- [88] C. Lee and I. Mudawar, "A mechanistic critical heat flux model for subcooled flow boiling based on local bulk flow conditions," *International Journal of Multiphase Flow*, vol. 14, pp. 711–728, nov 1988.
- [89] V. E. Doroshchuk, L. L. Levitan, and F. P. Lantzman, "Investigation into burnout in uniformly heated tubes," *ASME paper*, 1975.
- [90] F. W. Staub, "The Void Fraction in Subcooled Boiling—Prediction of the Initial Point of Net Vapor Generation," *Journal of Heat Transfer*, vol. 90, pp. 151–157, feb 1968.
- [91] R. C. Martinelli, "Heat transfer to molten metals," *Trans. Am. Soc. Mech. Eng.*, vol. 69, pp. 947–959, 1947.
- [92] C. F. Colebrook and C. M. White, "Experiments with fluid friction in roughened pipes," *Proceedings of the Royal Society of London. Series A - Mathematical and Physical Sciences*, vol. 161, pp. 367–381, aug 1937.
- [93] C. F. Colebrook, "Turbulent Flow in pipes with particular reference to the transition region between the smooth and rough pipe laws," *Journal of the Institution of Civil Engineers*, vol. 11, pp. 133–156, feb 1939.
- [94] S. Levy, "Forced convection subcooled boiling—prediction of vapor volumetric fraction," *International Journal of Heat and Mass Transfer*, vol. 10, pp. 951–965, jul 1967.
- [95] M. Styrikovich, E. I. Nevstrueva, and G. Dvorina, "The effect of two-phase flow pattern on the nature of heat transfer crisis in boiling," in *International Heat Transfer Conference Digital Library*, 1970.
- [96] M. Bruder and T. Sattelmayer, "An Empirical Correlation for the Void Fraction at Critical Heat Flux Close to the Wall for Subcooled Flow Boiling of a Low Boiling Refrigerant," *Heat and Mass Transfer Research Journal*, vol. 2, no. 2, 2018.
- [97] L. Tong, "Prediction of Departure from Nucleate Boiling for an Axially Non-Uniform Heat Flux Distribution," *Journal of Nuclear Energy*, vol. 21, pp. 241–248, 1967.
- [98] D. C. Groeneveld, S. C. Cheng, and T. Doan, "1986 AECL-UO critical heat flux lookup table," *Heat Transfer Engineering*, vol. 7, no. 1-2, pp. 46–62, 1986.
- [99] D. C. Groeneveld, L. K. H. Leung, P. L. Kirillov, V. P. Bobkov, I. P. Smogalev, V. N. Vinogradov, X. C. Huang, and E. Royer, "The 1995 look-up table for critical heat flux in tubes," *Nuclear Engineering and Design*, vol. 163, no. 1-2, pp. 1–23, 1996.
- [100] P. L. Kirillov, V. P. Bobkov, E. A. Boltenko, V. N. Vinogradov, I. B. Katan, and I. P. Smogalev, "Lookup tables of critical heat fluxes," *Soviet Atomic Energy*, vol. 71, no. 1, pp. 543–551, 1991.
- [101] G. P. Celata, M. Cumo, and A. Mariani, "The effect of the tube diameter on the critical heat flux in subcooled flow boiling," *International Journal of Heat and Mass Transfer*, vol. 39, no. 8, pp. 1755–1757, 1996.
- [102] R. A. Smith, "Boiling inside tubes: critical heat flux for upward flow in uniformly heated tubes," *ESDU Data Item*, 1986.
- [103] A. Tanase, S. C. Cheng, D. C. Groeneveld, and J. Q. Shan, "Diameter effect on critical heat flux," *Nuclear Engineering and Design*, vol. 239, no. 2, pp. 289–294, 2009.

- [104] M. El Nakla, M. Habib, W. Ahmed, A. Al-Sarkhi, R. Ben Mansour, and M. Y. Al-Awwad, "Application of the critical heat flux look-up table to large diameter tubes," *Science and Technology of Nuclear Installations*, vol. 2013, no. i, 2013.
- [105] J. P. Duarte and M. L. Corradini, "Hydraulic and heated equivalent diameters used in heat transfer correlations," *Nuclear Technology*, vol. 201, no. 1, pp. 99–102, 2018.
- [106] P. Hejzlar and N. E. Todreas, "Consideration of critical heat flux margin prediction by subcooled or low quality critical heat flux correlations," *Nuclear Engineering and Design*, vol. 163, pp. 215–223, 1996.
- [107] B. Bricard, P. Peturaud, and J.-M. Delhaye, "Understanding and Modelling Dnb in Forced Convective Boiling: Modelling of a Mechanism Based on Nucleation Site Dryout," *Multiphase Science and Technology*, vol. 9, no. 4, pp. 329–379, 1997.
- [108] V. S. Nikolayev and D. A. Beysens, "Boiling crisis and non-equilibrium drying transition," *Europhysics Letters*, vol. 47, no. 3, pp. 345–351, 1999.
- [109] V. S. Nikolayev and D. A. Beysens, "CHF as a Non-Equilibrium Drying Transition," in *Proceedings of the 4th International Conference on Multiphase Flow (ICMF4)*, (New Orleans, LA USA), 2001.
- [110] S. J. Ha and H. C. No, "A dry-spot model of critical heat flux in pool and forced convection boiling," *International Journal of Heat and Mass Transfer*, vol. 41, no. 2, pp. 303–311, 1998.
- [111] S. J. Ha and H. C. No, "A dry-spot model of critical heat flux applicable to both pool boiling and subcooled forced convection boiling," *International Journal of Heat and Mass Transfer*, vol. 43, pp. 241–250, 2000.
- [112] R. F. Gaertner, "Distribution of Active Sites in the Nucleate Boiling of Liquids," *Chemical Engineering Progress Symposium*, vol. 59, pp. 52–61, 1965.
- [113] J. Y. Choi, H. C. No, and J. Kim, "Development of a dry patch model for critical heat flux prediction," *International Journal of Heat and Mass Transfer*, vol. 100, pp. 386–395, 2016.
- [114] H. C. No, M. W. Song, S. J. Ha, I. C. Ju, and J. Y. Choi, "Observation-based CHF model development: Dry spot – Dry patch models," *Nuclear Engineering and Design*, vol. 342, no. November 2018, pp. 147–156, 2019.
- [115] C. E. Shannon, "Communication in the Presence of Noise," *Proceedings of the IRE*, vol. 37, no. 1, pp. 10–21, 1949.
- [116] N. Kurul and M. Z. Podowski, "Multidimensional effects in forced convection subcooled boiling," in *International Heat Transfer Conference Digital Library*, 1990.
- [117] L. A. Gilman, *Development of a General Purpose SubgridWall Boiling Model from Improved Physical Understanding for Use in Computational Fluid Dynamics*. Ph.d., Massachusetts Institute of Technology, 2014.
- [118] L. Gilman and E. Baglietto, "A self-consistent, physics-based boiling heat transfer modeling framework for use in computational fluid dynamics," *International Journal of Multiphase Flow*, vol. 95, pp. 35–53, 2017.

- [119] F. W. Dittus and L. M. K. Boelter, "Heat Transfer in Automobile Radiators of the Tubular Type," *University of California publications in Engineering*, vol. 2, p. 371, 1930.
- [120] F. W. Dittus and L. M. K. Boelter, "Heat Transfer in Automobile Radiators of the Tubular Type," *International Communications in Heat and Mass Transfer*, vol. 12, no. 1, pp. 3—22, 1985.
- [121] R. H. Winterton, "Where did the Dittus and Boelter equation come from?," *International Journal of Heat and Mass Transfer*, vol. 41, no. 4-5, pp. 809–810, 1998.
- [122] R. Kommajosyula, E. Demarly, and E. Baglietto, "Development and multi-level validation of a mechanistic heat flux partitioning model for boiling heat transfer," in *Proceedings of 18th International Topical Meeting on Nuclear Reactor Thermalhydraulics (NURETH-18)*, (Portland, OR), 2019.
- [123] J. H. Lienhard, *A heat transfer textbook*. Cambridge, Massachusetts, U.S.A.: Phlogiston Press, 1981.
- [124] M. Lemmert and J. Chawla, "Influence of flow velocity on surface boiling heat transfer coefficient," *Heat Transfer in Boiling*, vol. 237, no. 247, 1977.
- [125] M. Sultan and R. L. Judd, "Spatial distribution of active sites and bubble flux density," *Journal of Heat Transfer*, vol. 100, no. 1, pp. 56–62, 1978.
- [126] S. R. Yang and R. H. Kim, "A mathematical model of the pool boiling nucleation site density in terms of the surface characteristics," *International Journal of Heat and Mass Transfer*, vol. 31, no. 6, pp. 1127–1135, 1988.
- [127] T. Hibiki and M. Ishii, "Active nucleation site density in boiling systems," *International Journal of Heat and Mass Transfer*, vol. 46, no. 14, pp. 2587–2601, 2003.
- [128] N. Basu, G. R. Warrier, and V. K. Dhir, "Onset of Nucleate Boiling and Active Nucleation Site Density During Subcooled Flow Boiling," *Journal of Heat Transfer*, vol. 124, no. 4, p. 717, 2002.
- [129] V. Borishanskii, G. Bobrovich, and F. Minchenko, "Heat Transfer From a Tube To Water and To Ethanol in Nucleate Pool Boiling. in: S.S. Kutateladze (Ed.)," in *Symposium of Heat Transfer and Hydraulics in Two-Phase Media*, (Moscow), 1961.
- [130] Q. Li, Y. Jiao, M. Avramova, P. Chen, J. Yu, J. Chen, and J. Hou, "Development, verification and application of a new model for active nucleation site density in boiling systems," *Nuclear Engineering and Design*, vol. 328, no. December 2017, pp. 1–9, 2018.
- [131] V. H. Del Valle and D. B. Kenning, "Subcooled flow boiling at high heat flux," *International Journal of Heat and Mass Transfer*, vol. 28, no. 10, pp. 1907–1920, 1985.
- [132] T. Smith, *Notebook on Spatial Data Analysis*. Online, 2016.
- [133] J. F. Klausner, R. Mei, D. M. Bernhard, and L. Z. Zeng, "Vapor bubble departure in forced convection boiling," *International Journal of Heat and Mass Transfer*, vol. 36, no. 3, pp. 651–662, 1993.
- [134] L. Z. Zeng, J. F. Klausner, D. M. Bernhard, and R. Mei, "A unified model for the prediction of bubble detachment diameters in boiling systems- I. Pool boiling," *International Journal of Heat and Mass Transfer*, vol. 36, no. 9, pp. 2271–2279, 1993.

- [135] J. Cotton, A. J. Robinson, M. Shoukri, and J. S. Chang, "A two-phase flow pattern map for annular channels under a DC applied voltage and the application to electrohydrodynamic convective boiling analysis," *International Journal of Heat and Mass Transfer*, vol. 48, no. 25-26, pp. 5563–5579, 2005.
- [136] M. Colombo and M. Fairweather, "Prediction of bubble departure in forced convection boiling: A mechanistic model," *International Journal of Heat and Mass Transfer*, vol. 85, pp. 135–146, 2015.
- [137] R. Sugrue and J. Buongiorno, "A modified force-balance model for prediction of bubble departure diameter in subcooled flow boiling," *Nuclear Engineering and Design*, vol. 305, pp. 717–722, 2016.
- [138] T. Mazzocco, W. Ambrosini, R. Kommajosyula, and E. Baglietto, "A reassessed model for mechanistic prediction of bubble departure and lift off diameters," *International Journal of Heat and Mass Transfer*, vol. 117, pp. 119–124, 2018.
- [139] M. S. Plesset and S. A. Zwick, "The growth of vapor bubbles in superheated liquids," *Journal of Applied Physics*, vol. 25, no. 4, pp. 493–500, 1954.
- [140] R. Sugrue, J. Buongiorno, and T. McKrell, "An experimental study of bubble departure diameter in subcooled flow boiling including the effects of orientation angle, subcooling, mass flux, heat flux, and pressure," *Nuclear Engineering and Design*, vol. 279, pp. 182–188, 2014.
- [141] P. Guan, L. Jia, L. Yin, and Z. Tan, "Bubble departure size in flow boiling," *Heat and Mass Transfer/Waerme- und Stoffuebertragung*, vol. 51, pp. 921–930, jul 2015.
- [142] V. Prodanovic, D. Fraser, and M. Salcudean, "Bubble behavior in subcooled flow boiling of water at low pressures and low flow rates," *International Journal of Multiphase Flow*, vol. 28, pp. 1–19, jan 2002.
- [143] R. Situ, T. Hibiki, M. Ishii, and M. Mori, "Bubble lift-off size in forced convective subcooled boiling flow," *International Journal of Heat and Mass Transfer*, vol. 48, pp. 5536–5548, dec 2005.
- [144] G. Kocamustafaogullari, "Pressure dependence of bubble departure diameter for water," *International communications in heat and mass transfer*, vol. 10, no. 6, pp. 501—509, 1983.
- [145] Y. Y. Hsu, "On the size range of active nucleation cavities on a heating surface," *Journal of Heat Transfer*, vol. 84, no. 3, pp. 207—213, 1962.
- [146] R. Cole, "Bubble frequencies and departure volumes at subatmospheric pressures," *AIChE Journal*, vol. 13, no. 4, pp. 779–783, 1967.
- [147] R. Situ, M. Ishii, T. Hibiki, J. Y. Tu, G. H. Yeoh, and M. Mori, "Bubble departure frequency in forced convective subcooled boiling flow," *International Journal of Heat and Mass Transfer*, vol. 51, no. 25-26, pp. 6268–6282, 2008.
- [148] N. Basu, G. R. Warriar, and V. K. Dhir, "Wall heat flux partitioning during subcooled flow boiling: Part 1 - Model development," *Journal of Heat Transfer*, vol. 127, no. 2, pp. 131–140, 2005.

- [149] R. Podowski, D. Drew, R. J. Lahey, and M. Podowski, "A mechanistic model of the ebullition cycle in forced convection subcooled boiling," 1997.
- [150] N. Basu, *Modeling and Experiments for Wall Heat Flux Partitioning During Subcooled Flow Boiling of Water at Low Pressures*. PhD thesis, University of California Los Angeles, 2003.
- [151] J. Yoo, C. E. Estrada-Perez, and Y. A. Hassan, "Experimental study on bubble dynamics and wall heat transfer arising from a single nucleation site at subcooled flow boiling conditions - Part 2: Data analysis on sliding bubble characteristics and associated wall heat transfer," *International Journal of Multiphase Flow*, vol. 84, pp. 292–314, 2016.
- [152] V. K. Dhir and S. P. Liaw, "Framework for a Unified Model for Nucleate and Transition Pool Boiling," *Journal of Heat Transfer*, vol. 111, no. 3, p. 739, 1989.
- [153] E. Baglietto, E. Demarly, and R. Kommajosyula, "Boiling crisis as the stability limit to wall heat partitioning," *Applied Physics Letters*, vol. 114, no. 10, 2019.
- [154] R. J. Benjamin and A. R. Balakrishnan, "Nucleation site density in pool boiling of saturated pure liquids: Effect of surface microroughness and surface and liquid physical properties," *Experimental Thermal and Fluid Science*, vol. 15, no. 1, pp. 32–42, 1997.
- [155] S. J. Kim, I. C. Bang, J. Buongiorno, and L. W. Hu, "Surface wettability change during pool boiling of nanofluids and its effect on critical heat flux," *International Journal of Heat and Mass Transfer*, vol. 50, no. 19-20, pp. 4105–4116, 2007.
- [156] P. Sadasivan, C. Unal, and R. Nelson, "Perspective: Issues in CHF modeling—The need for new experiments," *Journal of Heat Transfer*, vol. 117, no. 3, pp. 558–567, 1995.
- [157] S. G. Kandlikar, "A theoretical model to predict pool boiling CHF incorporating effects of contact angle and orientation," *Journal of Heat Transfer*, vol. 123, no. 6, pp. 1071–1079, 2001.
- [158] J. D. Bernardin, I. Mudawar, C. B. Walsh, and E. I. Franses, "Contact angle temperature dependence for water droplets on practical aluminum surfaces," *International Journal of Heat and Mass Transfer*, 1997.
- [159] S. Yildiz, *Experimentelle Untersuchung der kritischen Warmestromdichte im Übergang von DNB-zum Dryout-Mechanismus in glatten and poros beschichteten Rohren bei niedrigen Drucken und Massenstromdichten*. Ph.d., Technischen Universität Berlin, 1997.
- [160] M. Stein, *Systematische Untersuchung der kritischen Warmestromdichte beim Stromungssieden von Wasser in lotrechten Kreisrohren mit und ohne poroseer Beschichtung*. Ph.d., Technischen Universität Berlin, 2004.
- [161] C. Fighetti and D. Reddy, "Parametric study of CHF data. Volume 3, Part 1. Critical heat flux data. Final report," sep 1982.
- [162] T. W. Hunt, H. S. Jacket, J. D. Roarty, and J. E. Zerbe, "An Investigation of Sub cooled and Quality Burnout in Circular Channels - WAPD-LSR(IM)-1," tech. rep., Bettis Atomic Power Laboratory, 1955.
- [163] V. I. Tolubinsky and D. Kostanchuk, "Vapour bubbles growth rate and heat transfer intensity at subcooled water boiling," in *Proceeding of International Heat Transfer Conference 4*, (Connecticut), pp. 1–11, Begellhouse, 1970.

- [164] S. Paine, W. Murphy, and W. Hackett, "A Study of Irradiation Effects in Type "A" Nickel and Type 347 Stainless Steel Tensile Specimens," tech. rep., Argonne National Laboratory, Argonne, IL, 1960.
- [165] T. Hayashi, T. Hazuku, T. Takamasa, and K. Takamori, "Contact Angle of Water Droplets in a High-Temperature, High-Pressure Environment," in *12th International Conference on Nuclear Engineering, Volume 1*, pp. 797–800, ASME, nov 2004.
- [166] Y. Hirose, T. Hayashi, T. Hazuku, and T. Takamasa, "Experimental Study on Contact Angle of Water Droplet in High-Temperature Condition," in *Volume 4: Computational Fluid Dynamics, Neutronics Methods and Coupled Codes; Student Paper Competition*, vol. 2006, pp. 709–716, ASME, sep 2006.
- [167] L. Zhang, J. H. Seong, and M. Bucci, "Percolative Scale-Free Behavior in the Boiling Crisis," *Physical Review Letters*, vol. 122, no. 13, 2019.

Appendix A

Vocabulary Definitions

The words used to describe the boiling crisis first reported by Nukiyama [36] in 1934 are multiple. When reading the literature one can be faced with terms such as "Burnout", "Critical Heat Flux", "Departure from Nucleate Boiling", "Dry-Out" or "Boiling Crisis". Their meaning is often close and sometimes used interchangeably in documents. In order to dissipate any confusion when referring to these terms, we let the following definitions hold true for the rest of the thesis:

- **Boiling Crisis:** Refers to the physical phenomenon occurring at high heat fluxes when boiling becomes so strong that vapor begins to cover the entire heating surface and force a sudden change in heat transfer mode.
- **Departure from Nucleate Boiling (DNB):** In the context of subcooled flow boiling, it refers to the particular type of boiling crisis noting the end of the nucleate boiling regime.
- **Dry-Out:** In the context of a high quality flow (saturated flow boiling), refers to the drying-out of the thin liquid film at the boiling surface. Is a distinct mechanism from DNB.
- **Critical Heat Flux (CHF):** Refers to the heat flux at which the boiling crisis occurs. Can be used for both DNB type and Dry-Out type boiling crisis.
- **Burnout:** Refers to the experimentally observed temperature excursion in the heater when CHF is reached. This term is often found in early CHF literature but seems to have fallen out of use recently.

Appendix B

Numerical Implementation

The model implementation was conducted using a 0-D approach that simplified the problem down to a single point representing the boiling quantities at the DNB location. Three principles allowed us to obtain accurate predictions:

- DNB is a local phenomenon: The upstream flow history is not necessary, only the local parameters at the DNB location matter for its prediction.
- The heat partitioning equation is explicit in superheat: for a given wall temperature, there exist a single wall heat flux that can be computed explicitly without requiring iterative methods.
- In a simple, fully developed channel geometry, the turbulent flow velocity distribution can be modeled with a wall function.

With these assumptions, an algorithm can be developed to produce boiling curve data for each test condition only using the thermohydraulic inputs, geometry feature (pipe diameter) and heater properties (contact angle, nucleation properties). The following pseudo-codes are given for illustrating the numerical implementation workflow. The actual algorithms developed for this work were coded on MATLAB2019a.

The first algorithm “*boiling_curve*” is the main script which initializes the maximum wall superheat in the boiling curve and the wall superheat array itself. For each value of the T_{sup} array, the script call the “*heat_partitioning*” function which will return the associated heat flux Q''_{wall} .

The second algorithm “*heat_partitioning*” is a sequential script that computes the necessary inputs to the wall heat flux partitioning equation. Sequentially, the flow non-dimensional numbers are evaluated (Re_f , Ja_{sup} , etc.), followed by the fundamental boiling quantities (D_d , D_{lo} , t_g , t_w , f , N''_b) after which the individual heat partitions (Q''_{fc} , Q''_{sc} , Q''_q , Q''_{ev}) are computed separately. In the end, the dry area fraction (S_{dry}) is obtained and the total wall heat flux output is assembled.

The algorithm function *CSR_interaction* is an example of the implementation of a bisection method used to solve for the non linear equation representing the nucleation site interaction phenomenon. The output of this function is the number of active bubble generating site density N''_b .

Algorithm 1: Algorithm computing the boiling curve and CHF for a given test condition

```

function: boiling_curve( $D_{hy}$ ,  $P$ ,  $G$ ,  $T_{sub}$ , heater.prop);
Input : Hydraulic Diameter ( $D_{hy}$ ), Pressure ( $P$ ), Mass Flux ( $G$ ), Local Subcooling ( $T_{sub}$ ),
        Heater Properties (heater.prop)
Output: Boiling Curve ( $Q''_{wall}[n]$ , CHF)
water.prop  $\leftarrow$  XSteam( $P$ ,  $T_{sub}$ );
if  $P > 120$  bar then
    |  $T_{max} = 8$  K;
else
    | if  $P > 50$  bar then
    | |  $T_{max} = 15$  K;
    | else
    | |  $T_{max} = 60$  K;
    | end if
end if
 $T_{sup} = [0.01 : 0.1 : T_{max}]$ ;
 $n = \text{length}(T_{sup})$ ;
for  $i = 1 : n$  do
    |  $Q''_{wall} = \text{heat\_partitioning}(\text{water.properties}, \text{heater.properties}, D_{hy}, P, G, T_{sub}, T_{sup}(i))$ 
end for
CHF =  $\max(Q''_{wall})$ 

```

Algorithm 2: Algorithm computing the heat flux partitioning for a given wall superheat

function: `heat_partitioning(water.prop, heater.prop, Dhy, P, G, Tsub, Tsup(i));`

Input : Water Properties (`water.prop`), Heater Properties (`heater.prop`), Hydraulic Diameter (`Dhy`), Pressure (`P`), Mass Flux (`G`), Local Subcooling (`Tsub`), Wall Superheat (`Tsup`)

Output: Wall Heat Flux (`Q''wall`)

$$Re_f = \frac{GD_{hy}}{water.\mu_f};$$

$$Re_g = \frac{GD_{hy}}{water.\mu_g};$$

$$Ja_{sub} = \frac{water.\rho_f water.cp_f T_{sub}}{water.\rho_g water.h_{fg}};$$

$$Ja_{sup} = \frac{water.\rho_f water.cp_f T_{sup}}{water.\rho_g water.h_{fg}};$$

$$[D_d, D_{lo}] = bubble_force_balance(D_{hy}, G, T_{sub}, T_{sup}, water.T_{sat}, water.\theta);$$

$$t_g = growth_model(T_{sup}, Ja_{sup}, water.prop, D_d);$$

$$t_w = 0.0061 \frac{Ja_{sub}^{0.6317}}{T_{sup}};$$

$$f = \frac{1}{t_g + t_w};$$

$$N'' = NSD_closure(T_{sup}, heater.prop, water.prop);$$

$$N''_b = CSR_interaction(N'', D_d, t_g, f);$$

$$\zeta = 0.15 \sin(\theta) \frac{N''}{N''_b};$$

$$Nu_f = 0.023 Re_f^{4/5} Pr_f^{0.4};$$

$$Q''_{fc} = Nu_f \frac{water.k_f}{D_{he}} (T_{sub} + T_{sup});$$

$$Q''_{sc} = sliding_conduction_hf(T_{sup}, T_{sub}, Nu, water.prop, D_d, D_{lo}, N''_b, t_w, t_g);$$

$$V_q = \frac{2\pi}{3} \left(\frac{D_d}{4}\right)^3;$$

$$Q''_q = water.\rho_f heater.cp V_q f N''_b \times 2;$$

$$V_{inc} = \frac{2}{3} \pi \left(\frac{D_d}{4}\right)^3;$$

$$\delta_{ml} = 4 \mu m;$$

$$Q''_{ev,inc} = water.\rho_g water.h_{fg} N''_b f V_{inc};$$

$$V_{ml} = \frac{1}{24} \pi \delta_{ml} D_d^2;$$

$$Q''_{ev,ml} = water.\rho_f water.h_{fg} f N''_b V_{ml};$$

$$Q''_{ev} = Q''_{ev,inc} + Q''_{ev,ml};$$

$$Nu_g = 0.023 Re_g^{4/5} Pr_g^{0.4};$$

$$Q''_{gas} = Nu_g \frac{water.k_g}{D_{he}} (T_{sub} + T_{sup});$$

$$S_{dry} = f t_g N''_b \pi \left(\zeta \frac{D_d}{2}\right);$$

$$Q''_{wall} = (1 - S_{dry}) (Q''_{fc} + Q''_{sc} + Q''_q + Q''_{ev}) + S_{dry} Q''_{gas};$$

Algorithm 3: Bisection algorithm computing the surface density of active bubble generating nucleation sites

function: CSR_interaction(N'' , D_d , t_g , f);

Input : Active cavity density (N''), Departure Diameter (D_d), growth time (t_g), Departure frequency (f)

Output: Active bubble density (N_b'')

$f = @(x) \quad x - N'' \exp(-\pi x t_g f \left(\frac{D_d}{2}\right)^2);$

$x1 = 1;$

$x2 = N'';$

$\epsilon = 2;$

while $\epsilon > 0.0005$ **do**

$x_{mid} = \frac{x1}{2} + \frac{x2}{2};$

if $f(x1) \times f(x_{mid}) > 0$ **then**

$x1 = x_{mid}$

end if

if $f(x2) \times f(x_{mid}) > 0$ **then**

$x2 = x_{mid}$

end if

$\epsilon = \frac{x2-x1}{x_{mid}};$

end while

$N_b'' = x_{mid};$

Appendix C

MIT Flow Boiling Results

The results shown in this appendix are using Richenderfer's experimental growth time. Subplots from top to bottom, left to right: experimental and modeled boiling curve, model heat flux partitions, evaporation heat flux components, bubble departure and liftoff diameters, experimental and modeled nucleation site density, experimental and modeled bubble departure frequency, bubble growth and wait time, dry area fraction and sliding length

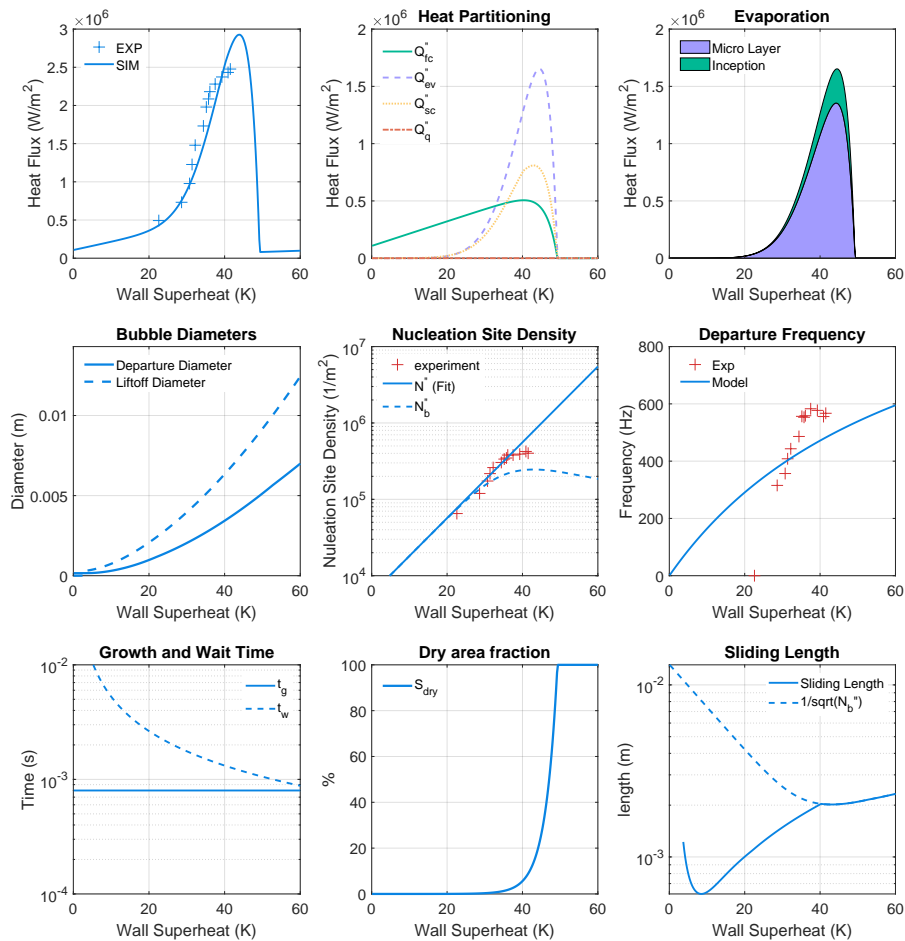


Figure C.1: Case #1, 1 bar, 10 K subcooling, 500 kg m⁻² s⁻¹

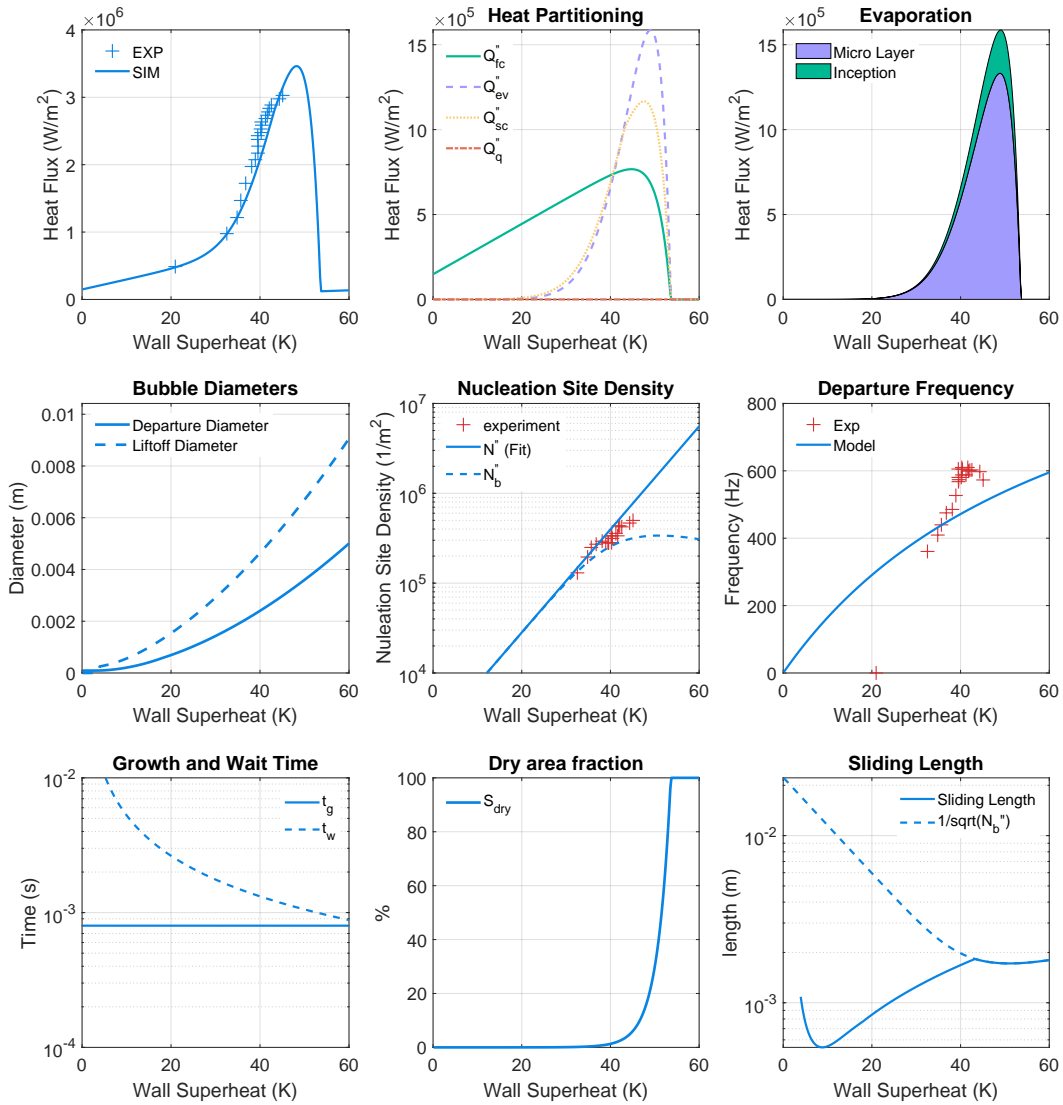


Figure C.2: Case #2, 1 bar, 10 K subcooling, $750 \text{ kg m}^{-2} \text{ s}^{-1}$

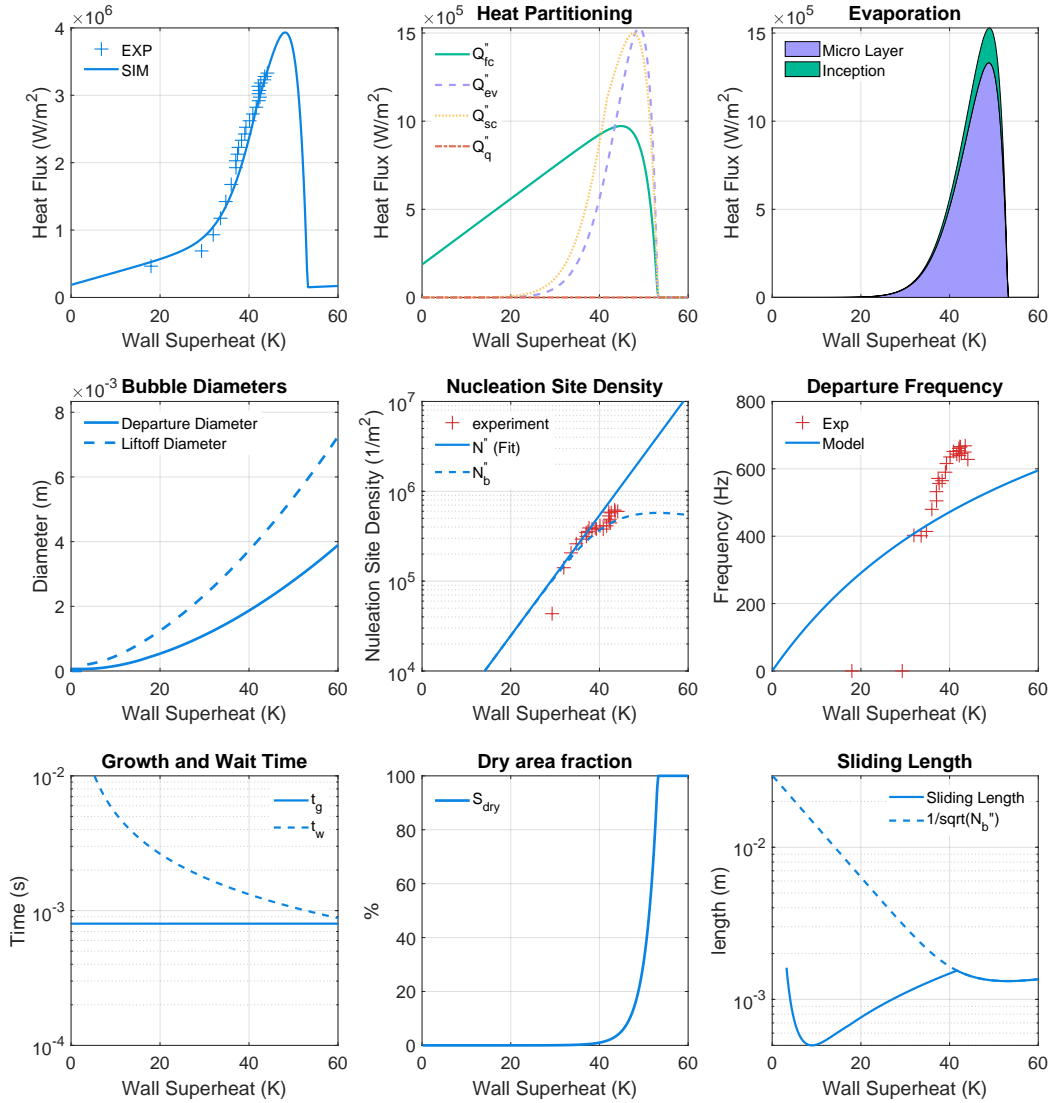


Figure C.3: Case #3, 1 bar, 10 K subcooling, $1000 \text{ kg m}^{-2} \text{ s}^{-1}$

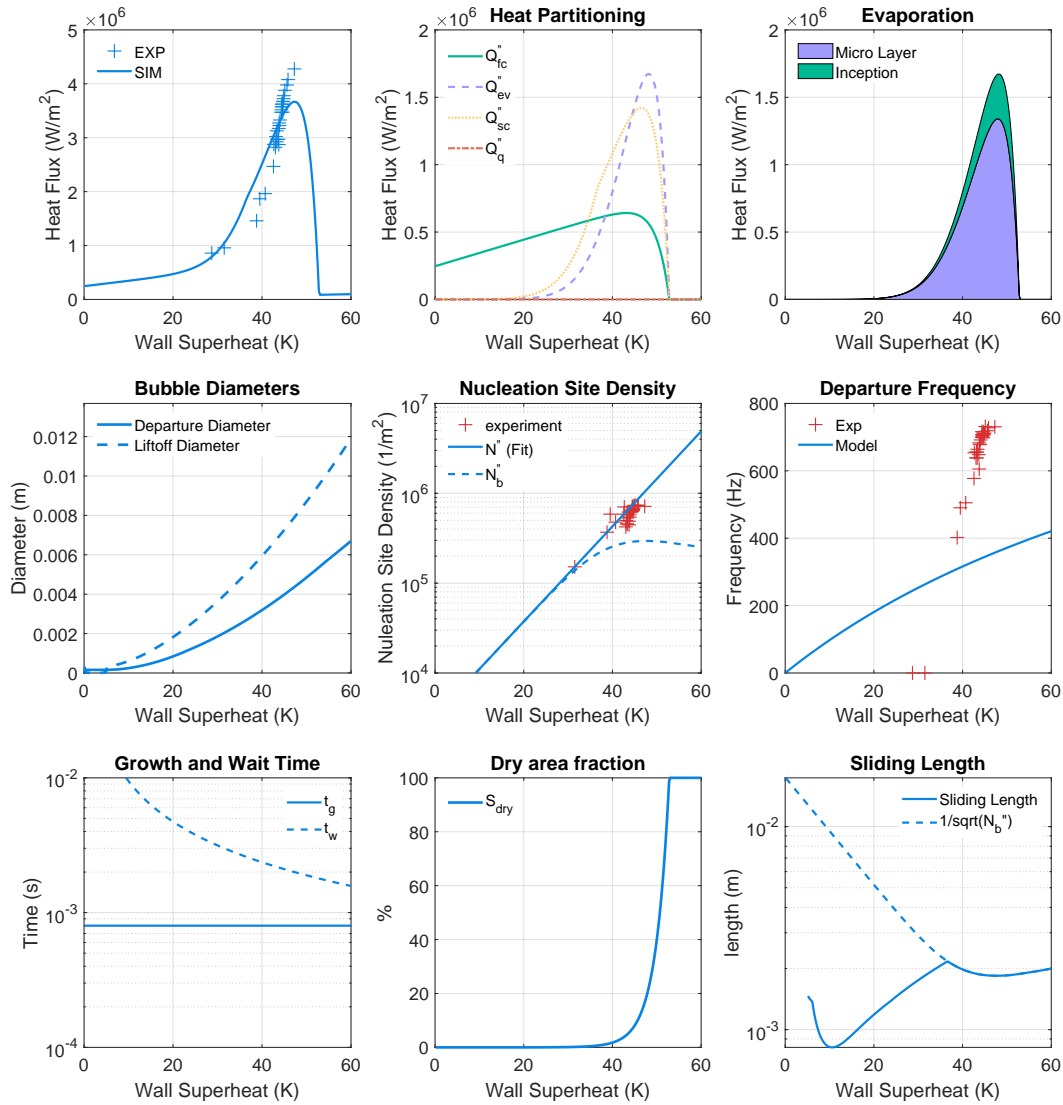


Figure C.4: Case #4, 1 bar, 25 K subcooling, $500 \text{ kg m}^{-2} \text{ s}^{-1}$

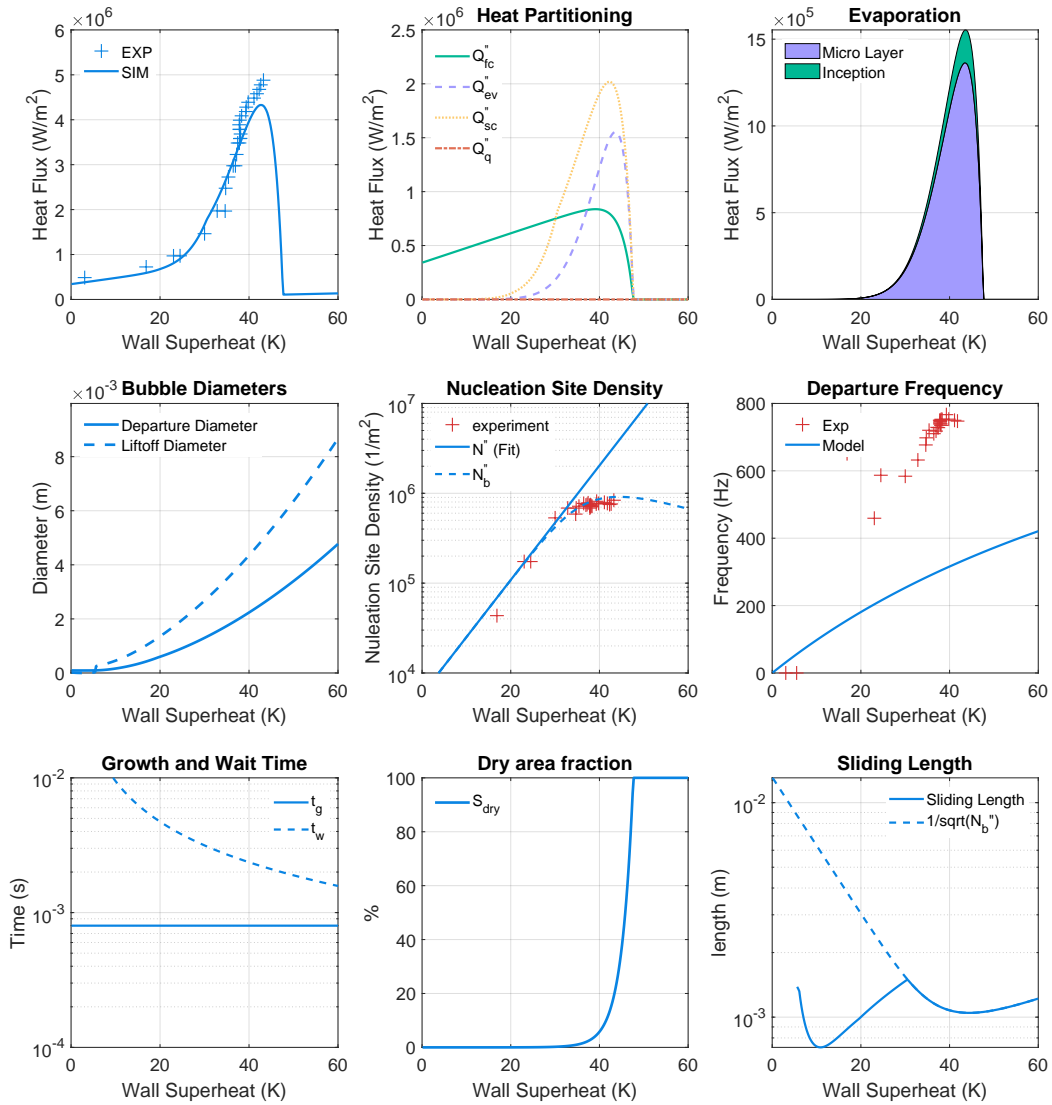


Figure C.5: Case #5, 1 bar, 25 K subcooling, $750 \text{ kg m}^{-2} \text{ s}^{-1}$

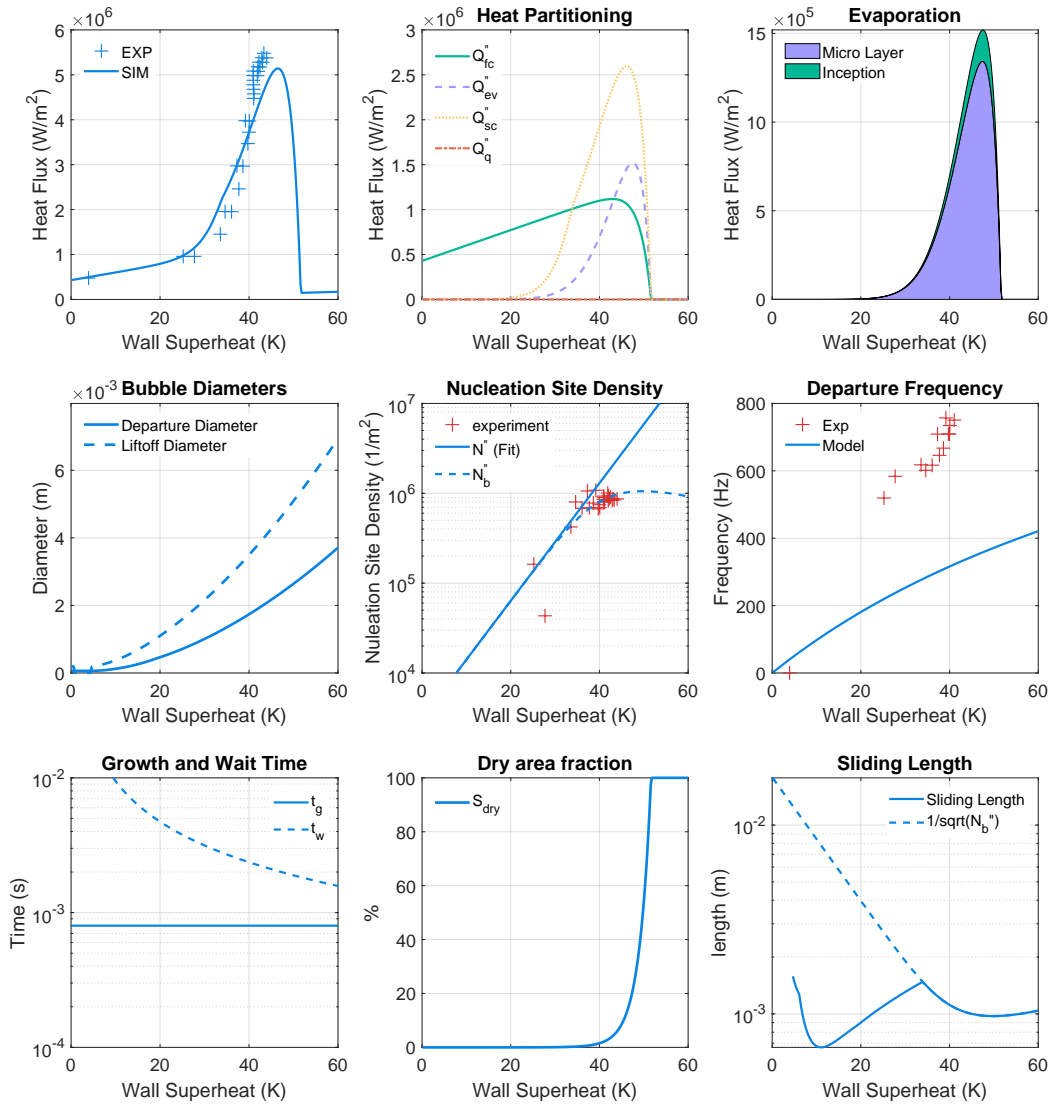


Figure C.6: Case #6, 1 bar, 25 K subcooling, $1000 \text{ kg m}^{-2} \text{ s}^{-1}$

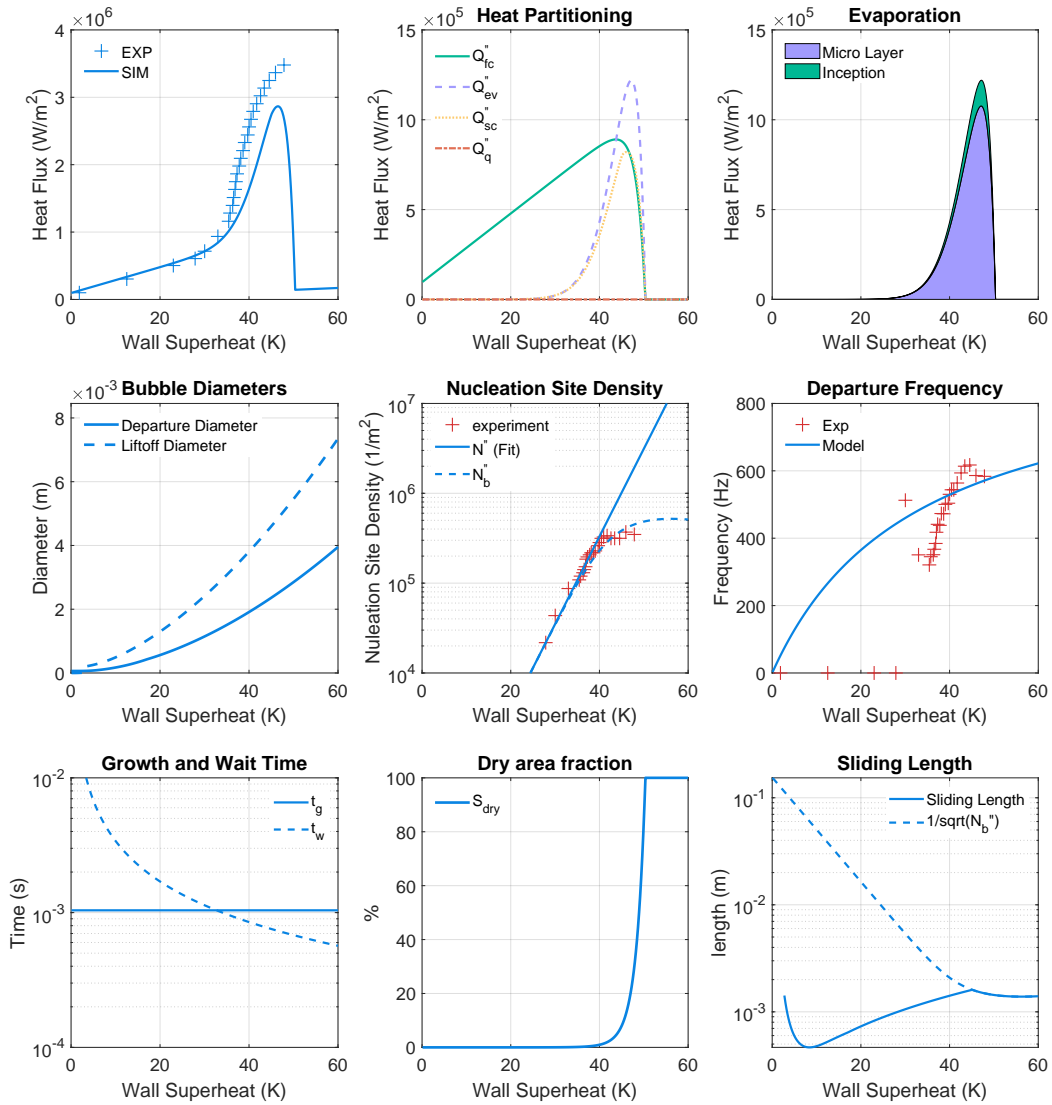


Figure C.7: Case #7, 1 bar, 5 K subcooling, $1000 \text{ kg m}^{-2} \text{ s}^{-1}$

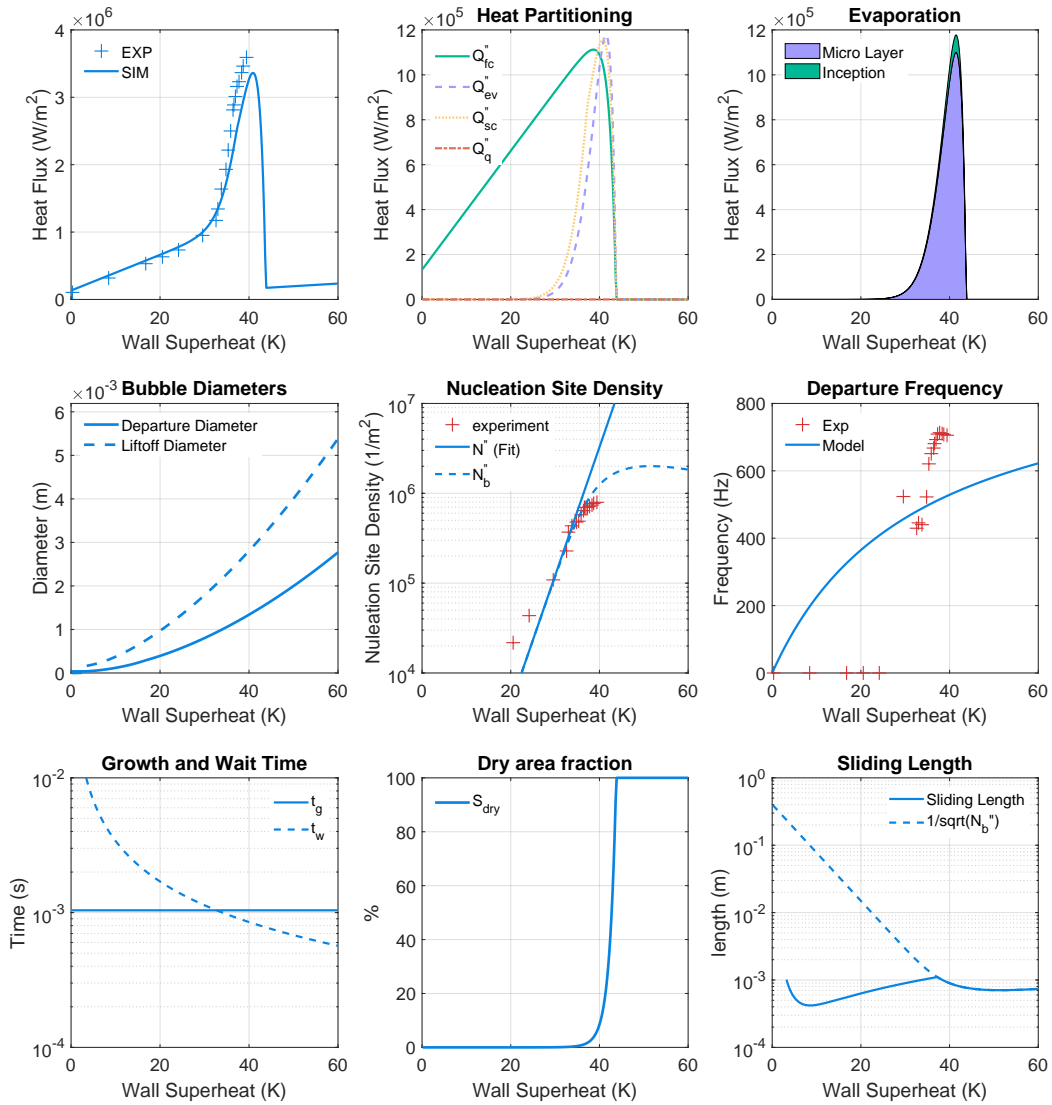


Figure C.8: Case #9, 1 bar, 5 K subcooling, $1500 \text{ kg m}^{-2} \text{ s}^{-1}$

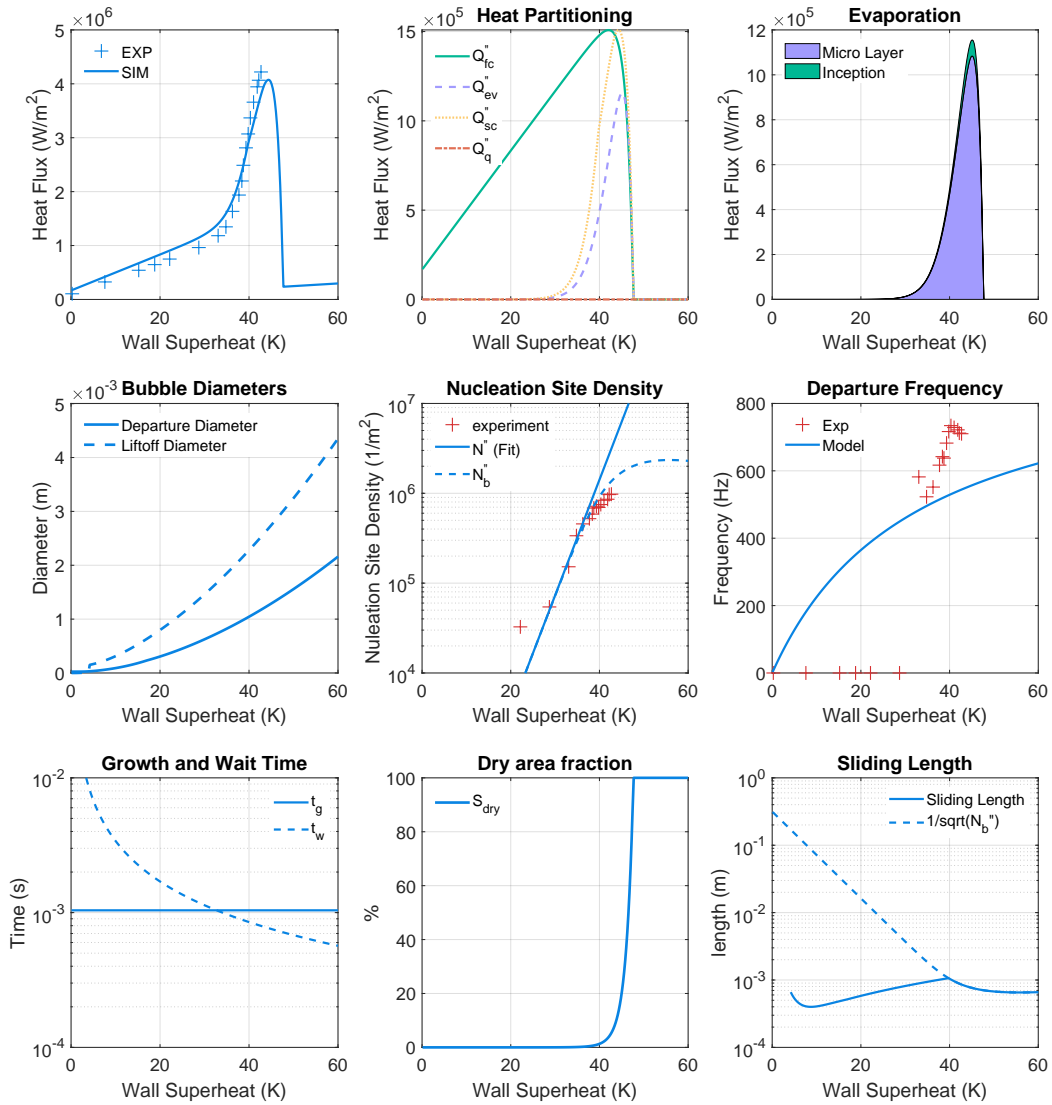


Figure C.9: Case #9, 1 bar, 5 K subcooling, $2000 \text{ kg m}^{-2} \text{ s}^{-1}$

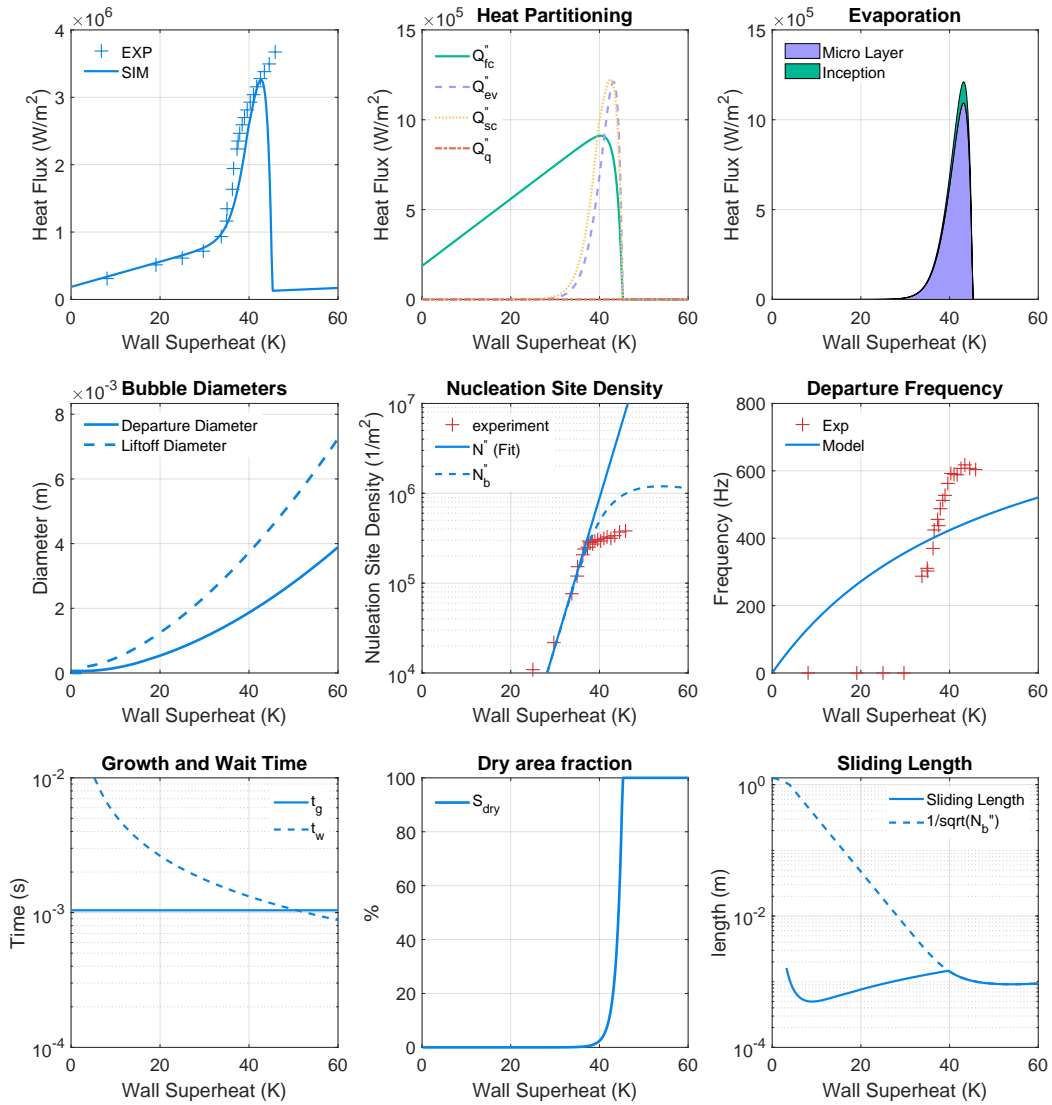


Figure C.10: Case #10, 1 bar, 10 K subcooling, $1000 \text{ kg m}^{-2} \text{ s}^{-1}$

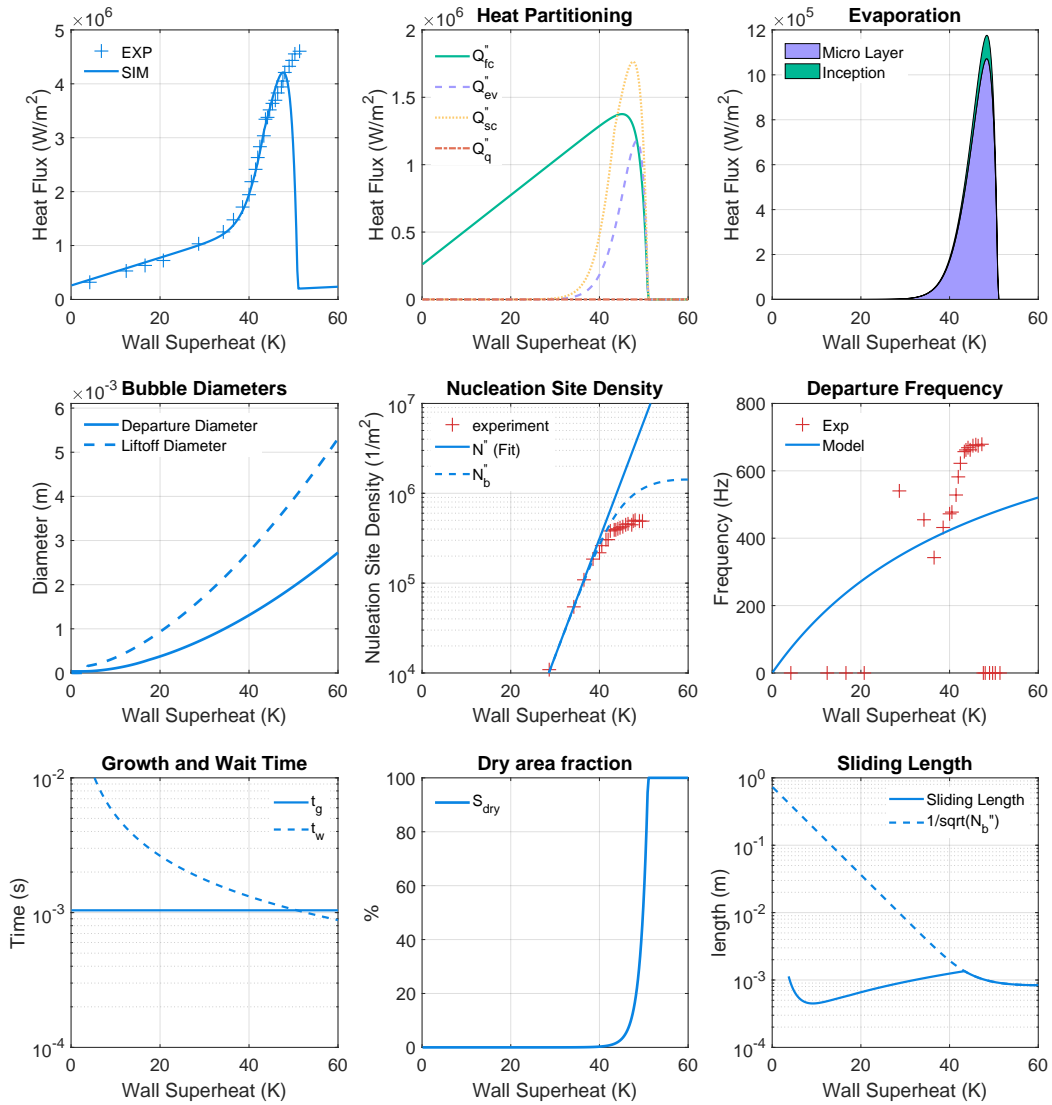


Figure C.11: Case #11, 1 bar, 10 K subcooling, $1500 \text{ kg m}^{-2} \text{ s}^{-1}$

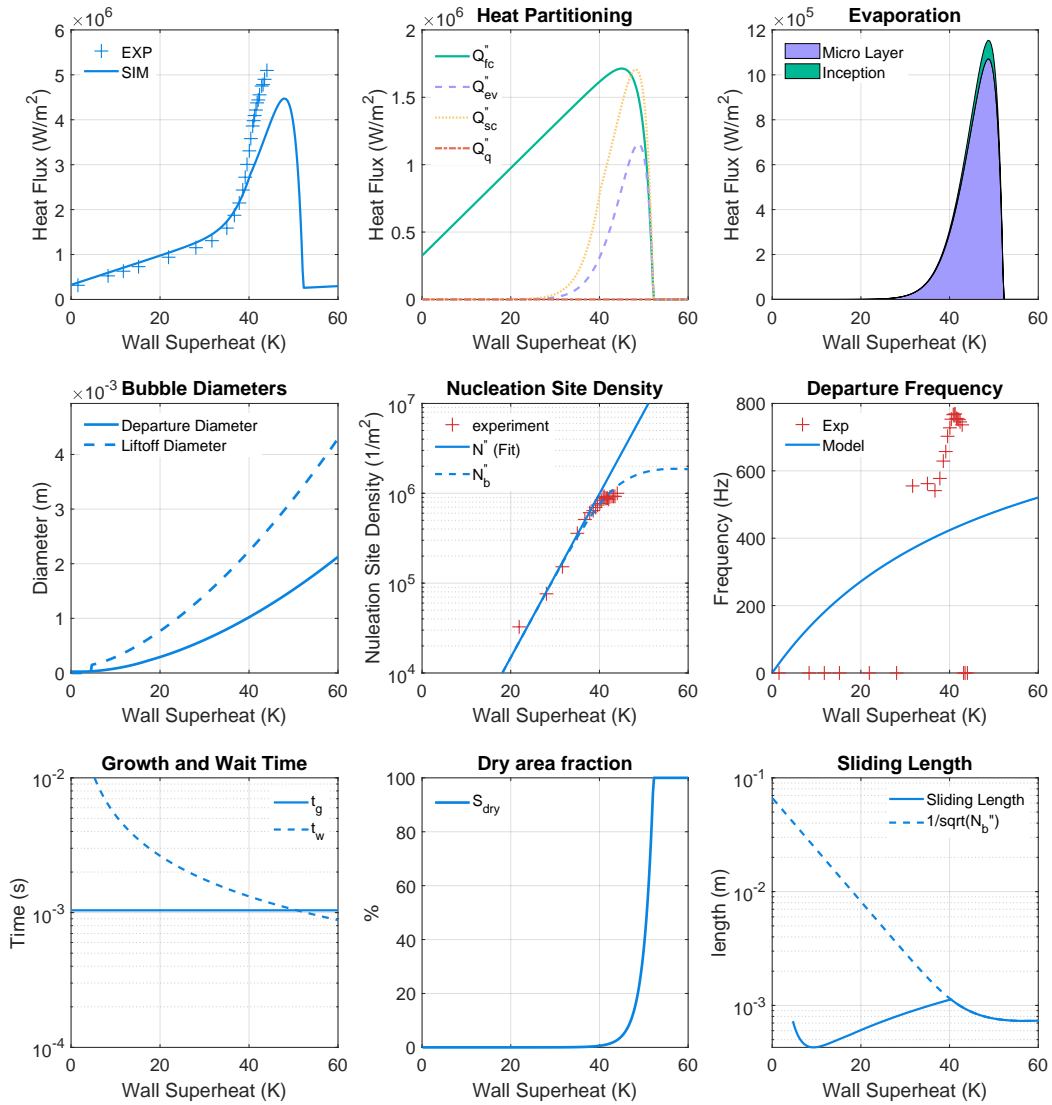


Figure C.12: Case #12, 1 bar, 10 K subcooling, $2000 \text{ kg m}^{-2} \text{ s}^{-1}$

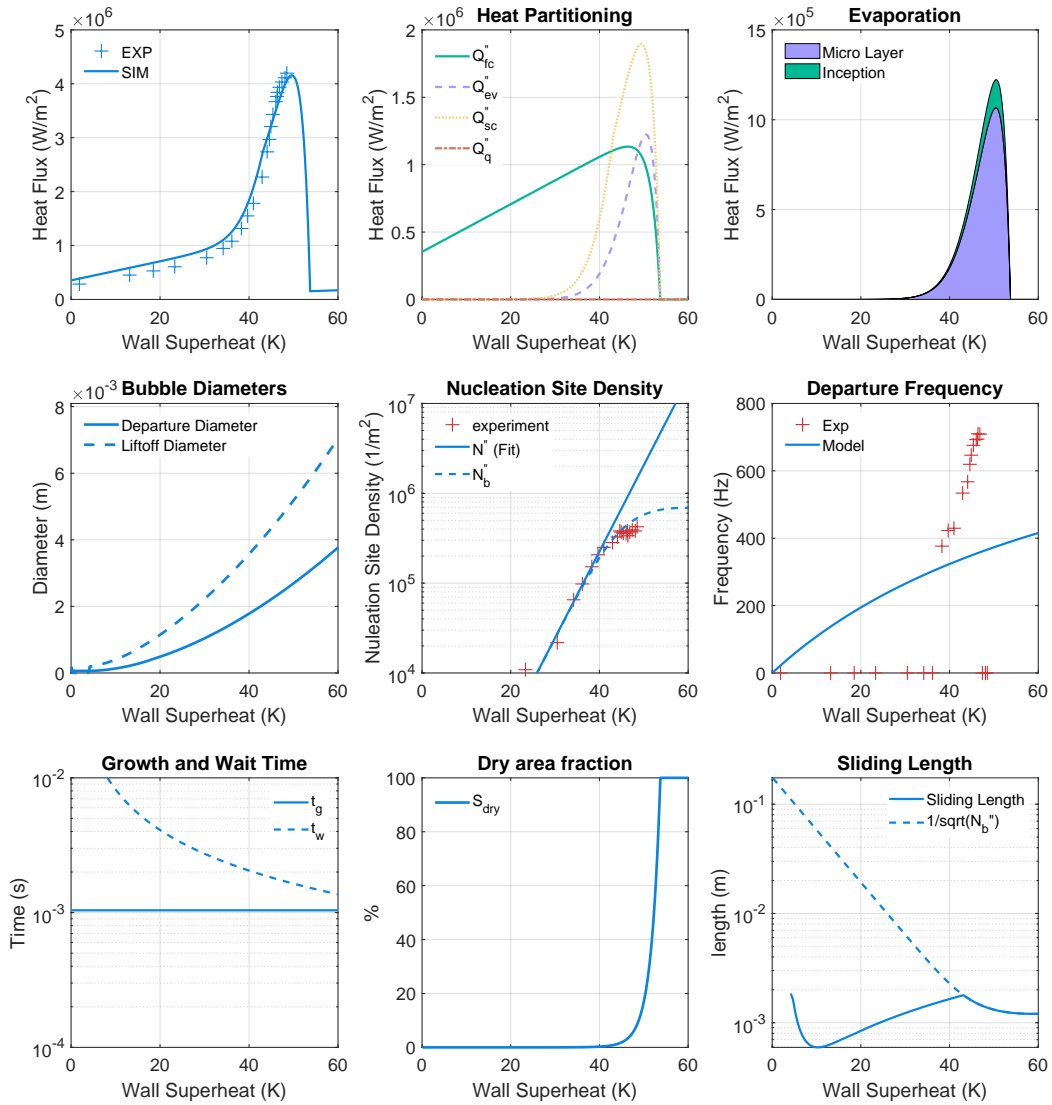


Figure C.13: Case #13, 1 bar, 20 K subcooling, $1000 \text{ kg m}^{-2} \text{ s}^{-1}$

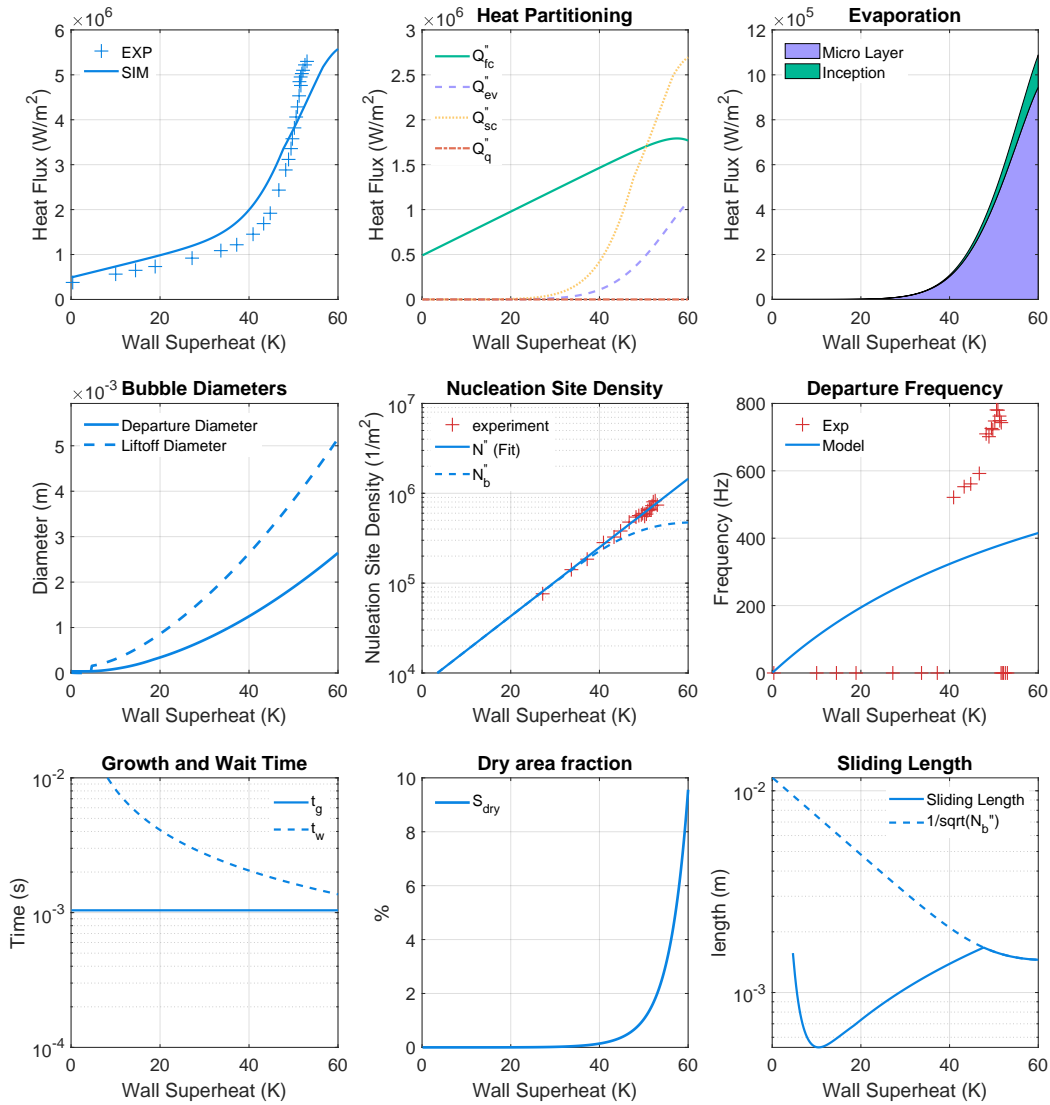


Figure C.14: Case #14, 1 bar, 20 K subcooling, $1500 \text{ kg m}^{-2} \text{ s}^{-1}$

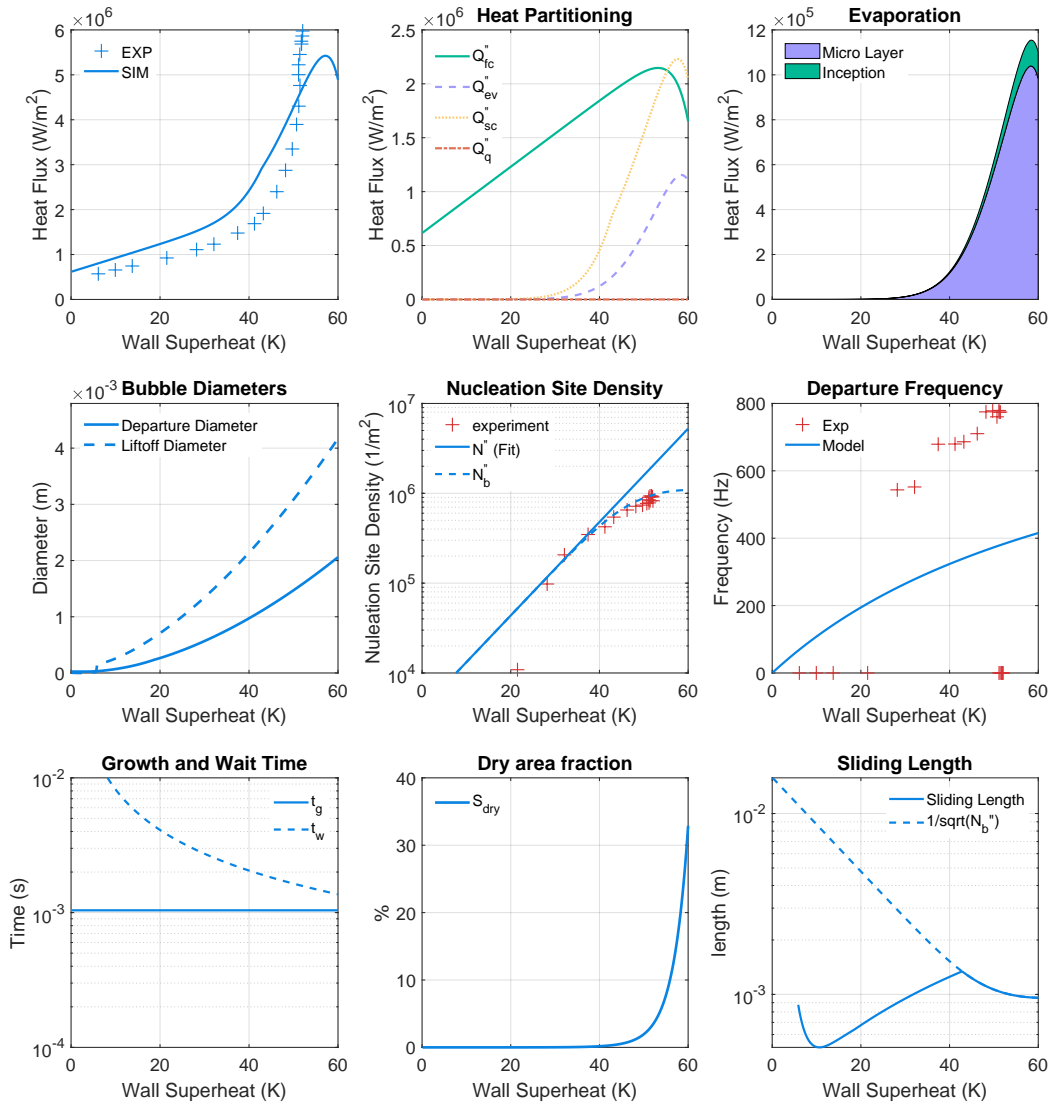


Figure C.15: Case #15, 1 bar, 20 K subcooling, $2000 \text{ kg m}^{-2} \text{ s}^{-1}$

Appendix D

High pressure databases inputs and model CHF prediction

D.1 Jens and Lottes 1951

Table D.1: Jens and Lottes[41] database inputs. 347 Stainless Steel, $L = 0.625$ m $D = 5.74$ mm, $P = 137.9$ bar

Case #	Mass Flux (kg/(m ² s))	Outlet Subcooling (K)	Experimental CHF (MW/m ²)	Simulated CHF (MW/m ²)
1	1302.0	21.67	3.50	3.39
2	1315.5	18.89	3.41	3.44
3	1315.5	22.22	3.38	3.38
4	1315.5	23.89	3.50	3.33
5	1315.5	5.56	3.53	2.96
6	1315.5	18.89	3.28	3.44
7	1315.5	25.56	3.19	3.26
8	5357.1	90.56	9.34	10.33
9	5262.2	75.56	8.93	8.75
10	1315.5	13.33	2.97	3.40
11	5262.2	78.89	8.36	9.09
12	5289.3	65.56	7.95	7.71
13	5357.1	46.67	7.51	5.71
14	10 497.0	71.11	11.90	10.76
15	10 497.0	67.78	11.20	10.32
16	5289.3	26.67	6.81	3.91
17	5316.4	26.67	6.56	3.92
18	5357.1	72.22	9.21	8.44
19	10 497.0	36.67	10.50	6.02
20	5262.2	16.67	5.93	3.93
21	9859.8	24.44	9.53	4.80
22	5248.6	8.89	5.05	3.56
23	10 470.0	18.89	8.90	4.72
24	5262.2	3.61	4.48	3.05
25	10 524.0	5.83	7.19	3.59
26	10 524.0	5.00	7.54	3.48
27	10 565.0	3.06	6.47	3.18

D.2 Hunt et al. 1955

Table D.2: Hunt et al. [162] database inputs. "A" Nickel, $L = 0.318$ m, $D = 5.74$ mm, $P = 137.9$ bar

Case #	Mass Flux (kg/(m ² s))	Outlet Subcooling (K)	Experimental CHF (MW/m ²)	Simulated CHF (MW/m ²)
1	1213.8	67.22	4.61	6.39
2	1216.5	51.67	4.61	4.99
3	782.5	32.22	3.22	2.92
4	3783.9	89.44	9.97	9.42
5	1871.6	60.00	5.33	5.86
6	5574.1	89.44	12.70	10.49
7	7364.3	89.44	14.80	11.58
8	3648.3	61.67	8.17	6.68
9	5397.8	67.22	10.20	8.05
10	1871.6	23.89	4.70	3.48
11	3594.0	50.56	6.94	5.57
12	5221.5	61.11	9.50	7.32
13	7106.6	89.44	9.97	11.43
14	8652.7	89.44	11.80	12.36
15	10524.0	89.44	12.90	13.47
16	1085.0	17.22	2.43	3.37
17	3607.6	37.22	6.21	4.26
18	6523.5	61.67	8.61	7.96
19	1019.9	13.89	2.08	3.31
20	1830.9	17.22	3.94	3.63
21	1898.7	13.89	3.88	3.60
22	3404.1	28.89	5.84	3.49
23	3594.0	24.44	6.94	3.69
24	8408.6	61.67	9.81	8.79
25	9873.4	61.67	10.60	9.43
26	1803.8	13.33	3.22	3.60
27	3390.6	22.78	5.30	3.70
28	3607.6	12.78	6.21	3.66
29	4963.8	31.67	6.75	4.06
30	3255.0	13.89	4.10	3.67
31	3390.6	3.89	5.30	3.04
32	3404.1	7.78	5.84	3.38
33	6428.5	33.89	7.19	4.69
34	7974.6	33.89	7.95	5.10
35	9412.2	33.89	8.55	5.48
36	4787.5	6.11	5.39	3.31
37	4963.8	15.00	6.75	3.88
38	6198.0	20.00	5.96	4.17
39	6211.5	12.22	6.34	3.89
40	7391.5	20.00	6.69	4.36
41	8924.0	20.00	7.07	4.61
42	6021.7	6.67	5.46	3.43
43	5791.1	1.67	4.20	2.80
44	7025.3	2.78	4.92	3.01
45	8340.8	2.78	5.17	3.06

D.3 Weatherhead, 1963

Table D.3: Weatherhead[43] database inputs. 304 Stainless Steel, $L = 0.457$ m, $P = 137.9$ bar

Case #	Internal Diameter (mm)	Mass Flux (kg/(m ² s))	Outlet Subcooling (K)	Experimental CHF (MW/m ²)	Simulated CHF (MW/m ²)
1	7.72	2563.30	31.50	5.36	3.41
2	7.72	2617.50	16.68	4.48	3.64
3	7.72	2712.50	10.33	4.07	3.50
4	7.72	2671.80	5.39	3.60	3.19
5	7.72	2644.70	29.42	5.27	3.25
6	7.72	2644.70	15.75	4.54	3.64
7	7.72	2698.90	7.57	3.88	3.35
8	7.72	2685.30	5.55	3.60	3.20
9	7.72	2007.20	38.63	5.11	3.95
10	7.72	2034.30	24.59	4.51	3.44
11	7.72	2020.80	15.57	4.01	3.63
12	7.72	2007.20	9.81	3.60	3.44
13	7.72	1980.10	2.01	3.12	2.63
14	7.72	1993.70	41.21	5.14	4.17
15	7.72	1668.20	41.21	5.21	4.13
16	7.72	1654.60	29.22	4.32	3.16
17	7.72	1654.60	23.40	4.07	3.47
18	7.72	1736.00	12.83	3.63	3.50
19	7.72	1695.30	3.59	3.09	2.81
20	7.72	1668.20	42.95	5.17	4.29
21	7.72	1654.60	28.81	4.48	3.19
22	7.72	1668.20	21.84	4.07	3.51
23	7.72	1668.20	11.75	3.60	3.44
24	7.72	1681.70	5.22	3.15	2.99
25	7.72	1335.90	25.58	3.63	3.21
26	7.72	1396.90	48.45	4.50	4.72
27	7.72	1350.80	20.48	3.56	3.39
28	7.72	1464.70	53.84	4.95	5.23
29	7.72	1383.40	31.68	4.07	3.21
30	7.72	1410.50	9.81	3.15	3.26
31	7.72	1369.80	63.74	5.33	6.08
32	7.72	1356.20	39.27	4.51	3.86
33	7.72	1356.20	61.64	4.95	5.88
34	7.72	1369.80	46.24	4.51	4.49
35	7.72	1356.20	39.48	4.10	3.88
36	7.72	1353.50	8.59	3.22	3.18
37	7.72	962.92	44.70	4.04	3.99
38	7.72	956.14	23.01	3.15	3.12
39	7.72	931.73	0.61	2.71	2.26
40	7.72	935.80	44.26	4.07	3.93
41	7.72	956.14	39.27	3.60	3.54
42	7.72	942.58	23.01	3.15	3.11
43	7.72	929.02	3.11	2.71	2.61
44	7.72	694.39	8.59	3.60	2.97
45	7.72	733.72	30.86	3.15	2.72

Continued on next page

Table D.3 – Continued from previous page

Case #	Internal Diameter (mm)	Mass Flux (kg/(m ² s))	Outlet Subcooling (K)	Experimental CHF (MW/m ²)	Simulated CHF (MW/m ²)
46	7.72	739.15	30.65	3.47	2.70
47	7.72	705.24	21.84	3.41	3.02
48	7.72	688.97	25.78	3.15	2.83
49	11.07	2075.00	48.45	3.28	4.80
50	11.07	1993.70	14.10	3.01	3.57
51	11.07	1993.70	1.38	2.64	2.50
52	11.07	1925.80	39.70	3.91	4.02
53	11.07	1953.00	23.60	3.60	3.48
54	11.07	2007.20	11.22	3.15	3.47
55	11.07	1993.70	6.38	2.83	3.13
56	11.07	1993.70	2.32	2.52	2.66
57	11.07	2007.20	36.92	4.16	3.78
58	11.07	2061.50	23.01	3.75	3.50
59	11.07	2034.30	14.28	3.42	3.59
60	11.07	2034.30	13.91	3.39	3.58
61	11.07	2034.30	11.75	3.15	3.50
62	11.07	2020.80	5.88	2.83	3.09
63	11.07	2047.90	1.38	2.54	2.51
64	11.07	1344.00	58.18	3.91	5.41
65	11.07	1326.40	42.08	3.60	3.99
66	11.07	1349.40	30.86	3.25	3.04
67	11.07	1356.20	18.57	2.96	3.36
68	11.07	1345.40	10.33	2.64	3.23
69	11.07	1342.70	1.38	2.32	2.43
70	11.07	1344.00	57.49	4.10	5.36
71	11.07	1329.10	41.21	3.68	3.91
72	11.07	1369.80	42.08	3.47	4.02
73	11.07	1356.20	28.60	3.19	3.00
74	11.07	1356.20	18.76	2.83	3.36
75	11.07	1369.80	9.81	2.50	3.21
76	11.07	1410.50	2.01	2.21	2.53
77	11.07	697.10	52.04	3.85	4.25
78	11.07	686.25	32.93	3.47	2.80
79	11.07	672.69	8.08	3.22	2.91
80	11.07	686.25	7.74	2.88	2.91
81	11.07	680.83	1.85	2.79	2.42
82	11.07	684.90	0.92	2.49	2.28
83	11.07	678.12	25.18	3.91	2.82
84	11.07	690.32	66.78	3.79	5.37
85	11.07	687.61	60.25	3.47	4.87
86	11.07	672.69	24.98	3.34	2.83
87	11.07	665.91	21.64	3.02	2.97
88	11.07	660.48	13.01	2.85	3.07
89	11.07	672.69	7.06	2.53	2.86
90	11.07	349.91	13.19	2.78	2.94